University of
Nottingham
UK | CHINA | MALAYSIA

Novel TiO_2 Nanotube Arrays for Photoelectrocatalysis Application

A Thesis submitted to
The University of Nottingham

By

Athil Khairi J. Al-Shihabi Al-Ani

BSc, MSc Chemical Engineering

for the degree of Doctor of Philosophy

School of Chemical and Environmental Engineering
The University of Nottingham
United Kingdom

January 2020

Abstract

The fast-growing energy and environmental concerns have motivated many researchers to move their efforts towards more sustainable and environmentally friendly renewable energy sources, particularly sunlight. Photoelectrocatalysis is a widely accepted technique that has great potential to utilise sunlight to enable desirable chemical reactions with low environmental impacts. This technique can employ an abundant, affordable, non-toxic, and environmentally friendly stable semiconductor as the photocatalyst, such as TiO_2 nanotube arrays (NTAs), to assist water electrolysis in producing a clean fuel under the illumination of solar light.

The present work aims to produce and use TiO_2 nanotube arrays (NTAs) as a photocatalyst formed on the Ti foil as a substrate by electrochemical anodization. The morphology and the performance of the NTAs are expected to be influenced by several parameters involving: electrolyte composition, applied voltage, drying method, and anodization duration. In this study, three parameters have been examined: (1) the drying method (2) anodization duration and (3) water purity (which can be reflected by water conductivity). The results showed that increasing the anodization time could affect the morphology of the as-prepared NTAs and invoke chemical dissolution.

This, in turn, caused aggregation of the nanotubes, rising upward and possibly weakening their adhesion on the substrate (Ti) and peeling them off. Some results confirmed that the sample, which was washed in acetonitrile for dehydration, demonstrated photocurrent density higher by about 2.5 times than that dried naturally in the air. The most prominent finding from this study is the effect of water purity on the NTAs morphology. It was noticed that when deionised water (DIW) was replaced by reverse osmosed water (ROW) in the electrolyte, its conductivity increased by about 8.97 %.

In this study, the simultaneous under-potential deposition of multiple elements was applied successfully to broadly cover the TiO_2 NTAs arrays to form a sensitiser of kesterite (Cu_2ZnSnS_4) to enhance the photoconversion efficiency and the transporting of the charge carrier. This enhancement was achieved by using a modified electrochemical atomic layer deposition (EC-ALD) method. The results have shown that it is extremely challenging to deposit multiple elements onto and maintain the well-organised structure of NTAs at the same time. The complexing agent ethylenediaminetetraacetic acid (EDTA) and the pH of precursor solutions were found to be the key factors to assist the successful simultaneous deposition.

The electrodeposition process, surface morphology, crystalline structure, and photocatalytic activity of the as-prepared Cu_2ZnSnS_4/TiO_2 NTAs were examined. The kesterite crystalline structure of Cu_2ZnSnS_4 was successfully deposited as a single phase.

After the sensitisation with CZTS thin film, an enhancement in photoconversion efficiency from 1.1 % for the pure TiO_2 NTAs to 2.0 % was observed, and the bandgap was reduced from 3.10 to 2.43 eV using the sensitiser Cu_2ZnSnS_4. The thickness of the deposited CZTS layer was estimated to be ca. 5.0 nm. A synergistic effect was observed in the photocatalytic properties of the novel CZTS/TiO_2 NTAs composite, and the hydrogen generation rate achieved a maximum of 49.0 mL $h^{-1}cm^{-2}$.

Applying the EC-ALD to produce the novel CZTS/TiO_2 NTAs photoanode from separate precursor solutions offered a significant improvement in the electrical and optical properties. The average inner diameter of the tubes was ca. 95.0 nm with a thickness of ca. 8.0 nm of CZTS. It was also found that the photocurrent density enhanced to ca. 3000.0 μA with 3-fold enhancement in the photoconversion efficiency. The XRD results showed that the intensity peaks of Cu_2ZnSnS_4 became stronger and sharper than those were observed with the film that deposited from a mixture of the precursors.

The samples that were doped near the inner layer, such as CZTS (50 m) / Ag (10 m) / CZTS (10 m) / TiO_2 NTAs and CZTS (50 m) / Ge (10 m) / CZTS (10 m) / TiO_2 NTAs exhibited a maximum stable photocurrent density of ca. 7.5 mA cm^{-2}. The metal doping near the inner layer was more effective than near the outer or the middle layer on the performance of the CZTS/TiO_2 NTAs composite. The bandgap of the Ag-doped CZTS/TiO_2 NTAs and Ge-doped CZTS/TiO_2 NTAs composites were drastically narrowed to a very close value of 1.88 and 1.86 eV.

A further thicken in the wall of the tubes was estimated to be ca. 10.0 nm (+/–5.0 nm), and the inner diameter was ranging from 85.0 to 90.0 nm after the sensitisation with CZTS followed by the metal doping with Ag and Ge, respectively. A cascade of multiple heterogeneous junctions in a coaxial manner was formed onto the nanotubes after the sensitisation and the doping with CZTS and Ge (the inside and outside surfaces of the walls of the nanotubes were uniformly and homogeneously coated).

Comprehensive advantageous can be merged from the as-synthesised and doped CZTS/TiO_2 NTAs photoanode, involving the significant enhancement in light-harvesting ability, a great cohesion between CZTS and the doped metals (Ge and Ag) and the transporting of the charge carrier that arises from the alignment in the stepwise band edge level of the produced photoanode. This approach probably suitable in synthesising multijunction semiconductor materials for the coating of highly structured substrates.

Contributions at the University of Nottingham

Publications

An abstract entitled ’’Controlling the simultaneous under-potential deposition of multiple elements on TiO_2 nanotube-arrays with enhancement of photocatalytic activity.’’ from the successful current research published in 13th International Conference on Electrochemistry / Barcelona / Spain, J Biosens Bioelectron 2019, volume 10.

July 2018-Dec 2018 Teamwork

Participated in the Young Entrepreneurs Scheme and Engineering YES competition 18. Worked effectively with 4 PhD students from the school of engineering to create a business plan in 4 days workshop at Jubilee Campus. Our group was the only successful group from the University of Nottingham, and we qualified for the final. We presented our business at the Royal Society of Chemistry and gained the trophy of the finalist.

Sep 2017

Attended and received a certificate in the conference organised by the University of Nottingham Energy Technologies Research Institute (ETRI), and the Institute of Physics Thin Films and Surfaces Group. For the same Energy Technologies Research Institute (ETRI), which held at the Jubilee Campus and presented a poster with a variety of postgraduate students from different disciplines.

Nov 2017 and Mar 2017

Participation of attending two conferences organised by the Institute of Materials, Minerals, and Mining (IOm^3),

- At Leicester University, as a postgraduate student, I earned a free membership with this institution (certificate of attending was received).
- At Manufacturing Technology Centre (MTC), Ansty, Coventry.

Oct 2016

Poster presentation at the event of Aida Lovelace at the University of Nottingham.

Apr 2016

Poster presentation at Link 16 Conference. A certificate of participation was received.

Dec 2015

Poster presentation at the Molten Salts & Ionic Liquids Discussion Group (MSDG) group at the Royal Society of Chemistry / London.

Acknowledgments

''My success is from the grace and mercy of God.''

This thesis is the account of my 36-month devoted work in the field of chemical and environmental engineering at The University of Nottingham, UK. I want to express my appreciation to all those who brought me closer to the completion of this thesis.

First of all, I would like to greatly acknowledge my supervisors Dr. Begum Tokay and Professor George Chen, for their crucial and supportive role to succeed in this work. Their motivation helped me a lot to overcome my health issues. Special thanks to Professor Wen Zhu for his continuous support that he provided during the whole period of my study. I cannot find words to describe my appreciation. He was always putting me in the right direction to proceed, like giving the secret keys to unlock the doors.

I want to thank my colleagues, Dr. Junfu Li and Dr. Grace Guan, for their kind assistance in the laboratory. I am also grateful to Dr. Baohe Chong for spending part of his time to tailor the scientific part of my thesis. I am thankful for every help provided by the staff of the Chemical and Environmental Engineering Department at the University of Nottingham.

Also, I appreciate the assistance that I have provided from the staff of Nanoscale and Microscale Research Centre (nmRC) and Wolfson building specifically, Dr. Elisabeth Steer, Dr. Nigel Neat, and Dr. Hannah Constantin, respectively. Dr. Fernandes is gratefully acknowledged for his assistance during the UV-Vis measurements in GSK Carbon Neutral Laboratory for Sustainable Chemistry at the University of Nottingham. A special thanks to the Higher Committee for Education Development in Iraq for their studentship. A Special thanks with love to my husband, Ahmed Jaber and my lovely children (Asif, Answer, Tamarah and Tara) for their unforgettable and hand by hand support to achieve our goals. Special thanks to my sister Hadeel for arranging my finance issues during my studying period. I am thankful to Dr. Amina Alani for her continuous assistance; she has proven that brotherhood is not solely a biological connection but also, offering supporting in crisis.

The continuous praying and encouragement from my parents during my whole life till now are the inspiration for me to go forward. Thanks, from the bottom of my heart to the most fabulous parents ever, whatever I have done is not enough to fulfil their support.

Table of Contents

List of Figures

List of Tables

Abbreviations

TiO_2 NTAs: Titanium dioxide nanotube arrays

CZTS: Cu_2ZnSnS_4

eV: electron volt

UV: ultraviolet

e^-/h^+ pairs: electron/hole pairs

EC-ALD: electrochemical atomic layer deposition

Ag: silver

Ge: germanium

Cu: copper

Zn: zinc

Sn: tin

S: sulfur

FEG-SEM: field emission gun scanning electron microscopy

XRD: x-ray diffractometer

UPD: under potential deposition

CV: cyclic voltammetry or cyclic voltammogram

LSV: linear sweep voltammetry or linear sweep voltammogram

EIS: electrochemical impedance spectroscopy

XPS: x-ray photoelectron spectroscopy

EDX: energy dispersive X-ray spectroscopy

PEC: photoelectrocatalytic or photoelectrocatalysis

CB: conduction band

VB: valance band

hv: photon of energy or energy of a photon

CSC: composite semiconductor

Eg: energy bandgap

RHE: reversible hydrogen electrode

J: photocurrent density

E: potential

A: amper

i: current

SC: semiconductor

ALD: atomic layer deposition

CVD: chemical vapour deposition

PVD: physical vapour deposition

PE-ALD: plasma-enhanced ALD

TFEL: thin film electroluminescent

NHE: normal hydrogen electrode

SILAR: successive-ion-layer-adsorption-reaction

nm: nanometre

μm: micrometre

DIW: deionized water

ROW: reverse osmosed water

CA: complexing agent

OCP: open circuit potential

Chapter 1: Introduction

1.1 Modification of the photoactivity of titanium dioxide nanotube arrays (TiO_2 NTAs)

Environmental pollution and the energy crisis have become two significant problems that are delay the sustainable development of many societies. Photocatalytic technology is one of the most effective pathways for solving these issues (Zhu et al., 2010). Photocatalytic decomposition of water molecules and so provides clean energy from the hydrogen produced, is believed to have the potential to solve the crisis brought about by fossil fuel depletion. This technique is an affordable and feasible way of addressing environmental issues (Zhu et al., 2010). Therefore, continuous efforts should be made to develop new materials that can combine functional properties with both environmental and economic sustainability goals (Scaramuzzo et al., 2014a).

TiO_2 NTAs synthesised on a Ti foil *via* electrochemical anodization are considered as a promising photocatalyst and broadly employed in water splitting applications. Additionally, the hollow nature of these nanotubes and their large surface area can provide unlimited active reaction sites. The large bandgap (ca.3.20 eV) of these NTAs is the reason behind the weakness in the performance of the TiO_2 NTAs that limiting their activity for light absorption in the ultraviolet (UV) range from the solar spectrum. Furthermore, if there are no adequate active reaction sites offered on the surface of the light-harvesting semiconductor, the photogenerated electron/hole pairs, which possess the required potentials for water splitting reactions, will possibly recombine. Therefore, previous researchers have used several techniques to accelerate the photoconversion efficiency and light-harvesting ability of TiO_2 NTAs such as metal-loading, impurity doping, inorganic adsorbates, polymer coating, dye-sensitisation, and charge transfer complexation, which are introduced depending on the utilisation of TiO_2 NTAs surface (Park et al., 2013). Among these techniques, the injection of electrons from other sources is the most applied approach in which two semiconductors with different bandgaps are integrated. A small bandgap semiconductor could be capable of generating photo-induced charges under visible light irradiation. The photo-generated electrons could then be transferred from the conduction bandgap of the small bandgap semiconductor to that of the large bandgap semiconductor by coupling as a composite.

In this regard, the kesterite (Cu_2ZnSnS_4, CZTS) was introduced as a promising candidate semiconductor. This was owing to its direct bandgap of 1.50 eV with a high absorption coefficient ($\propto > 10^4$ cm^{-1}), thus enabling immediate and quick absorption of photons. Besides, CZTS constituents are affordable, abundant, and non-toxic. Although different methodologies have been employed to investigate the electrodeposition of several types of semiconductors (binary or ternary) onto TiO_2 NTAs, most of them have missed highlighting the simultaneous electrodeposition of the quaternary CZTS *via* the underpotential deposition route. The main challenges in this process lie in controlling and managing the deposition parameters, including deposition duration, pH value of the individual precursor solution and the deposition bath, deposition potential (UPD), precursor concentration, and complexing agent concentration to achieve a successful deposition.

1.2 Electrochemical atomic layer deposition (EC-ALD) of nanostructured materials

The demand for an affordable and environmentally friendly technique to enhance the photocurrent generation and photon absorption of TiO_2 nanotube arrays (NTAs), has stimulated research to modify the electrical properties and charge transport of these NTAs. The most effective way to achieve this is by narrowing the bandgap of TiO_2 NTAs by utilising the semiconductor's coating (deposition of metal particles) onto TiO_2 NTAs walls to form a heterogeneous coaxial structure by minimising the deposition at the tube entrances.

Various methods have been employed to integrate the TiO_2 NTAs with sensitisers, including hydrothermal synthesis (Perera et al., 2012), sol-gel (Caruso et al., 2001), electrochemical atomic layer deposition (EC-ALD) and dipping (Wang and Luo, 2011). Generally, the most efficient method is EC-ALD since the other methods clog the nanotubes pore mouth enhances by the precipitation of the sensitiser, thus leading to a decrease in the adsorption capacity, and the specific surface area. The following parameters should meet the requirements of an ideal architecture for the integrated semiconductors: (1) the surface structure, (2) the geometrical structure, and (3) the contact form (Yin et al., 2007, Seabold et al., 2008). The EC-ALD has the advantage of being able to provide a uniform thin film coating of a narrow bandgap semiconductor onto large surface areas of nanostructured substrates. It also enables an efficient and a rapid charge transfer through the coupled semiconductors due to the significant interactions between the deposited layers (the interface properties from the atom-by-atom contact form) (Zhu et al., 2010).

Theoretically, the photocatalytic activity of the TiO_2 NTAs can be modified by the simultaneous underpotential deposition of the quaternary compound Cu_2ZnSnS_4.

The electrodeposition specifically depends on synthesising a successful substrate (highly ordered TiO_2 NTAs) by electrochemical anodization process. Controlling the deposition parameters including the deposition potential (UPD), the concentration of complexing agent ethylenediaminetetraacetic acid (EDTA), pH of deposition bath, deposition duration, and precursor concentration is a key strategy to overcome bulk deposition of metal ions, which may suppress the absorption ability of the nanotubes. Besides, the energy bandgap structure of CZTS/TiO_2 NTAs can be modulated by substituting elements, such as silver (Ag) and germanium (Ge), to meet the requirements needed for overall water splitting reactions and for further improvement in its photocatalytic performance.

1.3 Research motivation, aims and objectives

Improving the bandgap structure of TiO_2 NTAs might play a crucial role in photoelectrocatalytic applications and produce an inexhaustible and clean fuel (H_2) from the solar cell. Coating TiO_2 NTAs by Cu_2ZnSnS_4 (CZTS) *via* the simultaneous under potential deposition is an efficient way to improve the bandgap of these NTAs. Although CZTS has a narrow bandgap to respond to all the visible light, its valence band level is very high (around 0.30 eV, higher than the potential of oxygen evolution). It is unable to produce oxygen by water photolysis and as a result unable to bring about the overall water splitting. It is essential that CZTS to be doped by other elements, such as Ag and Ge to reduce its valence band, and also to enhance its conduction band energy level that is favorable to electron injection into the conduction band of TiO_2 NTAs. Consequently, the energy band structure of CZTS can be modulated by element substitution to meet the requirement of overall water splitting. Based on this, this research has hypothesized synthesising composite semiconductor CZTS/TiO_2 NTAs that can be used in solar cell manufacturing. Moreover, this would produce hydrogen, which is considered a renewable fuel and an alternative to fossil fuel to overcome environmental issues.

The main aim of this work is to:

- Determine and control the simultaneous underpotential deposition conditions of multiple elements (Cu, Zn, Sn, and S) onto TiO_2 NTAs electrodes.
- Produce the sensitiser Cu_2ZnSnS_4 utilising the modified electrochemical atomic layer deposition (EC-ALD) route in order to form the novel photoanode CZTS/TiO_2 NTAs, which will enhance the visible light response and photoconversion efficiency of TiO_2 NTAs.

The major objectives of this thesis are to:

- Determine optimum synthesis conditions for the TiO_2 NTAs, including applied voltage, anodization duration, and electrolyte concentration for repeatable methodology and product quality.
- Characterise the morphology and the crystalline structure of TiO_2 NTAs by using various characterisation techniques such as field emission gun scanning electron microscopy (FEG-SEM) and X-ray diffraction (XRD).
- Determine the optimum Cu_2ZnSnS_4 deposition conditions through precisely selecting the underpotential deposition (UPD) of the three elements (Cu, Zn and Sn) using cyclic voltammetry (CV).

- Evaluate the composition of CZTS elements by X-ray photoelectron spectroscopy (XPS) and energy dispersive X-ray (EDX), respectively.
- Determine the effect of the elemental doping time and position on the enhancement of the photoactivity properties of CZTS/TiO_2 NTAs. Moreover, determine the effect of doping parameters on the movement of photogenerated carriers under light irradiation.
- Measure the hydrogen production rate under light irradiation using a Hoffman voltameter.

1.4 Thesis structure

This thesis is divided into eight chapters.

Chapter 1 is an introduction to the wider perspective of the research area. It then narrows down to highlight the open questions still needing to be investigated. It also explains the motivation and the aim and objectives of the current study.

The background knowledge of this research is reviewed in **Chapter 2,** covering photocatalysis and the approaches to improving the efficiency of photocatalysis. It also discusses the bandgap energy (Eg) of a material, underpotential deposition (UPD), materials for electrodeposition, and the approaches that were employed to fabricate CZTS.

All chemicals and analytical equipment that were used in this research are illustrated in **Chapter 3**. Detailed experimental procedures and a research strategy are also provided.

Chapter 4 discusses the electrical and optical properties of titanium dioxide (TiO_2), techniques for synthesis of TiO_2 NTAs, and the anodization process. The factors affecting the formation of TiO_2 NTAs are also analysed. A comprehensive investigation of the simultaneous underpotential deposition of multiple elements (Cu, Zn, Sn and S) onto TiO_2 NTAs electrodes to form the sensitiser Cu_2ZnSnS_4 by EC-ALD route are reported in **Chapter 5**.

It also considers the parameters affecting the deposition of CZTS onto TiO_2 NTAs, including the effect of UPD potential on the synthesis of the novel CZTS/TiO_2 NTAs composite and the effect of the precursor concentration.

The alternative route for the electrodeposition of CZTS onto TiO_2 NTAs using separate precursor solutions of Cu, Zn, and Sn instead of the mixed one was conducted to prevent the bulk deposition of Cu, and to improve the quality of the deposited film (CZTS), this is illustrated in **Chapter 6**.

Chapter 7 explains the metal ion doping of the as-synthesised CZTS/TiO_2 NTAs and shows the influence of the doping time, which affects the charge transfer between dopant and substrate. It then discusses doping CZTS/TiO_2 NTAs with silver (Ag) and germanium

(Ge) and proceeds to illustrate the determination of the UPD potential of Ag and Ge on pure TiO_2 NTAs and CZTS/TiO_2 NTAs. Finally, this chapter depicts the characterisation of the doped CZTS/TiO_2 NTAs and reveals the conclusions of the interesting findings.

Chapter 8 summarises the highlights of the results and conclusions for the whole thesis and provides recommendations for future researchers.

Chapter 2: Literature review

2.1 Photoelectrocatalysis

Recently, there have been two fundamental problems that have delay the further development of society: environmental pollution and the energy crisis. The pioneer workers in the field have focused on photo-electrocatalysis technology that is expected to be an effective solution to solve these problems. Photoelectrocatalysis is an affordable process and capable of addressing the crisis due to the depletion of fossil fuel. This technique provides clean hydrogen energy by harvesting solar energy *via* the water-splitting process. The consolidated principles of the photoelectrocatalysis technique have gained in importance and are now effectively applied in organic compound oxidation, inorganic ion reduction, microorganism inactivation, hydrogen and electricity production, and CO_2 reduction (Bessegato et al., 2015).

The term "photoelectrocatalysis" described as a combination of photoelectrochemistry and photocatalyst activates under the light irradiation. The photocatalyst modifies the rate of a chemical reaction without being involved in the chemical transformation (Serpone and Pelizzetti, 1989, Kisch, 2014). It was found that the term Photoelectrocatalysis was a useful term indicating where all photoelectrochemical reactions take part (Figure 2-1).

Photocatalytic reactions may exist in two forms: homogeneous and heterogeneous. In recent years, the heterogeneous photocatalysis has been intensively studied, owing to the variety of environmental and energy-related applications (Kondarides, 2010b). The reaction scheme involves the formation of an interface between a solid photocatalyst (semiconductor) and a solution containing the reactants and the products. Fujishima and Honda (1972) revealed that various types of semiconductors could be used as a photocatalyst to accelerate heterogeneous photocatalysis.

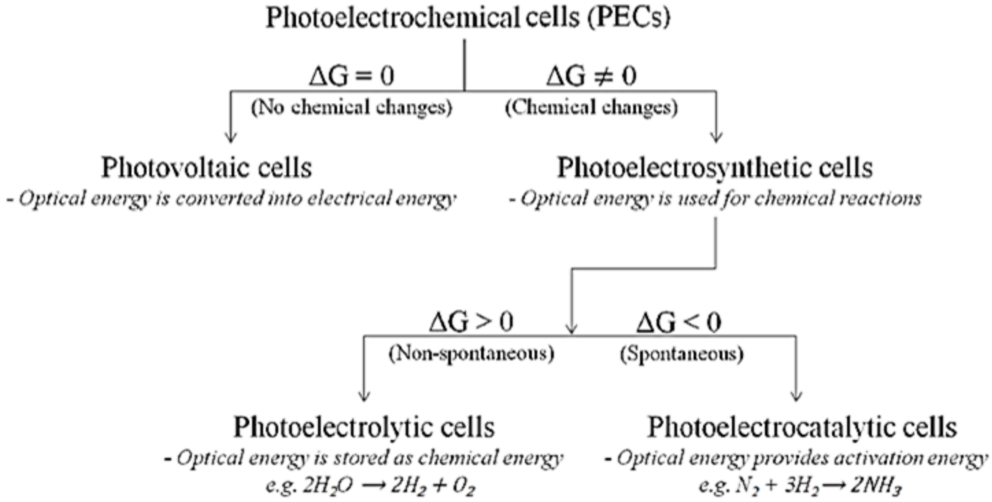

Figure 2-1: The classification of PECs by the Gibbs free energy change (Kim, 2014).

Classical heterogeneous catalysis is carried out in five steps (Ibhadon and Fitzpatrick, 2013) which are:

1. The reactants transferred to the surface through the fluid.

2. At least one reactant adsorbed on a surface.

3. The reaction takes place in the adsorption phase.

4. The products will be desorbed

5. The products removed from the region of the interface.

Conceptually, the photocatalytic reaction arises in the adsorption step; therefore, it can be distinguished from the conventional catalytic reaction; thus, the only difference lies in the activation mode. The conventional catalyst is activated thermally while the photocatalyst activates by light irradiation. It was reported that if the photocatalyst is in the excited state, the Gibbs free energy becomes greater than the activation energy of the reaction (Ohtani, 2010). Therefore, since the reaction will spontaneously occur, no additional energy sources are required to activate the photocatalyst. At this point, it is vital to notice that a photocatalyst will not be less than the activation energy of the reaction in comparison to a catalyst. Furthermore, two intrinsic parameters will play a vital role in inducing the non-spontaneous ($\Delta G>0$) and spontaneous ($\Delta G<0$) reactions: the standard potential of the half-cell reaction and the energy band structure of the photocatalysts. Kondarides (2010a) states that types of semiconductors, such as Si, CdS, ZnS, CdSe, ZnSe, ZnTe, GaAs, GaP, ZnO, $KTaO_3$, Ta_2Os, $SrTi0_3$, and TiO_2, are considered as the most appropriate photocatalysts used in photocatalytic reactions. Probably, this can be attributed to their unique physical and chemical properties. For instance: lifetimes of the excited state, electronic structure, charge transport characteristics, and ability to absorb the light. When the semiconductor is exposed to the light, the electrons will absorb a photon of energy hv equal to or higher than the bandgap energy (forbidden gap exists between the top of the valence band and the bottom of the conduction band ranged between 1.0 to 6.0 eV) of the semiconductor (Dilli, 2009). Therefore, in heterogeneous photocatalysis, the light plays a vital role in ejecting an electron from the filled valence band (VB) to the conduction band (CB) leading to the creation the electron/hole pairs (e^-/h^+) in the interface of the semiconductor leaving behind an empty state available (hole) (Equation 2-1) for another electron in the valence band energy levels (Daghrir et al., 2012, Dilli, 2009, Othmer, 1983) (Figure 2-2).

$$Sc + hv \rightarrow h_{VB}^{+} + e_{CB}^{-} \qquad \text{Eq. 2-1 (Othmer, 1983)}$$

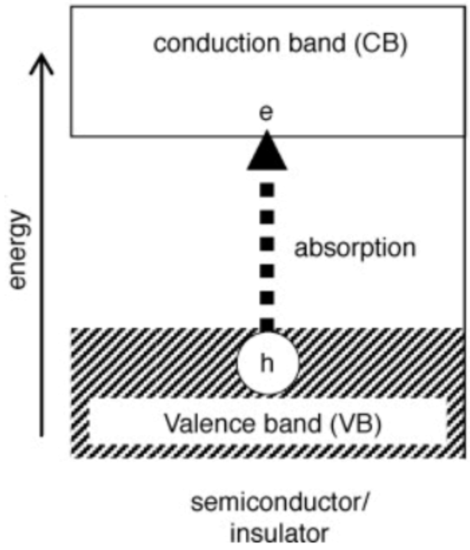

Figure 2-2: Photoabsorption by the transition of electrons in the valence band (VB) to the conduction band (CB) in a semiconductor (Ohtani, 2010).

In the presence of an electric field, the lifetime of the photogenerated species (charge carriers) will increase, and electron/hole pairs will be separated and adsorbed on the surface of the photocatalyst and invoke the chemical reactions. Figure 2-3 shows the difference between the surfaces of a catalyst and a photocatalyst that is excited by light illumination.

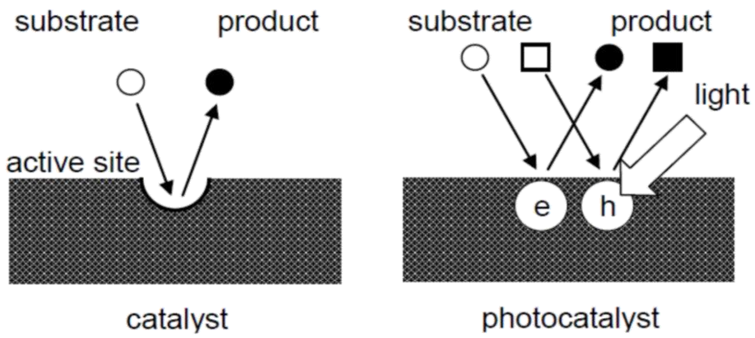

Figure 2-3: Difference in concepts of catalytic and photocatalytic reactions: A catalyst contains active sites of which a substrate is converted into a product, while no active sites are present on a photocatalyst (Ohtani, 2010).

2.1.1 Water splitting thermodynamics, kinetics and hydrogen production.

Water splitting by using solar energy has attracted considerable attention since the 1970s. The solar water splitting approaches include photocatalytic water splitting with homogeneous or heterogeneous photocatalysts and photoelectrocatalytic (PEC) water splitting with a PEC cell. Among these, the production of clean and renewable hydrogen fuel from water by heterogeneous photoelectrocatalytic techniques is considered the most promising approach (Chang, 2013). The main key sequences involved in the overall photocatalytic water splitting, are: (1) generating electron/hole pairs due to light absorption by a semiconductor, (2) charge separation and migration to the surface of the semiconductor, and (3) surface reactions for water reduction or oxidation (Ni et al., 2007).

Various methodologies have been applied in order to improve both the photocatalytic mechanism involved and to improve the ability to absorb a comprehensive spectrum of solar energy for semiconductor materials of wide bandgap (bandgap engineering) (Ni et al., 2007). Additionally, in order to gain an effective charge separation and migration, it is crucial to tune the physical properties of materials engineering, such as crystallinity, crystal structure, and particle size.

Nevertheless, if there are no adequate active reaction sites on the surface of the light-harvesting semiconductor, the photogenerated e^-/h^+ pairs, which possess the inherent potentials for the reactions of water splitting will recombine. Thermodynamically, the water-splitting reaction is considered as a hard reaction with $\Delta G = 237.0$ kJ mol^{-1} equal to 1.23 eV involving multiple electron transfer processes. From the same point of view, Hashimoto et al. (2005) revealed that when the semiconductor was utilised either as photocathode or photoanode for water electrolysis, the bandgap should be as a minimum 1.23 eV, which is the balance cell potential for water decomposition at 25.0 ℃ and 1.0 atm. They also found that despite many semiconductors of small bandgaps have been examined, none of them have succeeded in the water photoelectrolysis with visible light. In most cases, these photocatalysts have eroded in an aqueous electrolyte under illumination, i.e., the semiconductor was oxidised by the photogenerated holes required to facilitate the photocatalytic reactions on the surface. Therefore, to select the suitable photocatalyst for a water-splitting system, it is essential to examine hydrogen and oxygen evolution in the presence of sacrificial reagents donors and acceptors, respectively (Yang et al., 2013).

Moreover, Ravelli et al. (2009) stated that the metal oxide semiconductors, e.g. TiO_2 nanotube arrays (NTAs), ZnO and Cu_2O can satisfy the need of photocatalytic water splitting in which a suitable semiconductor must has a conduction band minimum (CBM) with an energy level more negative than the standard reduction potential (0 V vs. normal hydrogen electrode (NHE)). For instance, if the TiO_2 NTAs is employed as a photocatalyst under irradiation of light, highly oxidative holes will be produced. This is due to the valence band maximum (VBM) of TiO_2 NTAs that comprises of an O (2p) orbital (bandgap) and located at 3.0 eV vs. NHE (Kim, 2014).

Although utilising TiO_2 NTAs for photocatalytic water-decomposition technology is a cost-effective and environmentally friendly technique, which facilitate the production of the future economic hydrogen fuel, there are significant barriers, which hinder this process: (1) The weak activation of TiO_2 NTAs by visible light (2) the rapid recombination of photo-generated electron/hole pairs and (3) backward reaction (Ni et al., 2007).

Thus, several researchers have developed effective methods to overcome these problems. To prohibit the backward reactions and the rapid recombination of electron/hole pairs, some investigators have examined the effect of the addition of carbonate salts and sacrificial reagents. Other studies have focused on modifying TiO_2 NTAs *via* enhancing the photocatalysis properties using composite semiconductors, metal loading, dye sensitisation, metal ion doping, anion doping, and metal ion implantation.

The previously mentioned technologies have been developed and applied to TiO_2 NTAs for photocatalytic hydrogen production (Ni et al., 2007). Figure 2-4 illustrates the illumination of TiO_2 NTAs with light energy higher than its bandgap; this will lead to the production of electron/holes pairs, which are capable of invoke the chemical reactions (Ibhadon and Fitzpatrick, 2013).

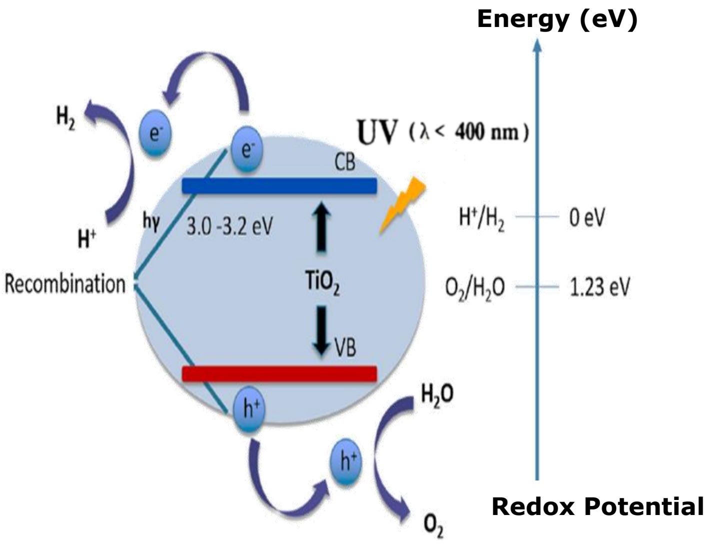

Figure 2-4: Schematic diagram for the illumination of TiO_2 with light energy higher than its bandgap (Jafari et al., 2016).

In response to the fundamentals as mentioned earlier, the mechanism of water-splitting are explained in the following equations (Yang et al., 2013):

Water oxidation half-reaction:

$$2H_2O + 4h^+ \rightarrow O_2 + 4H^+ \qquad \text{Eq. 2-2}$$

Reduction half-reaction:

$$2e^- + 2H^+ \rightarrow H_2 \qquad \text{Eq. 2-3}$$

Overall water splitting

$$H_2O \rightarrow {}^{1}/_{2}\, O_2 + H_2 \qquad \text{Eq. 2-4}$$

2.1.2 Reaction thermodynamics of photoelectrocatalytic (PEC) in photoelectrolytic and photoelectrocatalytic cells

The fundamental difference between the two PECs cell is the redox couple will reduce either by e- or oxidised by h$^+$. Both spontaneous and non-spontaneous overall reactions can be initiated if a redox reaction involved photo-excited charge carriers, which will chemically separate into two-compartment PEC, and both ΔG_h^+ and ΔG_e^- are negative (Figure 2-5).

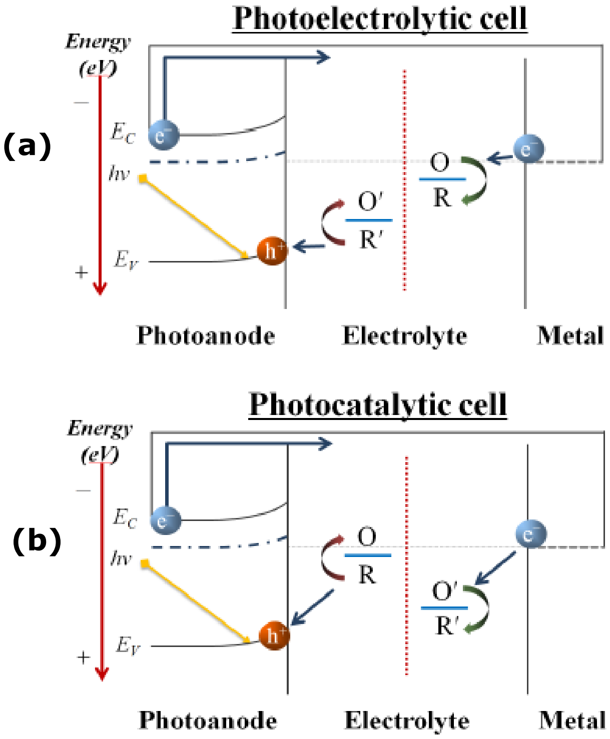

Figure 2-5: Schematic diagram of (a) a photoelectrolytic cell and (b) a photoelectrocatalytic cell when an n-type semiconductor is used as a photoanode material (Kim, 2014).

The photoelectrocatalytic reaction involves two redox couples (O/R and O'/R') where the standard potential of O/R is more negative than that of O'/R', while in the photoelectrolytic cell the reduction reaction by h^+ involves only the redox O/R, and in the oxidation (by O^-) only the redox O'/R' takes part (Figure 2-5-a and b). The overall reaction and half-cell reactions of a photoelectrocatalytic cell can be described as follows (Kim, 2014):

Overall reaction of a photoelectrocatalytic cell:

$O' + R \rightarrow R' + O$ Eq. 2-5

Cathode reaction: $\mathrm{O}' + \mathrm{ne}' \rightarrow \mathrm{R}'$ Eq. 2-6

Anode reaction: $\mathrm{R} \rightarrow \mathrm{O} + \mathrm{n}'$ Eq. 2-7

The following equations can calculate the standard cell voltage:

Standard cell voltage (E^0 Cell)

$= E^0$ (O'/R', reduction) + E^0 (R/O, oxidation)

$= E^0$ (O'/R', reduction) — E^0 (O/R, reduction) Eq. 2-8

Assume:

E^0 (O/R, reduction) $<$ E^0 (O'/R', reduction) Eq. 2-9

According to Figure 2-1, the standard cell voltage of a photoelectolytic cell should be negative; therefore, ΔG becomes positive as shown in the following equation:

$\Delta G = -nFE^0$ cell Eq. 2-10

where ΔG is the Gibbs free energy change for the overall reaction (kJ), n the stoichiometric number of electrons involved in the reaction, F the Faraday constant (C mol^{-1}) and E^0 Cell is the cell voltage (V).

In contrast, the redox O'/R' of a photoelectrocatalytic cell is reduced by O$^-$ while O/R oxidises by h$^+$, this can be described in the following equations:

The overall reaction of a photoelectrocatalytic cell:

$O' + R \rightarrow R' + O$ Eq. 2-11

Cathode reaction: $O' + ne' \rightarrow R'$ Eq. 2-12

Anode reaction: $R \rightarrow O + ne'$ Eq. 2-13

The standard cell voltage of the photoelectrocatalytic cell can be obtained by the following equations:

Cell voltage (E^0 Cell)

= E^0 *(O'/R', reduction)* + E^0 *(R/O, oxidation)*

= E^0 *(O'/R', reduction)* — E^0 *(O/R, reduction)* Eq. 2-14

The Gibbs free energy and the standard voltage of the photoelectrocatalytic cell will be positive and negative, respectively (Equations 2-10 and 2-9)(Kim, 2014).

As a summary, the overall chemical reaction in a PEC is mainly controlled by the photo-induced electron/hole pairs, which are induced by the redox couples, not the electronic structure of the photocatalyst. The optical energy generated from PEC is stored as chemical energy if the overall reaction in a PEC reduced by e$^-$, thus, the overall reaction becomes non-spontaneous since the redox couple has a standard potential more negative than that of another redox couple (Kim, 2014). In contrast, the optical energy is used to overcome the activation energy of a given reaction when the overall reaction becomes spontaneous.

2.1.3 Composite semiconductors (CSC)

During the photocatalytic reactions, the recombination between electron/hole pairs may occur at the surface of the semiconductor; this relates to the defects in the crystalline structure (Hoffmann et al., 1995, H. Kisch 2012). In order to inhibit the possibility of charge carrier recombination, several routes have been investigated to improve the photocatalytic efficiency. The fabrication of semiconductor composites is considered a promising and highly effective strategy to design an active photocatalyst system (Marschall, 2014). Rajeshwar et al. (2001) have defined the semiconductor-based composite as attractive materials that are employed in a variety of optoelectronic applications, including light-emitting devices and optical switches. Table 2-1 depicts some CSC, and their corresponding wavelength cut off limits. As shown in this list, the values of bandgap energy 0.1, 1.5 and 4.0 eV, which are in the regions of infrared and visible are ultimately approaching those of insulators.

Table 2-1: Some elemental and compound semiconductors and their optical characteristics. Reprinted from [(Rajeshwar et al., 2001)].

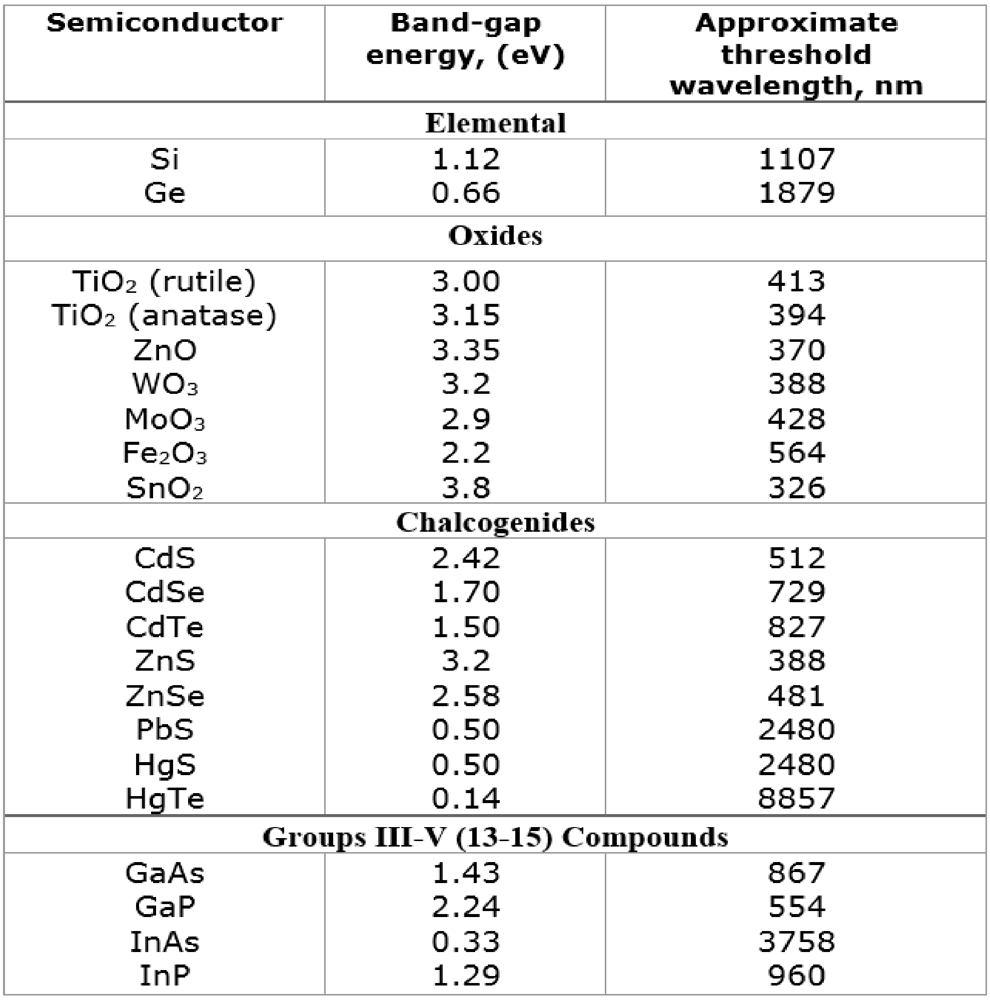

Semiconductor	Band-gap energy, (eV)	Approximate threshold wavelength, nm
Elemental		
Si	1.12	1107
Ge	0.66	1879
Oxides		
TiO_2 (rutile)	3.00	413
TiO_2 (anatase)	3.15	394
ZnO	3.35	370
WO_3	3.2	388
MoO_3	2.9	428
Fe_2O_3	2.2	564
SnO_2	3.8	326
Chalcogenides		
CdS	2.42	512
CdSe	1.70	729
CdTe	1.50	827
ZnS	3.2	388
ZnSe	2.58	481
PbS	0.50	2480
HgS	0.50	2480
HgTe	0.14	8857
Groups III-V (13-15) Compounds		
GaAs	1.43	867
GaP	2.24	554
InAs	0.33	3758
InP	1.29	960

The synthesis of composite semiconductors is critically affected by some fundamental properties, which play a vital role in the performance of the composite semiconductors as a photocatalyst. These include Optical, optoelectronic, and photoelectrochemical properties, semiconductor-based composite architectures, and preparation methodologies. Regarding the optical properties, the energy bandgap (Eg) critically effects the optical response of a semiconductor (Smith, 1964).

Previous researchers (Pleskov and Gurevich, 1986, Sato, 1998, Finklea, 1988, Ibanez and Rajeshwar, 1997) intensively studied the photophysical and electrochemical phenomena of composite semiconductors resulting from a medium capable of undergoing charge transfer as the redox agent involved in a liquid. They also had an interest in composite photoelectrochemical systems in the solid phase in contact with the redox medium (such as metals or polymers) in addition to the semiconductor element.

The semiconductors with a wide bandgap such as TiO_2 can be employed in a composite photocatalysis system in the presence of light illumination to accelerate the reaction rate on the surface of the semiconductor; therefore the photogenerated holes will be oxidised, and O_2 will be reduced by the electrons (Rajeshwar and Ibanez, 1995). As regards the architectures of the composite semiconductors, the phase of the semiconductor considered a critical factor is in building a composite system, either as two semiconductors dispersed in a continuous matrix (Figure 2-6-a) or as a composite resulting from alternating stacked layers (Figure 2-6-b).

In some composites, the nanoparticles of semiconductors are coated with a normal wide bandgap semiconductor in a core-shell geometry (Figure 2-6-c). This coating will enhance the light-emissive performance such in the compound (CdSe)ZnS. In different geometries, the particles of the semiconductors were physically contacted (coupled or decorated) (Figure 2-6-d).

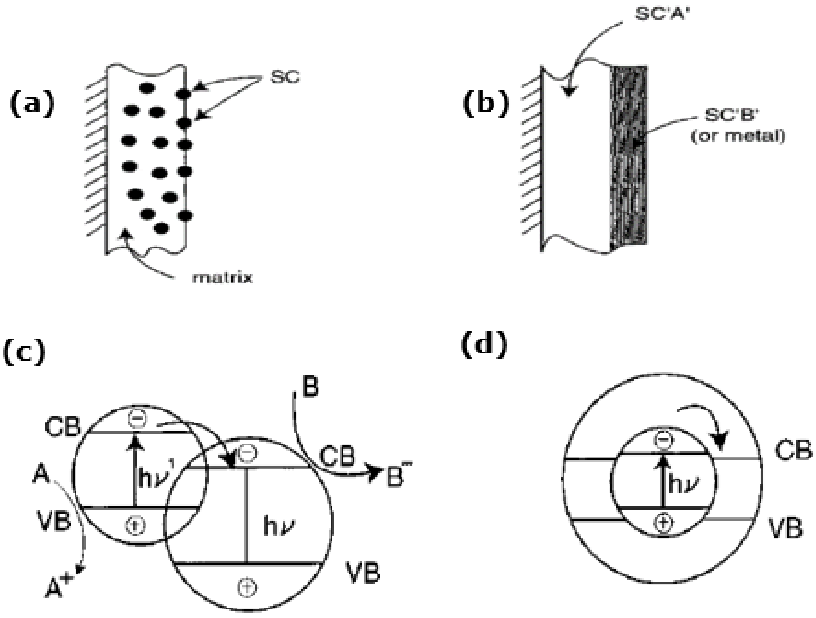

Figure 2-6: Schematic diagrams of four types of semiconductor-based composite architectures: (a) semiconductor/matrix; (b) layered configuration; (c) core-shell geometry; and (d) coupled semiconductors.

Among these CSc the two configurations c and d are particularly interesting and considered to have significant consequences dependant on their ability to enhance the photoelectrochemical properties. Furthermore, several types of semiconductors could be utilised to build composite systems, especially groups II-VI and III-V compounds, since they are prone to anodic photo corrosion in aqueous media (Bard and Wrighton, 1977, Gerischer, 1977, Meissner et al., 1988). In terms of preparation strategies, the main tasks for the researchers are activating the light absorption ability from UV to the visible region. These routes will be explained in section (2.2.). Generally, the key specifications that are highly desired and indeed, are required to design an ideal composite semiconductor (photocatalyst) (Marschall, 2014) are:

- High crystallinity
- Large surface area and good charge carrier separation
- Optimum band positions
- High chemical stability material
- Low cost

2.1.4 Current-potential relations under dark and irradiation conditions

In a PEC cell, which includes an n-type photoanode the hydrogen is normally generated at the cathode, and oxygen is generated at the anode. The electronic configuration (Fermi level) of the photoelectrodes can be controlled aided with a potentiostat. Therefore, the reaction conditions can be improved since a selected potential may be applied to control the redox reactions (Figure 2-7).

In order to obtain a photoanode semiconductor with highly photoinduced separation and charge transfer, it is worthwhile trying to find a tool powerful enough to study the semiconductor/electrolyte interface and the reaction kinetics (Li and Wu, 2015). Efforts have been made to establish standard methods to examine the performance of PECs (Chen et al., 2013b). One such tool was found to be an effective way to test the photoelectrochemical properties based on the relationship between the photocurrent density–voltage (J–V) curves.

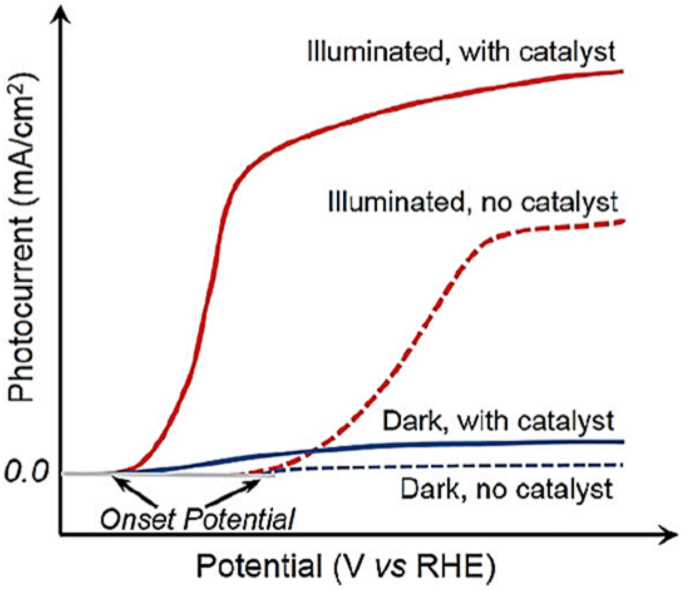

Figure 2-7 : Schematic illustration of photocurrent density–voltage curves obtained from an n-type semiconductor photoanode (Li and Wu, 2015).

Typically, to study the long-timescale charge recombination behaviour for a semiconductor photoelectrode, it is essential to acquire the transient photocurrent (Tafalla et al., 1990).

Theoretically, at an n-type photoanode, either e^- or h^+ are required for the interfacial charge transfer. When the dynamic equilibrium starts at the interface, the cathodic current flows once the oxidised species are reduced ($H^+ \rightarrow H_{ads}$ in Figure 2-8).

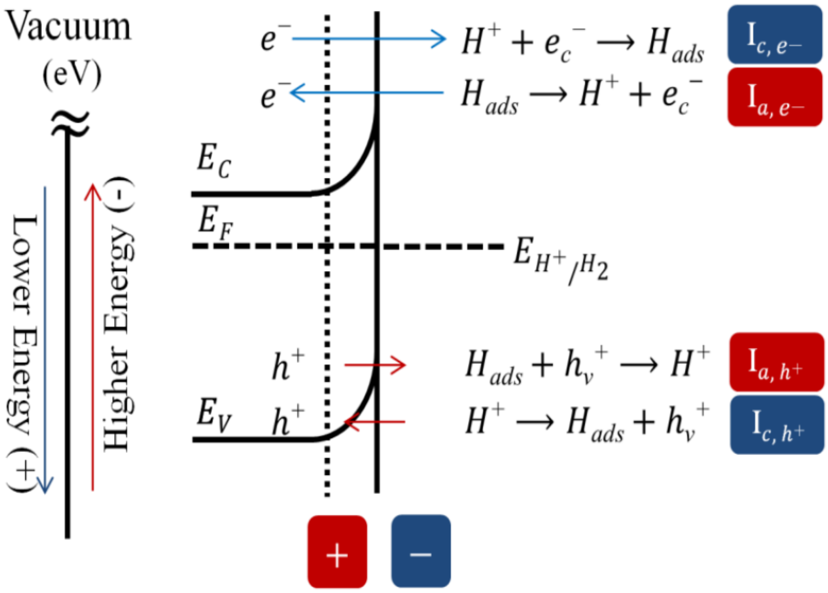

Figure 2-8: Energy diagram represents the opposite charge transfer processes by electrons and holes at the n-type semiconductor and electrolyte (H^+/H_2) interface (Kim, 2014).

Conversely, the anodic current flows across the interface when the current flow direction changes (reverse reaction occurrence). The overall net current at the interface expressed in the equation below:

Overall net current at the interface:

$$i = i_{e^-} + i_{h^+} = \left(i_{a,e^-} - i_{c,e^-}\right) + \left(i_{a,h^+} - i_{c,h^+}\right) \qquad \text{Eq. 2-15}$$

where:

i_{e-} is the net current induced by e-, i_{h^+} the net current induced by h^+, i_{a,e^-} the anodic current by e-, i_{c,e^-} the cathodic current by e-, i_{a,h^+} the anodic current by h^+ and i_{c,h^+} the cathodic current by h^+. Normally, in comparison with the major charge carrier density in an extrinsic semiconductor, the majority of them are negligible.

In an n-type semiconductor, since h^+ is considered the charge carrier, thus, it can neglect the small current produced by h^+ (Eq. 2-15*).* The photocurrent density (mA cm^{-2}) is a principal performance indicator for a PEC at an applied voltage of 1.23 and 0.00 V (vs. RHE, the reversible hydrogen electrode) for a photoanode and photocathode, respectively (Figure 2-8). The drastic increase in the numbers of the majority charge carrier causes the occurrence of the photocurrent density.

The optical performance can also be confirmed by quantitatively measuring the solar-to-chemical energy conversion efficiency (η) in the presence of an external bias to drive a redox reaction (Chen et al., 2013b) (Equation 2-16):

$$\eta = \frac{J\,(V_{redox} - V_{app})}{P_{light}} \qquad \text{Eq. 2-16}$$

where J is the measured photocurrent density (mA cm^{-2}), V_{redox} is the reaction redox potential, for electrochemical water splitting V_{redox} = 1.23 V, V_{app} is the applied external bias (open circuit potential, V), and P_{light} is the measured intensity of the full spectrum solar radiation (mW cm^{-2}).

For further validation, the quantum efficiency can be quantified by the incident photon-to-electron conversion efficiency (IPCE), which is calculated according to the following equation (Chen et al., 2013b):

$$\mathrm{IPCE} = 1240.\mathrm{J}/\lambda.P_{\lambda} \qquad \text{Eq. 2-17}$$

where:

λ: The wavelength of the incident light (nm)

P_{λ}: The measured irradiance at the specific wavelength (mW cm^{-2}).

2.2 Approaches to improve the photoefficiency of the photocatalyst

Employing semiconductors as photoelectrodes for PEC applications has prompted the previous and recent researchers to examine the optical and electrical properties of SC, which can be modified to meet the water splitting requirements. Since the 1980s, numerous approaches have been investigated as an attempt to inhibit the charge carrier recombination in heterogeneous photocatalysis.

It is essential to mention that there are several factors may affect the photoconversion efficiency; thus, various techniques have been introduced. These techniques could be classified according to the following categories:

1. Suppression of recombination (enhance the photogenerated electron/hole pairs for surface reactions) by:
    - Hole removal (Figure 2-9-a), where electron donners will be injected as sacrificial agents or hole scavengers. This technique requires continuous electron injection during the process.
    - Electron migration (Figure 2-9-b). If the metals having Fermi levels lower than that of the photocaralys, the photo-induced electrons can be transferred to the noble metal particles loaded on the surface of photoctalyst.
    - Travel distance reduction (Figure 2-9-c). Reduce the recombination by using nano-sized semiconductor materials

which capable to enhance the photo-induced charges at the surface reactions sites.

2. Suppression of backward reaction (the evolution of hydrogen and oxygen) by:
    - A thin film photocatalyst is used to separate H_2 and O_2 aided with H-type glass container. The photo-induced electrons transfer towards the metal substrate. The migrated e- then will reduce H^+ to H_2 on the catalyst sites. In contrast, the photo-induced holes will oxidise H_2O to O_2 at photocatalyst surface (active sites) (Figure 2-9-d).
    - Using Z-scheme system with two photocatalyst (Figure 2-9-e). For H_2 and O_2 revolution, a reverse redox mediator (OX/Red) is used as an electron donor and acceptor, respectively. Although the recombination can be suppressed with this mediator, it will continuously consume the photo-generated charges. Thus, the redox potential of the mediator should be between the H_2 valance band and O_2 conduction band evolution positions.
    - Using carbonate salts for indirect O_2 revolution (Figure 2-9-f). Carbonate radicals will be formed when the carbonate salt forms a coated layer once it is added to the system, which will react with photo-induced holes. The decomposition of peroxycarbonates that generated a complex reaction will assist the O_2 evolution, i.e., it is consider indirect evolution in

comparison with the H_2 which evoluted on the surface of the photocatalyst in such system.

3. Harvesting the visible light (increase photogenerated e^-/h^+ pairs under light illumination) by:
    - Narrowing the band gap energy (Figure 2-9-g) *via* (1) implanting metal ions physically into the lattice of the photocatalyst which attacked the surface at high voltage, such as Fe, Ni, V, Cr and Mn, etc. In this method the implanted ions will not consider as a recombination centre since it does not form the impurity energy level (Ni et al., 2007, Anpo et al., 2001), (2) Chemical doping with anions such as C, S, F, N, etc. this lead to shift the top of the valence band indicating to the replacement of Oxygen in the lattice.

      However, this method is less effective than implanting metal ions regards the less effect on the improvement of photocatalytic activity (Asahi et al., 2001) and (3) Chemical doping of rare metal ions which replaced the original metal ion into the lattice of the photocatalyst. This assist to form the impurity energy level where the photo-induced charges are trapped causing the reduction in the band gap. If the dopant ions concentration is too high, it will act as a recombination centre (Ni et al., 2007).
    - Electron injection from other sources (Figure 2-9-h) *via* (1) Utilising a dye sensitisation that has visible light sensitivity.

Under light illumination the dye is capable to inject electron into the conduction band of the photocatalytic. The dye will renewed aided with the sacrificial agents added to the solution or by the redox system (O'regan and Grätzel, 1991, Dhanalakshmi et al., 2001) and (2) Using a composite configuration by merging small band gap and large semiconductors is the most effective way to generate the photo-induced charges under visible light irradiation (Figure 2-9-i) (Crap, 2004).

The popular strategy is the decoration of photocatalyst materials with metal nanoparticles: The Fermi energy of the metal nanoparticle is usually lower than that of the semiconductor, facilitating electron transfer from the semiconductor to the metal *via* the Schottky-contact. The most commonly applied metals for such decoration include platinum (Pt), palladium (Pd), gold (Au), or rhodium (Rh) (Sakthivel et al., 2004, Ismail et al., 2013, Merka et al., 2012) due to their noble and/or catalytic character, but more abundant elements such as cobalt (Co) and nickel (Ni) (both as nanoparticles and complexes) have been applied (Tran et al., 2012, Wang et al., 2012, Artero et al., 2011).

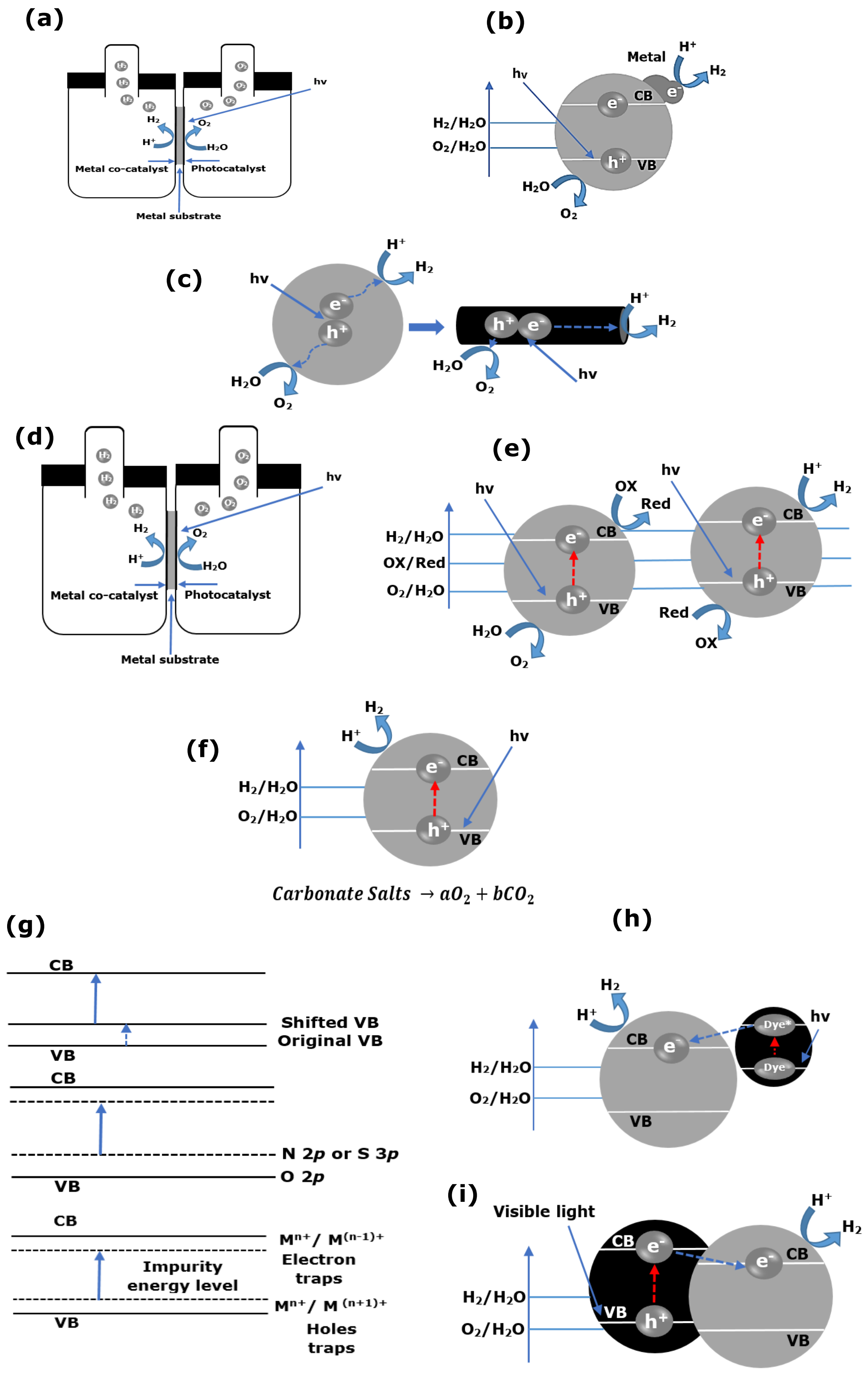

Figure 2-9: Techniques for the suppression the recombination.

2.2.1 Fundamentals of atomic layer deposition (ALD)

Several deposition techniques have been utilised to grow a thin film. It is necessary to briefly describe the other techniques before discussing the atomic layer deposition (ALD). These techniques are chemical vapor deposition (CVD) and physical vapor deposition (PVD). Each technique has advantages and disadvantages. In CVD, the process is performed in a specific reactor in which a solid material is deposited onto the heated substrate surface resulting from the gas phase chemical reaction; this allows the deposition of the thin film at a high rate (Kääriäinen et al., 2013). Several types of chemical reactions can occur, including reduction, oxidation, compound formation, disproportionation, and pyrolysis (Zhu and Zäch, 2009). Suntola (1989) stated that the precursor in CVD should satisfy specific requirements:

- having no association or reaction in the gas phase
- easy to decompose to the desired product at an acceptable temperature
- having sufficient vapor pressure to allow transport to the substrate surface

On the other hand, the PVD breaks down into two main processes: evaporation and sputtering, where the vapor particles are ejected through the physical process from the source into the vacuum. In PVD, the small clusters are removed from the source (liquid or solid) and travel in a vacuum chamber towards the substrate to form the thin film. The rate of the deposition in PVD processes is mainly influenced by source-substrate distance, substrate temperature, and system pressure.

Generally, the condensation of individual atoms or polyatomic species striking the substrate surface plays a crucial role in the growth of thin films. Although both CVD and PVD were commonly applied to produce thin films, there are some restrictions, which limit the usage of these processes. Crucially, in both methods, the growth of the film is continuously deposited and not easy to control. Furthermore, for trenched structures, it is difficult to obtain a high quality deposited film (no conformality) besides the high probability of gas-phase reactions (Kääriäinen et al., 2013). Therefore, to achieve a conformal and controllable deposition, atomic layer deposition is a significant technology was found to be the most effective technique to meet these requirements. It was initially known as "Molecular Layering" and was performed in Russia by Aleskovski and co-workers in the 1960s (Yang and Kang, 2006) with further expansion until the 1970s by Suntola using it for the growth of polycrystalline dielectric thin films (Mayer et al., 2003).

2.2.2 Characteristics of atomic layer deposition

The heterogeneous catalysts that having active catalytic materials disperse on a high surface area substrate, are in high demand in most of the modern industrial processes. Additionally, the conventional methods used to synthesis the heterogeneous catalysts may cause precipitations and involve chemistry-based ion exchange (Schwarz et al., 1995, Munnik et al., 2015). In the 21st century, the goal of improving the optimisation of the catalysts to synthesise sustainable products was achieved. The invention of ALD as an atomically-precisely control route facilitated the achievement of this goal (Lu et al., 2016). ALD is a unique modified process of CVD associated with the following advantages of (Moshe and Mastai, 2013, Yong and Jeong, 2002):

1. Self-limiting, superior conformality, precise, and easily controlled thickness film growth.
2. The thickness of the film depends only on the number of cycles.
3. Separate dosing of reactants
4. Independent of reactant fluxes.
5. The substrate size limits by the batch size
6. Suitability for scale-up and repetition

ALD is an epitaxial technique capable of controlling a precise thickness by angstrom resolution and coverage of high aspect ratio nanostructures, thus the targeted thickness of the desired compound is controlled by the number of ALD cycles of the precursor molecules (metal ions), which in turn ensures the self-limiting of substrate surface reactions (Saleem et al., 2014). Ritala and Leskelä (1999) verified that the conformality of ALD is inherent in the carefully controlled amount of pulse times and precursor amounts, which in turn prevents the extensive decomposition of the precursors and facilitates achieving the saturated state at all surfaces. A variety of products was employed using ALD to deposit several thin films, such as flat panel displays, fuel cells, microelectronic production, storage batteries or supercapacitors, catalysts, energy conversion including solar cells, and construction of optical and magnetic devices (Tanskanen et al., 2010). ALD is also a suitable technique for the deposition of dimensional structures and thin films (Aaltonen, 2005). In ALD, the growth surface (substrate) is exposed to an alternating sequence of gas-phase chemical precursor species separated by purge stages to inhibit gas-phase reactions (Puurunen, 2005). This technique also has the advantages of coating a uniform thin films of narrow bandgap compound semiconductors onto large surface area nanostructured substrates.

It also enables an efficient and rapid charge transfer through the coupled semiconductors because it results in significant interactions between the depositions layers (the interface properties from the atom-by-atom contact form)(Zhu et al., 2010). In terms of the commercial side, the atomic layer deposition has advantages that it can perform under ambient conditions, and it is particularly efficient in terms of materials utilisation because it consumes relatively small amounts of energy (Scragg, 2010).

2.2.3 Types of thin film growth

During atomic layer deposition, the growth surface of thin films is exposed to separated periods of alternating sequences of gas-phase chemical precursor species to prevent gas-phase reactions (George, 2009, Puurunen, 2005). The highly conformal thin films are produced at the correct conditions to reach saturation (characterised by self-limiting heterogeneous reactions between the gas-phase precursor species and surface-bound species) (Suntola, 1989, George, 2009). It was established that the growth of films of nanoscale thickness involves nucleation and growth on the surface of the substrate.

The crystallinity and the microstructure of the thin film will be governed by a nucleation step, which is an essential part of the process (Ghosh et al., 2000). These nucleation steps involve three basic modes (Figure 2-10) illustrated below:

1. Island or Volmer–Weber: It occurs when the bonds between adatoms (species) are stronger than the bonds with the substrate. The subsequent growth of the islands will continue and merge to form the film.

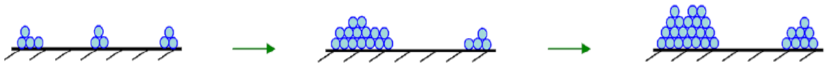

Island or Volmer–Weber mechanism

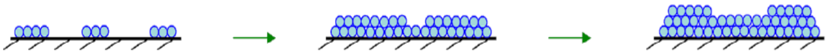

Layer or Frank–van der Merwe mechanism

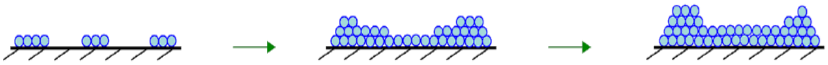

Island-layer or Stranski–Krastonov mechanism

Figure 2-10: Three basic modes if thin film early stage nucleation(Ghosh).

2. Layer or Frank–van der Merwe: It is an opposite type of growth to the island, in which the adatoms are strongly bonded to each other rather than with substrate, called an epitaxial growth, a monolayer firstly formed then followed by the s layer. Ehrlich and Hudda (1966) and Schwoebel and Shipsey (1966) demonstrated that this growth mode involves:

- Homo-epitaxy (Homogeneous nucleation): material identical to the substrate.
- Hetero epitaxy (Heterogeneous nucleation): different materials.

3. Island–layer or Stranki-Krastonov nucleation: This mechanism is a combination of epitaxial growth and Island growth. In this

growth mode, the stress develops during the formation of the films or nuclei.

2.2.4 Semiconductors based photocatalyst

Previous studies introduced photocatalysis semiconductors as materials that drive heterogeneous photochemical catalytic reactions on the surface of a solid-state semiconductor. It was found that the generation of fuels *via* the photoelectrocatalytic technique was based on two configurations: the particulate system and the photoelectrochemical (PEC) cell (Figure 2-11) that includes occurring of five main processes (Hoffmann et al., 1995, Linsebigler et al., 1995, Leary and Westwood, 2011):

1. Light absorption
2. Charge separation
3. Charge migration
4. Charge recombination and (V) redox reactions
5. Redox reactions

If the semiconductor absorbs photo energy greater than the bandgap energy (Eg), the electrons will be transported to the conduction band leaving holes in the valence band then the separated electrons and holes will migrate to the semiconductor/electrolyte interface through the semiconductor, and the redox reactions will occur to generate the

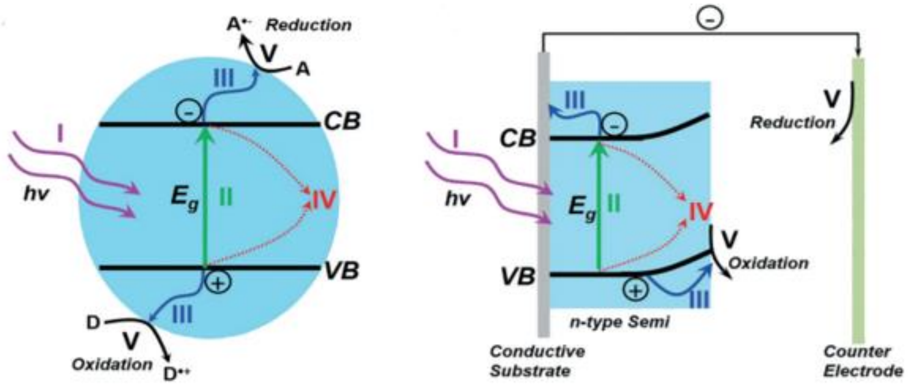

Figure 2-11: Scheme illustration of (a) a particulate photocatalyst, (b) a photoelectrochemical (PEC) cell with an n-type photoelectrode. Note: (I) light absorption, (II) charge separation, (III) charge migration, (IV) charge recombination and (V) redox reaction. CB = conduction band, VB = valence band, E_g = bandgap, A = acceptor, and D = donor (Li and Wu, 2015).

fuel. Macdonald and Barsoukov (2005) revealed that not all the collected photogenerated charge carriers could participate in the generation of the fuel because some of them will recombine in the bulk and the surface, and their energy dissipated. They believed that the solar-to-chemical energy conversion efficiency for semiconductor photocatalysts is mainly limited by charge recombination, which is considered the major factor for the loss of the excited charge carriers. Quantitatively, the produced hydrogen and oxygen can be measured using a gas chromatograph. Previous studies (Habisreutinger et al., 2013, Lewis and Nocera, 2006, Lewis, 2007, Norton, 2013, Grätzel, 2001, Walter et al., 2010) acknowledged that there are specific and essential requirements needed in a semiconductor utilised as a photocatalyst for solar water splitting (hydrogen and oxygen generation) including enabling light absorption, charge separation, migration, and transfer to the electrolyte solution for redox reactions.

The semiconductor should have a small bandgap to absorb the sunlight in a broad spectrum range to achieve a high theoretical maximum solar-to-hydrogen (STH) efficiency (Osterloh and Parkinson, 2011, Chen et al., 2012, Chen and Wang, 2012, Walter et al., 2010, Hisatomi et al., 2014, Kudo and Miseki, 2009, Benson et al., 2009). Figure 2-12 illustrates some of the studies that focused on selecting the semiconductor based on the band edge positions with respect to the vacuum level and the NHE.

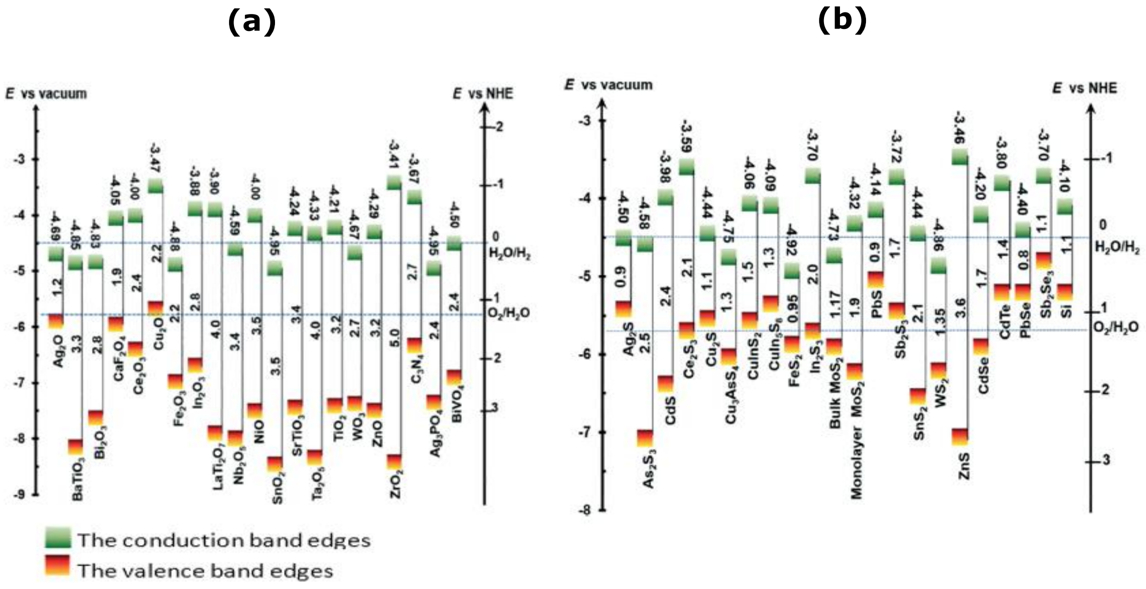

Figure 2-12: Band edge positions with respect to the vacuum level and the NHE for selected semiconductors at pH 0. (a) oxides, phosphates, and carbides; (b) chalcogenides and silicon. The top numbers show the exact conduction band level, and the number between squares is the bandgap. The two dashed lines indicate the water redox reaction potentials (Li and Wu, 2015).

Furthermore, the levels of the conduction and valence bands should straddle the redox potentials of the photocatalytic reaction as in the water-splitting reaction, which requires a Gibbs free energy of 237.18 kJ mol^{-1} and a minimum potential of 1.23 V at 298 K (Youngblood et al., 2009, Swierk and Mallouk, 2013).

Li and Wu (2015) have emphasised some properties that must be considered in employing the semiconductor as a photocatalyst:

1. High charge mobility and long charge carrier diffusion length to reduce the low charge recombination rate.
2. Strong catalytic activity toward water oxidation and reduction, respectively, to reduce the overpotential.
3. The semiconductor must have a high electrochemical, chemical, and photoelectrochemical stability in the electrolyte.
4. The semiconductor should be affordable, earth-abundant, environmentally friendly, and ideally to be synthesised *via* "green" processes to meet global sustainable development.

2.2.5 ALD growth mechanisms

During atomic layer deposition, the substrate is alternatively pulsed with the reactant's vapours including the purging of inert gas between reactants pulses. All the steps of the process should be saturated if the experimental conditions are adjusted accordingly. Principally, when the substrate is exposed to the pulsed precursors, the latter will chemisorb on the substrate forming a tightly bound monolayer with the surface (saturated reaction). A subsequent gas purging introduced in the chamber to remove the excess molecules or any by-products, this followed by the dose of the s precursor, which will encounter only the previously formed monolayer from the first precursor (Suntola, 1989, Leskelä and Ritala, 1995, Niinistö et al., 1996). Typically, the growth cycle of the thin film takes place in four stages: 1) Exposure of the first precursor, 2) Purge of the reaction chamber, 3) Exposure of the s precursor, and 4) A further purge of the reaction chamber (Leskelä and Ritala, 2003, Ritala and Leskelä, 2002, Kääriäinen et al., 2013) (Figure 2-13).

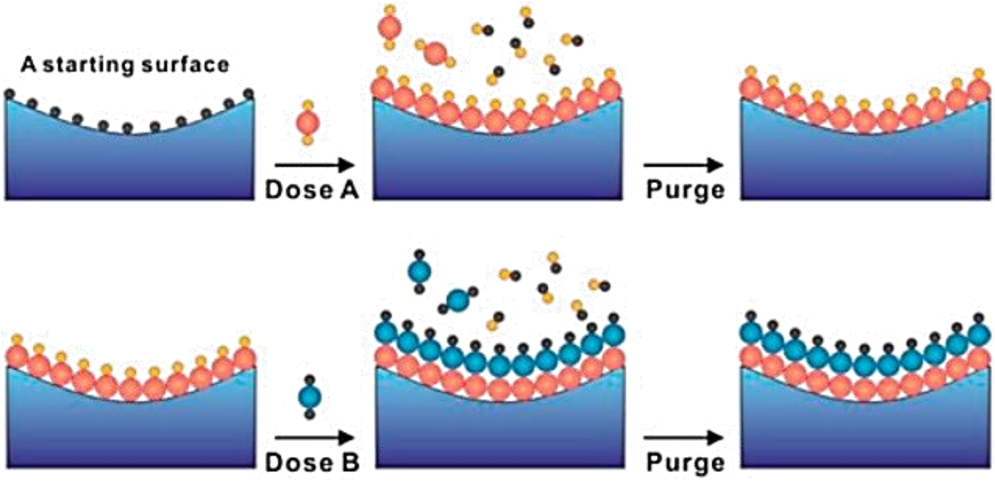

Figure 2-13: schematic diagram of the general ALD binary reaction sequence. Precursor A and B are sequentially introduced to a substrate surface with inert gas purging in between (Lu et al., 2013).

In the first stage, the substrate receives a single molecular layer when the first precursor reacts with all the sites on the substrate. At the second stage, with a sufficient purging period of Argon or Nitrogen, no reactive species in the gas-phase will be left to avoid the undesired gas phase reactions between precursors. In the third stage, a single molecular layer of the target material will form from the reaction between the second precursor as it reacts with one molecular layer of the first precursor, and the fourth stage involves pumping the residual of the precursor. The precursor adsorbs onto the surface and undergoes a ligand-exchange reaction with the surface-bound metal species and, consequently, becomes permanently bound to the growth surface (Travis and Adomaitis, 2013).

Depending on the type of reactor or cell configuration, these steps can be repeated to obtain the desired film thickness. Typically, the layer by layer growth mechanism (thickness increment per unit time), due to both reaction and purging steps (one cycle) will be ending within around 0.5 s to few seconds producing a deposited film of thickness ranged between 0.1-3.0 A° (Ritala and Leskela, 2001).

Some studies (Ritala et al., 1993, Ritala et al., 1994, Asikainen et al., 1996, Ihanus et al., 1997) revealed that the ALD deposition to grow polycrystalline films does not proceed entirely smoothly because of the nucleation stages involved during the deposition; thus it may roughen the surface. Generally, the growth of smooth surfaces is more likely to be obtained when the film is epitaxial (Yokoyama et al., 1994) or amorphous (Ott et al., 1996, George et al., 1996, Ritala et al., 1996). There are three types of ALD processes: Thermal ALD, catalytic ALD, and plasma-enhanced ALD (PE-ALD).

This research is mainly focused on the catalytic ALD since this method is carried out at low temperatures, making it more affordable than the other types. The ALD of SiO_2 from $SiCL_4$ and H_2O is an excellent example demonstrating the compensative binary reaction during ALD between the substrate and the reagent vapor precursors. The sequence of the binary reaction is shown in the following equations (Klaus et al., 1997):

$$SiOH^* + SiCl_4 \rightarrow SiOSiCl_3^* + HCl \qquad \text{Eq. 2-18}$$

$$SiCl^* + H_2O \rightarrow SiOH^* + HCl \qquad \text{Eq. 2-19}$$

Where: Asterisks (*): The surface species, the reaction between a surface functional group ($SiOH^*$ or $SiCl^*$) and the gas precursors involves in each half reaction.

The reaction on the surface continuous until the functional groups are replaced by new groups, which stops once no further reactivity of the precursors with the deposited surface occurs (Klaus et al., 1997).

2.2.6 Precursors of ALD

The deposited material *via* ALD depends on the type of precursor. Optimising the right precursor is a crucial step for a successful ALD. The precursors can be any state of matter-gases, volatile liquids or solids. These precursors typically include: inorganics materials such as: noble metals, chalcogenides, metal oxides (TiO_2 (Park et al., 2004), ZnO (Yan et al., 2001), ZrO_2 (Lee and Sung, 2004), and HfO_2 (Chen et al., 2005)), metal sulphides, metal nitrides and multicomponent materials may be deposited as well for instance Ba_1-xSrxTiO$_3$, $SrBi_2Ta_2O_9$ and $Ge_2Sb_2Te_5$ (Pore, 2010), alkoxides, alkyl compounds and halides could also be utilised as precursors. Furthermore, the precursors may include non-metals, which include water, ozone, hydrogen peroxide, and oxygen; hydrides from the fifth group in the periodic table; hydrazine, ammonia and amines for nitrogen (Ritala and Leskelä, 2002, Leskelä and Ritala, 2003). Table 2-5 summarises some of the materials deposited *via* ALD (Ritala and Leskelä, 1999).

Table 2-2: Examples of thin-film materials deposited by atomic layer (Ritala and Leskelä, 1999).

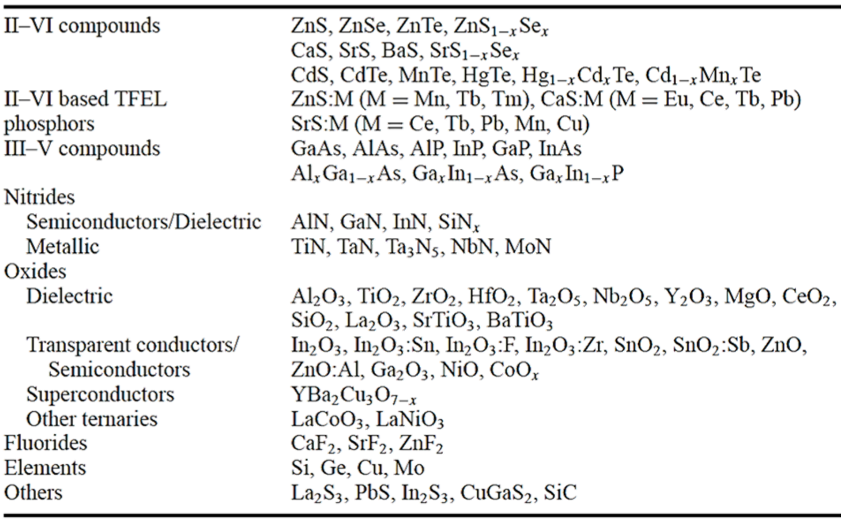

II–VI compounds	ZnS, ZnSe, ZnTe, $ZnS_{1-x}Se_x$ CaS, SrS, BaS, $SrS_{1-x}Se_x$ CdS, CdTe, MnTe, HgTe, $Hg_{1-x}Cd_xTe$, $Cd_{1-x}Mn_xTe$
II–VI based TFEL phosphors	ZnS:M (M = Mn, Tb, Tm), CaS:M (M = Eu, Ce, Tb, Pb) SrS:M (M = Ce, Tb, Pb, Mn, Cu)
III–V compounds	GaAs, AlAs, AlP, InP, GaP, InAs $Al_xGa_{1-x}As$, $Ga_xIn_{1-x}As$, $Ga_xIn_{1-x}P$
Nitrides	
Semiconductors/Dielectric	AlN, GaN, InN, SiN_x
Metallic	TiN, TaN, Ta_3N_5, NbN, MoN
Oxides	
Dielectric	Al_2O_3, TiO_2, ZrO_2, HfO_2, Ta_2O_5, Nb_2O_5, Y_2O_3, MgO, CeO_2, SiO_2, La_2O_3, $SrTiO_3$, $BaTiO_3$
Transparent conductors/ Semiconductors	In_2O_3, In_2O_3:Sn, In_2O_3:F, In_2O_3:Zr, SnO_2, SnO_2:Sb, ZnO, ZnO:Al, Ga_2O_3, NiO, CoO_x
Superconductors	$YBa_2Cu_3O_{7-x}$
Other ternaries	$LaCoO_3$, $LaNiO_3$
Fluorides	CaF_2, SrF_2, ZnF_2
Elements	Si, Ge, Cu, Mo
Others	La_2S_3, PbS, In_2S_3, $CuGaS_2$, SiC

The vapor pressure should be high enough to achieve an active feeding of precursor molecules to the ALD system, which should be provided with enough number of precursors to cover all the substrate surfaces. The advantage of self-limiting growth is in facilitating the stability of the evaporation rates during the deposition. In some cases, the precursors are heated (Leskelä and Ritala, 2003, Ritala and Leskelä, 2002, Becker, 2003). To summarise, some specific properties should be considered in selecting the precursors for an ALD system (Moshe and Mastai, 2013, Leskelä and Ritala, 2003), they should include:

- Being safe, non-toxic and affordable.
- Being thermally stable at the growth temperature, evaporable and extensively reactive and adsorbate with the substrate.
- Being inert volatile by-products and not causing etching with the substrate.

2.2.7 Factors affect ALD

The overall growth rate in atomic layer deposition is influenced by many factors, each of which affect the quality of the deposited film. Pore (2010) showed that the reaction kinetics of adsorption and desorption are key factors in any successful ALD system, if the ALD growth rate depends on the temperature. In the metal precursors, the size and the number of ligands may limit the adsorption density through steric effects. The unique self-limiting growth of ALD behaviour may also be affected by the condensation or thermal decomposition of the precursor. However, in the region of 'ALD-window,' the growth rate is independent of temperature, which makes for an ideal process (Pore, 2010). The present study will only consider the independent ALD as a modified process (electrochemical atomic layer deposition (EC-ALD)).

2.2.8 Challenges to ALD

Besides all the previously explained advantages, ALD also has several limitations. The method is a slow growth rate process in which one monolayer deposits per cycle. The thickness of the monolayer is a few angstroms per few seconds; hence, one-micron thickness will take a long time (h). Typically, the deposition rates are approximately 100.0-500.0 nm h^{-1}. Therefore, economically it is not suitable for many practical processes to produce thick films in micron ranges (Knez et al., 2007). Although the deposition rates are slow, high productivity can be achieved by using a large capacity chamber holding many substrates. Some industries, manufacture thin-film electroluminescent (TFEL) displays from 82 glass substrates with dimensions of 155.0 to 265.0 mm^2 (Ritala and Leskelä, 1999). Therefore, in future demand for super-thin films, the slowness of ALD will not be a significant problem. Moreover, there is a risk of impurities with ALD since it is a chemical process; this risk may occur from gas precursors or carrier gas. The presence of the impurities can lead to the growth of poor-quality films resulting from the incorporation of impurities. Thus, it is essential to select materials with a high degree of purity. Additionally, ALD is an unselective process, and a crucial pre-treatment step is required to achieve selectivity control (Leskelä and Ritala, 2003, Ritala and Leskelä, 2002, Becker, 2003).

2.2.9 Modified EC-ALD

Compared with the other epitaxy methods, it was found that the most efficient and popular method is the electrochemical atomic layer deposition (EC-ALD), since the other methods easily lead to plugging of the pore mouth of the nanotubes by the precipitation of the sensitiser, resulting in decrease the adsorption capacity and the specific surface area (Wang et al., 2014b). The EC-ALD technique has the advantages of coating a uniform thin films of narrow bandgap compound semiconductors onto large surface area nanostructured substrates. It also enables an efficient and rapid charge transfer through the coupled semiconductors, because it leads to significant interactions between the depositions layers (the interface properties from the atom-by-atom contact form) (Zhu et al., 2010). In terms of the commercial side, the atomic layer deposition has advantages include the fact of performing the process under ambient conditions. Undoubtedly, the deposition at low temperature avoids the heat-induced interdiffusion of component elements and degrading the quality of the device of a structure Consequently, there is no necessity to have a vacuum atmosphere (Zhang et al., 2009), i.e., it brings the advantages of there being less of a need for a homogeneous flux of the reactants through the reactor. These properties make EC- ALD processes reproducible and easy to scale up for large-area coatings without sacrificing conformity (Tiznado et al., 2008).

EC-ALD is particularly efficient in terms of materials utilisation because it consumes relatively small amounts of energy (Scragg, 2010). It is also capable of controlling a precise thickness by angstrom resolution and coverage of high aspect ratio nanostructures, thus the targeted thickness of the desired compound is controlled by the number of EC-ALD cycles of the precursor molecules (metal ions), which in turn ensure a self-limiting of substrate surface reactions (Saleem et al., 2014). Thereby, coaxial heterogeneous structures within a superthin coating can be obtained, which is preferred for reducing the charge carrier recombination probability.

Previously, electrochemical atomic layer deposition (EC-ALD), known as electrochemical atomic layer epitaxy (EC-ALE), was put forward by Stickney and co-workers (Gregory and Stickney, 1991, Stickney, 1999, Thambidurai et al., 2008).

EC-ALE based on the alternated underpotential deposition of the elements that form the compound semiconductor in a cycle. The underpotential deposition is a surface-limited phenomenon, an atomic layer of one element is deposited on a second at a potential prior to (under) the required potential to deposit the element on itself. Each deposition cycle forms a monolayer of the compound, and the number of deposition cycles controls the thickness of deposits. Therefore, it makes the deposits particularly suitable for devices as nanomaterials in modern technological applications (Zhang et al., 2009). When the deposited atoms completely cover the underlying heterogeneous atoms, the growth will continue on top of the homogeneous atoms. However, the growth process stops because the deposition controlled in the deposition potential range and the driving force is insufficient to grow atoms on top of the homogeneous atoms, simultaneously avoiding bulk-phase or island deposition.

This growth mechanism ensures morphological consistency between the deposition layer surface and the underlying substrate surface (Fernandes et al., 2009, Loglio et al., 2010). With the aid of this unique technique, the grain boundaries (as recombination centres) will be minimised. Suggesting that the doping element can directly enter the crystal lattice of the deposition layer through the atomic layer. Thus, the photocatalytic performance can effectively improve (Stickney, 2002). After each deposition, the electrode is rinsed using a blank solution. Generally, it is often best to use an electrode that has a flat and smooth surface (Zhu et al., 2007, Vaidyanathan et al., 2006). The deposition potentials of two or more species requires an adjustment step before the electrodeposition.

Recently, Demir and co-workers have employed a modified EC-ALD method (Öznülüer et al., 2005), through co-deposit S and Pb from a precursor solution contains S^{2+} and Pb^{2+} and the complexing agent ethylenediaminetetraacetic acid (EDTA). The addition of a complexing agent possibly will provide a stoichiometric deposition (Lin et al., 2016a). EC-ALE was employed to deposit several binary compound semiconductors (2001, Flowers et al., 2002, Wade et al., 2001, Vaidyanathan et al., 2003, Qiao et al., 2005, Zhu et al., 2005, Yang et al., 2006, Sheridan et al., 2013, Şişman et al., 2007). In general, the electrodeposition of metal ions on a substrate consists of adsorption, nucleation, and growth. It was found that several parameters may affect this deposition including (1) Time of deposition, (2) The localised current and potential on the electrode, which affects the morphology and the phase composition of the product, (3) pH value of the electrodeposition bath, (4) deposition potential (UPD) (5) competition between several electrochemical reactions (Leskelä and Ritala, 2003, Ritala and Leskelä, 2002) (Walsh and Herron, 1991, Chong et al., 2016). The Underpotential deposition (UPD) illustrated in detail with an example in sections 2.4 and 2.4.1.

2.3 Bandgap energy (Eg) of a material

For nanomaterials, semiconductors, and water splitting or solar applications, the bandgap is a key factor in optimising the route for synthesising these materials. The bandgap energy (forbidden energy) indicates the difference between the top of valance band (VB) and the bottom of the conduction band (CB) (Figure 2-14), thus with a specific amount of energy (photon, thermal or electrical) the electrons can transport across the bandgap towards the conduction band.

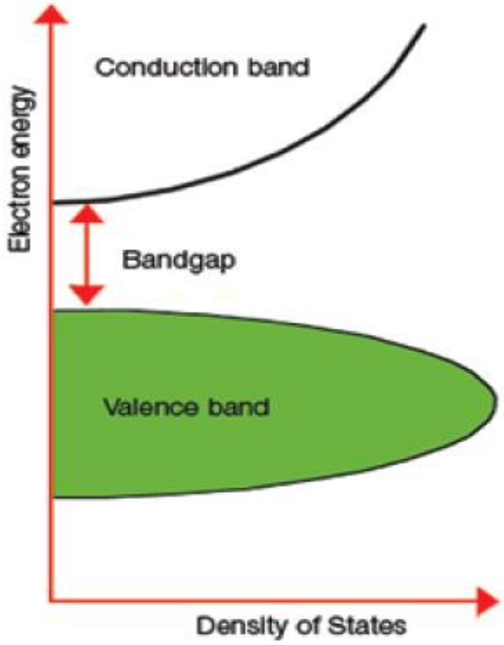

Figure 2-14: Bandgap diagram (Dharma et al., 2009).

The atoms of the crystal are bonding with the electrons in the valance band; if the electron moves from the VB (ground state), it will break the bonds leaving empty states in the VB, called "holes" which behaves as a positively charged particle (Dilli, 2009). Principally, if the material is exposed to external energy sources like the electric field, the free electrons in the CB can move in the opposite direction with the electric field. The holes in the valance band (if available) will also move and contribute to improve the conductivity of the material. Figure 2-15 depicts the effective mobility of the holes, which moves in the same direction of the applied electric field.

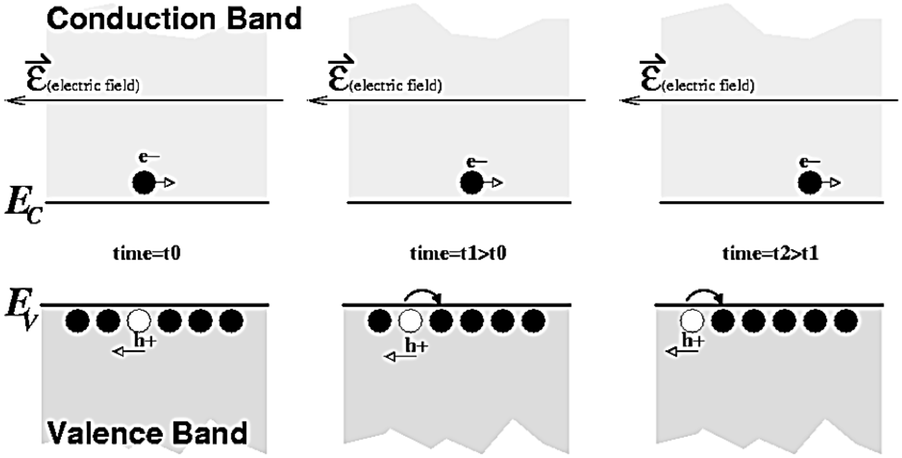

Figure 2-15: Motion of electrons in the VB under the influence of the electrical field (Dilli, 2009).

With regards to the photoelectrocatalysis, it is essential that the candidate is a conductive photocatalyst (semiconductor (SC)) in order to achieve successful charge separation. Usually, this happens by photoexciting the SC to create the charge carriers under light illumination (hv) by energy higher than the bandgap of the SC (hv ≥ Eg) (Figure 2-16-a, b and c). Thus, the electron will move from the VB to the CB, leading to generation of the electron/hole pair (e^-/h^+) (Figure 2-16-b). Ideally, this so-called "intrinsic semiconductor," which acquires enough thermal energy to make this jump where the electron and hole concentrations are equal. A semiconductor formed by introducing dopant atoms (impurities) into the crystal is called an "extrinsic semiconductor." Since the present study focusing on exploiting semiconductors for the photoelectrocatalytic process.

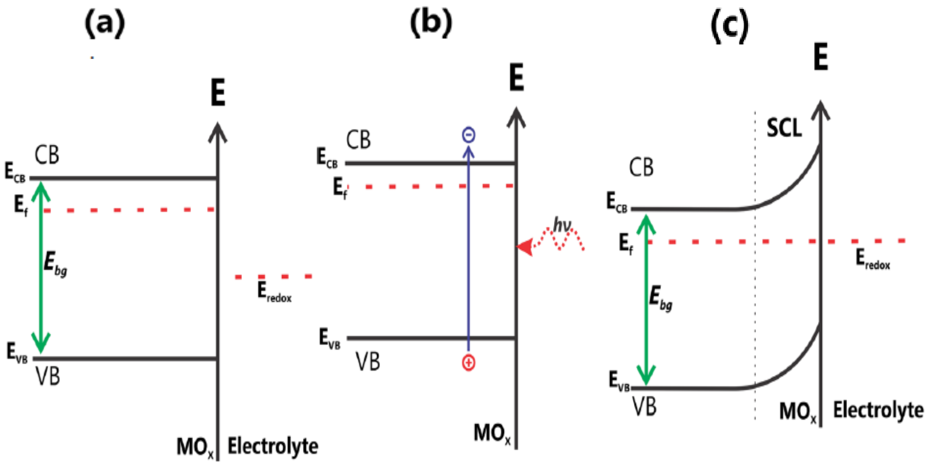

Figure 2-16: a-c Schematic diagram represents the mechanism of the charge carrier generation by photoexcitation in a semiconductor (MO_x) (Bessegato et al., 2015).

2.3.1 Doping of semiconductors (SCs)

There are two types of semiconductors, intrinsic and extrinsic. In the intrinsic SCs, the electrons in the VB are excited and transferred to the CB, leaving unoccupied states (h^+) in the VB. The extrinsic SCs formed from introducing impurities (dopants) into the crystal of an intrinsic SCs to enhance the conductivity of the SCs. This process called "doping." There are two types of extrinsic SCs or doping (Kondarides, 2010b, Dilli, 2009):

1. *N*-type: These are known as donor atoms where the dopant atoms (n) (electrons) jumped to the conduction band of SC crystal, leaving a positively charged atom behind. For instance doping of Si with elements from group V, such as Sb, As or P, N-doped TiO_2 nanotube with Ag nanoparticles (Gao et al., 2018), nitrogen-doped titanium dioxide (Ansari et al., 2016), Pt/N-codoped TiO_2 nanotube(Huang et al., 2007).
2. P-type: These are known as acceptors, the impurities or dopant atoms are taking away from the outer shell of the SC. The elements in group III (e.g., Ga, In, Al) are incorporated in the crystal structure of Si. When the electrons jump from the valance band of Si to the valance band of the element, a negatively charged atoms will be created in the outer shell of acceptor atoms. Figure 2-17 shows a general diagram for n-type and p-type doping in a semiconductor.

In the field of water-splitting (WS), doping with metal cations, non-metal anions, or non-metal molecules was extremely examined. Due to the formation of localised, or delocalised electronic states in semiconductors, doping can also facilitate the enhancement of the photoefficiency of generated e^-/h^+ pairs and effectively modulate the lattice face structure (Huang et al., 2016).

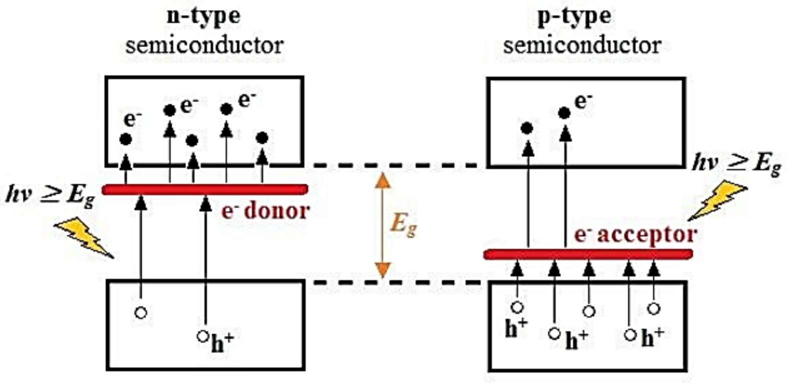

Figure 2-17: Schematic diagram of N-type and p-type doping in a semiconductor (Monfort and Plesch, 2018).

Principally, the doping process depends on the concentration of the dopant atoms thus, lower or higher dopant content may be introduced to the electronic state of the SC depending on that required modification based on the type of the SC (*N* or *P*) (Wang et al., 2014a). For instance, under the light irradiation, the photocatalytic activity of the wide bandgap photocatalyst TiO_2 is greatly enhanced by introducing a low content metal ion dopant as donor level above the VB (Figure 2-18-a) or an acceptor level below the CB (Figure 2-18-b).

Furthermore, significant changes can be observed in the photoactivity of TiO_2 when its crystal facet is exposed to the metal-ions of Cu (Wang et al., 2014a). Generally, enhancing the photoactivity towards H_2 evolution requires creating an acceptor level below the CB by utilising the cations: Ta^{5+} Sb^{5+}, Nb^{5+}, Rh^{3+}, La^{3+}, Rh^{5+}, Cr^{3+} (Li et al., 2015), while doping with the cations Sn^{2+}, Ag^{+} Pb^{2+}, Rh^{3+}, Bi^{3+} leads to the formation of the donor level above the VB (Chen et al., 2010b).

However, in some cases introducing the metal ions may act as trap sites that lead to the occurrence the undesirable recombination, which, in turns, reduces the photoactivity under the illumination of light (Queisser and Haller, 1998, Serpone and Emeline, 2012, Diebold, 2011).

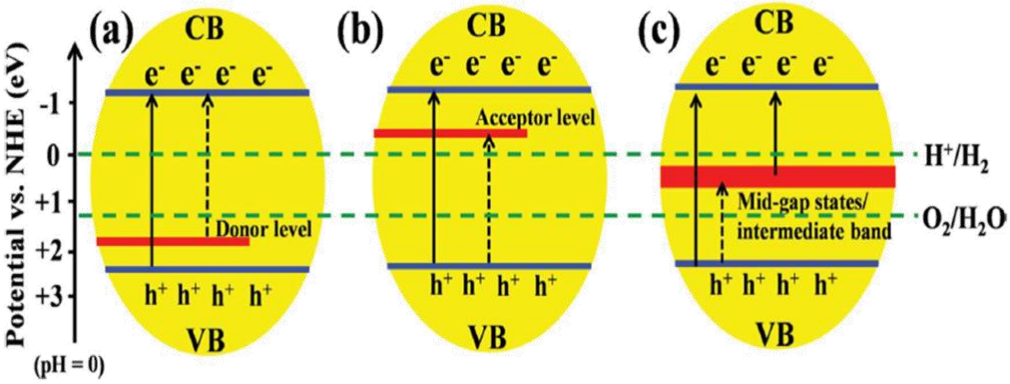

Figure 2-18: Metal ion doping formed by (a) donner level, (b) acceptor level, and (c) mid-gap states (Li et al., 2015).

Therefore, it is essential to carefully optimise the amount of dopant to achieve high photoactivity in WS systems. On the other hand, Serpone and Emeline (2012), (Mocatta et al., 2011) stated that doping with high dopant content may lead to multiphoton excitation for the wide bandgap SC through the formation of a band of delocalised states in the middle of the bandgap (the intermediate band or mid-gap states) (Figure 2-18-c). For instance, an improvement in the photoactivity with a photocurrent density of 3.52 mA cm^{-2} at 0.00 $V_{Ag/AgCl}$, was achieved in the thin films $CuGaS_2$ or $CuInS_2$ when Sn partially filled the intermediate band in their forbidden bandgaps (owing to the formation of the intermediate band located 0.80 eV above its valance band maximum). It is worth mentioning that improving the photochemical properties and light-harvesting ability for WS reactions can only be accomplished by mid-gap states with appropriate positions and enough powerful redox potentials (Li et al., 2015). Section 2.3.5. will present the selection of the appropriate semiconductors that straddle the bandgap for water-splitting systems and to enhance the photogenerated charge carriers.

2.3.2 The Fermi energy level between N-type semiconductor and electrolyte interface

In the bandgap energy theory, the Fermi level (E_f) is a crucial parameter that is defined as the available energy states to distribute the electrons in a solid material and follows the statistics of *Fermi-Dirac distribution* (E_f), which represents the probability of energy occupancy and is equal to 0.50. To achieve equilibrium between a semiconductor immersed into an electrolyte that contains the redox couple, the flow of the charges in the interface between these two phases will then depend on their Fermi level.

Precisely, the Fermi level (E_f) denotes the electrochemical potential of an electron. The electrochemical potential of a redox electrolyte ($E_{f,\ redox}$) can be calculated from Nernst equation below:

$$E_{red} = E^{\circ} - \frac{RT}{zF} \ln \frac{[Red]}{[OX]} \qquad \text{Eq. 2-19}$$

where:

$E°$ is the standard half-cell potential (V), R the universal gas constant (8.314 J mol^{-1} K^{-1}), T the temperature (K), z the stoichiometric number of electrons involved in the reaction, F the Faraday constant (96485.0 C mol^{-1}), [*Red*] the concentration of reduced species (mol L^{-1}) and [*Ox*] the concentration of oxidised species (mol L^{-1}). The Fermi level of a semiconductor ($E_{f,\ SC}$) represents the material characteristics; thus, a variation in the Fermi level of the redox ($E_{f,\ redox}$) may occur depending on the concentration of reduced or oxidised species.

2.3.3 Calculation of bandgap

In order to obtain a clear understanding relating to the bandgaps of the semiconductors, it is crucial to study their optical and electrical properties. Specifically, acquiring information about the bandgaps by measuring the absorption coefficient for several energies. The bandgap energy is a key factor that can provide a direct indication regarding the conductivity of a semiconductor, specifically in water-splitting systems, which require a narrow bandgap semiconductor to provide the photogenerated charge carriers. Consequently, this enhances the capability of the SC for harvesting light within the visible region (redshift) and raises the H_2 evolution generation rate. The bandgap could be measured practically or theoretically. Practically, photoluminescence spectroscopy (Channei et al., 2014, Wang et al., 2013, Nagaveni et al., 2004) and diffuse reflectance are the most commonly used techniques to determine the bandgap energy. However, several researchers tend instead to measure the bandgap of the semiconductors from the diffuse reflectance measurements using Tauc plot (Murphy, 2007, Shangguan et al., 2003, Chen et al., 2004, Wang et al., 2014b). It is considered the standard technique to determine the absorbance of both powder and solid SCSs.

Ebraheem and El-Saied (2013) had emphasised that for powder samples, the thickness required to absorb all the incident light before the backscattering should typically range between 1.0 to 3.0 mm. Furthermore, they revealed that the diffuse reflectance could feasibly apply for SCs capable of entirely absorbing or scattering the incident light, such as $ZnTiO_2$. This method will be explained in detail in the methodology (chapter 3).

2.3.4 Bandgap positions of semiconductors with respect to water splitting

To produce hydrogen *via* sustainable, clean, and economical technique has been the goal of the majority of the researchers in their quest to find an alternative to fossil fuels. The semiconductors are considered the most desirable materials for water-splitting due to their unique chemical and optical properties, including stability against passivation and corrosion (highly ionised), the absorbability for solar energy, which is extremely required for photoelectrochemistry processes dependent on bandgap energy. However, the bandgap of the semiconductor should be ≥ 1.23 eV potential to allow the possibility for the electrochemical decomposition of water and to convert the energy into H_2 and O_2. From thermodynamic point of view, Li et al. (2015) emphasised that the bottom of the conduction band (CB) of the photocatalyst must be located at a more negative potential than the reduction potential of H^+ to H_2 (–0.41 V vs. normal hydrogen electrode (NHE)), while the top of the valence band (VB) must exceed the oxidation potential of H_2O to O_2 (+0.82 V vs. NHE). Figure 2-19 illustrates some examples of photocatalysts that meet the requirements for water-splitting with their corresponding bandgaps.

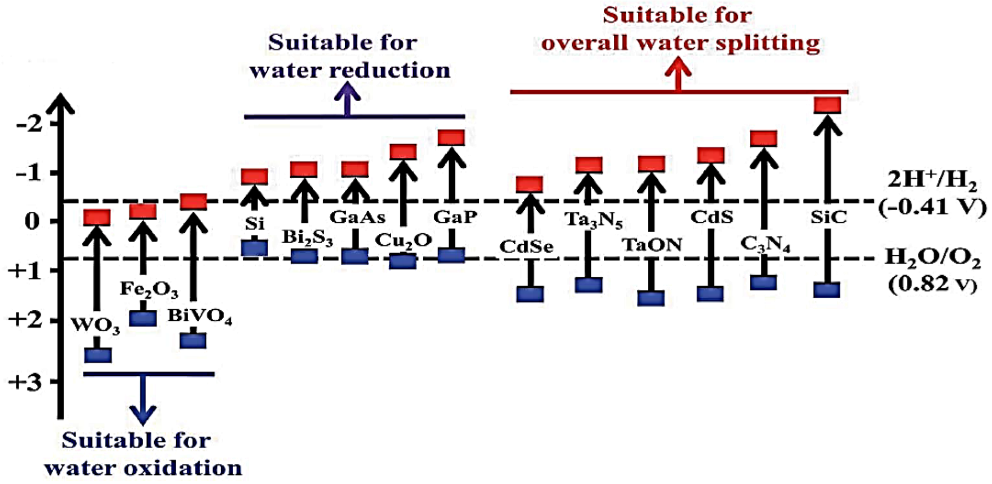

Figure 2-19: Bandgap position of some photocatalysts with respect to the water splitting redox potentials (Li et al., 2015).

Theoretically, the e^-/h^+ pairs produced when the photocatalyst absorbs photons at wavelengths below its bandgap, is then followed by the diffusion of these charge carriers to the water and the conducting substrate, which in turn drives the decomposition of water into hydrogen and oxygen.

Necessarily, the photocatalyst must have a large absorption coefficient to be able to absorb the photons on the surface, crucially, this depends on the wavelength (Murphy, 2007, Zimmermann, 2000). To summarise, The bandgap of the photocatalyst should straddle the oxidation and reduction reactions for water- splitting, which in some cases depends on the pH of the electrolyte (Sarswat et al., 2016).

2.4 Under potential deposition (UPD)

The phenomena of underpotential deposition (UPD) indicates to the onset electrochemical deposition potential of metal adatoms (M) onto a foreign substrate (S) at potential ranges more positive than those predicted by Nernest equation; thus, the resulting deposit is generally limited to less than a monolayer (Alanyalıoğlu et al., 2001). This phenomenon has been intensively subject to study in the past decades since the 1970s (Budevski et al., 1997, Kolb et al., 1974, Budevski et al., 2000). According to the fundamentals of electrocrystallisation of bulk metals, the concept of overvoltage refers to the occurrence of potential that involves positive quantities with prefix under, and this lead to the necessity to explain this contradictory (Oviedo et al., 2015). The overvoltage defines as:

$$\eta = E - E_{\frac{M(bulk)}{M^{z+}_{(aq)}}} \qquad \text{Eq. 2-20}$$

Where E is the actual electrode potential, and $E_{M(bulk)/M^{z+}_{(aq)}}$ denote to the Nernst equilibrium potential of the reaction:

$$\mathrm{M}_{(bulk)} \rightleftarrows \mathrm{M}^{z+}_{(aq)} + ze^{-} \qquad \text{Eq. 2-21}$$

Where $\mathrm{M}_{(bulk)}$ represents the bulk metallic material, and $\mathrm{M}^{z+}_{(aq)}$ stands for an ion in solution, bearing the charge number z. In general, the overvoltage always results with negative values of η; therefore, in the case of bulk materials, the metal deposits when $E < E_{M(bulk)/M^{z+}_{(aq)}}$, due to the kinetic hindrance. The reverse case occurs in the case of underpotential deposition; the deposition takes place when $\eta > 0$ because of $E > E_{M(bulk)/M^{z+}_{(aq)}}$(Oviedo et al., 2015). In reality, the deposition of M on S in UPD system is affected and controlled by many factors including adsorption of ions, potential window, interaction between adatoms (binding energy between the metal adatoms (M_{ads}) and S and nature of single-crystal faces (crystallographic misfit between M bulk lattice parameters and S. It is necessary to consider many routes each contributing to the potential of (sub) monolayer adsorption and bulk deposition, separately (Sudha and Sangaranarayanan, 2002). The formation of the monolayer M on S can be visualised as follow:

- Movement of solvated ions from the bulk to the reaction site, shedding of their solvation sheath.
- The formation of the subsequent bond with the substrate occurs when the electron leaves the substrate towards the metal ions.

A variety of applications utilise the underpotential deposition for preparing and designing surfaces among them production of compound semiconductors (Gregory and Stickney, 1991, Wade et al., 2001) electrocatalysis (Kokkinidis, 1986, Parsons and VanderNoot, 1988, Jarvi and Stuve, 1998, Doyle et al., 2003), design of biosensors (Aluoch et al., 2005, Noah et al., 2011, Li et al., 2013a), surface area measurement of metals (Chen et al., 2011a, Shao et al., 2013), etc.

The occurrence of the UPD phenomenon results in the formation of a two-dimensional phase, in some cases involving nucleation and growth routes, which take place under the influence of a potential difference (Budevski et al., 1997) (Figure 2-20).

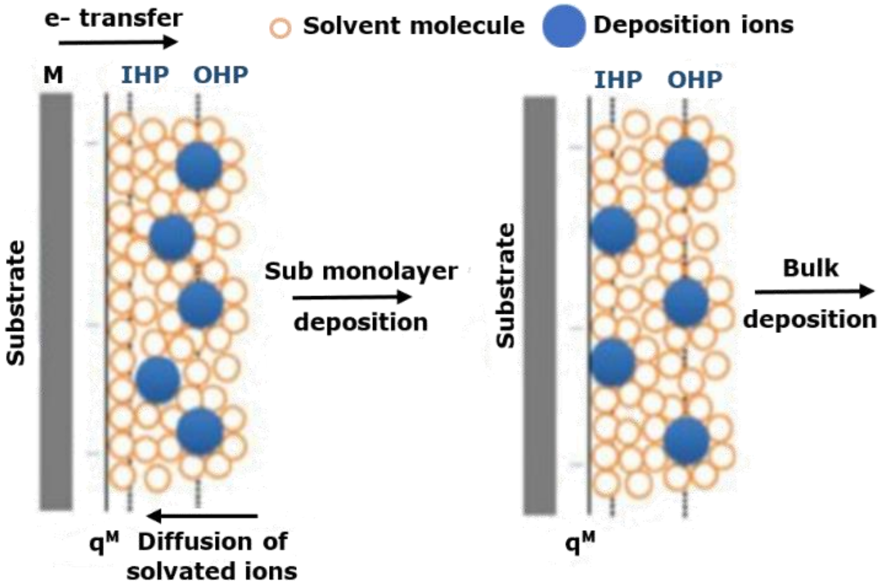

Figure 2-20: Schematic diagram represents the processes constituting UPD. IHP and OHP indicate inner and outer Helmholtz planes, respectively (Saji and Lee, 2013).

UPD phenomena has been used in a layer-by-layer fashion to grow binary compound thin film deposits such as CdS (Demir and Shannon, 1994, Demir and Shannon, 1996, Gichuhi et al., 1998, Foresti et al., 1998), ZnS (Gichuhi et al., 1999, Torimoto et al., 2000) and CdTe (Huang et al., 1995, Colletti et al., 1998).

Oviedo et al. (2015) showed that the electronic properties of the substrate material would alert from the monolayer obtained by UPD when the interfacial reactivity changed. They demonstrated that the

UPD phenomenon could be identified with the aid of many electrochemical and surface characterisation methods. However, electrochemical techniques, specifically cyclic voltammetry, is considered the most routine method to characterise the UPD potential. It offers valuable information on the kinetics and mechanisms of the processes occurring at the metal/solution interface.

Primarily, cyclic voltammetry technique involves monitoring the current continuously within the linear scanning for the potential of the working electrode at a constant scan rate (dE/dt) between two selected limits (start and end potentials). Due to the double layer charging, any reaction at the electrode can be detected as an overlaid current. The UPD potential of the metal adsorbate is represented by two cathodic (deposition) and anodic (dissolution) current density peaks. According to some previous studies (Alanyalıoğlu et al., 2001, Budevski et al., 1996) that focused on UPD potential and its role in the electrodeposition of metal ions on a conductive substrate; various parameters must be considered in the CV measurements to evaluate the behaviour of UPD potential, including:

- The presence of adsorbing anions in the electrolyte.
- pH value of the precursor solution. The pH plays a vital rule in tuning the reductive power of the metallic cations.

- The structure, number, and position of UPD potential peaks are found to depend strongly on the crystallographic orientation of the single crystal electrode (substrate), on which the adsorption takes place and the density of crystals imperfections for instance: vacancies, kinks, and steps (Budevski et al., 1996).

It was found that the surface state of the substrate plays a crucial role in the primary stages in the deposition of metals (Chen et al., 1992, Mrozek et al., 1995, Uchida et al., 1995, Ogaki and Itaya, 1995, Garcia et al., 1998). An example will be shown below to demonstrate the effect of crystal orientation of the substrate on the UPD potential evaluation. In the fundamentals of electrochemistry, Gold (Au) and Silver (Ag) have been extensively employed as substrate and metal adatoms, respectively and in evaluating the UPD behaviour relating to the strong interactions between Ag and Au surfaces there is mostly no misfit between them) (Cullity, 1978). Figure 2-21-a and b illustrates the cyclic voltammograms of Ag onto Au (100) / Ag^+, SO_4^{2-} and Au (111) / Ag^+, SO_4^{2-} systems, respectively.

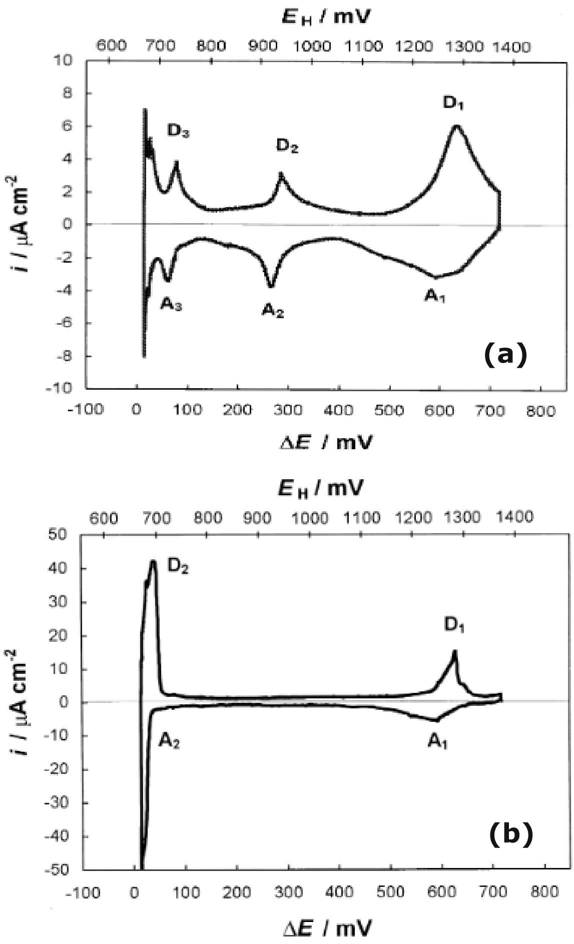

Figure 2-21: Cyclic voltammograms for the UPD of Ag in 5 x 10^{-3} MAg_2SO_4 + 0.5 MH_2SO_4 solution at T=298 K on (a) Au (100) and (b) Au (111) substrates recorded at scan rate 7.0 mV s^{-1}. The upper-scale corresponds to the normal hydrogen electrode, while the lower refers to the bulk Ag deposition potential. Reprinted from (Garcia et al., 1998).

Garcia et al. (1998) noticed that within the potential range 15.00 ≤ ΔE (mV) ≤ 7.20 three adsorption (reduction) (A1, A2, and A3) and desorption (oxidation) (D1, D2 and D3) peaks could be observed in the case of Au (100) (Figure 21-a), while in the case of Au (111) system, only two adsorption-desorption peaks (A1, A2, and D1, D2 (Figure 2-21-b), respectively. These results have been revisited by Rooryck et al. (2000).

They proposed that the second UPD adsorption peak for Ag at 80.0 mV s^{-1}, which is more positive than the first UPD, has appeared because it caused to transformation of the substrate (Au (111)) to an alloy phase surface.

2.5 Materials for electrodeposition

TiO_2 nanotube arrays are by far the most extensively used semiconductor in photocatalysis since they are non-toxic, abundant, and environmentally friendly. Although TiO_2 NTAs are a stable photocatalyst under the illumination of solar light, they are only activated in the UV region (4.0 to 5.0 % of solar energy spectrum) with a wide bandgap of 3.2 eV. Therefore, the electrodeposition of metal ions was found to be an exciting way to modify the photoefficiency of TiO_2 NTAs by utilising solar light absorber materials, such as the quaternary Kesterite Cu_2ZnSnS_4 (CZTS) in which its constituents are abundant, affordable, and non-toxic. The detailed explanation of the properties of CZTS will be illustrated in the sections below.

2.5.1 The quaternary Kesterite Cu_2ZnSnS_4 (CZTS) compound

Isoelectronic substitution is the most studied path to driven semiconductor compounds from existing semiconductors, and this can be done when two species (atoms or molecules) have the same numbers of valence electrons combined in one chemical bond (Figure 2-22).

Previously, CIGS was the most common compound semiconductor from group I–III-VI, which extensively used as an absorber thin film that derived mainly from a silicon basis. However, so many conditions, such as environmental safety (e.g., toxicity), availability, and producibility in industrial-scale are all required for compound semiconductors to fulfil their role as viable solar cell materials conditions (Flammersberger, 2010).

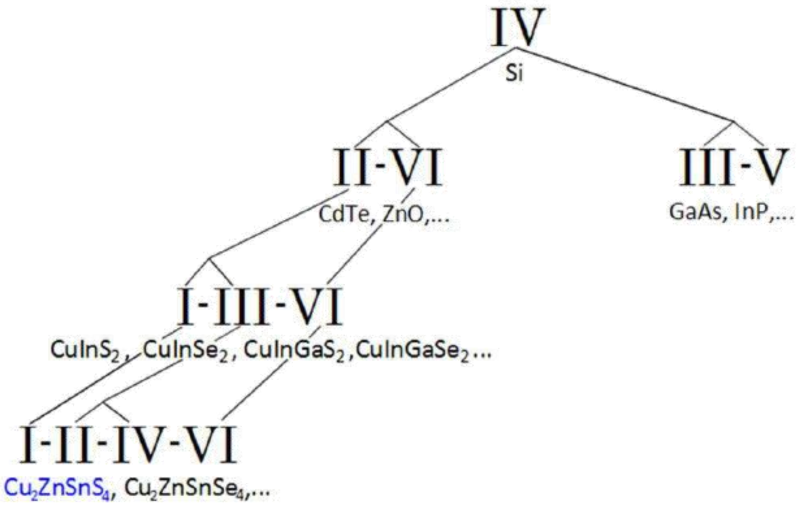

Figure 2-22: Various possible compound semiconductors obtained by the gradual substitution of elements by elements of groups from higher and lower group numbers (Flammersberger, 2010).

Other semiconductors made by the gradual substitution of elements by other elements have the same properties; for instance, Cu_2ZnSnS_4 (CZTS). CZTS is one of the most promising quaternary chalcogenides light-absorbing material for harvesting solar energy, which can be employed for low cost and high efficiency thin film applications (Ananthoju et al., 2016). CZTS constituent is copper, zinc, tin, and sulfur, none of which are harmful to the environment (non-toxic) and sufficiently abundant (Abermann, 2013, Nelson, 2003). CZTS possesses the p-type conductivity properties (explained earlier) that make it the desirable candidate for thin film photovoltaics including narrow bandgap (1.5 eV), solar-to electricity power conversion efficiencies over 8.0 % and high absorption coefficient of more than 10^4 cm^{-1} (Sarswat et al., 2012) (Abusnina, 2016).

2.5.2 Properties of CZTS

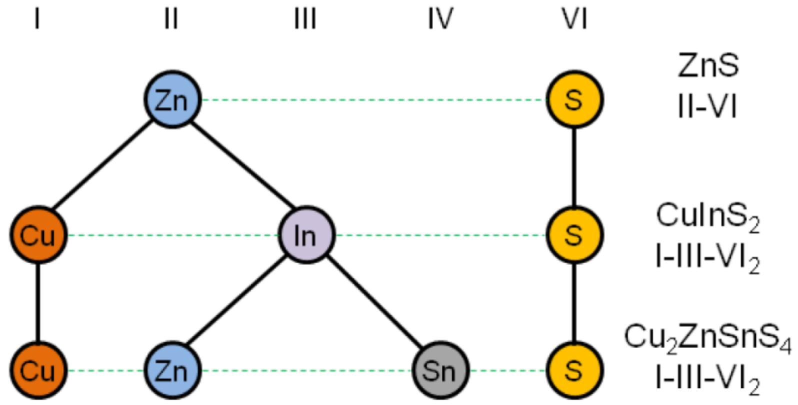

Figure 2-23: Derivation of the quaternary CZTS compound from binary and ternary compounds (Abusnina, 2016).

The quaternary compound Cu_2ZnSnS_4 (CZTS) is derived from the isoelectronic replacement of compounds from group II-VI, such as zinc-blende (ZnS). Two group-II atoms are replaced with one group-I, and one group-III atom to obtain a semiconductor of group I-III-VI2 Cu-based chalcopyrite $CuInS_2$ (CIS). Then by substituting I atoms with group-II atoms, such as Zn and another half with group-IV atoms, such as Sn, Cu_2ZnSnS_4 was produced (Abusnina, 2016).

Similarly, Cu(In, Ga)Se$_2$ (CIGS) and CdTe from the group I–III-VI, where two atoms of Indium were substituted by one atom of zinc and one atom of tin (Tlemçani et al., 2015) (Figure 2-23).

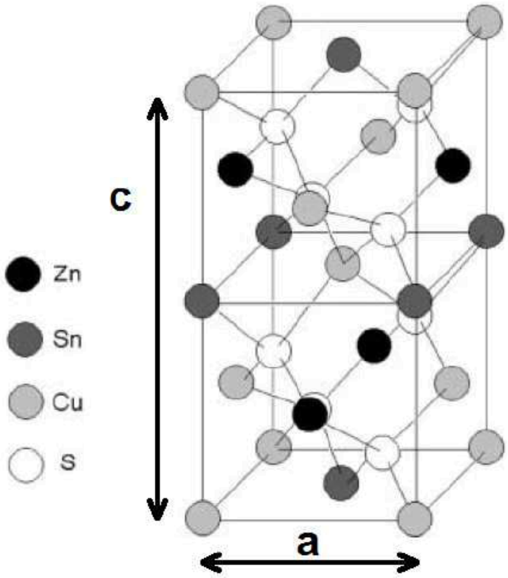

Figure 2-24: Kesterite structure in which CZTS crystallises (Bernardini et al., 2000).

It was found that both the crystalline quality and stoichiometry of the absorber material play a vital role in its performance as an absorber thin film. In order to achieve the desired stoichiometry and best crystallinity, it is essential to optimise the growth and phase formation of the absorber material (Sarswat et al., 2012). The crystal structure of CZTS is shown in Figure 2-24.

Previous studies (Seol et al., 2003, Tanaka et al., 2005, Hall et al., 1978, Schorr, 2007) showed that CZTS and CZTSe crystallize into two crystal structure according to the space group: Kesterite (KS)-type structure (space group I4) and stannite (ST)-type structure (space group I42m) (Figure 2-25).

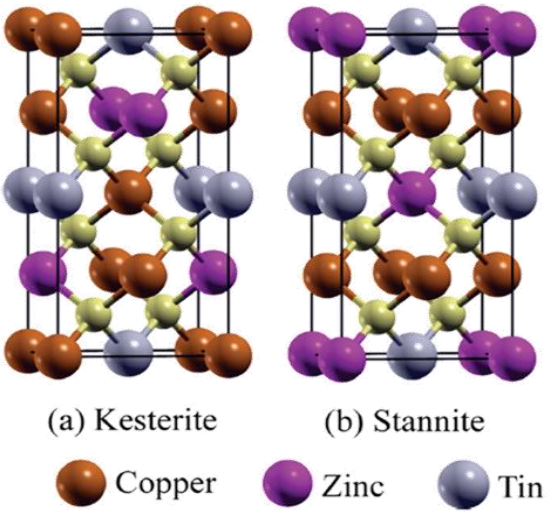

Figure 2-25: CZTS crystalline structures: (a) Kesterite and (b) stannite (Khare et al., 2012).

The KS structure is more stable than the ST (Chen et al., 2009, Kumar and Persson, 2013, Paier et al., 2009). Schorr (2011) and co-workers established that CZTS and CZTSe crystallise in the kesterite-type structure with a disorder within the Cu–Zn layers at z = ¼ and ¾. Both experimental and theoretical results emphasised that kesterite is the more stable type of structure.

Furthermore, the previous literature has acknowledged that the synthesised stannite CZTS films are supposed to be disordered kesterites. All secondary phases have a detrimental effect on CZTS performance, and many of them are hard to detect and are commonly present. Common phases include ZnS, SnS, CuS, and Cu_2SnS_3. Indeed, both KS and ST exhibit tetragonal structures but they mainly differ in terms of Zn and Cu position in the lattice. In the stannite-type structure, ZnSn layers alternate with Cu_2 layers while in the kesterite-type structure, the cation layers CuSn, CuZn, CuSn, and CuZn alternate at $z = 0$, ¼, ½, and ¾, respectively.

Some measurements, including Hall effect and Hot-probe method, have confirmed that during the synthesis of the thin film, kesterite CZTS exhibited a spontaneously *p*-type conductivity, which synthesised *via* Hall effect measurements and Hot-probe method (Nakayama and Ito, 1996, Tanaka et al., 2005).

CZTS possesses a direct bandgap where both the top of the valence band and the bottom of the conduction band occur at the same value of momentum (Figure 2-26) (Chen et al., 2011b), this makes CZTS a promising acceptor to the electrons.

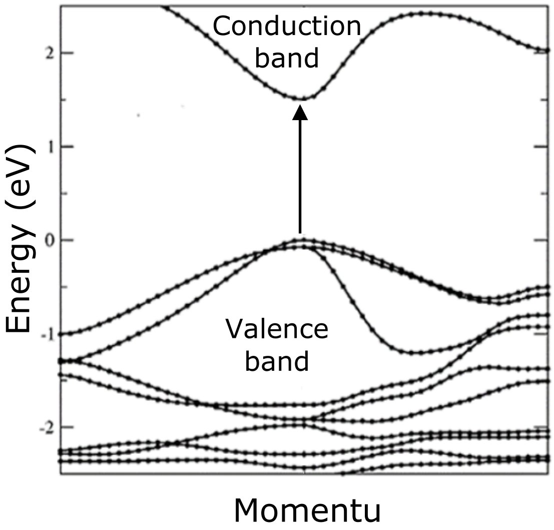

Figure 2-26: Band structure of kesterite CZTS (Persson, 2010).

The theoretical calculations (Chen et al., 2009, Paier et al., 2009, Persson, 2010) reported the values of the bandgap of the kesterite CZTS in the range of 1.47 to 1.64 eV, which is in reasonable agreement with the experimental value ca.1.50 eV (Seol et al., 2003, Tanaka et al., 2005, Hönes et al., 2009). Some literature (Babu et al., 2008, Katagiri, 2005, Katagiri et al., 1997) revealed that the bandgap value of 1.50 eV might vary depending on the material composition or by utilising different conditions in the sulfurization process. According to the crystalline structure (mentioned previously) during the fabrication of CZTS, different phases of CZTS may occur. Chen et al. (2013a) reported that the CZTS compositions that are Zn-rich show photoefficiency higher than those of Cu-poor since the Cu vacancies, which give rise in the shallow acceptors in CZTS are enhanced in Cu-poor compositions; while Zn-rich condition suppresses the substitution of Cu in Zn sites, which results in relatively deep acceptors (Chen et al., 2010a). In terms of photoelectrocatalytic applications, CZTS is considered one of the most promising candidates from the chalcogenides group that may assist in water splitting. Undoubtedly, the possibility of achieving successful water decomposition depends on the route utilised to synthesise CZTS (since it is a P-type SC) and the choice of the photoanode (n-type SC) to generate the best system for hydrogen evolution. Sarswat et al. (2016) examined the combination of some photoanodes with CZTS as water splitting systems, such as CZTS-WO_3, CZTS-$BiVO_4$, and CZTS-TiO_2 nanotubular arrays. Previous studies (Ito and Nakazawa, 1988, Kumar et al., 2009b, Katagiri et al., 2009) reported that the kesterite CZTS and its compounds have an optical absorption coefficient ($\propto$) in the visible region of the electromagnetic spectrum larger than 10^4 cm^{-1}, which makes it more readily able to absorb the photons. Additionally, it facilitates the absorption of the incident light with energies higher than the bandgap in only a few microns.

2.5.3 Intrinsic defects

The optical and electronic properties of any semiconductor is affected by their defects, which play a vital role in controlling the bandgap as well as the material doping, and recombination properties (Walukiewicz, 1989).

During the growth of CZTS, several intrinsic defects can be formed, including antisites CuZn, ZnCu, CuSn, SnCu, ZnSn, and SnZn (CuZn: copper on Zn site), and interstitials (Cui, Zni, Sni, and Si), and the vacancies of Cu, Zn, Sn, and S (VCu, VZn, VSn, and VS) (Abusnina, 2016). Vasekar and Dhakal (2013) revealed that the intrinsic doping assists the doping behaviour of Kesterite, similar to the other chalcopyrite counterparts. They reported that this is possibly controlled by the antisite donor defects (CuZn or CuSn), which are responsible for the p-type behaviour of CZTS. Siebentritt and Schorr (2012) have demonstrated that the p-type behaviour of CZTS may also result from direct creation of copper vacancy and compensation for ZnCu antisite and the S vacancy.

2.6 Approaches to the fabrication of CZTS

As a quaternary compound, CZTS usually contains other ternary and binary phases; therefore, it will be difficult to control the stoichiometry in terms of synthesis parameters, which require precise control (Lin et al., 2013, Gurav et al., 2013). Various approaches have been conducted to synthesis the thin film CZTS including:

- Chemical methods includes: photochemical deposition (Moriya et al., 2006), sulfurization of electrochemically deposited metallic precursors (Araki et al., 2009), sol-gel sulfurization methods (Tanaka et al., 2009), sol-gel spin-coated deposition

(Yeh et al., 2009), and spray pyrolysis (Nakayama and Ito, 1996).

- physical vapour methods, such as co-evaporation (Tanaka et al., 2006), RF magnetron sputtering (Seol et al., 2003), hybrid sputtering (Tanaka et al., 2005).

Furthermore, there are synthesis processes based on solutions (Vasekar and Dhakal, 2013). Previous studies demonstrated that it is hard to synthesis the thin film CZTS with a controlled stoichiometry and high conversion efficiency by using common synthetic methods. Friedlmeier et al. (1997) reported the highest conversion efficiency of 2.3 % of CZTS was achieved, which fabricated by thermal evaporation of the elements and binary chalcogenides in a high vacuum. Wang et al. (2014c) have synthesised the thin film CZTS using a spin coating method with the highest efficiency of 12.60 %. Nguyen et al. (2015) studied the effect of annealing on the crystallisation of the CZTS absorber, which was prepared by the hot-injection method, they reported a conversion efficiency of 4.94 %. Theoretically, CZTS is expected to have efficiency better than 30.00 % (Zhou et al., 2012). Wang and Demopoulos (2015) have studied the growth of Cu_2ZnSnS_4 nanocrystalline on TiO_2 nanorod arrays *via* the controlled method successive-ion-layer-adsorption-reaction (SILAR). Although they have achieved an internal quantum efficiency of ~ 60.00 % with a short circuit current density of 3.22 $mA.cm^{-2}$, they required to heat the reaction solution. Lin et al. (2016b) fabricated the quaternary

CZTS using the sputtering route. They were capable of obtaining an approximate stoichiometry of 2:1:1:4 of CZTS but with uncontrollable film thickness. Some researchers have studied the fabrication of thin films by conducting electrodeposition techniques, which have developed over the past five decades and are widely used in the industries. The chemical methods mentioned earlier can be classified into two categories: i) vapour-phase deposition (e.g., chemical vapour deposition, evaporation, molecular beam epitaxy, sputtering and atomic layer deposition), and (ii) liquid-based deposition (e.g., electrochemical deposition, chemical solution deposition, Langmuir–Blodgett films and self-assembled monolayers) Ghosh et al. (2000) Stickney (1999) and co-workers were the first to show that electrochemical atomic layer (EC-ALD) deposition as the most efficient and popular method compared with the other epitaxy methods to fabricate or integrate thin films as explained earlier. They reported that EC-ALD is capable of controlling a precise thickness by angstrom resolution and coverage of high aspect ratio nanostructures; thus the targeted thickness of the desired compound is controlled by the number of EC-ALD cycles of the precursor molecules (metal ions), which in turn ensure a self-limiting of substrate surface reactions (Scragg, 2010, Saleem et al., 2014). To obtain an excellent optical absorption, researchers have studied the electrodeposition and fabrication of the thin film CZTS on various substrates, such as TiO_2 nanorods (NRs) (Hou et al., 2014), Ag

(Zhang et al., 2009), and ITO (Reith and Hopman, 2012). The EC-ALD requires preparing precursor solutions for the constituents of CZTS, i.e., Cu, Zn, and Sn solutions at room temperature, followed by annealing the sulfur deposition in a furnace (elevated-temperature sulfurization (Sarswat and Free, 2012)). Some parameters could be tuned to achieve the desired thickness including the temperature, deposition time, precursor's composition and pH of the precursor solution.

Chapter 3: Methodology

This chapter outlines the structure of this study, including chemicals and materials used, experimental procedures, and adopted analytical techniques. All the materials, equipment, and details of the methods utilised in the experiments are presented here, respectively; this followed by a description of the electrochemical characterisation of CZTS/TiO_2 NTAs. Afterward, a brief introduction is given explaining the fundamentals of the analytical techniques involved including EDX, XPS, FEG-SEM, XRD and UV-Visible spectrometry.

3.1 Materials, chemicals and equipment

All materials and chemicals for the synthesis of TiO_2 NTAs and the coating were listed (Table 3-1, Table 3-2, and Table 3-3) and purchased from Sigma-Aldrich, VWR chemicals, and Fisher Scientific. All materials and chemicals were used without additional treatment unless otherwise specified. A few exceptions were listed as follows:

- Ti sheet was greased with acetone, followed by washing with deionised water several times to eliminate any contamination that may exist.
- 5.0 M of the concentrated sodium hydroxide (NaOH) solution was diluted in 100.0 mL deionised water (DIW).
- Potassium chloride was used to prepare a solution of 3.0 mol L^{-1}, to be injected into the capillary tube of the reference electrode (Ag/AgCl).

- 1.0 M of the concentrated HCl was diluted into 100.0 mL deionised water to remove any metals, which may be deposited on the Pt wire counter electrode (CE) during the electrodeposition process.

Table 3-1: Chemicals and materials.

Chemical/Material	**Chemical formula**	**Supplier**	**Notes**
Ammonium Floride	NH_4F	Sigma-Aldrich	ACS reagent, ≥98.00%
Acetone	CH_3COCH_3	VWR Chemicals	ACS reagent, ≥99.50%
Ethanol, absolute	CH_3CH_2OH	Sigma-Aldrich	ACS reagent, ≥ 99.80%
Ethylene Glycol (Ethanediol)	$C_2H_6O_2$	Fisher	Laboratory reagent grade
Copper Sulfate	$CuSO_4$	Sigma-Aldrich	≥99.00 %
Zinc Sulfate	$ZnSO_4$	Sigma-Aldrich	≥99.00 %
Tin (II) Chloride dehydrate	$SnCl_2.{}_2H_2O$	Sigma-Aldrich	≥98.00 %
Sulfur	S	Sigma-Aldrich	99.50-100.50 %
Trisodiumcetrate titrahydrate	$Na_3C_6H_5O_7$	Sigma-Aldrich	Reagent
EthylenDiem titr-aaciticacid	$C_{10}H_{16}N_2O_8$	Sigma-Aldrich	99.00-101.00 % (complexing agent)
Sodium Sulfate	Na_2SO_4	Sigma-Aldrich	
Sodium Sulfide	Na_2S	Sigma-Aldrich	ACS reagent, ≥ 99.80
Sodium Sulfite	Na_2SO_3	Sigma-Aldrich	ACS reagent, ≥ 99.80 %
Acetonitrile	C_2H_3N	Fisher	Absorbance, 99.99 %
Hydrochloric acid	HCl	Fisher	S.G. ca.37.00 %
Deionised water	H_2O	Direct-Q®5UV	Ultrapure water
Reverse osmosed water	H_2O	Millipore Corporation	Millipore grade
Potassium chloride	KCl	Sigma-Aldrich	Laboratory reagent grade 99.90 %

Ammonium hydroxide solution	NH_4OH	Sigma-Aldrich	Reagent, 28.00-30.00% NH_3 basis
Acetic acid, glacial	CH_3COOH	Fisher	Laboratory reagent grade
Ti sheet	Ti	Unicorn metals ltd	0.2 mm thickness
Ag/AgCl reference electrode	Ag/AgCl	CH Instrument	With porous Teflon tip
Pt wire	Pt	CH Instrument	1.0 mm diameter
Silver nitrate	$AgNO_3$	Fisher	
Germanium oxide	GeO_2	Sigma-Aldrich	

Table 3-2: Equipment list for preparation of substrate and precursor solutions.

Equipment	Manufacturer	Model
System DC power supply	Agilent	6645A, 0.0 to 120.0 V / 0.0 to 1.5 A
Tube furnace	ELITE	Eurotherm, TSH 12/50/300-2416
Light Source	Newport	500.0 W Xe DC arc lamps
Centrifuge	Hettich Zentrifugen	Rotofix 32 A
Potentiostat	Autolab, IVIUM Technologies	PGSTAT 100, Ivium-n-Stat
Pump	EDWARDS	PM 13128.0 to 820.3

Table 3-3: Analytical equipment.

Equipment	Manufacturer	Model
X-ray diffractometer (XRD)	Bruker	D8 Advance
Energy-dispersive X-ray spectroscopy (EDX)	JEOL	6490 LV SEM
Field Emission Gun Scanning electron microscope (FEG-SEM)	JEOL	7100F
X-ray photoelectron spectrometer (XPS)	AXIS ULTRA	Kratos DLD
UV-Vis-NIR spectroscopy	Agilent	Cary 5000

3.2 Experimental

3.2.1 The anodization cell for TiO_2 NTAs synthesis

The titanium nanotube arrays (TiO_2 NTAs) were successfully synthesised according to the method outlined in the literature (Scaramuzzo et al., 2014b, Zhu et al., 2010) by two steps anodization route. Many researchers prepared TiO_2 NTAs in this way and they studied the effect of different parameters on their morphology and performance (electrical and optical), but it was essential to obtain a successful substrate (well-organised TiO_2 NTAs with the desired electrical and optical properties) to enable the electrodeposition of the thin film CZTS onto TiO_2 NTAs and as a consequence to improve the photoelectrochemical properties of these nanotubes.

3.2.2 Synthesis of TiO_2 NTAs via electrochemical anodization and surface treatment

The TiO_2 NTAs were successfully synthesised *via* an electrochemical anodization technique using Agilent DC power supply (6645A, 0.0 to 120.0 V / 0.0 to 1.5A). Prior to anodization, a Ti foil (thickness 0.20 mm and purity 99.90 %) was cut into 35.0 mm × 10.0 mm, then cleaned with acetone and deionised water for 30.0 m in an ultrasonic bath, respectively then dried under nitrogen flow. The anodization electrolyte contained 0.32 wt % ammonium fluoride (NH_4F), which was added to 40.00 mL ethylene glycol ($C_2H_6O_2$) in a glass container and 4.00 vol % of reverse osmosed water (ROW, resistivity = 0.0476 MΩ-cm) was slowly added to the ethylene glycol for 1 h with constant stirring. The anodization cell was formed of two electrode configurations, a Ti sheet as an anode (WE) and Pt wire as a cathode (CE) (Figure 3-1-a and b).

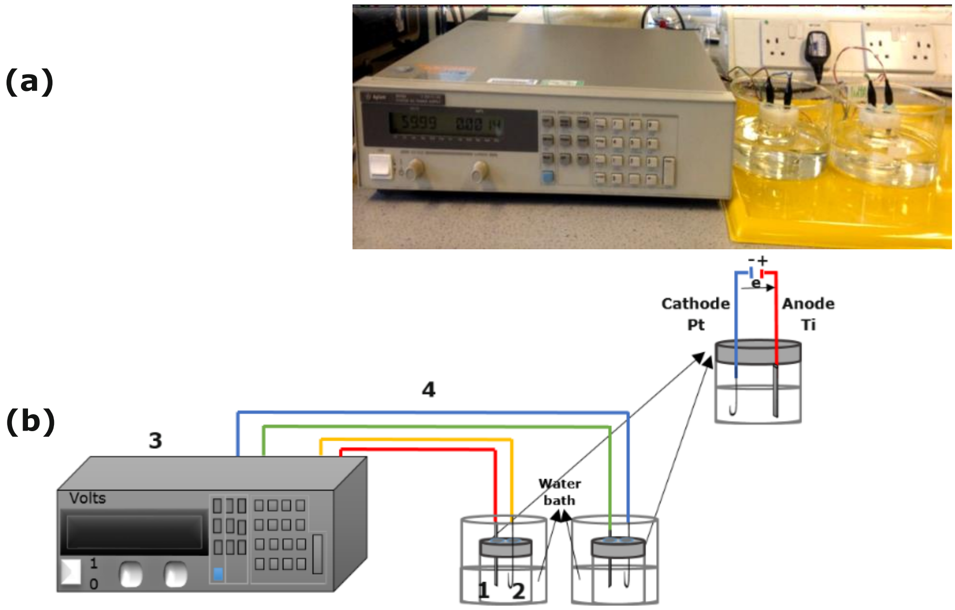

Figure 3-1: Experimental apparatus of electrochemical anodization cell. (a) the actual electrochemical anodization process for synthesizing TiO_2 NTAs. (b) brief explanation: (1) Ti sheet (WE), (2) Pt wire (CE), (3) DC power supply and (4) Connections.

The anodization was performed in two steps:

1. 20.0 m anodization at a constant bias applied voltage of 60.0 V. The sample was washed with plenty of ROW and soaked into ethanol for 5.0 m to remove the residual electrolyte and left to dry naturally in air; this was followed by thermal annealing at 700.0 ℃ for 1.0 h, (at a heating and cooling rate of 2.0 ℃ m^{-1}) in tube furnace (Elite, TSH 12/50/300-2416).

2. 6.0 h anodization at a constant bias applied voltage of 60.0 V; then the sample was soaked in ethanol for 10.0 m and

annealed at 450.0 ℃ for 2.0 h (heating and cooling rate of 2.0 ℃ m^{-1}) to convert the amorphous phase to an anatase crystalline phase (Li et al., 2012, Jennings et al., 2008).

3.3 TiO_2 NTAs drying methods

Previous studies (Palmas et al., 2011, Zhu et al., 2011a, Srimuangmak and Niyomwas, 2011, Paulose et al., 2006b) have investigated several parameters in the synthesis of TiO_2 NTAs, in order to obtain a well-organised TiO_2 NTAs with a length ranged of 20.0 to 134.0 µm, wall thickness 8.0 to 10.0 nm, and inner pore diameter ranged from 20.0 to 150.0 nm.

However, the effect of the drying method, which was used after the second anodization step, was not reported. To improve the performance of the TiO_2 NTAs, and for comparison with those naturally dried (the TiO_2 NTAs left to dry naturally in air), two drying methods were carried out during the preparation of TiO_2 NTAs in this research: Acetonitrile vacuum drying and Freeze drying.

3.3.1 Acetonitrile vacuum drying

Acetonitrile (C_2H_3N) used as a solvent for many reasons: (1) it can dissolve the electrolyte (2) acetonitrile used as a dehydrating solvent owing to its ability to dissolve in both water and ethanol freely. It is also considered as the most appropriate solvent for the drying method because it has a low freezing temperature (–45.0 ℃) and weak in polarity (KATOH, 1979). Figure 3-2 illustrates a diagram for the experimental apparatus of acetonitrile vacuum drying.

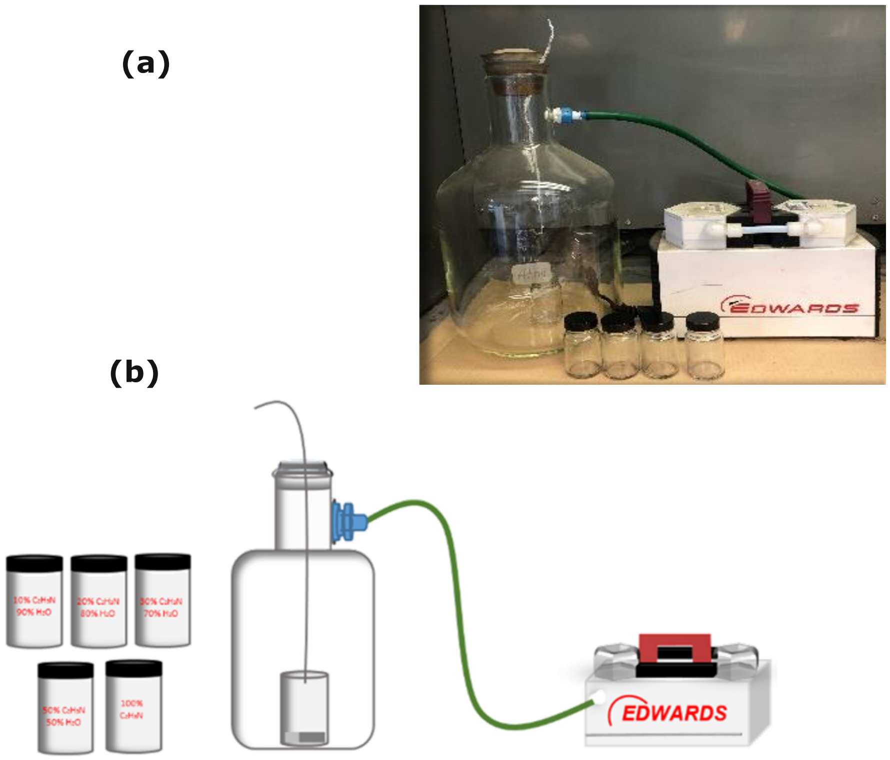

Figure 3-2: Experimental apparatus of acetonitrile vacuum drying: (a) the actual acetonitrile vacuum drying and (b) the sketch map.

After the second anodization step (6.0 h), the sample was washed with DIW and soaked in ethanol for 10.0 m. This was followed by evaporation in a vacuum chamber at a temperature above the freezing point. The sample was dehydrated in a graded series of acetonitrile washes, which involves five solutions of 20.0 vol % of C_2H_3N in DIW, and deionised water, which was prepared as follows:

1. 50.0 vol % C_2H_3N + 50.0 vol % H_2O

2. 70.0 vol % C_2H_3N + 30.0 vol % H_2O

3. 80.0 vol % C_2H_3N + 20 vol % H_2O

4. 90.0 vol % C_2H_3N + 10.0 vol % H_2O

5. 100.0 vol % C_2H_3N

The sample was immersed in each solution for 20.0 m to remove the water and any residual electrolyte. After that, the sample was placed in 100.0 % acetonitrile in an unsealed glass container located in a bell jar that was sealed tightly by a rubber bung ready to be evacuated. The sample will then be dehydrated after the graded series of acetonitrile washes.

The solvent in the container was cooled then frozen aided by the evacuation. The frozen acetonitrile in the sample sublimates in the vacuum; then, the sample dried after about 1 h 30 m. The sample was taken out and observed under light irradiation to check the photocurrent density after annealing. For comparison, two samples were prepared and then compared by drying them naturally, drying one in the air and the other one by acetonitrile vacuum.

3.3.2 Freeze drying

The Freeze drying was conducted following the s anodization step. The freeze drying means the removal of solvents or water from a previously frozen material *via* the sublimation (Labconco, 2008). This drying method consisted of pre-freezing and drying steps.

The sample was placed in a plastic jar (Figure 3-3*) and was sealed with a perforated piece of foil to allow evacuation. The sample was then located on the top tray of the dryer and was evacuated under pressure 7.0 mbar; this was followed by the pre-freezing step at temperature −30.0 ℃.

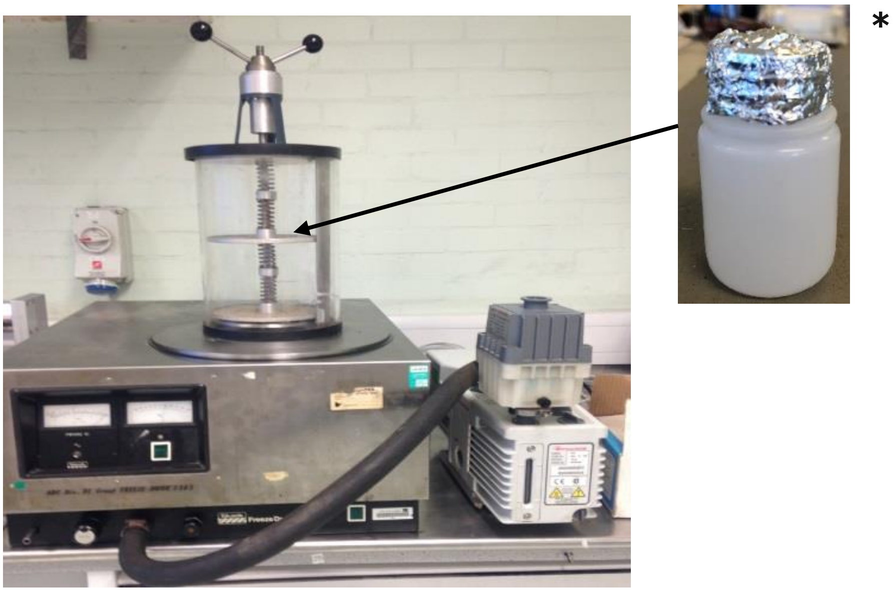

Figure 3-3: Freeze dryer equipped with vacuum pump. (*) represents the sample placed on the top tray of the dryer.

3.4 Electrochemical atomic layer deposition (EC-ALD) of CZTS onto TiO_2 NTAs

The uniformly coated CZTS/TiO_2 NTAs were synthesised by the electrochemical atomic layer deposition method described in the literature (Tlemçani et al., 2015). Several researchers (Zhu et al., 2010, Kar et al., 2006, Abedinisohi, 2013, Liu et al., 2012) were studied the electrodeposition of two and three metal ions onto TiO_2 NTAs, however, none were researching the simultaneous underpotential deposition (UPD) of the quaternary compound CZTS onto these nanotubes. The ions of Cu, Zn and Sn were competitively electrodeposited once their precursor solutions were mixed. Certainly, this depended on their affinity and conductivity towards the substrate (TiO_2 NTAs), which in turn enabled the penetration of the ions to form chemical bonds with the substrate.

3.4.1 Preparation of precursor solutions

Aqueous electrolytes of Cu, Zn and Sn were prepared separately by mixing 0.02 M $CuSO_4$ (Sigma Aldrich, purity ≥ 99.00 %), 0.20 M $ZnSO_4$ (Sigma Aldrich, ≥ 99.00 %) and 0.01 M $SnCl_2$ (Sigma Aldrich, ≥ 98.00 %) in deionised water. Sn solution was further centrifuged (20,000.0 rpm, 30.0 m) to obtain a well-dissolved solution to eliminate the excess of tin hydroxide ($Sn(OH)_2$), which was suspended in the water due to impurities present in the powder ($SnCl_2$). 0.20 M of trisodium citrate dihydrate ($Na_3C_6H_5O_7$) (Sigma Aldrich, ≥ 98.00 %) was added to each electrolyte.

Degassing step was performed by purging N_2 into the precursor solutions for 30.0 m to remove the dissolved oxygen. The air exposure to the precursor solutions was minimised by sealing the containers using Parafilm. The electrolytes were mixed on magnetic stirrers for 2.0 h. Ethylenediaminetetraacetic acid (0.00 to 0.60 M $EDTA^{2-}$, Fisher, 99.00 %) was used as a complexing agent to shift the UPD potential towards the negative side, where needed. The pH value of the solutions was adjusted by 5.00 M NaOH and 0.50 M acetic acid solutions to reach the desired value between 4.7 to 7.0.

3.4.2 A conventional three-electrode cell

After determining the UPD potential range for the simultaneous deposition of each element and adjusting the pH of the individual precursor solutions, the precursor solutions were mixed on a magnetic stirrer for 15.0 m, and the final pH of the electrodeposition bath was recorded. Subsequently, the electrodeposition was carried out for 7.0 h at room temperature by employing an electrochemical workstation (Metrohm, PGSTAT100 Autolab Co., Ltd, UK).

The EC-ALD cell (Figure 3-4) consists of three electrodes, the as-prepared TiO_2 NTAs as working electrode (WE), platinum (Pt) wire as a counter electrode (CE) and Ag/AgCl (in 3.00 M KCl) as a reference electrode (RE). This electrochemical workstation was employed for any deposition or CV experiments which were performed in this study.

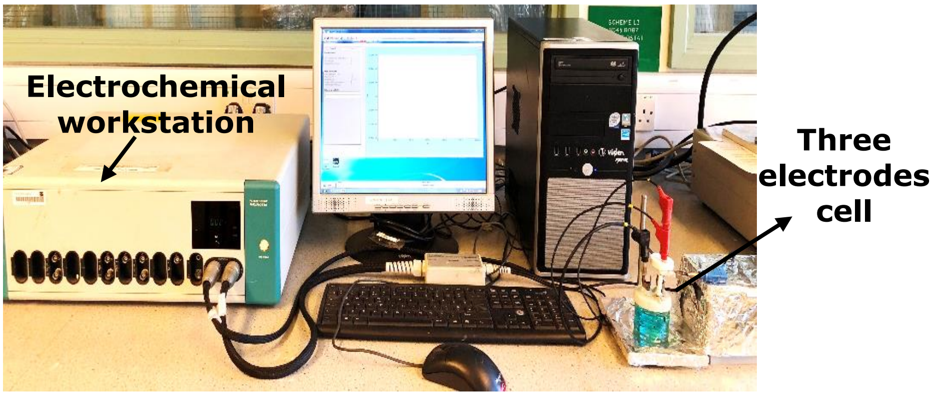

Figure 3-4: Experimental apparatus of electrochemical atomic layer deposition (EC-ALD).

3.4.3 Sulfurization process

Sulfurization implies to annealing the metal precursor in sulfur ambient to merge sulfur and convert the precursor into CZTS film. The sulfurization process includes sulfur powder as a source for sulfur vapour inside the quartz tube. Prior to the sulfurization, the N_2 was purged inside the tube to prepare a clean environment for the sample.

After electrodeposition of Cu, Zn and Sn, the coated sample was rinsed with deionised water (DIW) and left to dry naturally for 16.0 h and transferred to a tube furnace (Elite, TSH 12/50/300-2416) for annealing step at 585.0 ℃ for 2.0 h in nitrogen flowrate = 20.0 mL m^{-1}. The nitrogen function was to carry the sulfur vapour inside the tube and to remove any impurities or by-products that may be produced during the sulfurization. Two ceramic boats were placed inside the quartz tube in the furnace: the first one contains elemental sulfur (2.00 g), followed by another one where the coated substrate was placed.

Both sides of the quartz tube were sealed with holed silicon bungs. The outlet of the quartz tube was joined with a washing bottle filled with DIW to collect the excess sulfur vapour and to avoid any contamination in the lab environment. After the sulfurization, the sample was cooled down to room temperature naturally. Figures 3-5-a, b, and c illustrate the actual and the schematic diagrams for the sulfurization process.

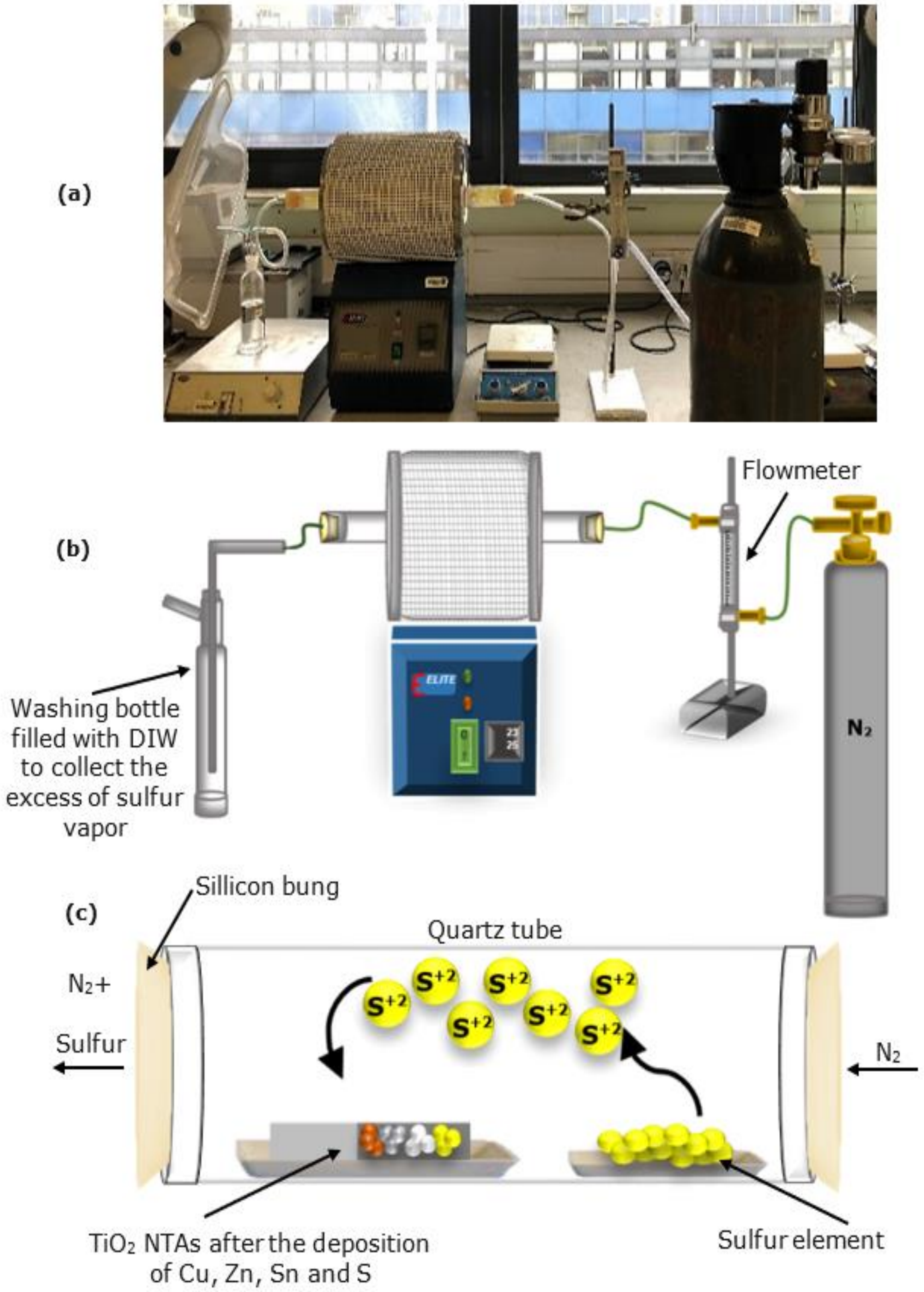

Figure 3-5: The sulfurization process in the tube furnace. (a) the actual equipment used in the sulfurization process; (b) the sketch map of the sulfurization process and (c) brief explanation for the sublimation of Sulfur onto the substrate.

3.4.4 Determination of UPD potential for Cu, Zn and Sn

The electrochemical workstation was employed to conduct cyclic voltammetry (CV) measurements to determine the UPD potential of individual elements. The determination of the UPD potential for Cu, Zn, and Sn was a crucial step in achieving their simultaneous electrodeposition onto TiO_2 NTAs, and to avoid the bulk deposition which may occur, resulting in clogging of the tube moth and reducing its photocatalytic activity.

The CV experiments were performed within the following applied potential ranges for Cu (–1.500 to 1.000 V), Zn (–0.350 to 0.850 V) and Sn (–0.500 to 1.500 V). Measurements were carried out at the scan rate = 20.0 mV s^{-1}.

The co-deposition of Cu, Zn, and Sn is the most challenging step in this study due to the variation between their redox potentials ($Cu^{2+} \rightarrow Cu$, $Zn^{2+} \rightarrow Zn$, and $Sn^{2+} \rightarrow Sn$, E_0 = –0.345 V, –0.762 V and –0.140 V, respectively). To overcome this issue, the addition of a complexing agent to the precursor solutions may provide a stoichiometric deposition and forming the ligands, which in turn will restrict the movement of the metal ions and keep them stable in the solution to prevent any possibility of bulk deposition may take place. Section 3.4.5. illustrates in detail how the complexing agent assists the formation of ligands.

3.4.5 Shifting of UPD potential by the addition of complexing agent (CA)

Employing a complexing agent (CA), such as ethylenediamine- tetra-aceticacid (EDTA), diethylenetriaminepentaacetic acid (DTPA) and diethylenetriamine-penta acid (DTPMP)) was an essential pre-treatment step for the precursor solutions to shift the UPD potentials, specifically for Cu and Zn. Optimising the complexing agent is crucially dependent on the pH value of the solution (basic or acetic (pH ca. 9.0 or pH ca. 2.5 respectively)); hence, specific CA was needed to encourage the formation of OH^- or H^+. The latter one was not suitable in this work since it controls the H^+ ions and prevents the production of H_2.

However, the pH of the precursors, in general, is neutral (pH ca. 7.0); therefore, any complexing agent was appropriate to be utilised in this study. EDTA ($C_{10}H_{16}N_2O_8$) was selected as a CA to adjust the UPD potential. It is the most common chelating agent in analytical chemistry since its metal complexes are water soluble.

The EDTA molecule has six different donor atoms and so forms highly stable ratio 1:1 chelate complexes with metal ions by six ligands: Four O (four carboxylic acid groups (acidic hydrogens are red)) and two N (two amine groups with lone pair electrons (green dots)) (Figure 3-6) (PIRKANNIEMI, 2007).

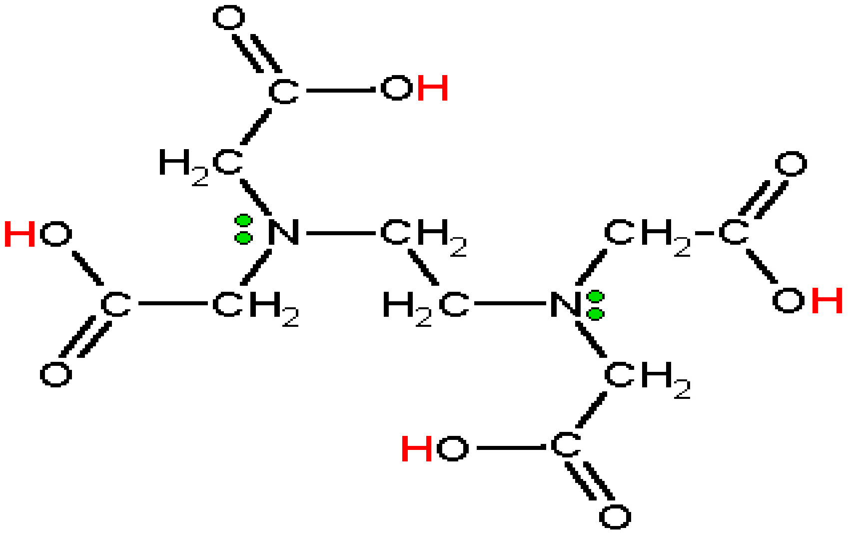

Figure 3-6: Structure of the EDTA. Green and red dots are representing the two amine groups with lone pair electrons, and the four carboxylic acid groups (acidic hydrogens), respectively. Reprinted from (PIRKANNIEMI, 2007).

The four negative charges will be on the four acid functional groups and will bond to each zinc and Cu ions. The molecular structure of the complexes (Zn-EDTA and Cu-EDTA) formed is explained in Figure 3-7-a and b.

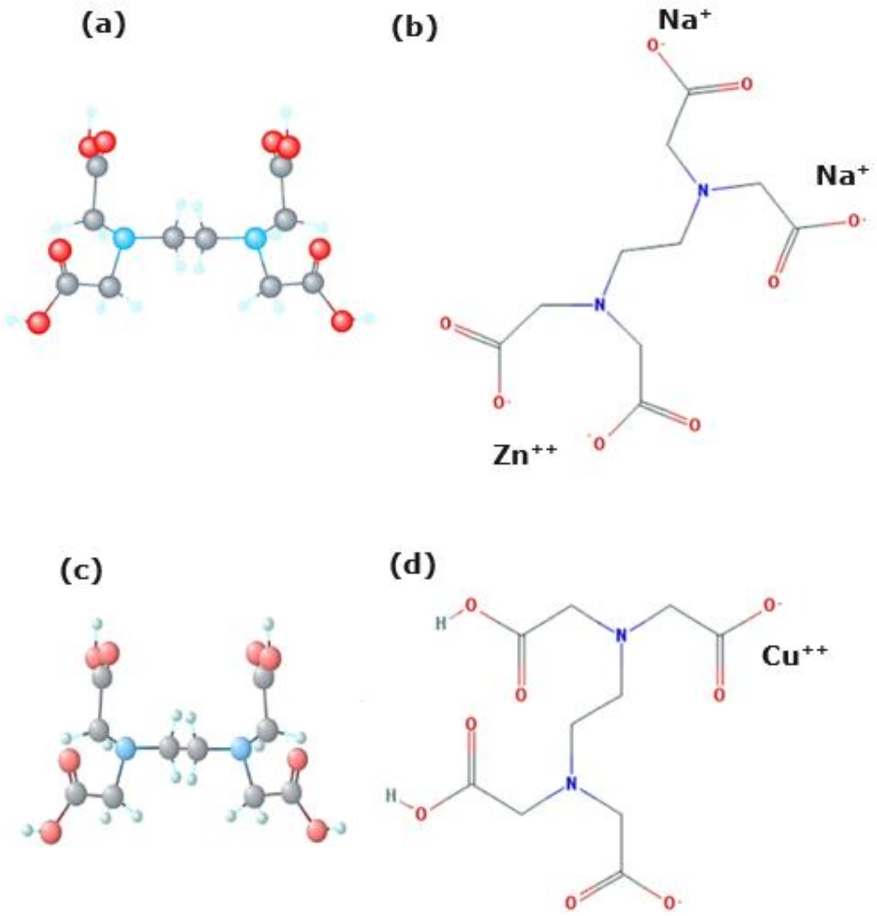

Figure 3-7: The molecular structure of Zn-EDTA complex (a) 3D comformer (b) 2D structure, and Cu-EDTA complex (c) 3D comformer (d) 2D structure (Ihlenfeldt et al., 2009, Bolton et al., 2011).

The corresponding chemical reactions produced from the complexing coordination of Zn and Cu with EDTA are:

$$Zn^{2+} + EDTA \rightarrow [ZnEDTA]^{2-} + 4H^{+} \qquad \text{Eq. 3-1}$$

$$Cu^{2+} + EDTA \rightarrow [CuEDTA]^{2-} + 4H^{+} \qquad \text{Eq. 3-2}$$

3.4.6 pH adjustment and UPD potential shifting

The concept of the underpotential deposition shift refers to the difference between the potential desorption peak (oxidation peak) for a layer of a metal M adsorbed on a foreign substrate S and the potential of the corresponding dissolution peak (reduction peak) of the pure metal M (Kolb et al., 1974, Gerischer et al., 1974, D.M. Kolb, 1975). The UPD potential of the three elements essentially should lie in a common region, so the resulting deposited film will generally be limited to an atomic layer. Moreover, the pH of the precursor solutions should be close to each other to allow homogeneous atomic layer deposition.

The pH value of the precursor solutions was adjusted in the range of 4.7 to 7.0 depending on several parameters, including the concentrations of the metal salts, EDTA concentration, pH value of the individual solution, UPD potential value and deposition duration. Three values of EDTA concentration (0.00, 0.10, and 0.30 M) were added to the precursor solutions of Cu and Zn, and the shifting process was performed by applying CV when required using the electrochemical workstation. For Zn, the UPD potential shift was limited between the ranges –0.500 V to 1.500 V, while for Cu, the UPD potential shift was limited between the ranges –1.500 V to 1.000 V.

3.4.7 EC-ALD of CZTS onto TiO_2 NTAs from individual precursor solutions

For further improvement in the photocatalytic properties of the composite CZTS/TiO_2 NTAs, the deposition was conducted at UPD potential −0.650 V for 1.0 h from individual precursor solutions of Cu, Zn, and Sn. The pH value of the Cu solution was adjusted to 7.00 to avoid bulk deposition, while the pH of Zn and Sn was maintained at their original values 4.70 and 6.83, respectively. Six containers were prepared involving: three containers of Cu, Zn, and Sn precursor solutions with three DIW containers to rinse the sample after each deposition step. The sample was first immersed into Cu for 1.0 h then immersed in DIW for 10.0 s to remove any Cu residue. This step was repeated for Zn and Sn. The sample was then transferred to the annealing in the S environment in the tube furnace for 6.0 h at 585.0 ℃.

3.4.8 Doping the composite CZTS/TiO_2 NTAs with germanium (Ge) and silver (Ag)

To enhance the conductivity and to improve the absorption performance of the as-synthesised CZTS/TiO_2 NTAs composite, elemental doping with Silver (Ag) and Germanium (Ge) metal ions was conducted in this study. Silver was selected from among noble metals to modify CZTS/TiO_2 NTAs owing to its ability to act as an electron trap; this can hinder the recombination of e^-/h^+ pairs. Ag is relatively affordable in comparison to other noble metals and also possesses special behaviour for oxygen adsorption (Liang et al., 2011). The doping experiment was conducted on TiO_2 NTAs before and after the coating with CZTS by preparing a precursor solution as a source of silver ions containing 0.005 M silver nitrate ($AgNO_3$, Fisher), 0.20 M trisodium, pH = 8.27. The CV measurements was performed at the applied potential window of –1.500 V to 1.000 V at scan rate 10.00 mV s^{-1} to identify the UPD potential of Ag onto pure TiO_2 NTAs and CZTS/TiO_2 NTAs.

Concerning the doping with germanium (Ge), Ge was selected as p-dopant to enhance the optical properties of TiO_2 NTAs, given that the electron mobility in Ge is four times the hole mobility, and Ge has small bandgap 0.67 eV, which allows infrared light absorbance efficiently (Liang et al., 2007, Bakos et al., 1991, Liang et al., 2009). The UPD potential of Ge was also identified *via* preparing a precursor solution as a source of Ge ions containing 0.0025 M germanium oxide (GeO_2, Sigma-Aldrich), 0.200 M trisodium, pH=8.57. The CV measurements were performed at the applied potential window of –0.500 V to 0.500 V with a three scan rate 20.00 mV s^{-1} to identify the UPD potential of Ge onto pure TiO_2 NTAs and CZTS/TiO_2 NTAs composite. The sample was rinsed with DIW after each CZT deposition step, followed by an extra rinsing step in Ag blank solution (solution contains trisodium and DIW, pH = 8.27).

It was essential to stabilise the pH value of the sample before immersing it in an Ag solution to prevent the precipitation of Ag at low pH values (< 8.27). The sample was then transferred to the annealing step in the S environment in the tube furnace for 6.0 h at 585.0 ℃. The same procedure was repeated for Ge doping except the pH of blank Ge was maintained at 8.57.

3.4.9 Electrochemical characterisation

1. Cyclic voltammetry (CV) and Linear sweep voltammetry

In this study, the properties of mass transfer and the kinetics of electrons were characterised by employing two forms of voltammetry, including cyclic voltammetry (CV) and linear sweep voltammetry (LSV). In both CV and LSV forms, the applied voltage for the working electrode was scanned linearly, and the current response was recorded and plotted from the instrument as a function of the applied potential (Figure 3-8).

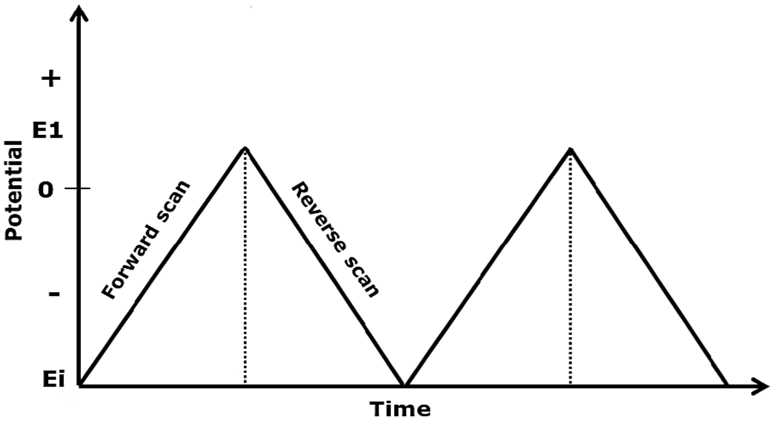

Figure 3-8: typical waveform in a cyclic and linear sweep voltammetry.

Figure 3-8 depicts the typical waveform of the potential vs. time signal for CV and LSV voltammetry forms. In cyclic voltammetry, the reaction direction is reversible, and the potential sweep starts at the pre-set potential (E_1) back to the initial value (E_i). Repeating the potential sweep resulted in multiple scans ($E_i \rightarrow E_1 \rightarrow E_i$), whereas in linear sweep voltammetry, no potential reversible sweep takes place, the potential scan starts from the initial value (E_i) to the pre-set value (E_1). This voltammetry form was employed to test the photocatalytic activity of the photoanodes TiO_2 NTAs and CZTS/TiO_2 NTAs under light irradiation. The experiment was performed in a three-electrode configuration (described above), the anodic potential sweep starts from the open circuit potential (OCP) to the potential where oxygen evolution initiates. The recorded current in this potential range is considered the photocurrent. Cyclic voltammetry was utilised to determine the UPD potentials of Cu, Zn, and Sn from their precursor solutions on pure individual TiO_2 NTAs substrates.

Additionally, CV was also utilised to identify the UPD potentials of Ag and Ge on pure TiO_2 NTAs substrates. These experiments are detailed and explained in chapter 5.

2. Chronoamperometry

Chronoamperometry is a time-dependent electrochemical technique where the potential of the working electrode is set at a specific value, and the current monitored as a function of a pre-set period. Figure 3-9 shows the typical waveform of potential-time signals in chronoamperometry.

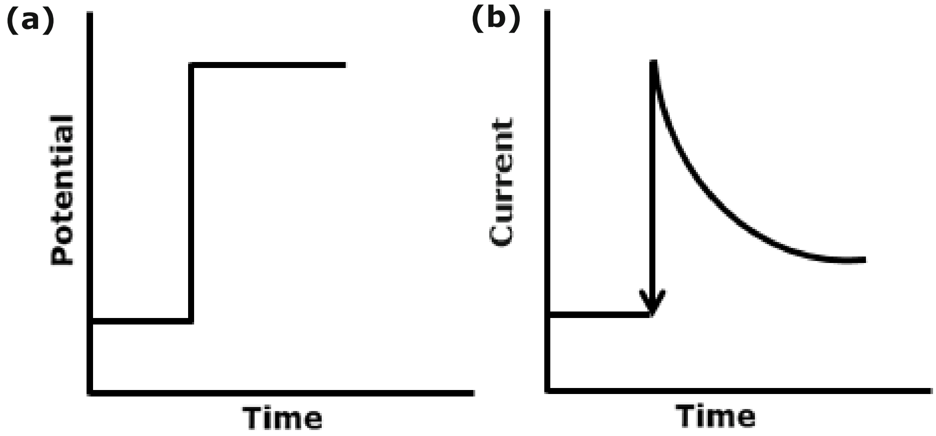

Figure 3-9: Typical (a) input and (b) output waveforms for chronoamperometry.

The chronoamperometry was used principally for the following functions:

1. Electrochemical atomic layer deposition of Cu, Zn, and Sn onto TiO_2 NTAs substrates at the pre-determined UPD potential within the range 0.200 to −1.000 V (this is the common UPD potential range obtained from CVs and assists the simultaneous deposition of the three metal ions), the electrodeposition was conducted for 7.0 h.

2. To test the H_2 generation rate of pure TiO_2 NTAs and after the coating with CZTS under the illumination of light. In these experiments, 0.500 V was the applied potential, which was obtained from exposing the photoanodes to the light. LSV (section 3.5.1.) was utilised in these measurements.
3. Determine the photoresponse of CZTS/TiO_2 NTAs composite under pulsed illumination at a constant applied potential of 0.500 V (vs. Ag/AgCl). These measurements were conducted to test the charge transport in the as-synthesised CZTS/TiO_2 NTAs composite.

3.5 CZTS/TiO_2 NTAs characterisation

General research strategy

The as-synthesised pure TiO_2 NTAs and the novel CZTS/TiO_2 NTAs composite were characterised with the aid of various analytical techniques. In order to achieve a highly effective and successful deposition, it was essential to optimise the optical and electrical performance of the TiO_2 NTAs substrates. Primarily, the anatase crystalline phase of the as-prepared TiO_2 NTAs substrates was identified by the X-ray diffraction (XRD). The surface morphology was analysed by using field emission gun-scanning electron microscopy (FEG-SEM). A necessary step for testing the photocurrent under light irradiation was conducted to verify the performance of TiO_2 NTAs substrates under light irradiation after the electrodeposition of CZTS onto TiO_2 NTAs.

The kesterite crystalline structure of CZTS was identified with XRD and FEG-SEM to verify the heterogeneous coaxial structure of the as-synthesised CZTS/TiO_2 NTAs composite. An SEM equipped for energy dispersive spectroscopy (EDX) was utilised to determine the composition of the deposited elements (Cu, Zn, Sn, and S) at 15.0 kV. The most challenging part of this research was to deposit the compound Cu_2ZnSnS_4 with a stoichiometric ratio of 2:1:1:4 for several reasons, specifically the overlapping of K peaks of Cu and Zn ($K\propto1$ = 8.040 and 8.639, $K\propto2$ = 8.028 and 8.616), respectively. Therefore, for further accurate elemental detection, X-ray photoelectron spectroscopy (XPS) was used for this purpose. The photocurrent density of CZTS/TiO_2 NTAs was also verified with LSV. UV-Vis spectroscopy was employed to examine the capacity for harvesting the light of pure TiO_2 NTAs before and after the electrodeposition of the composite CZTS. Here, to gain confidence in the new photoanode, the H_2 generation rate of the coated TiO_2 NTAs was tested by using Hoffman voltameter.

3.6 Fundamentals of analytical techniques

3.6.1 Analytical techniques using X-rays

The crystal structure of a material is commonly analysed by using a non-destructive X-ray, which is produced when a beam of high energy (e.g., ions, electrons, neutrons, and protons) are scattered a crystalline surface of interest. A bulky X-ray tube was employed for elemental analysis by EDX, as discussed earlier. XRD analysis requires an atomic distance of wavelength similar to the radius of unit-cell spacing in a crystal (ca. 0.1 nm) to identify the crystalline structure of a sample. In some analytical technique, the radiation source could be K∝ and Kβ X-rays for some elements.

In XRD, the X-rays are produced by a cathode ray tube hitting a metal, usually Cu or Mo, with a beam of electrons emitted from a hot filament (often tungsten). These X-rays are then filtered to produce monochromatic radiation, collimated to concentrate them, and then direct them toward the sample. An elastic scattering occurs when the X-rays penetrate a medium composes of particles possessing wavelength smaller than that of the incident X-rays. The X-rays will maintain their intrinsic energy while varying their direction during the scattering process. Once the X-rays hit the arranged atoms with a fixed distance (crystals), the diffraction pattern will be produced from the interference of the scattered X-rays (Figure 3-10).

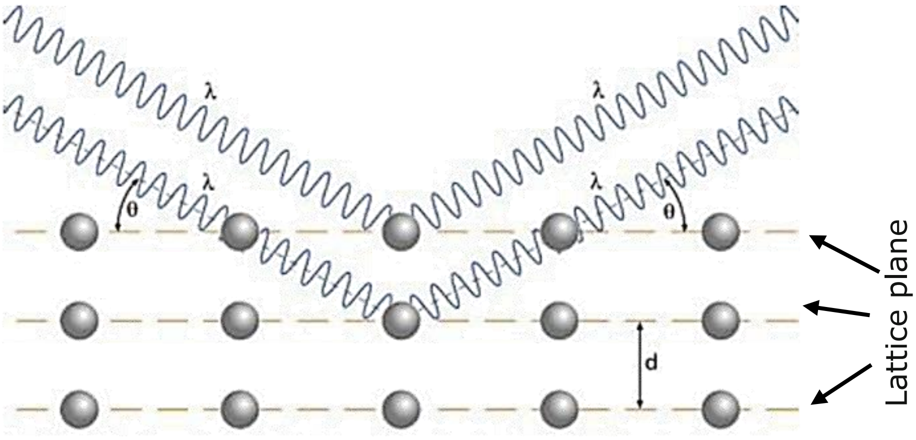

Figure 3-10: Schematic illustration of Bragg condition and Bragg's law (Dönmez, 2013).

The diffraction angles are acquired by scanning a sample with angles of the incident X-ray ranging from 0.0 to 90.0°. By plotting the X-ray intensity (counts s^{-1}) against the angle of the incident X-ray, a series of peaks are formed. The atomic and molecular structure of a powder or metal can then be determined by comparing these peak patterns with standard reference patterns. The relationship for XRD is described by Bragg's Law:

$$n\lambda = 2d\ sin\theta \qquad \text{Eq. 3-3}$$

Where: n: is an integer, λ: the wavelength of the X-rays, d: inter-planar spacing and θ: The diffraction angle in degrees.

In XPS, weak X-rays are required to gain the surface elemental information in comparison with XRD. Here, the energy of photon X-rays (hv) are produced by ejecting an electron from a core level. Then the electron spectrometer will analyse the emitted photoelectrons, and the data presented as a graph of intensity (counts s^{-1}) against the electron energy - the X-ray induced photoelectron spectrum (Watts and Wolstenholme, 2003) (Figure 3-11).

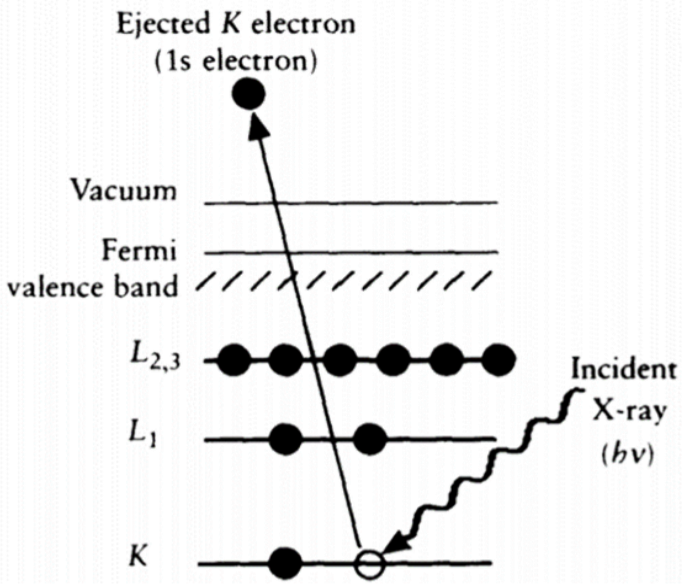

Figure 3-11: Schematic diagram of photoionization of an atom by the ejection of a 1s electron during the XPS process (Watts and Wolstenholme, 2003)

The kinetic energy (E_K) of the electron represents the experimental quantity measured by the spectrometer, which in turn, dependents on the photon energy of the X-rays, the binding energy of the electron (E_B) is the parameter which specifically identifies the electron. The parameters involved in the XPS experiment are shown in the relationship below:

$$E_B = h_v - E_k - W \qquad \text{Eq. 3-4}$$

where:

h_v: The photon energy, E_k: The kinetic energy of the electron, and W: The spectrometer work function. The photoemission process involves of ejecting an electron in the K shell of the atom (1s photoelectron). The electronic structure of a target element will then be reproduced more precisely by the photoelectron spectrum due to the low photon energy in the spectrum in comparison with the high binding energy between the electrons.

3.6.2 Analytical techniques using an electron beam.

An electron beam is a focused stream of electrons emitted from an electron gun which is composed of a filament, a positive electrode and negative electrode. The electrons can be emitted either by applying a large electric field to the filament (field emission type) or by superheating the filament using an electric current (thermionic emission type) (Flegler et al., 1993). Since subatomic particles negatively charge the electrons, the emitted electrons from the filament can be attracted by the positive electrode. Thus, it is possible to control the speed of the emitted electrons from the electron gun by adjusting the potential of the positive electrode (the accelerating voltage 1.0 ca. 30.0 kV). Firstly, a random spray pattern is exhibited by the emitted electrons. The stream of the electrons is then focused by an electromagnetic lens (condenser lens) onto a very fine focal spot (1.0 ca. 5.0 nm).

Once the electron beam strikes the sample, and due to the interaction between the primary electron (electron from the beam) and the electrons of the sample, several signals can be detected. The electrons near the surface are the most exposed to the primary electron. In this case, the electron in the atomic shell is ejected owing to the transfer of energy from the primary electron. This ejected electron is called a secondary electron (SE), and has low energy in comparison with the primary electron. To establish a topographic observation of a surface, SE is the most useful signal in SEM due to ejecting an electron from a lower energy state (inner atomic shell) to fill the vacancy caused by an electron in a higher energy state (outer atomic shell). The difference between the two energy states is emitted as an X-ray. These emitted X-rays are utilised for EDX to observe and identify the composition of a surface.

In SEM, the surface of a specimen is scanned with a finely focused electron beam of several nanometres. The emitted information will be converted into an electrical signal and amplified, followed by observation of the amplified information using a Cathode Ray Tube (CRT). The function of CRT is simultaneously controlling the brightness of the corresponding spot with the scanning of the electron beam on the surface of a specimen. Therefore, this information is displayed as images on the CRT (Figure 3-12).

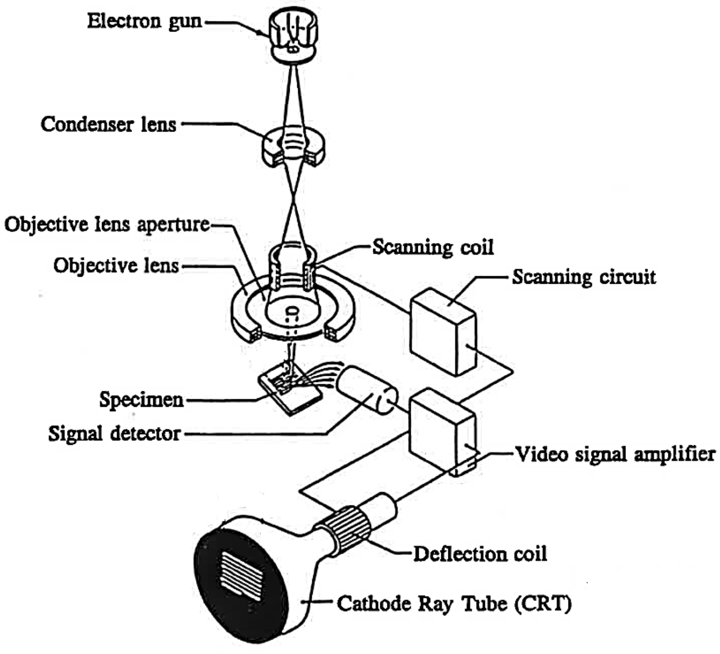

Figure 3-12: Principles of SEM (Behera, 2015).

In this study field emission gun scanning electron microscopy (FEG-SEM) was utilised to show the morphology and the dimensions (tube diameter, tube length and the thickness of coating) of TiO_2 NTAs before and after the coating with CZTS instead of the normal SEM. FEG-SEM is capable of providing topographical and elemental information. However, the images produced are ca. 3.0 to 6.0 times clearer than SEM with unlimited depth of field (magnifications of 10.0 x to 300,000.0 x) (Photometric, 2015, Oct 23).

3.6.3 Ultraviolet–visible–near-infrared spectroscopy (UV-Vis-NIR).

UV-Vis-NIR spectroscopy is an instrument of an electromagnetic

spectrum measures the optical properties of a sample in the wavelength ranges:

- 190.0 ca. 400.0 nm UV radiation
- 400.0 ca. 800.0 nm Visible radiation
- 800.0 ca. 2500.0 nm Near infra-red radiation

The principles of such spectroscopy measurements rely on expose the sample to a known wavelength and measuring how much light is absorbed or reflected. An Agilent Technologies Cary 5000 UV/Vis/NIR spectrometer with 150.0 mm integrating sphere was employed to directly measure the absorbance and the transmittance of pure TiO_2 NTAs substrates before and after the deposition of CZTS.

The bandgap energy was calculated from the relationship between the absorbance ($\propto$) and the incident photon energy $(h\nu)$ shown in Equation 3-5 and Equation 3-6, respectively:

$$h\nu = 1240/\lambda \qquad \text{Eq. 3-5}$$

By applying Tauc relation (Hassanien and Akl, 2016):

$$\propto h\nu = A\,(h\nu - Eg)^{m} \qquad \text{Eq. 3-6}$$

where h is Planck's constant, ν is the frequency of the incident photons, A is a constant depending on the transition probability, λ is the wavelength (nm), and m can take values of 1/2, 3/2, or 2 for directly-allowed, directly-forbidden, and indirectly-allowed transitions, respectively. The absorption coefficient is related to the optical bandgap energy (Eg) of the semiconductor (Equation 3-6).

The optical bandgap energy is calculated by considering an indirectly-allowed transition for TiO_2 NTAs (n = 2.0) (Fernandes et al., 2010, Kumar et al., 2009a), and reading the intercept of the extended linear part of the $(\propto h\nu)^2$ vs. $h\nu$ plot with the abscissa.

3.7 Photocatalytic measurements

The photocatalytic performance of the novel CZTS/TiO_2 NTAs composite was examined in a photoelectrochemical cell (PEC) with Pt wire as a counter electrode and the resulting CZTS/TiO_2 NTAs as working electrode. The workstation was also used to control the applied potential and record the photocurrent simultaneously. The measurements were conducted in an electrolyte containing 0.280 M of sodium sulfide (Na_2S) and 0.320 M of sodium sulfite (Na_2SO_3) as sacrificial reagents under illumination (100.00 mW cm^{-2}) using a light source (500 W Xe DC Mercury Xenon arc lamps, Newport) (Figure 3-13). This light source was connected to a power supply, and the illumination was performed using a current of 7.7 A.

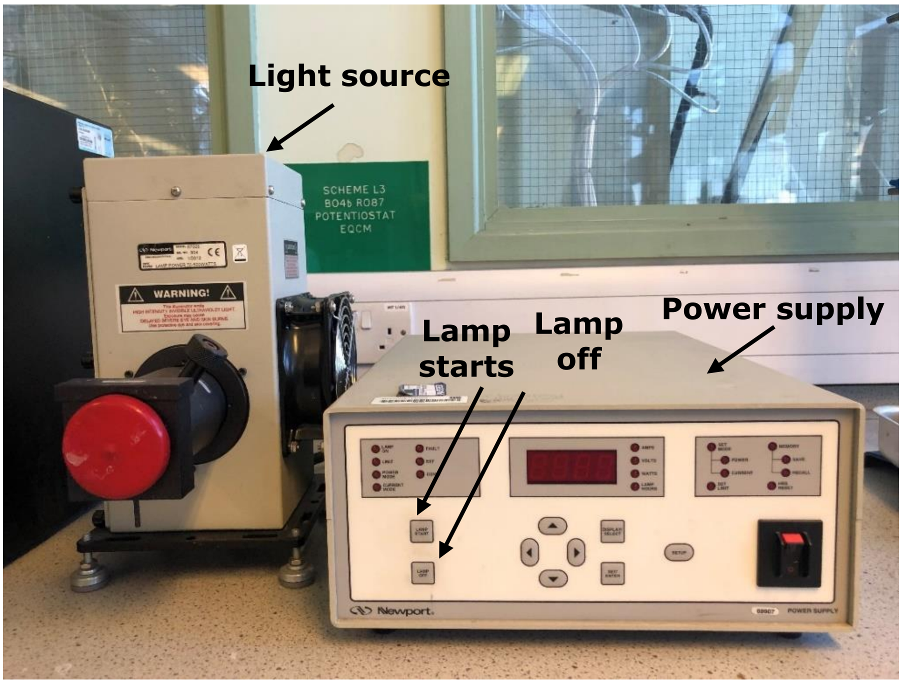

Figure 3-13: Light source equipped with power supply utilise d for photocatalytic performance test.

3.7.1 Photocurrent density and photoconversion efficiency

The photocurrent density of TiO_2 NTAs before and after the deposition was measured using a three conventional cell (mentioned earlier), and the entire theory of the photocurrent density was previously described in section 3.4.6.1. The TiO_2 NTAs substrate (35.0 mm × 10.0 mm) was exposed to the light source placed at 5.0 cm distance, and it was biased by applying a voltage of open circuit potential 1.50 V. The current was simultaneously recorded, and the output was the I-V curve.

The photoconversion efficincy of TiO_2 NTAs and CZTS/TiO_2 NTAs was calculated using the following formula:

$$\eta(\%) = \mathrm{j_p}\left[\frac{\mathrm{E^0_{Rev}} - |\mathrm{E_{app}}|}{\mathrm{I_0}}\right] * 100 \qquad \text{Eq. 3-7}$$

where $\mathrm{E^0_{Rev}}$ (total power output), which is the potential (= 1.23 V) corresponding to the Gibbs Free Energy change per photon in the water-splitting reaction. E_{app} (electric power input) = E_{meas} - E_{aoc}, wherein E_{meas} is the electrode potential vs. Ag/AgCl of the working electrode, and E_{aoc} is the electrode potential vs. Ag/AgCl of the same working electrode at open-circuit condition under the same illumination and in the same electrolyte. $\mathrm{j_p}$ is the corresponding photocurrent density, and $\mathrm{I_0}$ (light power input) denotes the intensity of incident light (Zhu et al., 2010).

3.7.2 Hydrogen generation

It is important to check the hydrogen generation rate from the modified TiO_2 NTAs to ensure that the observed photocurrent density is due to the hydrogen evolution (Iwashina and Kudo, 2011). The hydrogen generation rate was measured for 30.0 m by employing Hoffman Voltameter (Scientific Glass Laboratories (SGL)) (Figure 3-15) under light irradiation using the same light source. Hoffman Voltameter comprises three joined up glass cylinders (1, 2, and 3 in Figure 3-14), respectively).

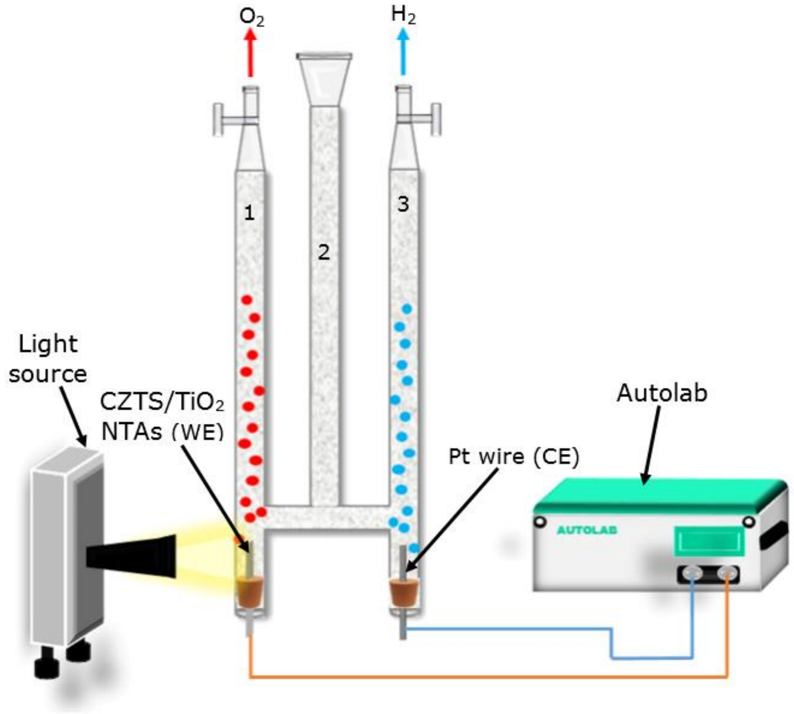

Figure 3-14: Schematic diagram of Hoffman Voltameter employed to measure the hydrogen generation rate from the as-synthesised CZTS/TiO_2 NTAs.

Cylinders 1 and 3 are similar to an inverted burette, while cylinder 2 has funnel mouth where the electrolyte (0.280 M of sodium sulfide (Na_2S) and 0.320 M of sodium sulfite (Na_2SO_3) was added. At the bottom of cylinder 1 and 3 the as-synthesised CZTS/TiO_2 NTAs and Pt electrodes were placed and connected to the electrochemistry workstation as WE and CE, respectively. The experiment was performed at the applied potential -0.500 V. H_2 production was observed at the cathode and recorded each 10.0 m. During exposure of the sample to the light source, the valves of cylinder 1 and 3 were closed while adding the electrolyte to allow the electrolyte to rise upwards, once the cylinders were filled, the valves were opened; then the gases displace the electrolyte. When the current passes through the Hoffman's voltmeter, gaseous H_2 is formed at the Pt electrode and gaseous O_2 is formed at the photoanode (CZTS/TiO_2 NTAs).

Chapter 4: Preparation of TiO_2 NTAs via electrochemical anodization

4.1 Background on the Electrical and optical properties of Titanium Dioxide (TiO_2)

During the past decade, the N-type semiconductor TiO_2 has attracted considerable attention as a photocatalyst since it is non-toxic, abundant, commercially available, chemically stable, and affordable amongst metal oxides (Bessegato et al., 2015). Due to the remarkable photocatalytic activity and electrochemical characteristics of TiO_2, it is considered a versatile semiconductor, which finds itself widely applied in various applications, such as the generation of hydrogen from water photolysis, electrochemical energy storage, biomedical applications, dye-sensitised solar cells at room-temperature, hydrogen gas sensing and degradation of organic pollutants (Raja et al., 2006b). Bessegato et al. (2015) showed that the 1D highly ordered (self-organised) TiO_2 nanotubes (TNT) have a wide bandgap (3.0 to 3.2 eV) (equivalent to radiation near the UV range from the solar spectrum) with a high surface area structure. Therefore, the positive hole is distinctly capable of oxidising a water molecule to oxygen (Wang and Chen, 2013). In addition, the tubular symmetries prevent the low recombination of light-induced electron/hole pairs, which occurs within the valence and conduction bands, leading to high photocurrent conversion efficiency. With TNT attached to the parent titanium substrate the transport of the photoinduced electrons from the photoanode to the cathode is improves, thus enhancing the photocatalytic activity of TNT (Bessegato et al., 2015). Grimes and Mor (2009) reported that the self-ordered architecture of NTAs takes into consideration the precise control of the geometrical elements, permitting one to accomplish a material with particular light absorption and a wide range of characteristics (Figure 4-1).

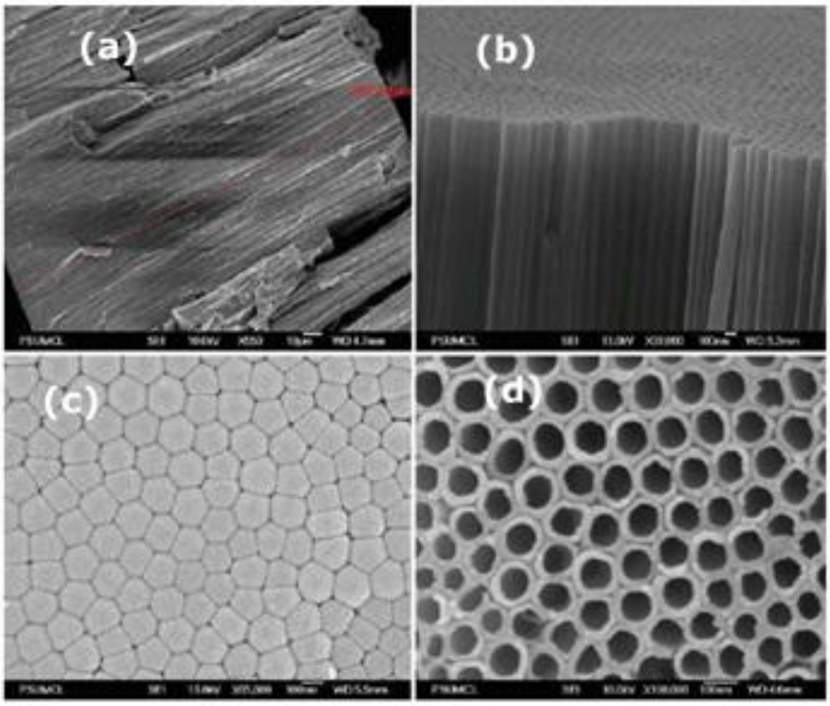

Figure 4-1: Illustrative FESEM (a) and (b) cross-sectional, (c) bottom and (d) top images of a nanotube array sample grown at 60.00 V in an ethylene glycol electrolyte containing 0.25 wt% NH_4F (Grimes and Mor, 2009).

Furthermore, the architecture of TiO_2 NTAs considered the ideal semiconductor for water photoelectrolysis, with a length ca. 30.00 μm, these nanotubes can exhibit a photoconversion efficiency of 16.25 % under UV-spectrum illumination (320.0 to 400.0 nm). Daghrir et al. 2012 identified that water could be decomposed under UV light into hydrogen and oxygen without the application of an external voltage, as shown in Figure 4-2.

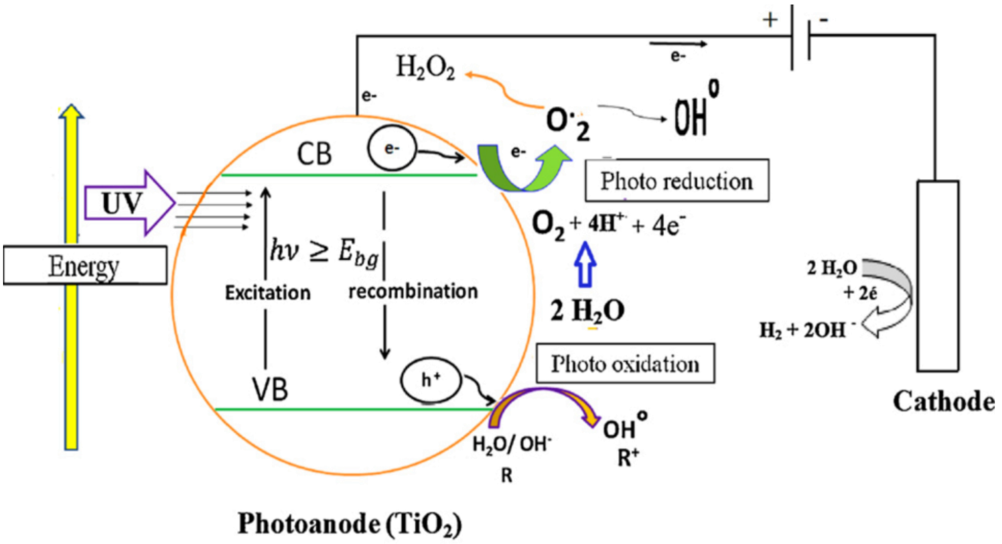

Figure 4-2: Mechanism of photoelectrocatalytic process using TiO_2 photocatalyst and the reactions that occur at the surface (Daghrir et al., 2012).

The decomposition occurred when the surface of the photoanode TiO_2 illuminates with the light of wavelength larger than its bandgap, around 415.0 nm (3.0 eV). Then the photocurrent flowed from the platinum counter electrode to the TiO_2 electrode through the external circuit.

As shown in the following equations, the path of the current revealed that the hydrogen evolution (reduction reaction) takes place

at the Pt electrode, and the oxygen evolution occurs at the TiO_2 electrode (oxidation reaction).

Reaction at photoanode TiO_2:

$$TiO_2 + h_v \rightarrow\ e^- +\ h^+ \qquad \text{Eq. 4-1}$$

Pt cathode reaction / hydrogen evolution:

$$2H_2O + 4h^+ \rightarrow\ O_2 + 4H^+ \qquad \text{Eq. 4-2}$$

Overall reaction:

$$2H^+ + 2e^- \rightarrow\ H_2 \qquad \text{Eq. 4-3}$$

The highly well-arranged TiO_2 TNT offers a large specific surface area (typically 8.0 to 10.0 and 5.0 to 7.0 nm in outer and inner diameters, respectively (Sekino, 2010, Zhu et al., 2011a)), with no decrease in geometric and structural order. In addition, the large specific surface area is well-matched for full solar energy harvesting, making a larger number of active reaction positions for the chemical reactions. Therefore, photogenerated holes will easily access many solution ions under UV irradiation. Zhu et al. (2010) acknowledged that due to the distinctive feature that characterises the TNT (including reducing the recombination of the photogenerated electron and hole pairs, which can quickly enter the conductive substrate of the TiO_2 (TNT)), TiO_2 TNT can show particularly good optical catalytic activity.

4.1.1 Crystal Structure of Titanium Dioxide

Titanium oxide belongs to the group of transition metal oxides. Naturally, TiO_2 exists in four commonly known polymorph crystalline phases: two metastable polymorph phases include brookite (orthorhombic) and anatase (tetragonal), one stable phase, rutile (tetragonal) and TiO_2 (monoclinic) (Gupta and Tripathi, 2011). In addition to these polymorphs, there are two high-pressure forms synthesised from the rutile phase: TiO_2 (H) (Simons and Dachille, 1967) and TiO_2 (II) with a PbO_2 structure (Latroche et al., 1989) (Figure 4-3) and Table 4-1 display the crystal structure properties of TiO_2.

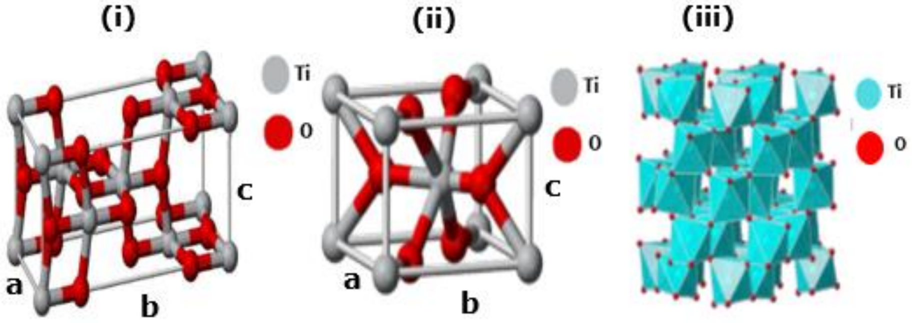

Figure 4-3: Crystalline structures of TiO_2, (i) anatase, (ii) rutile and (iii) brookite (Latroche et al., 1989) .

Table 4-1: Crystal structure data for TiO_2. Modified from (Gupta and Tripathi, 2011).

Properties	Rutile	Anatase	Brookite
Crystal structure	Tetragonal	Tetragonal	Orthorhombic
Lattice constant (Å)	a = 4.5936 c =2.9587	a = 3.784 c = 9.515	a = 9.184 b = 5.447 c = 5.154
Energy gap eV	3.06	3.29	3.26

1. TiO_2 in the stable rutile phase

The rutile TiO_2 form has a tetragonal structure that contains six atoms per unit cell (TiO_6 octahedron), and it is slightly distorted (Chen and Mao, 2007, Thompson and Yates, 2006, Diebold, 2003) (Figure 4-3-ii). However, depending on the preparation conditions, the rutile phase can be active or inactive (Sclafani et al., 1990). At most temperatures and pressures up to 60.0 kbar, TiO_2 (II) becomes the thermodynamically favorable phase, and the rutile phase will be stable (Navrotsky et al., 1967). After reaching a certain particle size (particle sizes greater than 14.0 nm), anatase and brookite structures transformed into the rutile phase. Once the rutile phase formed, it grows much faster than the anatase (Zhang et al., 2000).

2. TiO_2 in the metastable anatase phase

Anatase TiO_2 also has a tetragonal structure similar to the Rutile one; however, the distortion of the Rutile TiO_6 octahedron is slightly larger for the TiO_2 anatase phase (Linsebigler et al., 1995, Simons and Dachille, 1967, Latroche et al., 1989, Cromer and Herrington, 1955, Baur, 1961, Mo and Ching, 1995) (Figure 4-3-i). Studies showed that the anatase phase is more stable than the rutile at 0.0 K, but the energy difference between these two phases is small (~ 2.0 to 10.0 kJ mol^{-1}) (Muscat et al., 2002). Among the other polymorphs, the anatase TiO_2 is the most desired crystalline phase for solar cell and biomedical applications. This is due to its higher electron mobility, lower density, and low dielectric constant (Carp et al., 2004). Tanaka et al. (1991) revealed that the anatase phase of TiO_2 shows an improved photoreactivity due to its high Fermi level, low capacity to absorb oxygen, and a high degree of hydroxylation. Based on the indirect bandgap of the anatase TiO_2, the photoexcited electrons can conserve momentum; thus, the photogenerated e^-/h^+ pairs lifetime becomes longer (Figure 4-4). Crucially, the indirect bandgap facilitates the recombination of electrons from the bottom of the conduction band (CB) with the holes in the top of the valance band (VB); therefore, the reaction time and the length of diffusion between the photo-excited electrons and holes will increase.

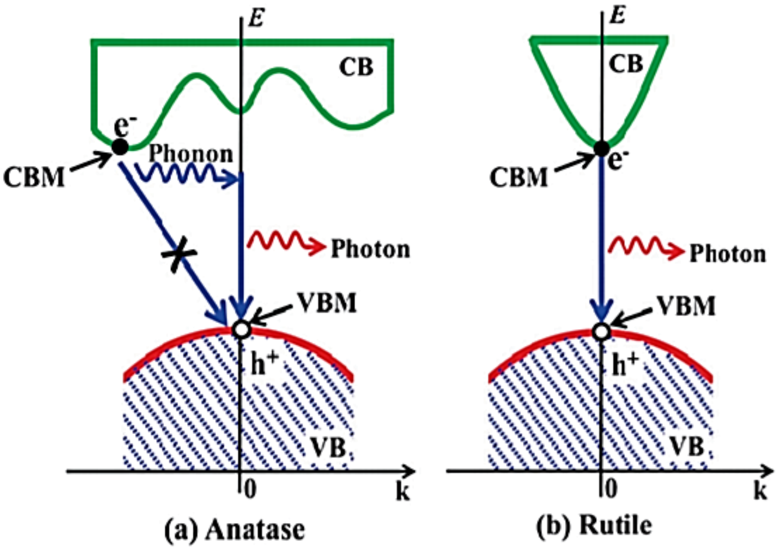

Figure 4-4: Schematic diagram represents a comparison for the recombination process of the photogenrated e^-/h^+ pairs within (a) indirect gap anatase and (b) direct gap rutile (Zhang et al., 2014).

3. TiO_2 in the brookite structure.

The Brookite TiO_2 belongs to the orthorhombic crystal system. The unit cell is composed of eight formula units of TiO_2 and formed by edge-sharing TiO_6 octahedra (Figure 4-3-iii). It is more complicated compared to the anatase and rutile phases; it has a larger cell volume, and it is the least dense of the three forms, and is not often used for experimental investigations (Thompson and Yates, 2006).

4.1.2 Techniques for synthesis of TiO_2 NTAs

After the discovery of carbon nanotubes (Iijima, 1991), the researchers have carried out studies on a variety one dimensional (1D) nanomaterials, such as ZnO (Huang et al., 2001) and TiO_2 (Fröschl et al., 2012, Liu et al., 2002, Perillo and Rodriguez, 2012). In recent years, TiO_2 received significant amount of attention due to the feasibility of fabricating the highly ordered nanotubes, and the wide range of applications, for instance, photovoltaic cells (Mor et al., 2006), gas sensors (Paulose et al., 2006a, Lin et al., 2011, Şennik et al., 2010), degradation of organic pollutants and generation of hydrogen by water photolysis (Raja et al., 2006b), electrochemical energy storage, biomedical applications (Rajh et al., 2014) and dye-sensitised solar cells (Mor et al., 2006). Many approaches were employed to synthesize the TiO_2 nanotubes such as sol-gel methods (Kasuga et al., 1998, Jung et al., 2002), hydrothermal treatment (Wang et al., 2008), templating synthesis (Lee et al., 2004), and anodic oxidisation (Gong et al., 2001, Ge et al., 2008, Zhu et al., 2011a).

4.1.3 Anodization process

Nowadays, the most fabricated nanostructures of TiO_2 are the self-organised TiO_2 nanotube arrays (NTAs). Various methods have been employed to synthesise these nanotubes, such as template-assisted, sol-gel, hydro/solvothermal, or seeded growth (Jarosz et al., 2015). The conventional electrochemical anodization process can be employed to synthesise the highly ordered TiO_2 nanotubular structures. The anodization process is a low-cost process, and it permits easy control of the dimensions of TiO_2 NTAs by tuning the parameters of this process.

The formation of TiO_2 NTAs through anodization method by using Fluoride-based electrolytes was first reported by (Gong et al., 2001). They emphasised that the electrochemical anodization is mostly considered simpler and cheaper in comparison with other synthesising methods. Moreover, the electrochemical anodization is versatile and easy to scale up method for coating any shape of titanium, and other metals surfaces with dense and defined nanotubes are possible (Roy et al., 2011).

The electrochemical anodization is a self-organising approach to the growing array of oxide nanotubes, which arranged vertically on the surface of a titanium substrate. This method offers well-defined nanotubes in the amorphous state that have controllable morphologies (tube length, pore size, and wall thickness). In terms of photocatalytic applications, it was found that the electrochemical anodization proved as the most effectively and frequently used route to produce the nanotube structure of TiO_2 while the product that obtained from other methods such as hydrothermal and template are powder form (Torres et al., 2014). Generally, the electrochemical anodization cell consists of two electrodes: a wire or plate of platinum and titanium sheet as cathode and anode, respectively (Figure 4-5).

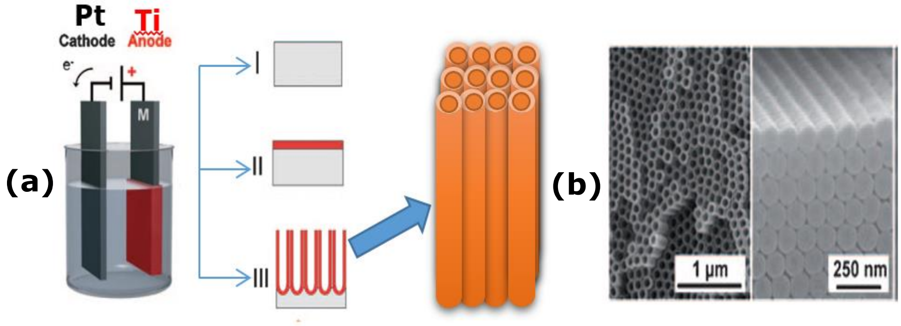

Figure 4-5: Depiction of an electrochemical anodization cell: a) I) metal electropolishing, II) formation of compact anodic oxides, III) self-ordered oxides nanotubes. b) Top and side view of highly ordered TiO_2 nanotubes arrays (Roy et al., 2011).

These electrodes immersed into an electrolyte containing fluoride ion. When the voltage is applied, the electrons moved from the electrolyte to the anode. Then surface metal atoms exposed to oxygen ions inside the electrolyte. These atoms react and integrate with the oxide layer. The electrons mobile through the dc power and return to the cathode. Then they will combine and react with hydrogen ions. Here, hydrogen ions bubbled off as hydrogen gas if a suitable electrolyte pH is set (Grimes and Mor, 2009). The growth of the oxide barrier layer can be examined by recording the current–time characteristics (Figure 4-6). The anodization of titanium and other metals in the aqueous electrolyte to form a thick oxide layer with considerable thickness (ca. 1.0 µm) is known for more than 50.0 years.

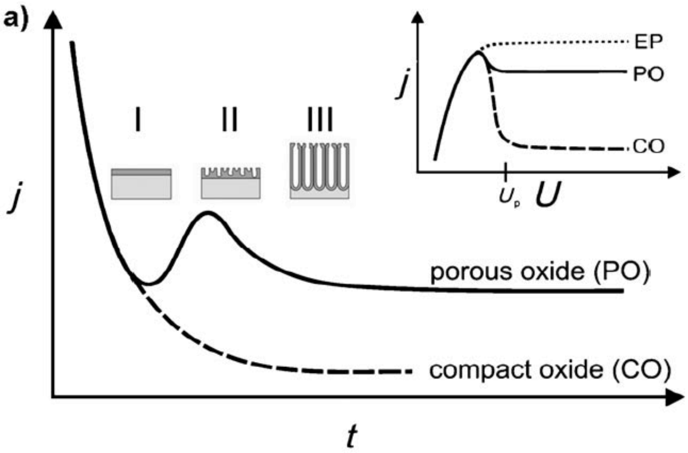

Figure 4-6: Typical current–time (j–t) characteristics after a voltage applied in the absence (--) and presence (−) of fluoride ions in the electrolyte. Either compact oxide (fluoride free) or porous/tubular metal oxide formation (containing fluoride) forms by different morphological stages (I–II-III) (Roy et al., 2011).

The growth of this layer proportionally depends on the applied voltage with a growth factor approximately 1.0 to 5.0 nm V^{-1} up to a voltage (Peláez-Abellán et al., 2012). The dimensions of the nanotube arrays, including wall thickness, tube length, tube-to-tube spacing, and pore diameter and wall roughness, are crucially influencing the performance of the nanotubes. The well-organised nanotube arrays have an amorphous or crystalline structure that is controlled by a variety of electrochemical parameters: including the time of anodization, applied voltage, and electrolyte composition (Grimes and Mor, 2009).

The typical amorphous structure of the TiO_2 NTAs was reported at low voltages, and the crystallisation then occurs at higher voltages. These structures are anatase, rutile, or both depending on the anodizing conditions and the presence of the fluoride ions (Peláez-Abellán et al., 2012).

Figure 4-7 illustrates the self-organised nanotubular/nonporous structures of TiO_2 NTAs. Ly et al. (2013) revealed that the self-organised TiO_2 nanotubes could be perpendicularly fabricated by electrochemical anodization in an electrolyte containing ammonium fluoride (NH_4F), which has a significant effect on the nanotube's length and pore diameter beside the applied voltage.

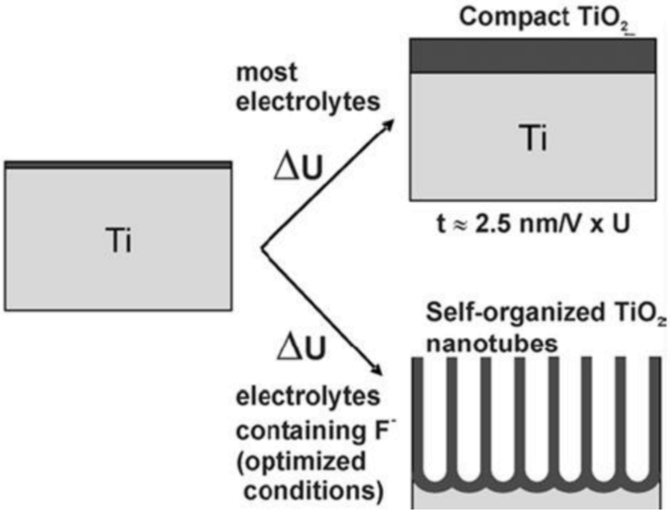

Figure 4-7: Schematic set-up for anodization process (Peláez-Abellán et al., 2012).

Three main processes take place during the formation of NTAs are: (1) In the onset of anodization, the thin oxide layer formed on the titanium substrate, which occurred due to the interaction of O^{2-}on the metal surface. The following reactions represent the growth of the oxide layer (Zhu et al., 2011a):

$$2H_2O \rightarrow O_2 + 4e^- + 4H^+ \qquad \text{Eq. 4-4}$$

$$Ti + O_2 \rightarrow TiO_2 \qquad \text{Eq. 4-5}$$

After the localised dissolution of TiO_2 by fluoride ions, the pores can be observed on the surface of the TiO_2 layer regarding the migration of the anions through the oxide layer, which will react with the substrate. Meanwhile, the cations Ti^{4+} that rejected from the metal/oxide interface will move toward the interface of oxide/electrolyte under the applied electrical field. The pores became deeper when the electric field increased at the bottom of the pores (Wang and Chen, 2013). (2) Field-assisted dissolution of the oxide at the oxide/electrolyte interface caused by the dissolution of Ti^{4+} into the electrolyte. (3) Chemical dissolution of the TiO_2 in the acidic electrolyte, according to Equation (4-6) (Zhu et al., 2011a); hence, the tubular structure of the TiO_2 formed (Ly et al., 2013).

$$TiO_2 + 6F^- + 4H^+ \rightarrow TiF_6^{2-} + 2H_2O \qquad \text{Eq. 4-6}$$

Figure 4-8 illustrates the anodization of Ti in the absence (resulting in flat layers), and the presence of fluorides (Peláez-Abellán et al., 2012).

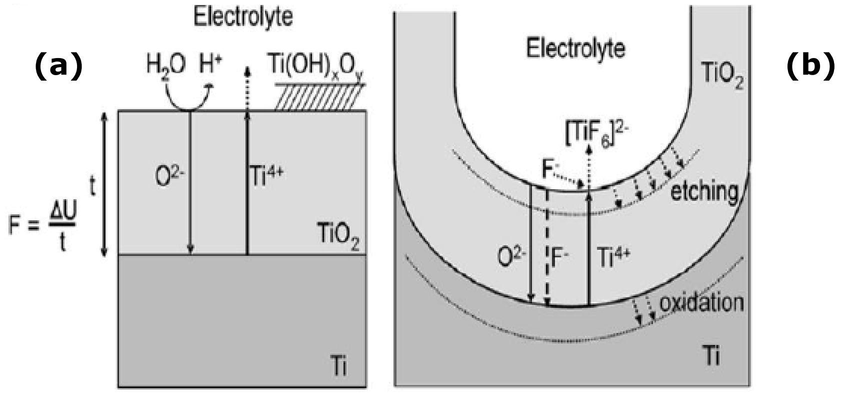

Figure 4-8: Schematic representation of Ti anodization (a) in the absence and (b) in the presence of fluorides (Peláez-Abellán et al., 2012).

Zhu et al. (2011a) revealed that the chemical dissolution of titania in the acidic electrolyte plays a vital role in the formation of NTAs by maintaining the electrochemical etching (field-assisted oxidation) active; thus, the thickness of the barrier oxide layer reduced as represented in Equation 4-6, the rate of the chemical dissolution was determined by the concentration of F^- and H^+ ions. The typical morphologies of nanotubes listed as pore size from 20.0 to 350.0 nm, wall thickness ranged between 5.0 to 30.0 nm, and the length range around 0.2 to 1000.0 µm. Besides, the selection of the suitable anodization variables may control the nanotube’s aspect ratio (length to outer diameter ratio ca. 10.0 to 20,000.0) (Ong et al., 2005).

In photocatalytic applications, there are optimal geometric areas and lengths of the nanotubes required to absorb the incident illuminated light. The light would be unable to reach the bottom of the tube if the length of the nanotube exceeds 100.0 microns. The electrons that are photogenerated in the nanotube walls need to travel very long distances to reach the underlying conducting substrate; therefore these electrons will recombine with the holes during the long distance travelled; however, the light will not fully be absorbed if the NTAs are too short (Ong et al., 2005).

The photogenerated holes will access a large number of solution ions if the geometric surface area is significantly large since it will possess many active sites needed for the chemical reactions. Therefore, to harvest an excessive amount of incident photons, a large surface area with a fixed pore size is required.

4.2 Discussion of the results

4.2.1 Factors affecting the formation of TiO_2 NTAs

In order to optimise the most efficient experimental conditions necessary to produce highly ordered and well organised anatase TiO_2 nanotube arrays, a number of parameters were studied, including:

1. Drying methods (acetonitrile vacuum drying and freeze-drying).
2. Time of anodization.
3. Water purity.

1. Drying methods

Several studies have focused on examining the effect of different parameters in attempting improve the adhesion properties and the morphology of the nanotubes, such as water content in the electrolyte (Zhu et al., 2011a, Srimuangmak and Niyomwas, 2011), the applied voltage (Srimuangmak and Niyomwas, 2011), the concentration of NH_4F in electrolytes (Chang et al., 2014), the annealing temperature (Li et al., 2013b). In this thesis, for the first time, the drying methods have been studied as a new parameter to demonstrate its effect on the electrical and optical properties of the TiO_2 NTAs.

These methods include:

- Acetonitrile vacuum drying method
- Freeze drying method

The acetonitrile (C_2H_3N) is used as a solvent for many reasons including, (1) the ability to dissolve the electrolyte (2) it can be used as a dehydrating solvent owing to its ability to dissolve in water and ethanol freely. It is also considered as the most appropriate solvent for the drying method since it has a low freezing temperature (–45.00 ℃) and has weak polarity (KATOH, 1979). Two samples were prepared under the same conditions in terms of anodization time of 8.0 h, at a constant bias applied voltage of 60.00 V and electrolyte composition: 0.32 wt % ammonium fluoride (NH_4F) in 40.00 mL ethylene glycol and 4.00 vol% water.

The photocurrent of the samples was recorded at 10.00 and 20.00 mV s^{-1} scan rates to test their stability under light irradiation. Figure 4-9 shows the photocurrent density (water oxidation under the illumination of light) vs. the potential for both TiO_2 NTAs dried naturally in the air and *via* the acetonitrile vacuum. The photoelectrochemical activity of as-synthesised nanotubes was examined by exposing the photoanode TiO_2 NTAs to a simulated solar UV-visible light. An aqueous solution contained 0.28 M Na_2S and 0.32 M Na_2SO_3 used as a sacrificial electrolyte to prohibit the backward reactions and the rapid recombination of e^-/h^+ pairs (Ni et al., 2007). The photocurrent density of the sample dried by the acetonitrile vacuum method is approximately 2.5 times higher than the one dried naturally in the air. These samples exhibited a photocurrent density pattern in agreement with the literature (Sun et al., 2015).

The linear increase observed up to 1.0 V reveals that under light exposure, the generated photocurrent is represented by a linear pattern. After 1.0 V, the system reaches a steady state where the water splitting was created, and the H_2 bubbles on the cathode (Pt) were observed during the measurements. High photocurrent might be referring to the ability to absorb numerous amounts of light.

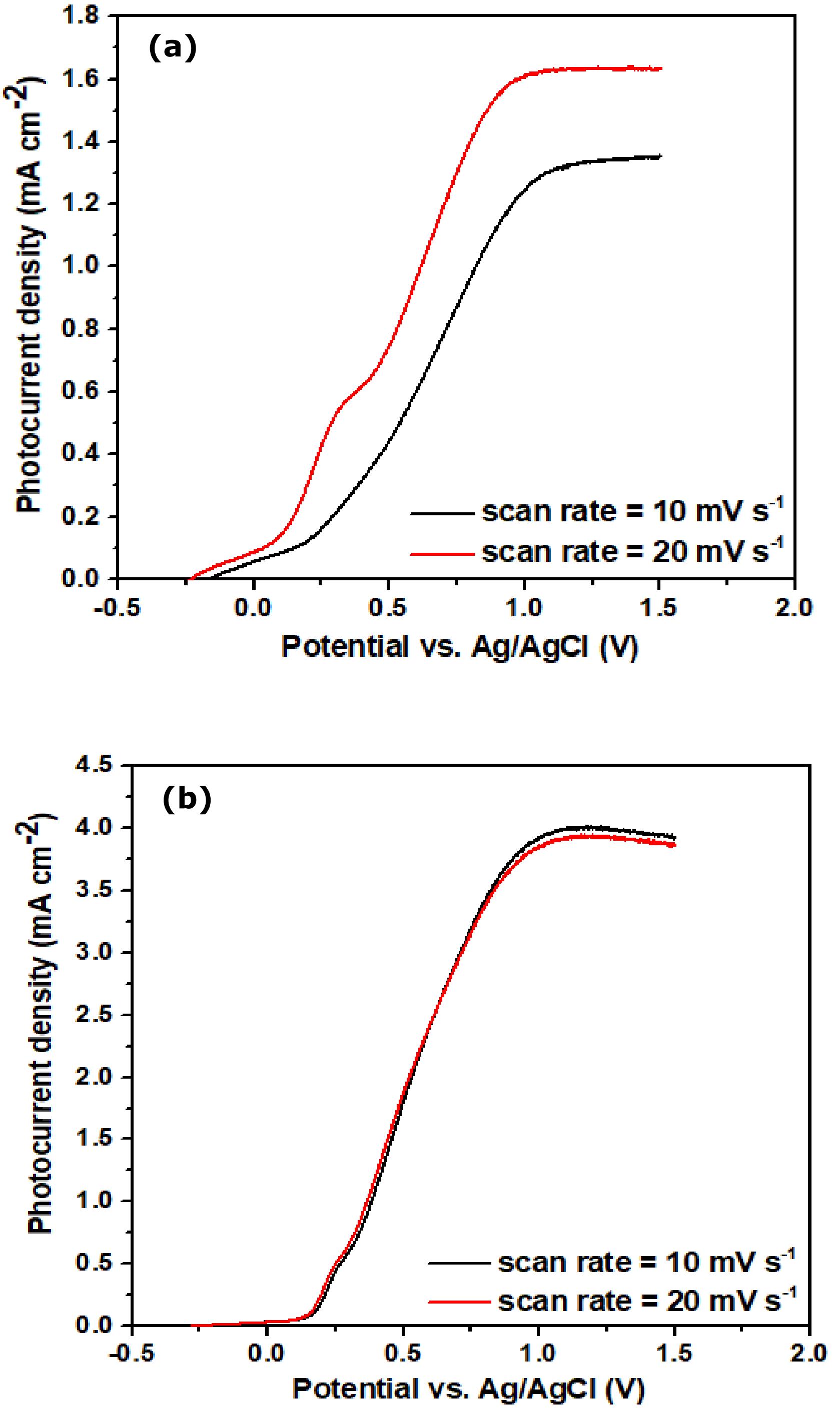

Figure 4-9: Photoelectrochemical properties (photocurrent density) of TiO_2 NTAs under light irradiation prepared with anodization duration 8.00 h at a constant bias applied voltage of 60.00 V. (a) dried naturally (b) dried by acetonitrile vacuum.

The reaction mechanism on each electrode can be described by the following chemical reactions (Štengl and Králová, 2011).

Anode reactions:

$$TiO_2 + h_\nu \rightarrow e^- + h^+ \qquad \text{Eq. 4-7}$$

$$2S^{2-} + 2h^+ \rightarrow S_2^{2-} \qquad \text{Eq. 4-8}$$

$$S_2^{2-} + SO_3^{2-} \rightarrow S_2O_3^{2-} + S^{2-} \qquad \text{Eq. 4-9}$$

$$SO_3^{2-} + S^{2-} + 2h^+ \rightarrow S_2O_3^{2-} \qquad \text{Eq. 4-10}$$

$$S_2O_3^{2-} + 2OH^- + 2h^+ \rightarrow SO_4^{2-} + 2H^+ \qquad \text{Eq. 4-11}$$

Cathode reaction:

$$2\,e^- + 2H_2O \rightarrow H_2 + 2OH^- \qquad \text{Eq. 4-12}$$

The role of the Na_2S solution is as a hole scavenger for the S^{2-} ions, which rejected from Na_2S will react with two holes to form S_2^{2-} (Equation 4-8). The other hole scavenger (SO_3^{2-} ions) are added to the reaction to prevent a back reaction by reducing S_2^{2-} to S^{2-} (Equation 4-9), and they can react with S^{2-} to produce $S_2O_3^{2-}$ to prevent any negative deposition of sulfur onto TiO_2 (Equation 4-10). Photo-generated holes irreversibly oxidise the reducing agents (Na_2S / Na_2SO_3) instead of water, providing an electron-rich photocatalyst with enhanced photoactivity, photocatalytic efficiency and H_2 evolution reaction (Štengl and Králová, 2011, Kim et al., 2013, Wei et al., 2013, Kim et al., 2011, Chang, 2013).

The Electrochemical impedance spectroscopy (EIS) measurements were conducted to elucidate the mechanism of charge transfer across the TiO_2 NTAs dried *via* acetonitrile vacuum and naturally in the air (Figure 4-10).

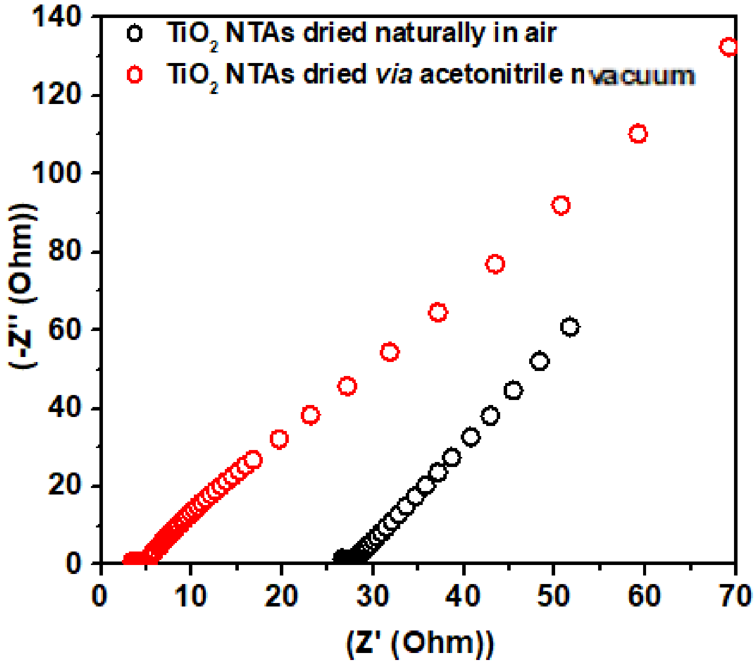

Figure 4-10: EIS Nyquist plots for TiO_2 NTAs prepared by anodization for 8.00 h at a constant bias applied voltage of 60.00 V. (blak) dried naturally and (red) dried via acetonitrile vacuum.

Figure 4-10 compares the Nyquist plots of the two samples. The sample dried *via* acetonitrile vacuum exhibits resistance of 5.0 Ω while the one dried naturally exhibits a higher resistance of 25.0 Ω. The difference in the resistance can possibly be ascribed to the strong adhesion between the synthesised nanotubes and the metal underlayer, resulting in reducing the defects and consequently improving the conductivity.

To further understand the influence of the acetonitrile vacuum on the electric and optical characteristics of TiO_2 NTAs, the I-t curves were measured to test the current stability under pulsed illumination of light (Figure 4-11). Both samples were exposed to pulsed illumination for 20.0 m. The light was pulsed 1.0 m (on/off illumination) at an applied bias of 1.0 V vs. Ag/AgCl.

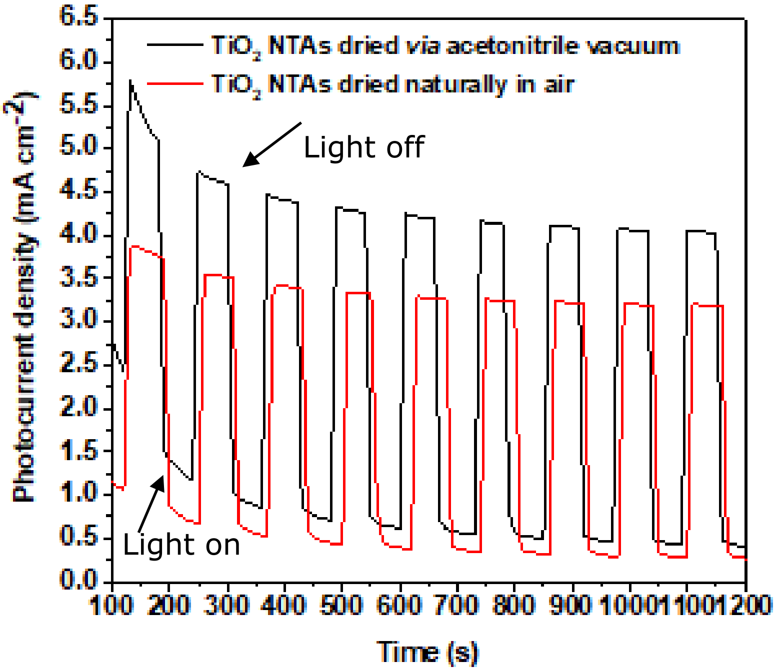

Figure 4-11: Photocurrent response of pulse illumination of TiO_2 NTAs compares two samples (black) dried with acetonitrile vacuum drying and (red) died naturally. The measurments performed at an applied bias of 1.0 V vs. Ag/AgCl.

The sample dried by acetonitrile vacuum showed a photocurrent of 0.0058 A while the one dried naturally showed a photocurrent of 0.0038 A. This variation in the photocurrent showed that the improvement in their electrical conjunction leads to an enhancement in the light absorption ability of TiO_2 NTAs.

The reproducibility was checked by repeating the results three times and was found to be within the limits of (±10.0 %).

The TiO_2 NTAs were dried via a freeze drying method to verify the optimum cohesion for the TiO_2 NTAs with the metal layer. Figure 4-12 a and b show a comparison between TiO_2 NTAs substrates dried naturally in the air and dried by the freeze drying method, respectively.

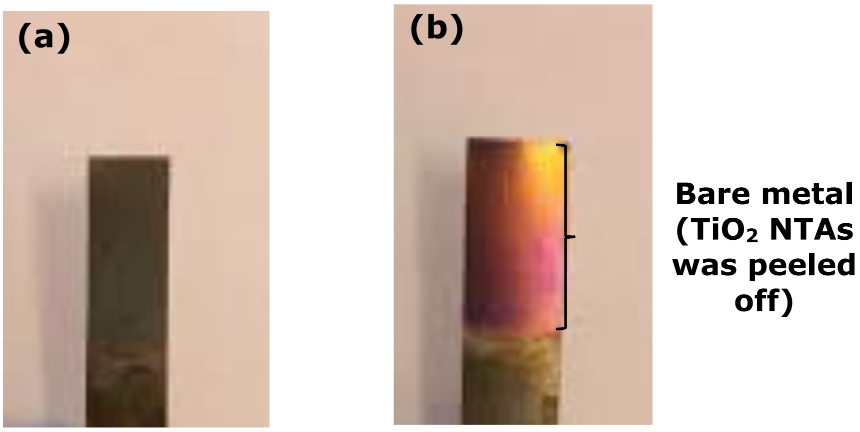

Figure 4-12: Titanium substrates (a) The typical sample with complete adhesion of TiO_2 NTAs on the metal sheet naturally in air (b) sample dried by freeze drying method where the TiO_2 NTAs peeled off after 2.00 h annealing at 450.00 ℃.

A sample was prepared from an electrolyte containing 0.32 wt % NH_4F, 4.00 vol % water, and 40.00 mL ethylene glycol at an applied voltage of 60.00 V for 6.00 h anodization duration.

After the second anodization step, the sample was maintained in the vacuum to be evacuated at 7.00 mbar and pre-freeze at temperature −30.00 ℃ for 25.00 m. The freeze-dried TiO_2 NTAs sample was completely peeled off, leaving bare metal after the annealing step. This suggests that the nanotubes have not entirely dried; possibly attributed to weakening of the chemical bonds between the nanotubes and the metal substrate, which might be damaged due to the existence of the residual of the electrolyte that should be dried before the annealing step to obtain cohesive and well-organised nanotubes. Therefore, this method was not considered further for the synthesis of the nanotubes.

2. Anodization time

Anodization time is one of the key parameters that influence the morphology of the nanotubes (tube length, tube diameter, and growth rate). Figure 4-13 and Figure 4-14 illustrate the photoelectrochemical properties of the samples prepared with 6.00, 8.00, 18.00, and 24.00 h anodization time in electrolyte contains 0.32 wt % NH_4F in 40.00 mL ethylene glycol and 4.00 vol % water, respectively.

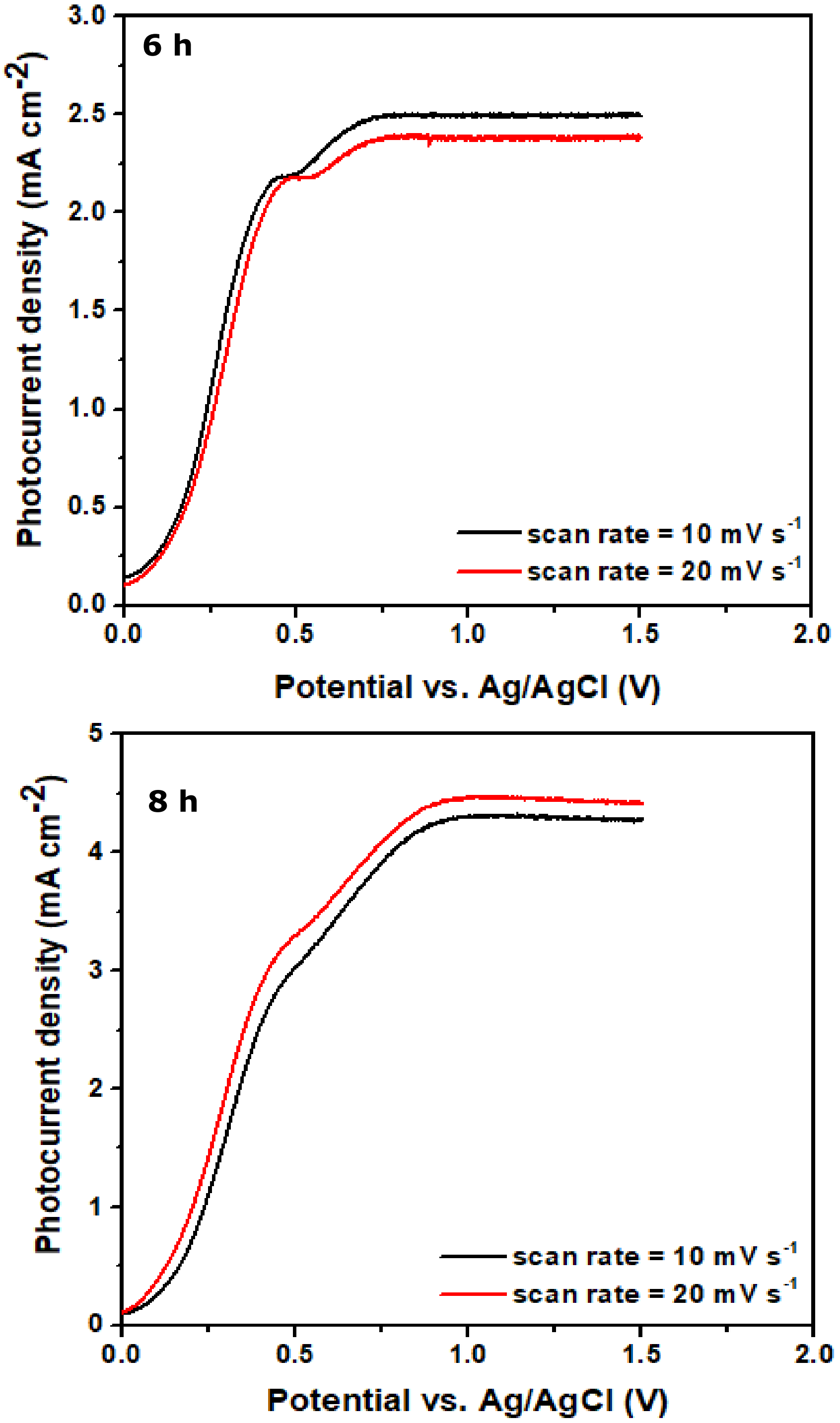

Figure 4-13: Photoelectrochemical properties of TiO_2 NTAs under light irradiation prepared for 6.00 and 8.00 h anodization duration, at a constant bias applied voltage of 60.00 V in electrolyte contains 0.32 wt % NH_4F in 40.00 mL ethylene glycol and 4.00 vol % water.

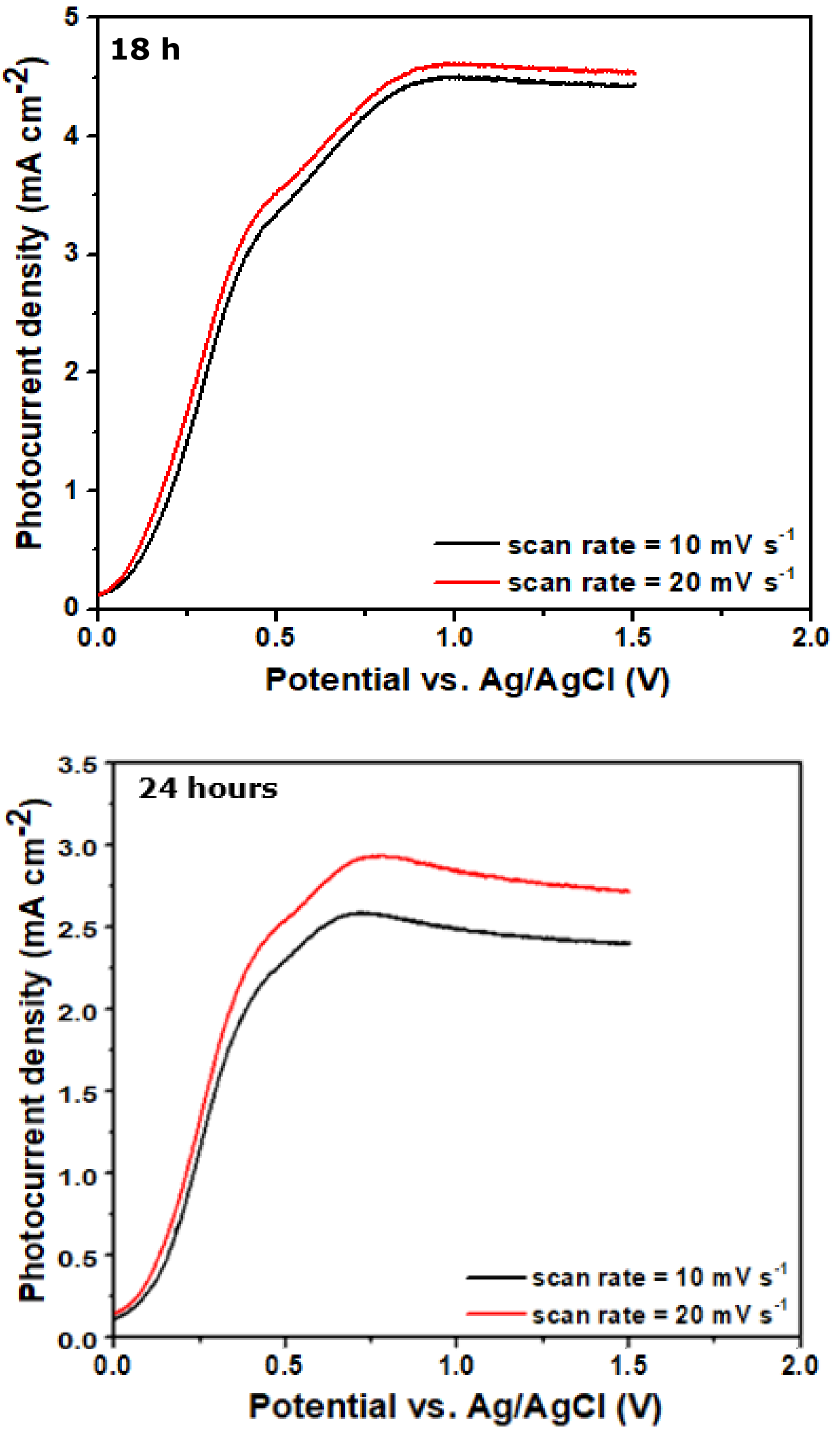

Figure 4-14: Photoelectrochemical properties of TiO_2 NTAs under light irradiation prepared for 18.00 and 24.00 h anodization duration, at a constant bias applied voltage of 60.00 V in electrolyte contains 0.32 wt % NH_4F in 40.00 mL ethylene glycol and 4.00 vol % water.

It was observed that these photoanodes demonstrated a reasonable value of photocurrent density between 1.5 to 4.0 mA cm^{-2} (Raja et al., 2006a, Zhu et al., 2011a); hence, these nanotubes may possess a high surface area and allow photoelectrolysis of water under light irradiation. However, it is not adequate evidence for the well-organised characteristic of the nanotube arrays. Therefore, an SEM characterisation was performed on these photoanodes. Figure 4-15 shows SEM images of the as-prepared nanotube arrays with different anodization duration.

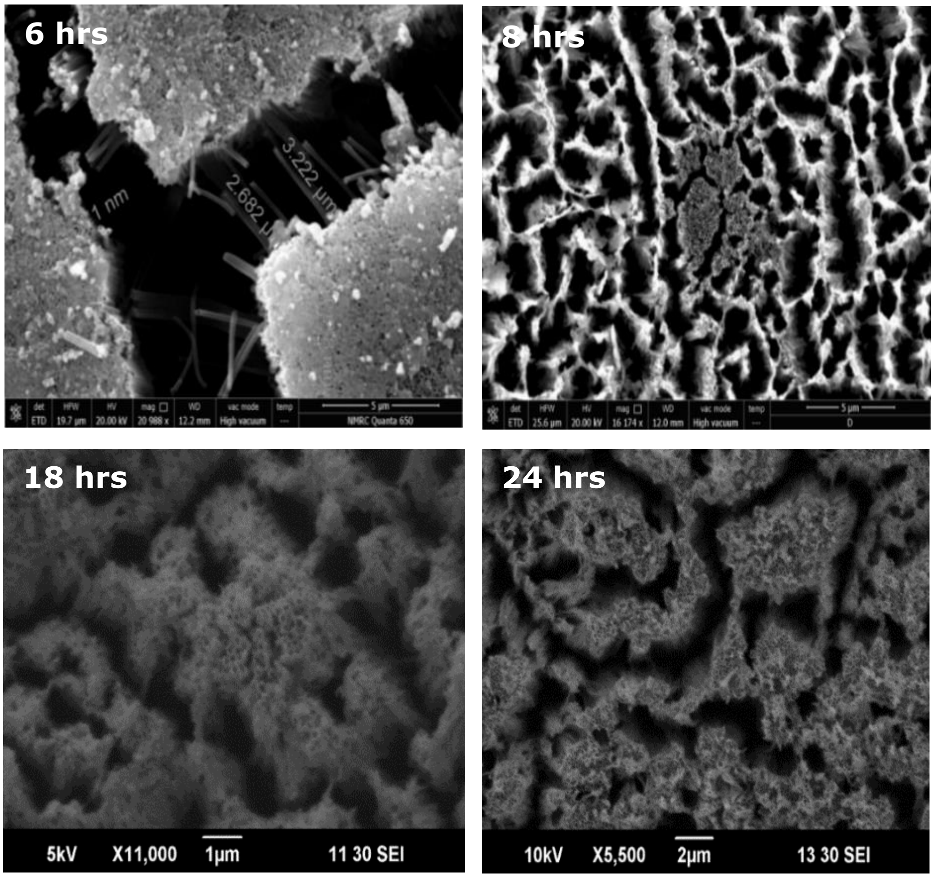

Figure 4- 15: Top SEM view of TiO_2 nanotube arrays prepared for 6.00, 8.00, 18.00 and 24.00 h anodization duration, at a constant bias applied voltage of 60.00 V in electrolyte contains 0.32 wt % NH4F in 40.00 mL ethylene glycol and 4.00 vol % deionized water (DIW). Annealed at 450.00 ℃.

The nanotubes in these images seem to be aggregated, leaving huge gaps between the tubes. This aggregation of nanotubes on the surface can be explained as follows. The nanotube arrays rise upward; therefore, the bond strength between the metal and the tubes will be reduced, and the thin film peeled from the Ti substrate. The chemical dissolution on the top of the tube will be increased, and lead to a reduction in the length of the tubes (Zhu et al., 2011b) (Zhu et al., 2011a). These findings might be attributable to a number of reasons; either the water content increased in the electrolyte due to the hygroscopic nature of ethylene glycol, which can absorb water from the ambient during the anodization, or the conductivity of the water that utilised to prepare the electrolyte was reduced.

Furthermore, this morphology is probably due to increasing in the anodization time. As a result of continuous anodization, the nanotube arrays could not stay vertically oriented due to the collapse of the nanotubes. Besides, long anodization time led to the erosion rate being faster than the oxide layer growth and caused the collapse of nanotubes (Wang and Chen, 2013). Investigating the influence of the anodization time was shown to be insufficient to acquire a well-organised nanotube array. Therefore, water purity was investigated in order to improve the morphology of NTAs.

3. Water purity

Various parameters (e.g., anodization time and drying methods) were studied to determine the reasons behind the non-well-organised morphology of the TiO_2 NTAs. During the initial experiments, deionised water (DIW) was used in preparing the electrolyte, according to some studies (Valota et al., 2009, Chang et al., 2014). The maximum theoretical value of resistivity of DIW (the resistivity is the tendency of water without ions to resist conducting electricity) is 18.2 to 18.3 MΩ cm at 25.0 ℃. The presence of anions or cations is crucial in the anodization process since these ions are the charge carriers in an electrochemical cell. During the second anodization process, the recorded current was 0.0002 A, which is very low compared to the maximum current that was set at 0.0015 A. Evidently, this is due to the high resistance of the oxide layer, which was expected to peel off after 6.0 h to invoke the growth of the tubular structure of NTAs. Whereas when the deionised water (DIW) was replaced by reverse osmosed water (ROW), the well-organized TiO_2 NTAs were obtainable (Figure 4-16) due to the drop in the electrolyte conductivity. The estimated average inner diameter of the resulting nanotubes measured by SEM is 111.0 nm, ranging between 72.0 to 115.0 nm.

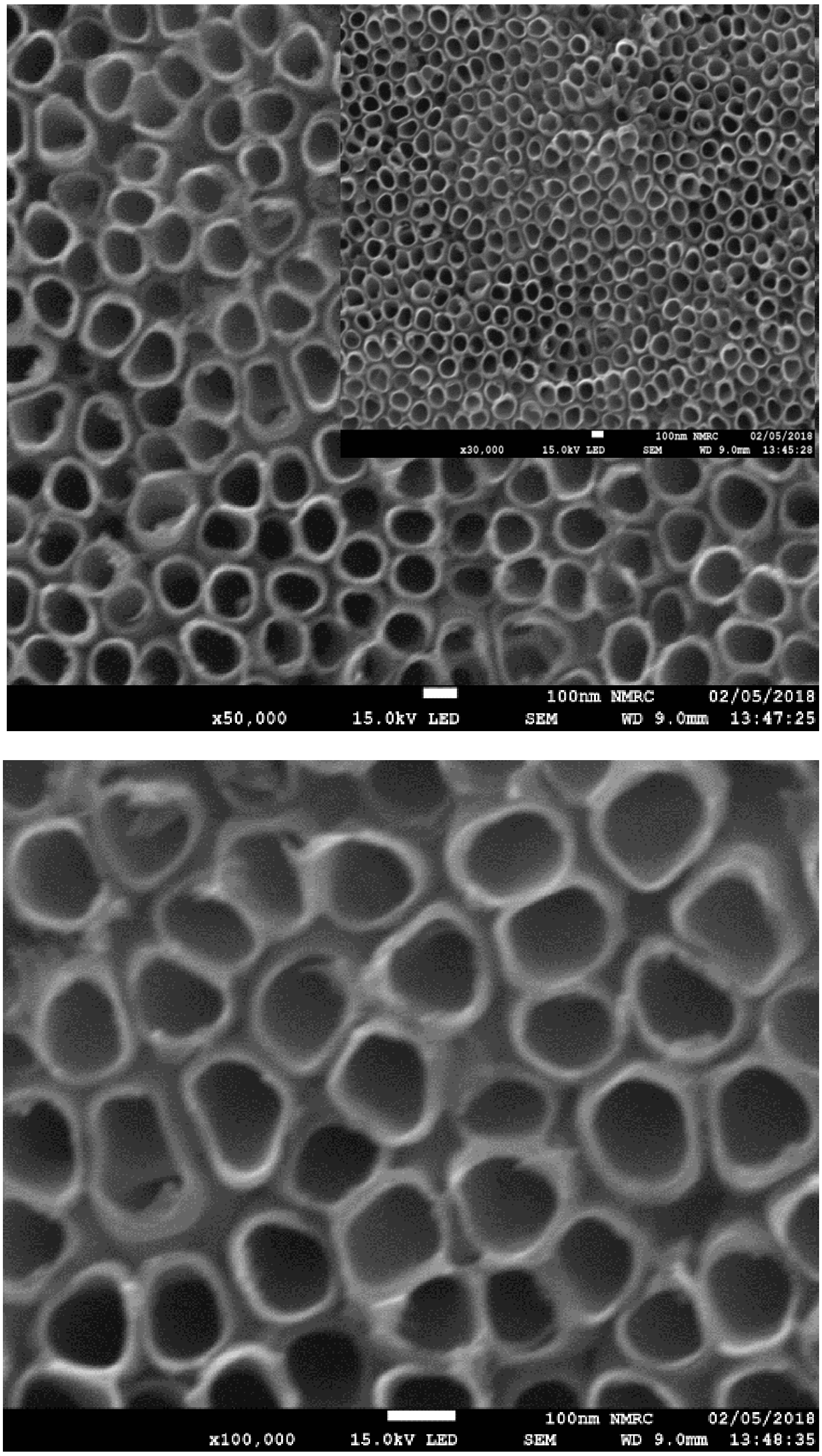

Figure 4-16: Top-surface FEG-SEM micrographs at different magnifications of TiO_2 nanotube arrays, prepared for 6.00 h anodization, at a constant bias applied voltage of 60.00 V in electrolyte contains 0.32 wt % NH_4F in 40.00 mL ethylene glycol and 4.00 vol % reverse osmosed water (ROW). Annealed at 450.00 ℃.

Figure 4-17 depicts the FEG-SEM images of the cross-sectional area of the TiO_2 NTAs. This sample was prepared for 6.00 h anodization, at a constant bias applied voltage of 60.00 V in electrolyte contains 0.32 wt % NH_4F in 40.00 mL ethylene glycol and 4.00 vol % ROW, annealed at 450 ℃. The tubular structure of these nanotubes was also confirmed from the cross-sectional images illustrated in Figure 4-17-d, e, and f. The estimated measured tube length ranged between 75.00 to 90.00 µ (Figure 4-17-a, b, and c). In comparison with the literature (Zhu et al., 2011b, Pichat, 2014) this length range is considered reasonably suitable for nanotubes as light absorbers.

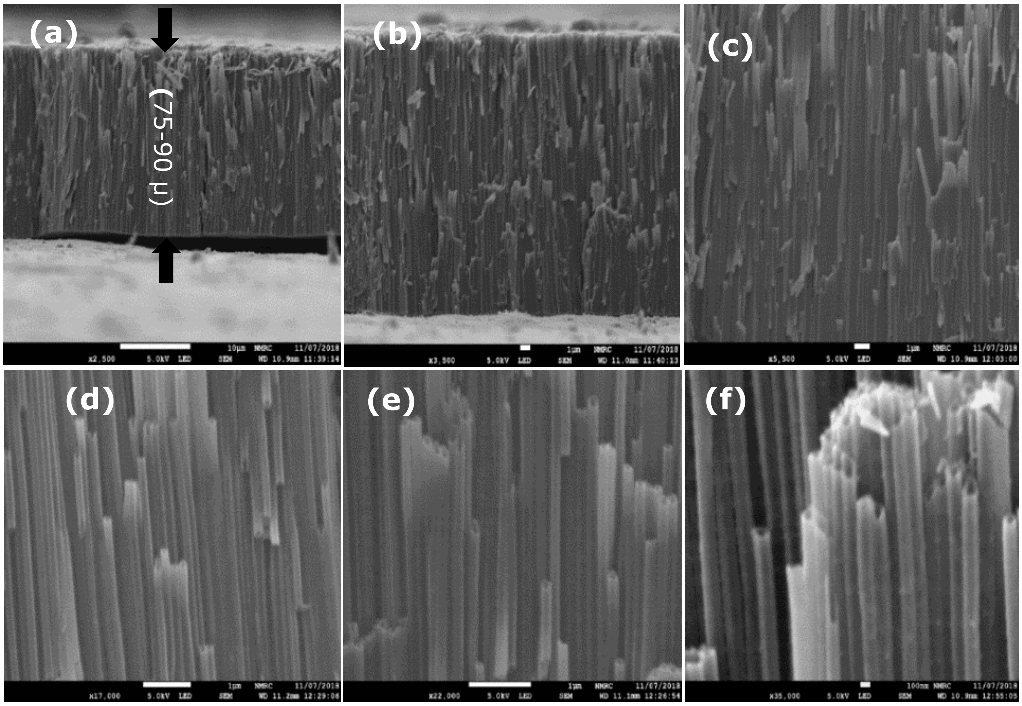

Figure 4-17: Cross-section area FEG-SEM micrographs at different magnifications of TiO_2 nanotube arrays, prepared for 6.00 h anodization, at a constant bias applied voltage of 60.00 V in electrolyte contains 0.32 wt% NH4F in 40.00 mL ethylene glycol and 4.00 vol% reverse osmosed water (ROW). Annealed at 450.00 ℃.

4.3 Conclusion

The TiO_2 NTAs synthesised by the electrochemical anodization technique showed a well-organised NTAs morphology with a considerable performance achieved after investigating significant parameters that assisted these achievements, including anodization time, drying method, and water purity. It was observed that by increasing the anodization time up to 24.0 h, the TiO_2 NTAs demonstrated grass morphology or aggregated nanotubes, which are inappropriate for photocatalysis that requires highly ordered nanotubes with an average pore diameter ca. 111.0 nm. Interestingly, findings revealed that the conductivity of the electrolyte plays a vital role in fabricating well-organised NTAs, this was observed when DIW was replaced by ROW to prepare the electrolyte, enhancing the electrolyte conductivity by 8.97 %. Meanwhile, TiO_2 NTAs exhibited an improvement in the morphology (75.00 to 90.00 µ tube length and 72.0 to 115.0 nm tube diameter). It was found that the drying of TiO_2 NTAs by using the acetonitrile vacuum could modify the conductivity of TiO_2 NTAs, which was successfully achieved when the sample dried by acetonitrile vacuum revealed a photocurrent density higher by 2.5 times than the one dried naturally in the air. The pulse illumination results of this sample revealed a stable photocurrent response under pulse illumination and an increment in the photocurrent density up to 0.0058 mA cm^{-2} in contrast with the sample dried naturally in the air, which exhibited 0.0038 mA cm^{-2}.

Chapter 5: Electrochemical Atomic Layer Deposition of CZTS

5.1 Underpotential deposition of Cu, Zn and Sn onto individual TiO_2 NTAs

There are several phase formation phenomena included in the complex electrochemical deposition of metals (M) onto foreign substrates (S). At the initial stage, the electrodeposition involves adsorption reactions as well as two dimensional (2D) and three-dimensional (3D) nucleation and growth processes (Oviedo et al., 2016). Therefore, to deposit CZTS onto TiO_2 NTAs as a single compound, it was necessary to determine the UPD potential separately for each metal (Cu, Zn, and Sn) on a pure substrate (TiO_2 NTAs) in order to facilitate the simultaneous deposition of these metals onto TiO_2 NTAs and to prevent depositing them as individual phases.

5.2 Determination of the UPD potential of Cu, Zn and Sn

Prior to the deposition of CZTS by EC-ALD, the optimised UPD potential of each metal (Cu, Zn, and Sn) was determined separately *via* CV. Figure 5-1 shows the CV measurements of Cu, Sn, and Zn on separate TiO_2 NTAs substrates. Figure 5-1-i depicts the cyclic voltammetry behaviour of Cu on TiO_2 NTAs substrate from a precursor solution consisting of 0.02 M $CuSO_4$ + 0.20 M trisodium citrate (pH = 6.30).

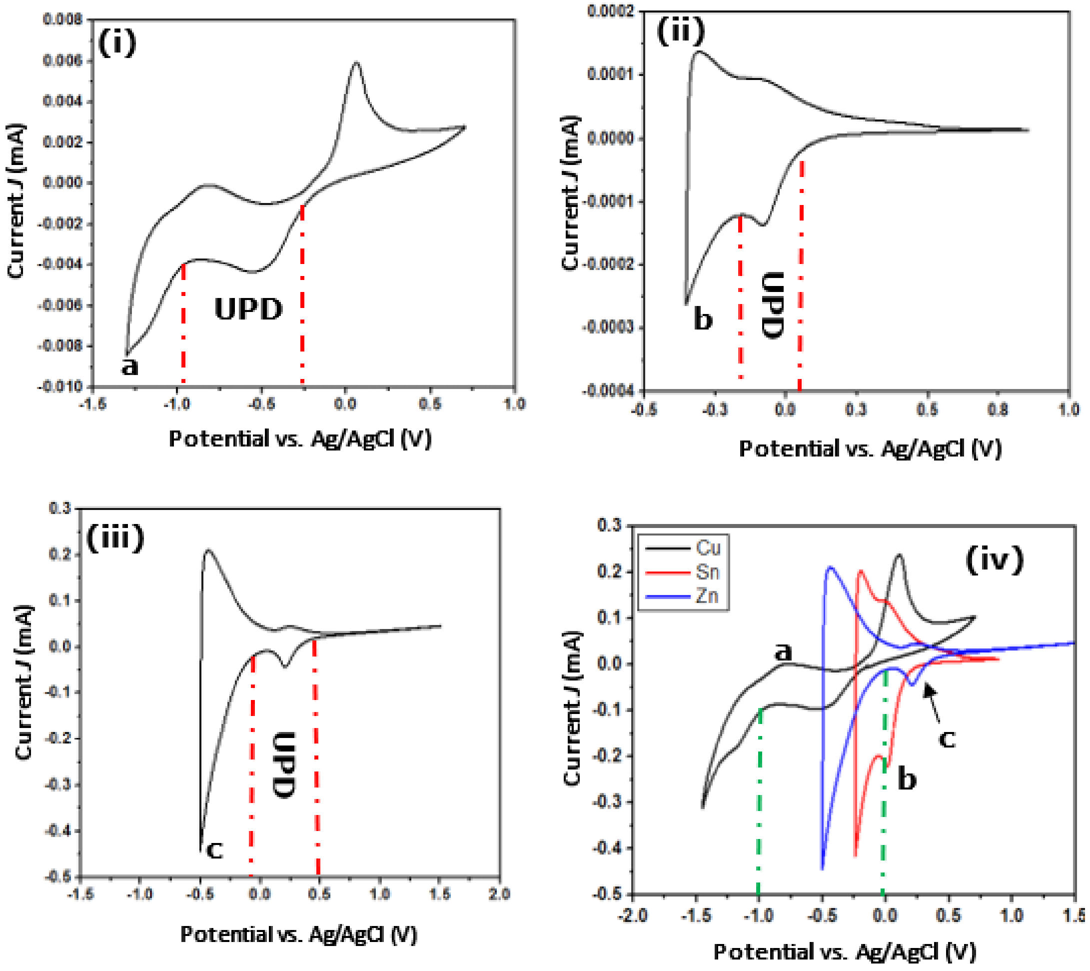

Figure 5-1: Cyclic voltammograms of TiO_2 NTAs electrode recorded at scan rate = 20.00 mV s^{-1} in solutions contain: (i) 0.02 M $CuSO_4$; (ii) 0.01 M $SnCl_2$, (iii) 0.20 M $ZnSO_4$. (iv) Overlap of i, ii and iii, in which the black arrow represents the UPD of Zn where the deposition starts on the substrate. All solutions include 0.20 M trisodium citrate (EDTA-free).

The reduction peak of the UPD potential of Cu was successfully identified as –0.500 V, which is more positive than the bulk reduction potential of –1.171 V (feature a in Figure 5-1-i). It is essential to limit the deposition of Cu within the UPD potential range of –1.000 to –0.240 V to prevent any bulk deposition of Cu ions onto the substrate, which may reduce the surface area of the TiO_2 NTAs may also increase their wall thickness and as a result, clog the NTAs pore mouths.

Figure 5-1-ii shows the cyclic voltammogram of Sn onto TiO_2 NTAs substrate in a solution containing 0.01 M $SnCl_2$ + 0.20 M trisodium citrate (pH = 6.88). The reduction peak of the UPD potential settled at −0.120 V while the bulk reduction potential obtained at −0.347 V (feature b in Figure 5-1-ii). This suggests that the deposition of Sn should be limited to within the range of −0.260 to 0.010 V to prevent any bulk of Sn ions that may cause damage to substrate morphology. According to these findings, the UPD potential values of Cu and Sn (−0.500 and −0.120 V, respectively) are found to lie within a roughly common UPD region (Figure 5-1-iv), and the pH values of their precursor solutions are similar (6.30 and 6.88 respectively). This indicates that both elements can be simultaneously deposited on the substrate using the same potential. Figure 5-1-iii illustrates the CV of Zn onto TiO_2 NTAs substrate from a solution contains 0.20 M $ZnSO_4$ + 0.20 M trisodium citrate (pH = 5.3). The UPD reduction peak was identified at a potential of 0.210 V and bulk potential of −0.499 V (feature c in Figure 5-1-iii). The deposition of Zn should be in the UPD potential range of (−0.031 to 0.500 V) to prevent bulk deposition. However, the UPD potential for Zn is not lying in a common region with Cu and Sn; it is more positive (black arrow in Figure 5-1-iv). Therefore, the UPD potential of Zn should be shifted to an appropriate common potential range within the UPD ranges of Cu and Sn to facilitate the simultaneous deposition of these elements and to prevent any bulk of Zn when the common potential is applied.

It has been reported that a complexing agent can bring a stoichiometric deposition onto the substrate using UPD (Zhu et al., 2010, Zhang et al., 2009), EDTA was used as a complexing agent in Zn precursor solutions to shift the UPD potential towards the negative (cathodic) side. Figure 5-2 illustrates the CVs of Zn on TiO_2 NTAs substrate before 0.00 M EDTA and after adding EDTA (0.01 and 0.30 M) in Zn solutions with corresponding pH values of 5.9, 4.7 and 2.9, respectively.

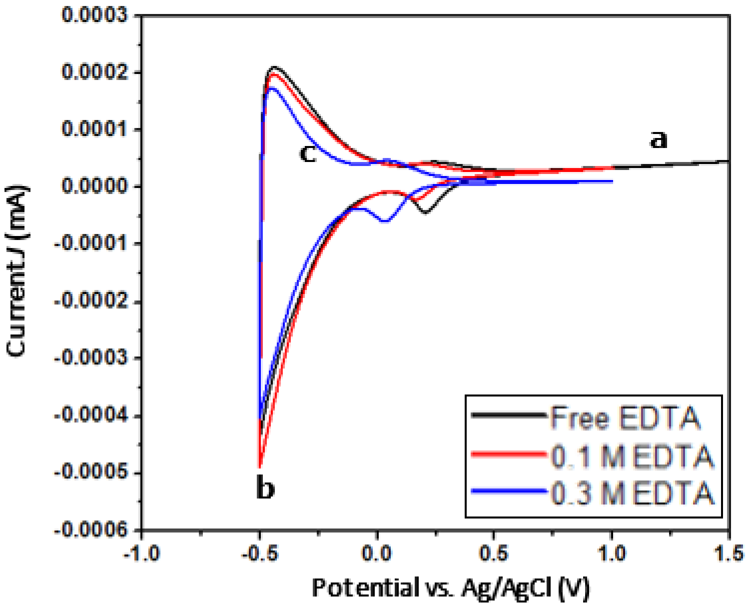

Figure 5-2: Cyclic voltammograms of TiO_2 NTAs electrode recorded at scan rate = 20.0 mV s^{-1} in solutions containing: 0.2 M $ZnSO_4$ + 0.2 M trisodium citrate with various EDTA concentration: (EDTA-free, 0.1 M and 0.3 M). The pH value of these pH solutions was maintained at their original values with no adjustment.

The pH of these solutions was maintained at their original values with no adjustment to avoid the precipitation of $Zn(OH)_2$ that may occur at EDTA concentration < 0.30 M in Zn precursor solution. A significant shift in the UPD potential can be observed from 0.250 V (no EDTA) to 0.031 V and 0.015 V when 0.10 M EDTA and 0.30 M EDTA added into solutions, respectively. This will prevent the bulk deposition of Zn at positive potentials. Figure 5-3 shows that the Zn precursor solution with 0.30 M EDTA concentration has created a common UPD potential range (-0.200 to -1.000 V) for the three elements for their simultaneous underpotential deposition.

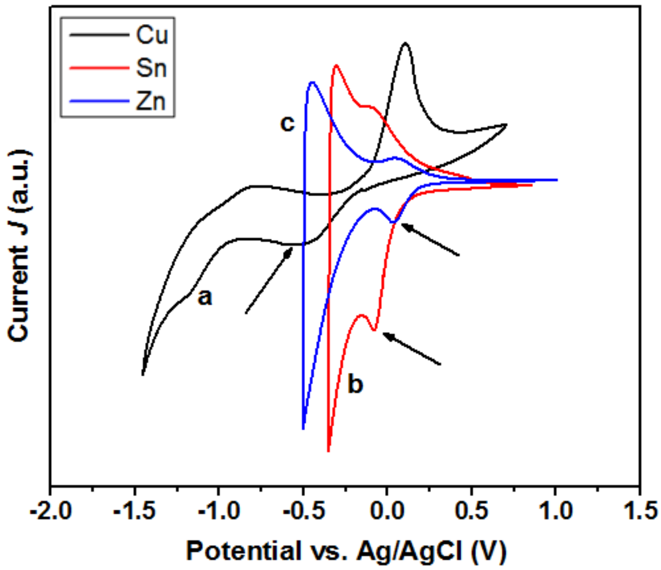

Figure 5-3: Cyclic voltammograms of TiO_2 NTAs electrode recorded at scan rate = 20.0 mV s^{-1} from solutions containing: (a) 0.02 M $CuSO_4$; (b) 0.01 M $SnCl_2$ and (c) 0.20 M $ZnSO_4$ + 0.30 M EDTA. All solutions include 0.20 M trisodium citrate. Black arrows represent the UPDs of the three metals.

5.2.1 Effect of pH value on shifting the UPD potential

The influence of pH values of individual precursor solutions on the underpotential deposition of Zn was also studied (Figure 5-4).

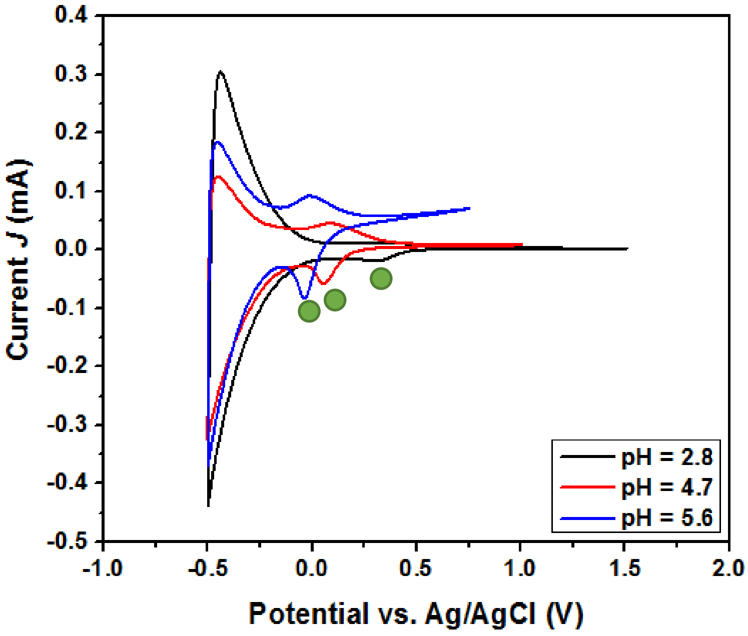

Figure 5-4: Cyclic voltammograms of TiO_2 NTAs electrode recorded at scan rate = 20.00 mV s^{-1} in solutions containing: 0.4 M $ZnSO_4$ + 0.2 M trisodium + free EDTA with different pH values. Green dots represent UPD potential values.

The deposition of Zn is sensitive to pH values since a severe shift towards the negative was found when the pH was increased from 2.80 to 4.70; this suggests that the deposition of Zn can be significantly increased by using low pH value to shift the UPD potential of Zn towards the positive. On the other hand, Cu was easily and excessively deposited onto TiO_2 NTAs relative to Zn and Sn as shown in EDX spectrums (Appendix A). As shown in Figure 5-5, the recorded current of the UPD peak of Cu (0.010 mA) was approximately one order of magnitude larger than that of Zn (0.001 mA). Therefore, it is essential to reduce the deposition amount of Cu while enhancing the deposition amount of Zn and Sn to obtain a single phase of CZTS.

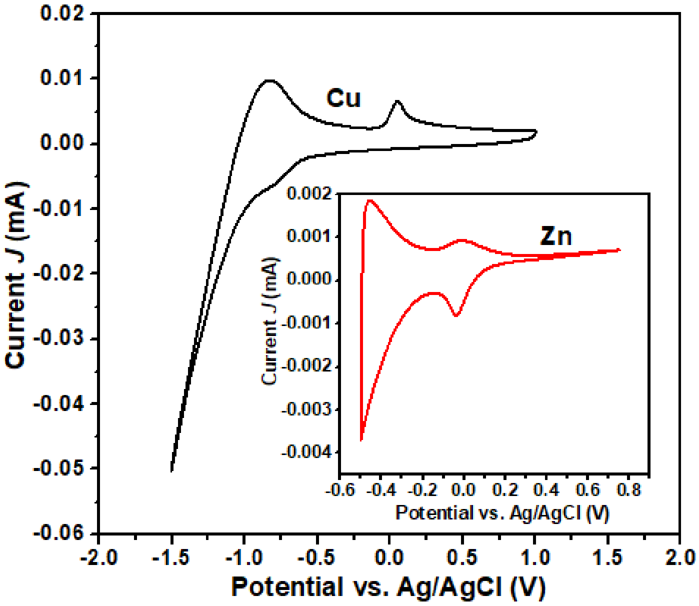

Figure 5-5: Cyclic voltammograms of TiO_2 NTAs electrode recorded at scan rate = 20.0 mV s^{-1} shows the current scale comparison between the under-potential deposition of Cu and Zn.

5.2.2 Effect of EDTA concentration

Adding a complexing agent was a crucial step in enhancing the chances of achieving successful simultaneous deposition of Cu, Zn, and Sn. To limit the Cu deposition, adding EDTA into the Cu solution was helpful to reduce the activity of Cu ions. The deposition amount of Cu could significantly be reduced by increasing the EDTA concentration in Cu precursor solution. Figure 5-6-a and b show the effect of EDTA concentration on the deposition of Cu on separate substrates (TiO_2 NTAs).

These cyclic voltammograms indicate that EDTA concentration larger than 0.10 M leads to a dramatic shift of the UPD potential of Cu towards the cathodic side from −0.500 to −0.820 V (green dotes and black arrow in Figure 5-6-a); thus the bulk deposition of Cu can be avoided even at more negative UPD potential values (≥ 0.820 V). Furthermore, the effect of pH values on the deposition behaviour of Cu also was explored.

Figure 5-6-b depicts the cyclic voltammograms of Cu onto separate TiO_2 NTAs substrates from solutions with various pH values. Similarly, the UPD undergoes a negative shift in the wake of the increasing pH. However, in comparison with Zn, the Cu deposition seems to be only slightly affected by the pH value of precursor solutions. This gap between the UPD potentials did not exceeded ca. −0.065 V or less so the UPD potential values are still close, although the pH value changed considerably. Therefore, with high EDTA concentration and a broad pH range to suit other element deposition, the deposition amount of Cu can be controlled, while the deposition of Zn and Sn can be optimised by using a different pH value.

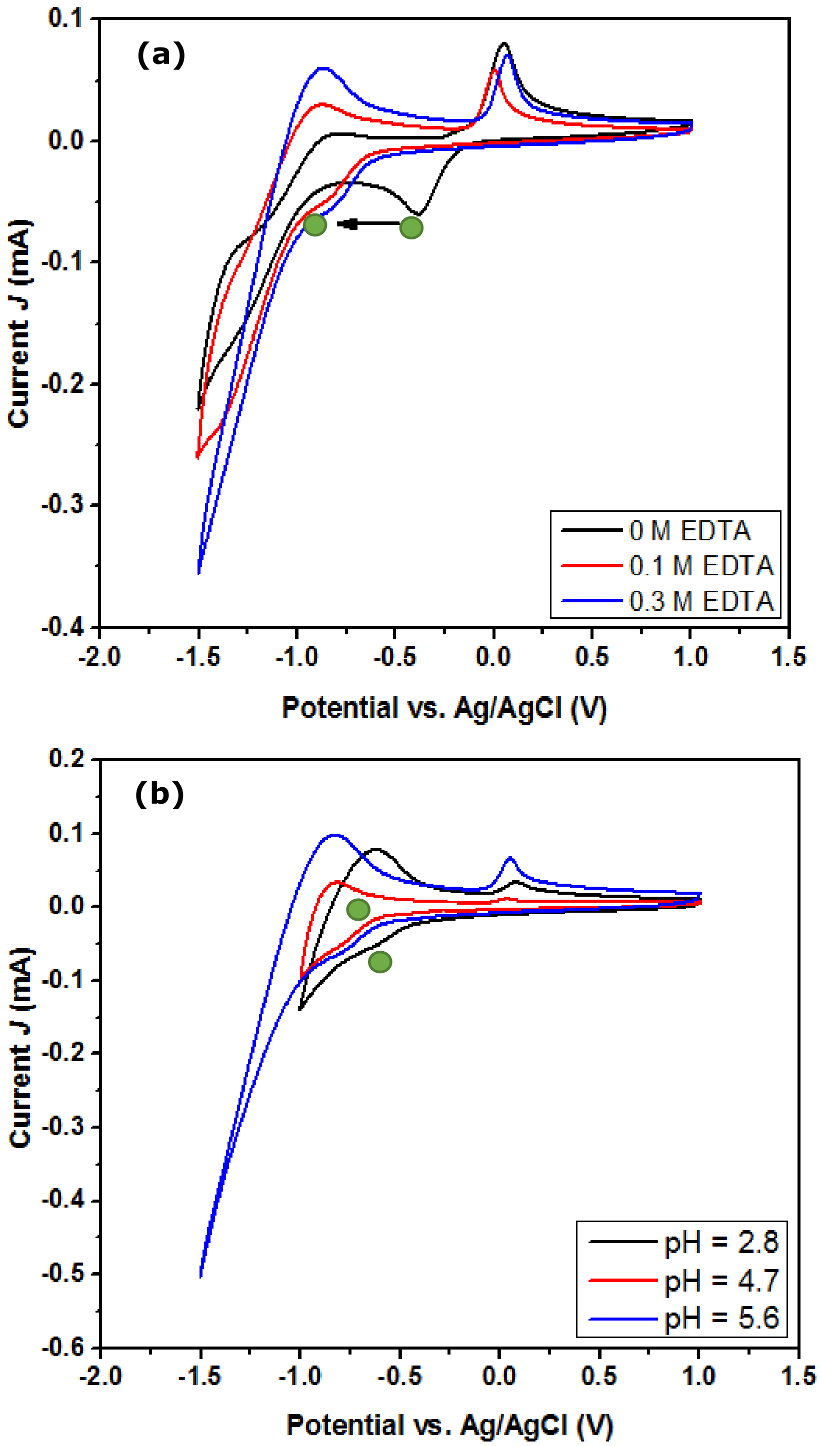

Figure 5-6: Cyclic voltammograms of TiO_2 NTAs electrode recorded at scan rate = 20.00 mV s^{-1} in solutions containing: (a) 0.005 M $CuSO_4$ + 0.200 M trisodium with 0.0, 0.1 and 0.3 M EDTA (pH of all solutions maintained at 5.50, black arrow represents the cathodic shift in UPD potential) and (b) 0.005 M $CuSO_4$ + 0.200 M trisodium + 0.400 M EDTA. These solutions prepared at pH values: 2.80, 4.70 and 5.60). Green dots represent UPD potential values.

Figure 5-7-a and b show the XRD diffraction patterns of the pure and CZTS sensitised TiO_2 NTAs.

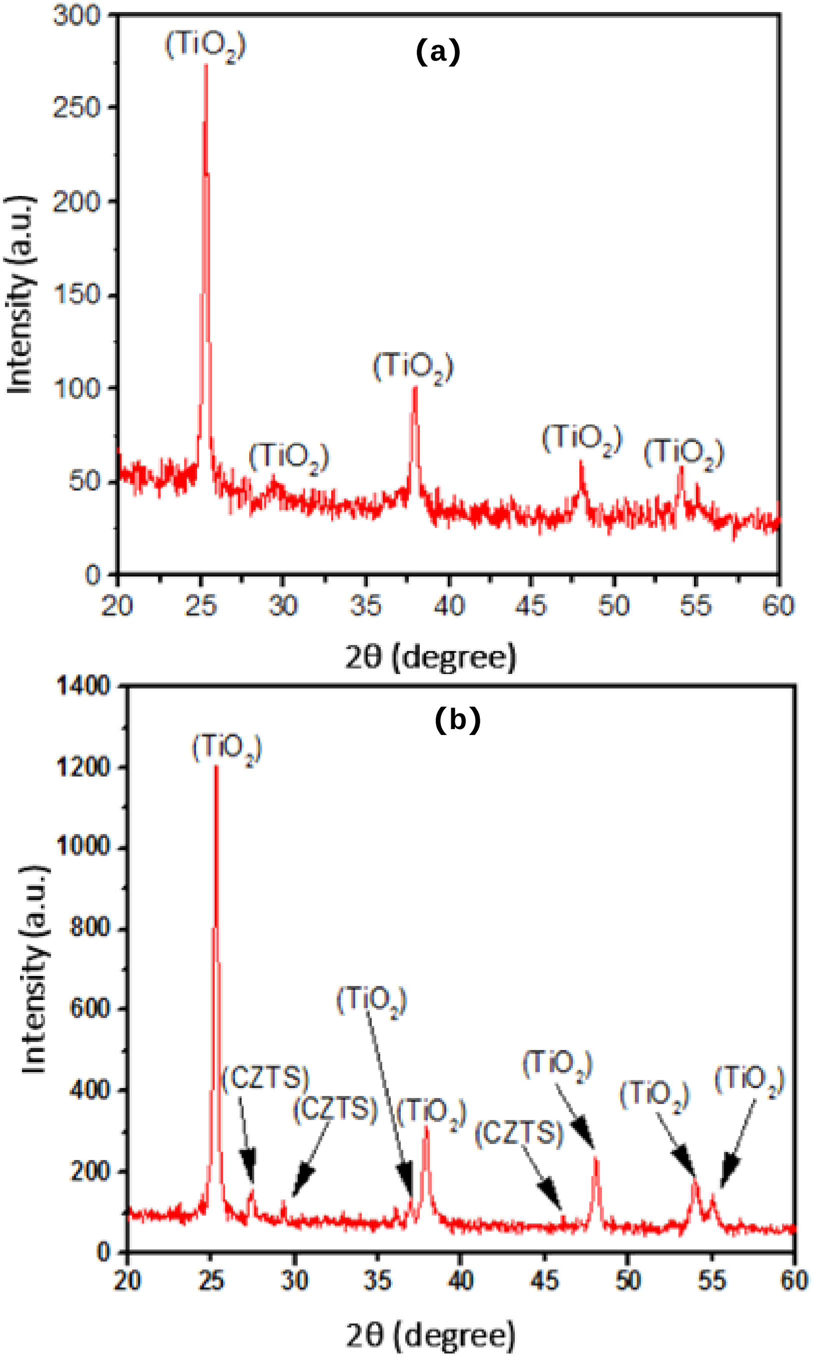

Figure 5-7: XRD diffractograms of (a) pure anatase TiO_2 NTAs substrate annealed at 450.0 ℃ for 2.0 h and (b) CZTS electrodeposited onto TiO_2 NTAs at UPD potential = −0.500 V.

The diffraction peaks located at 2θ = 25.4°, 37.9°, 48.0°, and 55.0°, corresponding to the crystalline orientations (101), (004), (200) and (211), respectively representing the anatase TiO_2 NTAs (Figure 5-7-a). The peaks corresponding to the diffraction angles 2θ = 27.5°, 29.1°and 47.1° in Figure 5-7-b represent the crystalline orientations of (101), (112) and (200) and characterize the Kesterite structure of CZTS (ICDD No: 00-026-0575). Significantly, only the single-phase CZTS peaks, without any superfluous elements of Cu, Zn, Sn, and S, were identified. Figure 5-8 shows the top-surface FEG-SEM images of pure TiO_2 NTAs (Figures 5-8-a, b, and c) and the as-prepared CZTS/TiO_2 NTAs (Figure 5-8-d, e and f) at various magnifications.

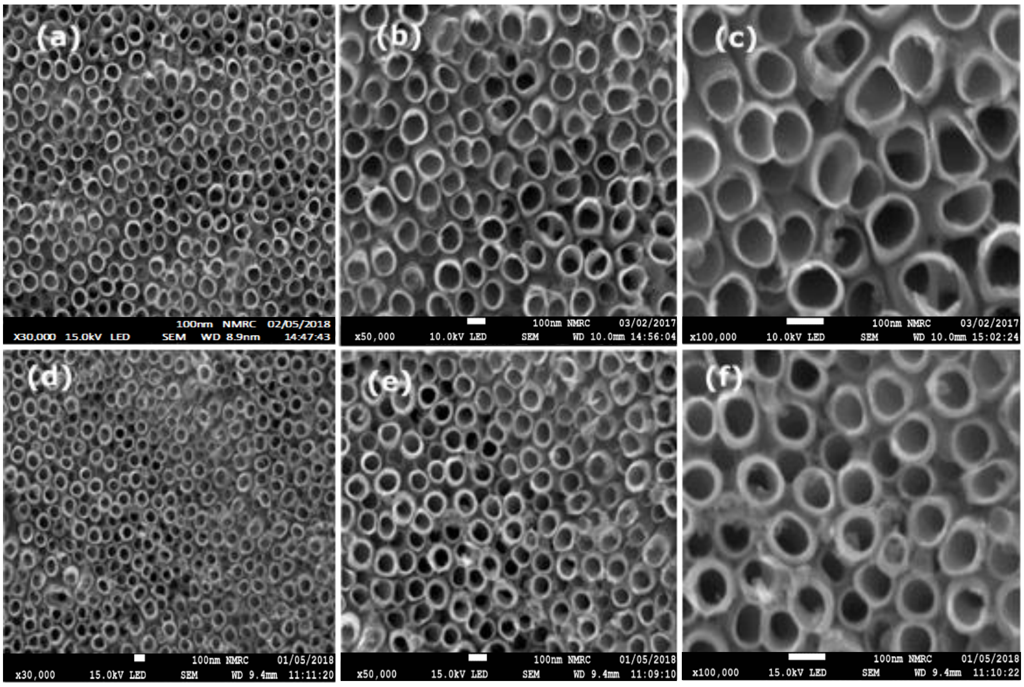

Figure 5-8: Top-surface FEG-SEM micrographs of pure TiO_2 NTAs (a, b and c) and CZTS (d, e, and f) electrodeposited on UPD potential = −0.500 V vs Ag/AgCl at the magnifications (X30,000.0, X50,000.0 and X100,000.0).

The well-organised pure TiO_2 NTAs were synthesised successfully *via* a two steps electrochemical anodization route (Figure 5-8-a). The inner diameter of the tube was estimated as ca. 111.0 ± 15.0 nm with a wall thickness of few nanometres (Figure 5-8-c). However, from the FEG-SEM images (shown in Figure 5-8-f), the average inner diameter of the coated TiO_2 NTAs with CZTS reduced to ca. 100.0 nm, and the wall thickness became thicker relative to that in Figure 5-8-c, suggesting that the coating layer was ca. 5.0 ± 0.5 nm. Furthermore, the well-ordered structure of the nanotubes was maintained after the electrodeposition of the elements. Figure 5-9 demonstrates the typical current density versus time curve during the simultaneous deposition of CZTS thin film by EC-ALD on TiO_2 NTAs substrate at UPD potential = -0.500 V from a mix of precursor solutions of Cu, Zn, and Sn.

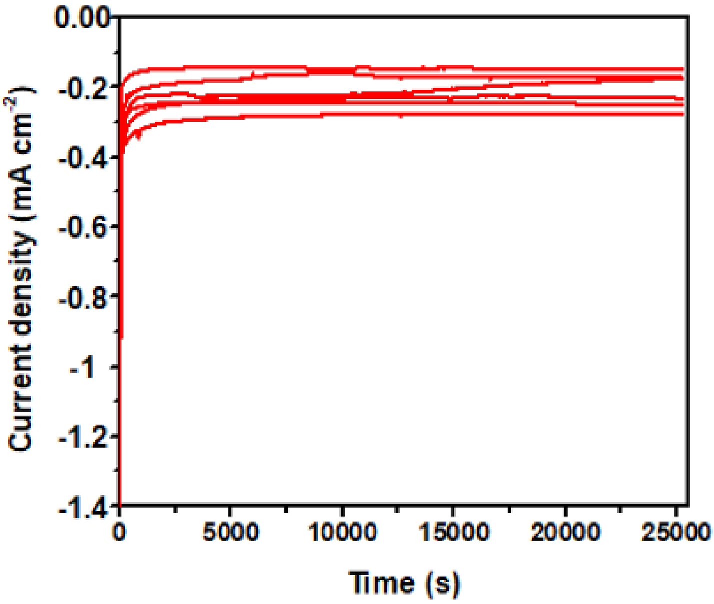

Figure 5-9: Current density versus time during the simultaneous deposition of CZTS thin films by EC-ALD on TiO_2 NTAs substrate at UPD potential = –0.500 V. Multiple scans represent the repeatability of the recoded current density for multiple EC-ALD.

Throughout the electrodeposition, the recorded cathodic current density exhibited an almost constant value ranging −0.2 to −3.5 mA cm^{-2} for 25200.0 s, indicating that the well-organised structure of TiO_2 NTAs remained orderly and was not affected by the deposited materials owing to the absence of the bulk deposition of the deposited metals. This finding was broadly repeated for the simultaneous deposition of CZT onto TiO_2 NTAs by using the EC-ALD route, which was shown by the multi scan of the recoded current density. Farinella et al. (2014) fabricated CZTS by a potentiostatic deposition from aqueous baths onto ITO substrates supported by polyethylene terephthalate (PET). They obtained CZTS in a bath mixing 2.5 mL of $CuSO_4$, 15.0 mL of $ZnSO_4$, 2.5 mL of $SnSO_4$ and 60.0 mL of $Na_2S_2O_3$, and the cathodic current density gradually reached a constant value of about −0.2 mA cm^{-2} after 1800.0 s.

UV-Vis measurements were performed to exam the capacity for harvesting the light from pure TiO_2 NTAs and CZTS/TiO_2 NTAs. Figure 5-10-a illustrates the UV-Vis absorbance of pure TiO_2 NTAs and CZTS/TiO_2 NTAs.

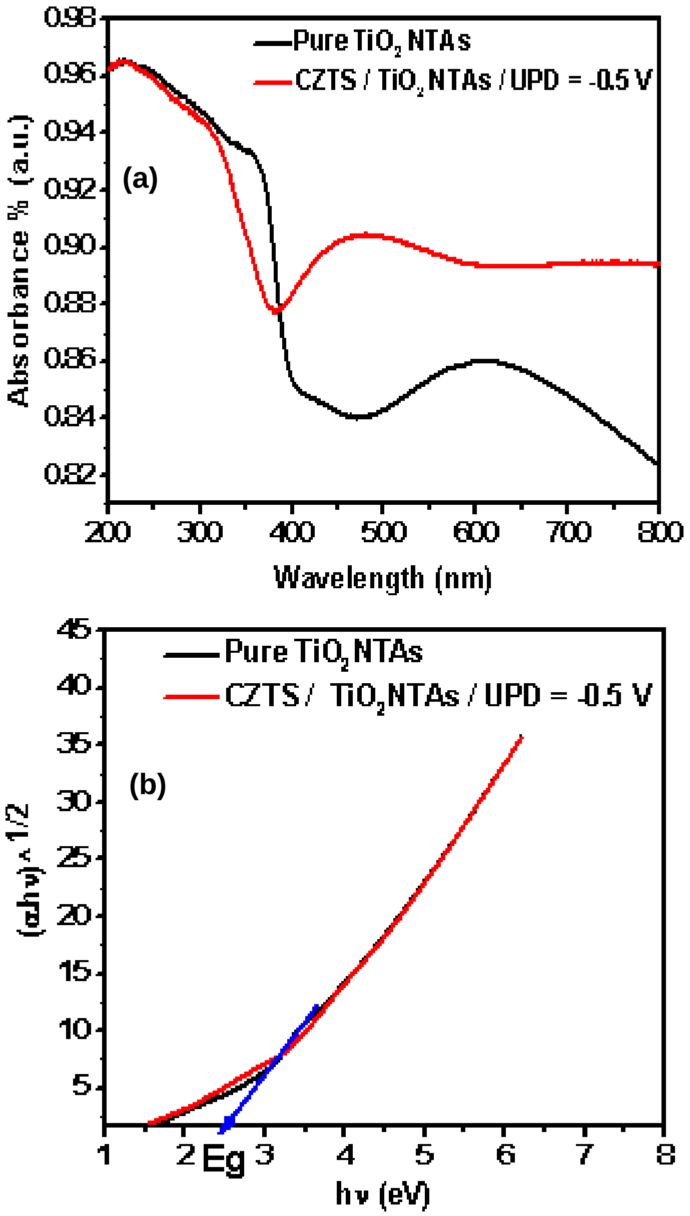

Figure 5-10: (a) UV-Vis absorbance spectra of pure TiO_2-NTAs and the as-synthesised CZTS/TiO_2 NTAs at UPD = –0.500 V, (b) Data of Figure 5-10-a transformed using the Kubelka−Munk function for the extraction of the optical bandgap energy (Eg) (blue arrow).

In comparison with pure TiO_2 NTAs (400.0 nm), a significant shift in the wavelength towards the visible region (510.0 nm) for CZTS/TiO_2 NTAs was observed (red curve) and the bandgap energy was calculated from the relationship between the absorbance ($\propto$) and the incident photon energy $(h\nu)$ shown in Equations (5-1) and (5-2) respectively:

$$h\nu = 1240/\lambda \qquad \text{Eq. 5-1}$$

By applying Tauc relation (Hassanien and Akl, 2016):

$$\propto h\nu = A\,(h\nu - Eg)^{m} \qquad \text{Eq. 5-2}$$

where A is a constant dependent on the transition probability, and m is equal to 0.5 for the indirect gap and 2.0 for the direct gap. The bandgap energy is calculated from the plot of $(\propto h\nu)^{1/2}$ vs. incident photon energy $(h\nu)$ (Ghrairi and Bouaicha, 2012, Hassanien and Akl, 2016) and by extrapolating to zero using a linear fit (Murphy, 2007, Shangguan et al., 2003, Chen et al., 2004). The bandgap of pure TiO_2 NTAs was narrowed from 3.10 eV to 2.43 eV after integrating CZTS with TiO_2 NTAs (Figure 5-11-b).

Figure 5-11-a shows the photocurrent density of the heterogeneous CZTS/TiO_2 NTAs that fabricated at deposition potential = –0.500 V; data for the corresponding pure TiO_2 NTAs before sensitisation is also provided.

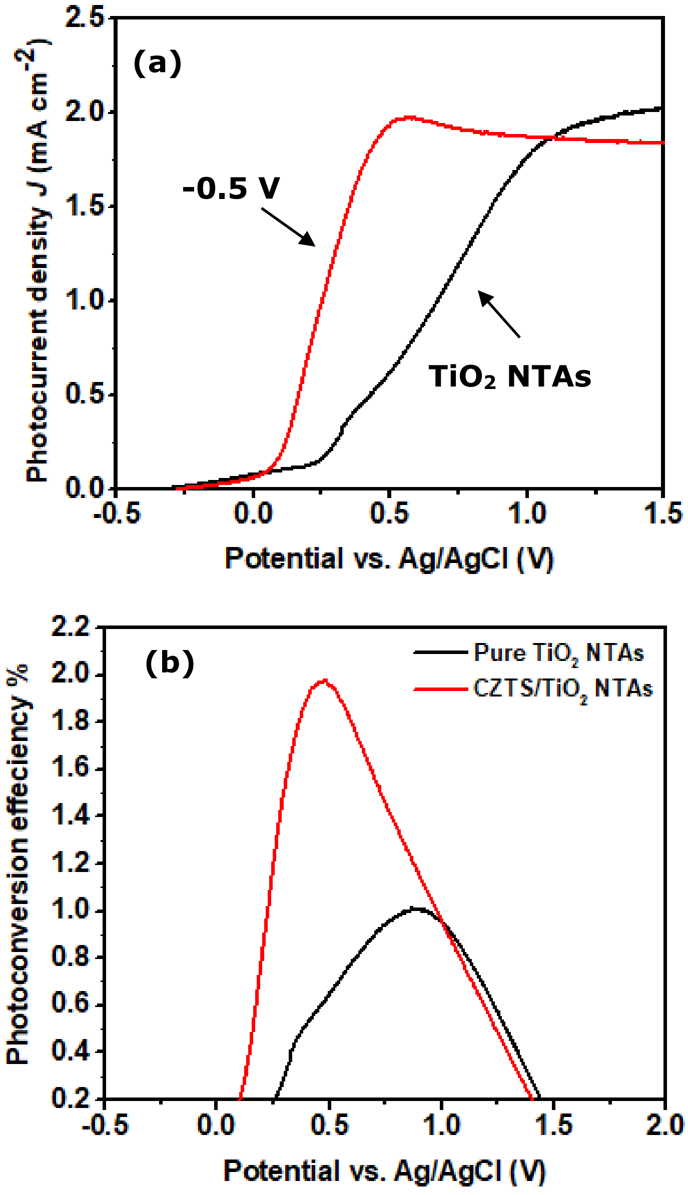

Figure 5-11: (a) Photocurrent density and (b) corresponding photoconversion efficiency of CZTS/TiO_2 NTAs sample fabricated on UPD potential = –0.500 V. Maximum enhancement of 81.0 % in the photoconversion efficiency was achieved under 100.0 mW cm^{-2} full spectrum illumnation.

Figure 5-11-b shows the photoconversion efficiency (η), which is defined as the overall ratio of the maximum energy output that can be obtained from the final products, hydrogen and oxygen, to the energy supplied in the form of light to produce them (Varghese and Grimes, 2008). The as-synthesised CZTS/TiO_2 NTAs photoanode demonstrated an enhancement in the photoconversion efficiency to 2.0 % in comparison with the pure TiO_2 NTAs (1.1%). A maximum hydrogen generation rate of 49.000 mL h^{-1} cm^{-2} from CZTS/TiO_2 NTAs photo-electrode was achieved under light irradiation. This rate is much higher than the range of 0.247 to 10.240 mL h^{-1} cm^{-2} that was reported in the literature for the water-splitting applications (Ye et al., 2012, Hensel et al., 2010, Setiadi, 2011, Sadanandam et al., 2013, Sun et al., 2017).

5.3 Parameters affecting the deposition of CZTS onto TiO_2 NTAs

The electrochemical deposition of metals on a conductive substrate is affected by several parameters, including:

- pH value of the individual precursor solutions
- EDTA concentration
- Deposition potential (UPD)
- Time of deposition
- Precursors’ concentration

These parameters have a specific effect on the electrodeposition of CZTS onto TiO_2 NTAs, such as suppression of the metal ions, causing bulk deposition, shifting the UPD potential towards the negative or the positive side. However, it is crucial to investigate the impact of each of these when attempting to obtain a homogeneous deposition to obtain the kesterite CZTS with a stoichiometric ratio of 2:1:1:4 (Cu_2ZnSnS_4).

5.3.1 Effect of UPD potential on the synthesis of CZTS/TiO_2 NTAs

XRD diffraction patterns (Figure 5-12) shows the comparison when applying the previously determined UPD potential range (–0.200 to –1.000 V) to deposit CZTS on individual substrates (TiO_2 NTAs) for 7.0 h of deposition time and sulfurization at 585.0 ℃. These samples prepared from precursor solutions containing 0.02 M $CuSO_4$ + 0.30 M EDTA, 0.20 M $ZnSO_4$, and 0.10 $SnCl_2$; each solution contains 0.20 M trisodium at pH = 6.34 for the final solution after mixing the three precursors. The diffraction peaks located at $2\theta = 25.4°$, 37.9°, 48.0°, and 55.0°, corresponding to the crystalline orientations of (101), (004), (200) and (211), respectively that represent the anatase phase of TiO_2 NTAs were clearly observed at deposition potentials of –0.200, –0.500 and –0.600 V. However, the XRD peaks of CZTS are more evident at –0.500 and –0.600 V. This suggests decreasing the deposition potential from –0.200 to –0.600 V increases the deposited amount of the elements (inducing the reduction process of metal ions on the substrate); this was also observed by Zhu et al. (2010) when they decreased the deposition potential from –0.650 to –0.700 V to deposit CdS onto TiO_2 NTAs. Therefore, the UPD potential should be optimised correctly to ensure the simultaneous deposition of the elements.

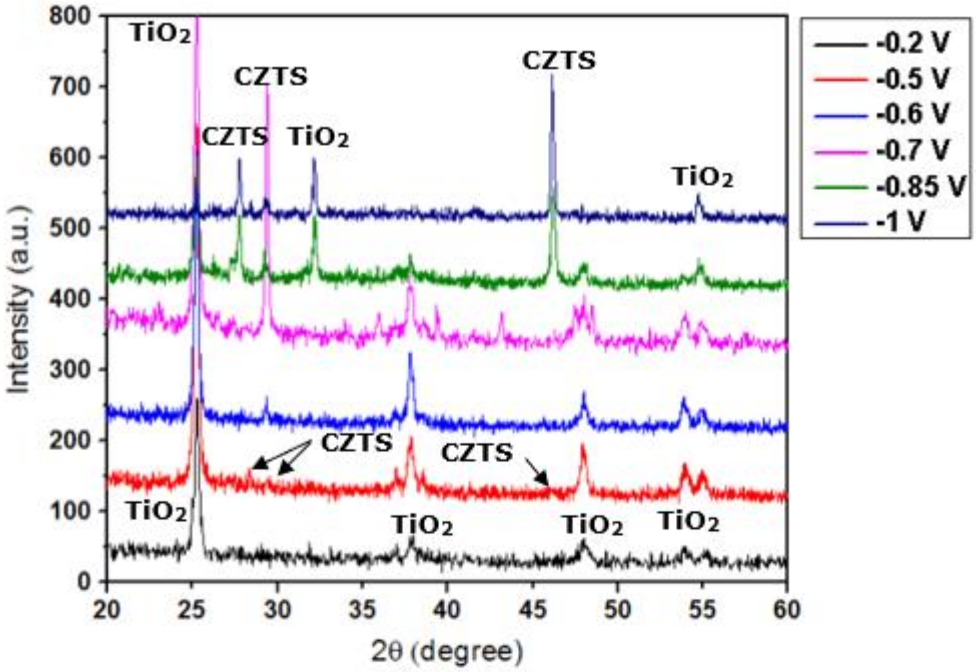

Figure 5-12: XRD diffractograms of CZTS electrodeposited onto TiO_2 NTAs at deposition potentials (UPD) of -0.200, -0.500, -0.600, -0.700, -0.850 and -1.000 V vs Ag/AgCl. The values of UPD potentials related to the common range of UPD for CU, Zn and Sn. These CZTS/ TiO_2 NTA photoanodes annealed for 5.0 h and 30.0 m at 585.0 ℃ in sulfur environment.

However, when the deposition potential further decreased from –0.600 to –1.000 V, it suppressed the peaks of TiO_2 NTAs, and the intensity of CZTS peaks became noticeably stronger, this may indicate that the deposited metals have covered the surface of the substrate, causing clogging of the pore mouth of the nanotubes due to the bulk deposition. This phenomenon may occur when the interaction or binding energy between the adatoms (metal cations) is larger than the binding energy with the substrate, i.e., the driving force is inadequate to grow atoms on the top surface of the homogeneous atoms (Zhu et al., 2010). Figure 5-13 shows FEG-SEM images of the top surface of as-synthesised CZTS/TiO_2 NTAs at UPD = −0.850 V. The white arrow (Figure 5-13 -a) represents a crack on the top surface of the as-synthesised CZTS/TiO_2 NTAs that is shown more clearly using larger magnifications in Figure 5-13-b-d. The crack probably resulted due to high stresses during the electrodeposition and caused peeling off the thin film from the substrate.

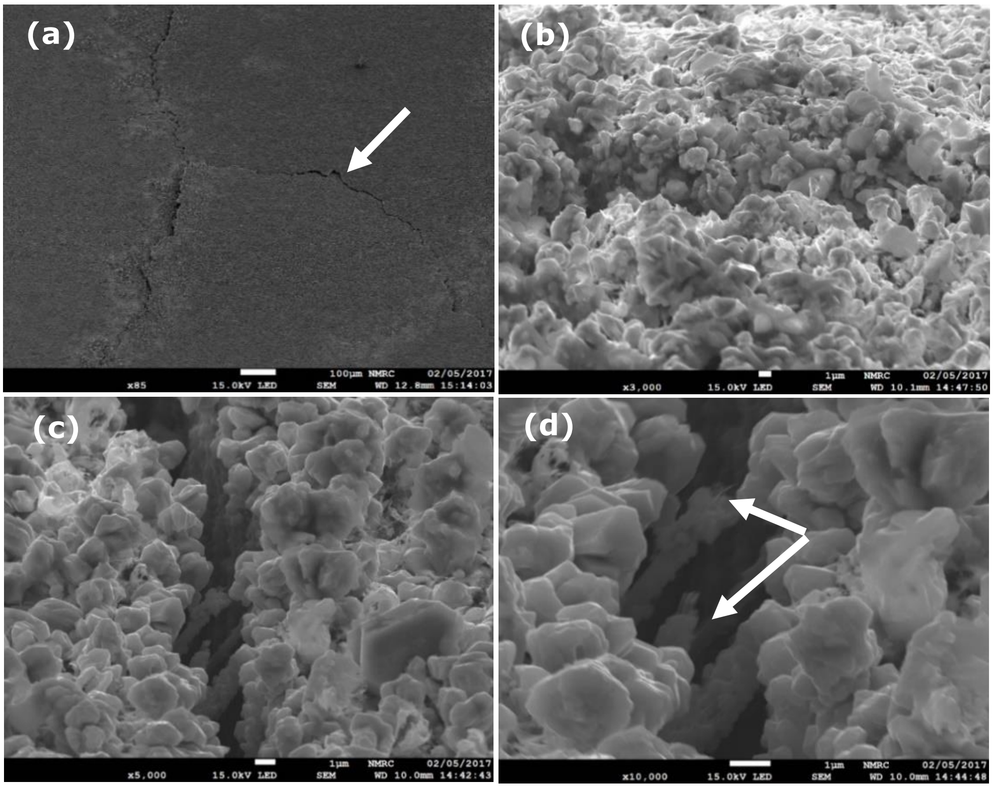

Figure 5-13: Top-surface images of CZTS electrodeposited onto TiO_2 NTAs at UPD = −0.850 V (vs. Ag/AgCl) at various magnifications. The white arrows represent the surface of a tube covered with the deposited film (CZTS).

Figure 5-14-a-d shows the side view of the same sample at low magnifications. The dark area (red arrow Figure 5-14-a) represents the electrodeposited CZTS, which peeled off from the substrate, while the light area (blue arrow Figure 5-14-a) represents the nanotube arrays (substrate). It was established that the stresses in epitaxial thin films could cause the failure of the films through cracking and may cause the de-cohesion from the substrate (Magnfält, 2014).

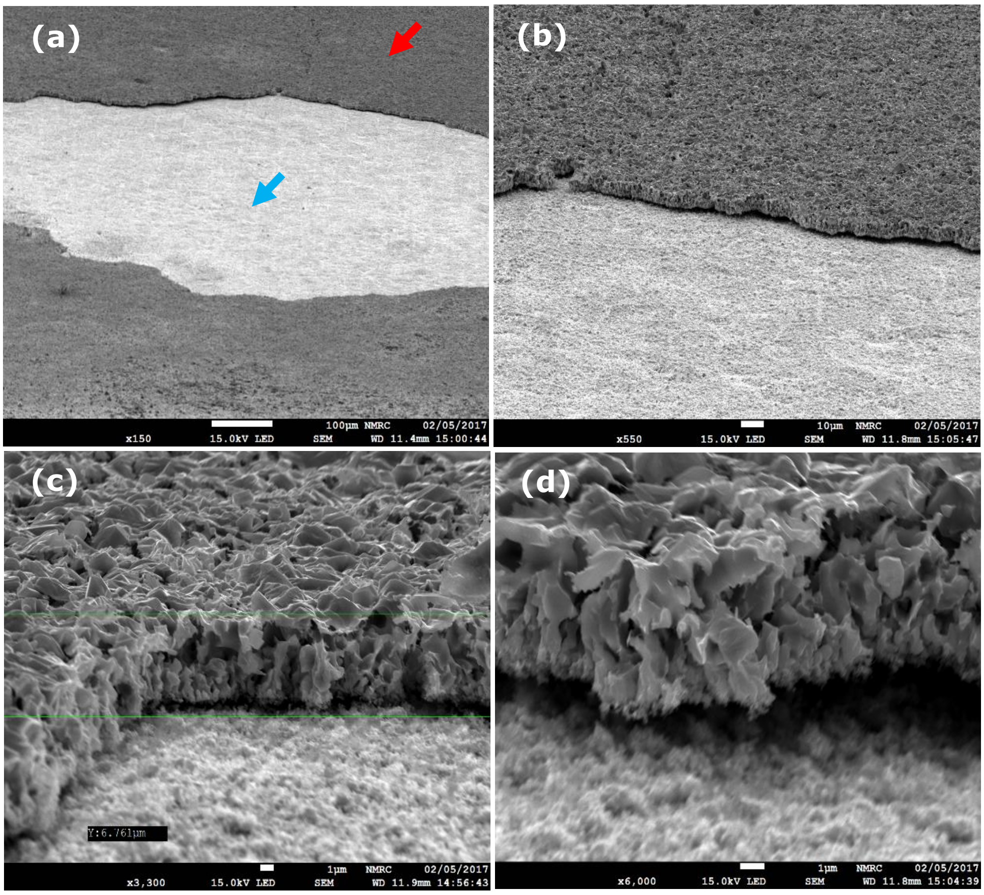

Figure 5-14: Side view FEG-SEM micrographs of CZTS electrodeposited onto TiO_2 NTAs at UPD = -0.850 V vs Ag/AgCl at different magnifications.

Zhu's group demonstrated that the bulk deposition affects the coaxial heterogeneous structure by coating the TiO_2 NTAs with CdS onto for a 5.0 h deposition duration (Zhu et al., 2010). They showed that by decreasing the deposition potential from −0.650 to −0.750 V, the average inner diameter of the nanotubes was reduced. Moreover, the problem of island deposition occurred, which negated the features of two-dimensional atomic layer deposition of UPD. The thickness of CZTS was measured (Figure 5-14-c) approximately 7.0 μm, which is relatively thick in comparison with the expected thickness of a thin film deposited by electrodeposition (< 10.0 to 20.0 nm) (Venables et al., 1984). Therefore, it was essential to select a UPD value more positive than −0.850 V to avoid the bulk deposition; thus, the UPD value was increased to −0.700 V.

Figure 5-15-a and b show the top surface images of CZTS deposited onto TiO_2 NTAs at UPD = −0.700 V. Although the nanotubes can be observed on the surface, this UPD potential caused bulk deposition of the CZTS film, which clogged the tube pore mouth (red arrow in Figure 5-15-a and b), and this will , in turn, reduce the surface area of the nanotubes and weaken their photoactivity.

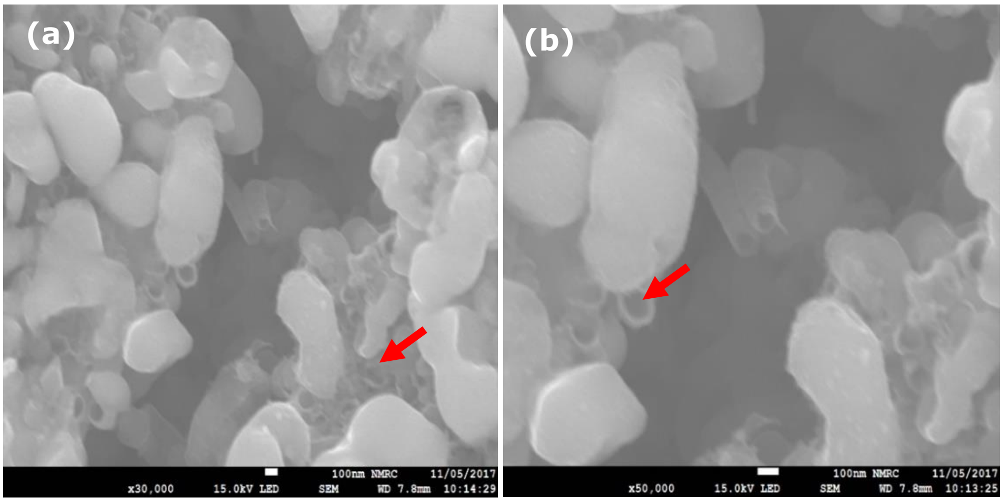

Figure 5-15: Top-surface FEG-SEM micrographs of CZTS electrodeposited onto TiO_2 NTAs substrate at UPD = –0.700 V (vs. Ag/AgCl) at different magnifications (a and b). The red arrows represented the clogging of the tube pore mouth by the deposited film and damaged the well-aligned morphology of the TiO_2 NTAs.

The EDX analysis (Figure 5-16) confirmed the bulk deposition for some of the deposited elements (Cu and S). The quantity of 37.68 % atoms of Cu was more than expected from the stoichiometric ratio for the compound Cu_2ZnSnS_4 (2:1:1:4) by ca. 25.0 times.

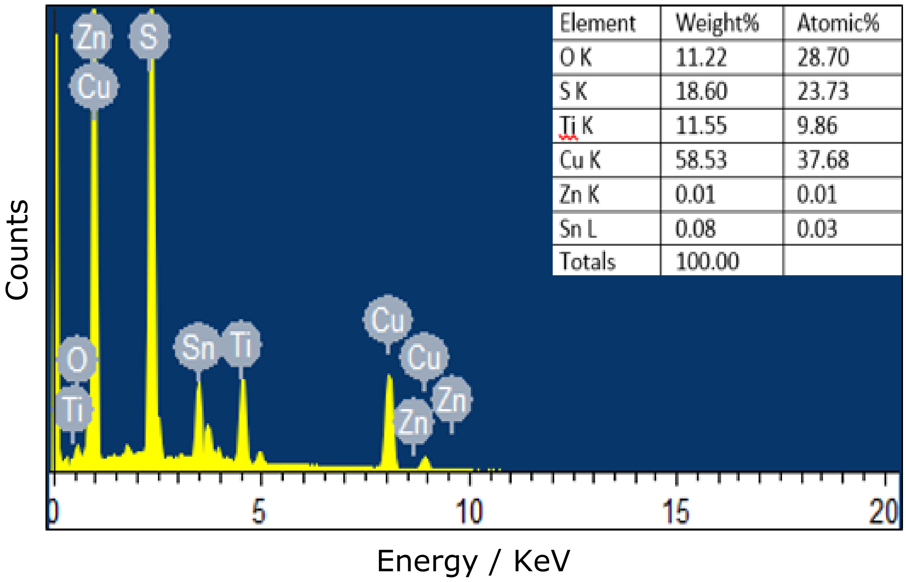

Element	Weight%	Atomic%
O K	11.22	28.70
S K	18.60	23.73
Ti K	11.55	9.86
Cu K	58.53	37.68
Zn K	0.01	0.01
Sn L	0.08	0.03
Totals	100.00	

Figure 5-16: EDX spectrum of the as-prepared CZTS/TiO_2 NTAs formed in solutions contain: 0.20 M $ZnSO_4$ + 0.3 M EDTA, 0.02 M $CuSO_4$ and 0.01 M $SnCl_2$. All solutions contain 0.20 trisodium citrate. The deposition was conducted at UPD = –0.700 V. EDX conducted atv 15 kV.

Sn and Zn quantities are lower than the detection accuracy of the equipment (1.00 %). Furthermore, the EDX analysis did not give the expected 2:1 stoichiometric ratio of O to Ti (ca. O, 50.73 %, Ti, 29.41 %) and the characteristic peaks of Ti and O were weak in comparison to those of Cu and S, indicating the extensive coverage of the substrate by the deposited film.

The quantity of S in the deposition process mainly depended on the quantity of the other elements, the S deposition was performed in the furnace after coating the sample with Cu, Zn, and Sn, the chemical bonds between S and the other deposited elements were produced during the sulfurization process in the tube furnace. Since Cu revealed a high % atom content, S will mostly react with Cu, which accumulated as islands on the top surface of the substrate. Owing to the affinity of Cu towards TiO_2 NTAs, Cu can facilitate the transportation of electrons to the electrode enhancing? its effective conductivity (Su et al., 2012), suggesting that Cu adatoms virtually cover the surface of the substrate, leaving no active sites for Zn and Sn to be adsorbed and move to the growth phase.

With respect to the complex morphology of TiO_2 NTAs that was a great challenge in controlling the simultaneous deposition of Cu, Zn, and Sn, while maintaining the nanotubes well-aligned, it is essential to prevent the bulk deposition of the deposited elements by limiting the deposition potential at –0.650 V that confirmed from the XRD results and FEG-SEM images. The as-synthesised CZTS/TiO_2 NTAs was further characterised using XPS to prove the existence of the elements on the surface of the substrate. Figure 5-17 illustrates the elemental composition of CZTS/TiO_2 NTAs from a high resolution XPS analysis.

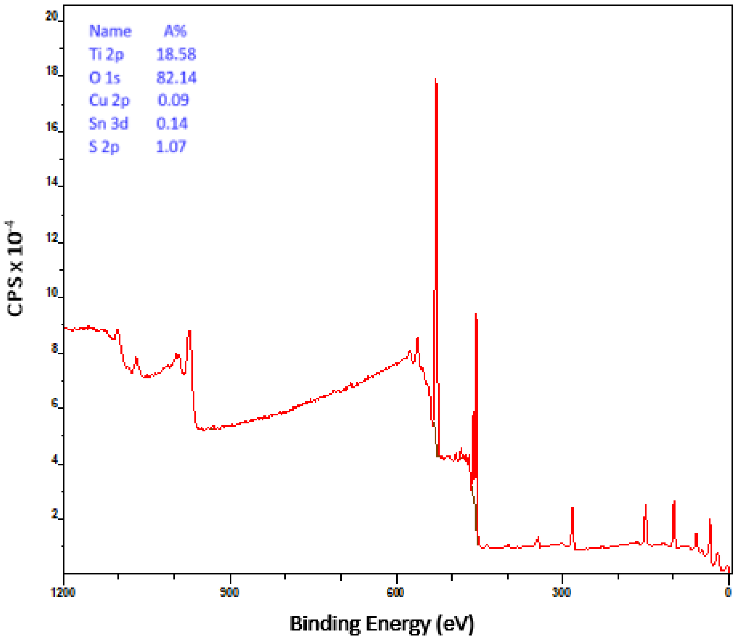

Figure 5-17: XPS wide-scan spectrum of CZTS/TiO_2 NTAs. Showing the presence of Cu, Sn, Ti, O and S. Zn 2p is not visible on either spectrum.

All the elements were detected on the surface of the substrate, except Zn. The absence of the Zn peak suggests a non CZTS thin film on the top of the substrate surface. The elemental analysis also did not reveal any Zn, this is a confirmation that the deposited thin film was not sufficient to cover the inner and the outer wall of the nanotubes, and this can probably be attributed to a thin layer of the coating being deposited on the substrate, so that Zn is below detection levels. Further investigation or another methodological route were required to improve the quality of the coating and consequently to improve the photocatalytic performance for the TiO_2 NTAs.

5.3.2 Precursor' concentration

The concentration of the precursors is one of the essential parameters that was investigated in this study. Since the previous results revealed that the deposited amount of Zn and Sn was not enough to achieve a stochiometric ratio similar to 2:1:1:4 due to the domination of Cu on the substrate, the $ZnSO_4$ and $SnCl_2$ precursor concentration was increased from 0.20 to 0.40 M and from 0.01 M to 0.02 M, respectively. To avoid the bulk deposition of Cu, selecting a UPD potential more positive than −0.700 V was essential.

Figure 5-18 depicts the EDX spectrums of the as-synthesised CZTS/TiO_2 NTAs formed at UPD = –0.650 V, with their corresponding SEM images that show islands of Cu deposited on the substrate and clogging the mouth of the nanotubes, this may weaken the photocatalytic activity and even damaged the well-aligned morphology of TiO_2 NTAs.

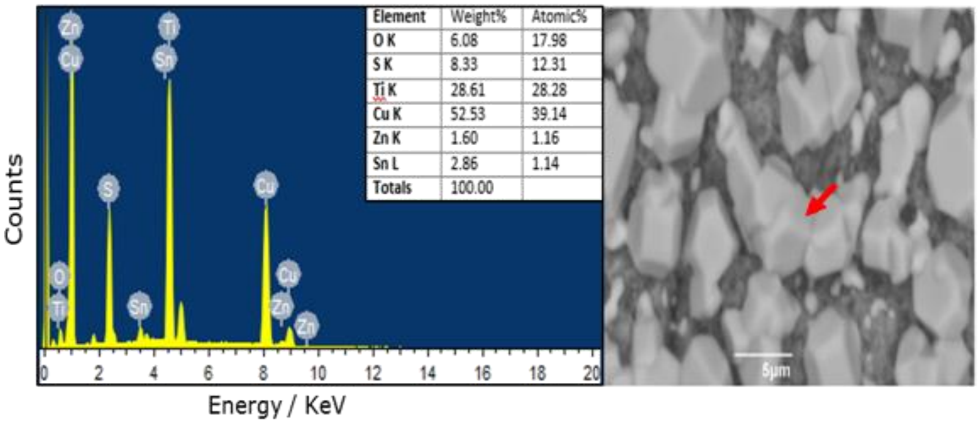

Element	Weight%	Atomic%
O K	6.08	17.98
S K	8.33	12.31
Ti K	28.61	28.28
Cu K	52.53	39.14
Zn K	1.60	1.16
Sn L	2.86	1.14
Totals	100.00	

Figure 5-18: EDX spectrums with the corresponding top surface SEM image of CZTS/TiO_2 NTAs prepared in solutions contain: 0.40 M $ZnSO_4$ + 0.30 M EDTA, 0.02 M $CuSO_4$ and 0.02 M $SnCl_2$. All solutions contain 0.20 trisodium citrate. The deposition was conducted at UPD = –0.650 V. Red arrow represents Cu bulk deposition. EDX conducted atv 15 kV.

The red arrow in Figure 5-18 represents the bulk deposition of Cu. The quantitative analysis of this sample demonstrated a rise in the atom % of Zn and Sn by approximately 1.00 %, which matches the expected stoichiometric ratio between Zn and Sn (1:1) of the format Cu_2ZnSnS_4 compound (2:1:1:4).

However, the average atom % of Cu is still higher than the required stoichiometric ratio by approximately 50.00 %; thus, the bulk or island phase is still occurring (red arrow), which relates to Cu bulk deposition.

Although the atomic layer deposition by UPD is independent of the concentration of precursors as mentioned earlier, this experiment has revealed the opposite since the amount of the deposited elements slightly improved after increasing their concentrations.

Reith and Hopman (2012) have deposited the kesterite onto indium tin oxide (ITO) substrates by electrodeposition. They reported that high precursor concentrations led to higher deposited amounts.

5.4 Summary

This chapter presented and discussed a successful simultaneous underpotential deposition of multiple elements onto TiO_2 NTAs substrates using the EC-ALD technique from mixed precursor solutions. The results revealed that three crucial criteria should be considered to enhance the deposition of Zn and Sn and to suppress the bulk deposition of Cu: (i) reduce the pH value of the deposition bath to ca. 4.70; (ii) increase EDTA concentration in the precursor solution of Cu (> 0.30 M) and (iii) avoid deposition potentials (UPD) more negative than −0.650 V.

The Kesterite structure of CZTS was successfully synthesised as single phase without superfluous elements of Cu, Zn, Sn, and S. A red shift was observed from 400.0 nm for pure nanotubes to 510.0 nm for CZTS/TiO_2 NTAs, respectively. The bandgap was narrowed from 3.10 eV of pure TiO_2 NTAs to 2.43 eV of CZTS/TiO_2 NTAs. After sensitising the nanotubes with CZTS, an enhancement in the photoconversion efficiency from 1.1 % to 2.0 %, was obtained. More importantly, the well-organised nanotubes morphology was maintained after the coating with CZTS using the EC-ALD technique without clogging the tube mouth.

The thickness of CZTS layer was estimated ca. 5.0 ± 0.5 nm and the average inner diameter of TiO_2 NTAs was reduced from ca. 111.0 ± 15.0 nm (pure TiO_2 NTAs) to ca. 100.0 nm after the sensitisation with the CZTS thin film. The novel photoanode of CZTS/TiO_2 NTAs demonstrated a synergistic effect on the photocatalytic properties and hydrogen generation rate by achieving a maximum hydrogen generation rate of 49.0 mL h^{-1} cm^{-2}.

Chapter 6: EC-ALD of CZTS via separate precursor solutions approach

6.1 Advantageous of individual EC-ALD

To improve the quality of the deposited film and for further enhancement in the photocatalytic activity of the novel CZTS/ TiO_2 NTAs photoanode, the electrochemical atomic layer deposition (EC-ALD) was performed using an alternative approach to prevent the domination of Cu deposition on the substrate, which was suppressing the deposition of Zn and Sn. This approach was employed to allow enough time for Zn to bond with the substrate by depositing the elements from their precursor solutions separately (Cu, Zn, and Sn) instead of mixing; this may assist in avoiding complexing Sn and Zn with the complexing agent that exists in the Cu solution. The pH of Zn and Sn precursor solutions was maintained at their original values of 4.70 and 6.83, while the pH of the Cu solution was adjusted to 7.00 to avoid any bulk of Cu may occur, the deposition was conducted at UPD potential = –0.650 V for one h for each element onto individual TiO_2 NTAs substrate.

6.2 XRD, EDX and FEG-SEM characterisation

Figure 6-1 compares the XRD diffraction patterns of the pure and CZTS sensitised TiO_2 NTAs. The CZTS electrodeposited onto TiO_2 NTAs at UPD potential = –0.500 V for 7.0 h (red scan) from mixture at UPD potential = –0.650 for 1.0 h, and from separate (blue scan) precursor solutions, respectively.

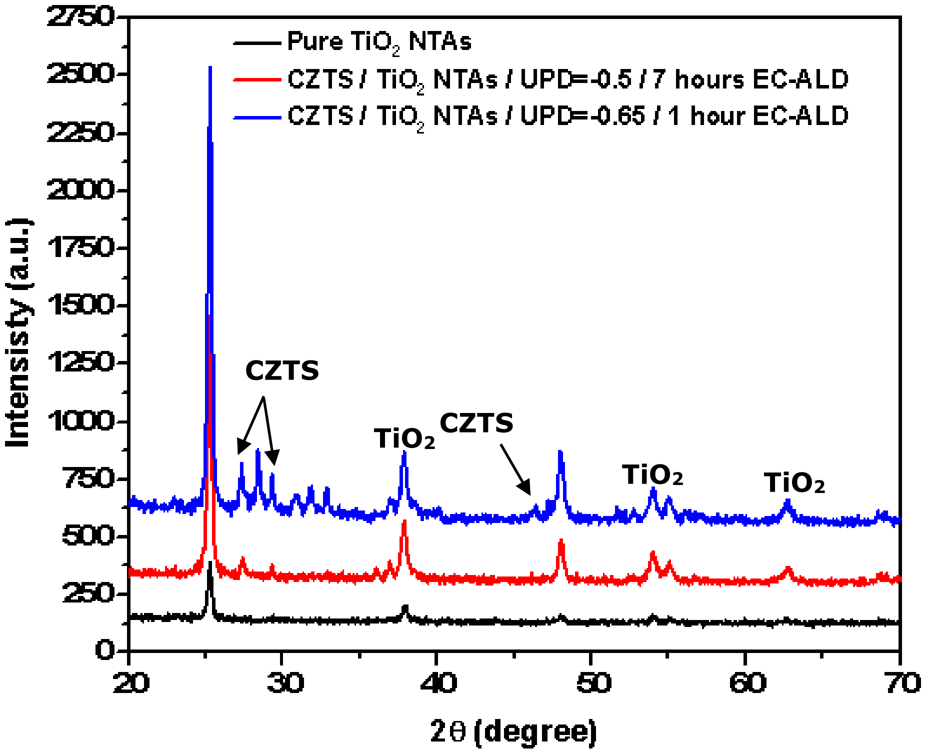

Figure 6-1: XRD patterns of pure anatase TiO_2 NTAs substrate and CZTS electrodeposited onto TiO_2 NTAs at UPD potential = –0.500 V for 7.0 h (red scan) from the mixture and at UPD potential = –0.650 V for 1.0 h (blue scan) from separate precursor solutions, respectively.

The characteristic peaks corresponding to the Kesterite structure of CZTS thin film became stronger when it was deposited from individual precursor solutions, in comparison with the one that deposited from mixed precursor solutions. This suggest that sufficient time was provided for Zn and Sn ions to be reduced on the substrates individually. Moreover, the suppression of these ions was prevented due to the complexing agent EDTA's presence in the Cu solution. The EDX results show strong evidence for the existence of the pure CZTS (Figure 6-2).

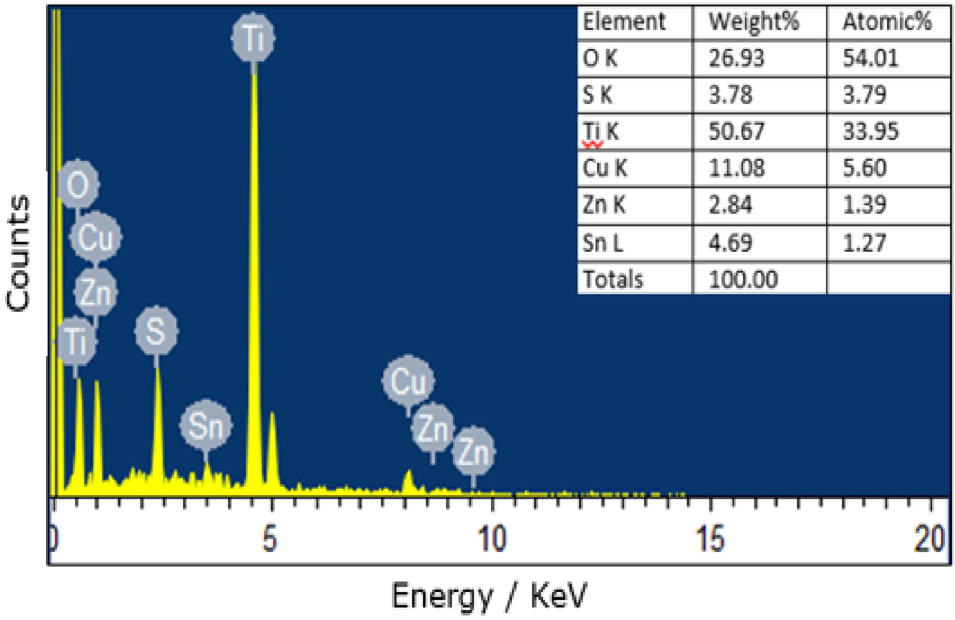

Element	Weight%	Atomic%
O K	26.93	54.01
S K	3.78	3.79
Ti K	50.67	33.95
Cu K	11.08	5.60
Zn K	2.84	1.39
Sn L	4.69	1.27
Totals	100.00	

Figure 6-2: EDX spectrums of CZTS/TiO_2 NTAs prepared in separate solutions contain: 0.400 M $ZnSO_4$ + 0.000 M EDTA, 0.005 M $CuSO_4$ + 0.400 M EDTA and 0.020 M $SnCl_2$. All solutions contain 0.200 trisodium citrate. The deposition of each element was conducted at UPD = −0.650 V for 1.0 h. EDX was conducted at 15 kV.

The quantitative analysis demonstrated a stoichiometric ratio relatively close to 2:1:1:4 that was to be expected from the composite Cu_2ZnSnS_4 (Cu, 5.60 % Zn, 1.39 %, Sn, 1.27 % and S, 3.79 %).

It must be emphasised that individual EC-ALD was significantly assisted in improving the quality of the CZTS thin film by obtaining a homogeneous deposition of the deposited elements. Furthermore, the morphological characteristic of the CZTS/TiO_2 NTAs photoanode confirmed the successful simultaneous deposition from separate precursor solutions. Figure 6-3 illustrates the top surface FEG-SEM images of the sample synthesised from separate precursor solutions. Each element (Cu, Zn, and Sn) was deposited onto TiO_2 NTAs substrate at UPD potential = –0.650 V.

The wall of the CZTS/TiO_2 NTAs photoanode was thickened when the electrodeposition was conducted from separate precursor solutions (Figure 6-3-c-f) relative to the pure TiO_2 NTAs (Figure 6-3-a and b). The average inner diameter of the tubes was reduced to ca. 95.0 nm, suggesting that the CZTS coating layer was ca. 8.0 nm, while the pure TiO_2 NTAs had an average inner diameter of ca. 111.0 nm with a wall thickness of few nanometres. This may indicate that the deposited layer of CZTS was homogeneously covering the inner and the outer layer of the wall of the nanotubes (see further FEG-SEM images in appendix B).

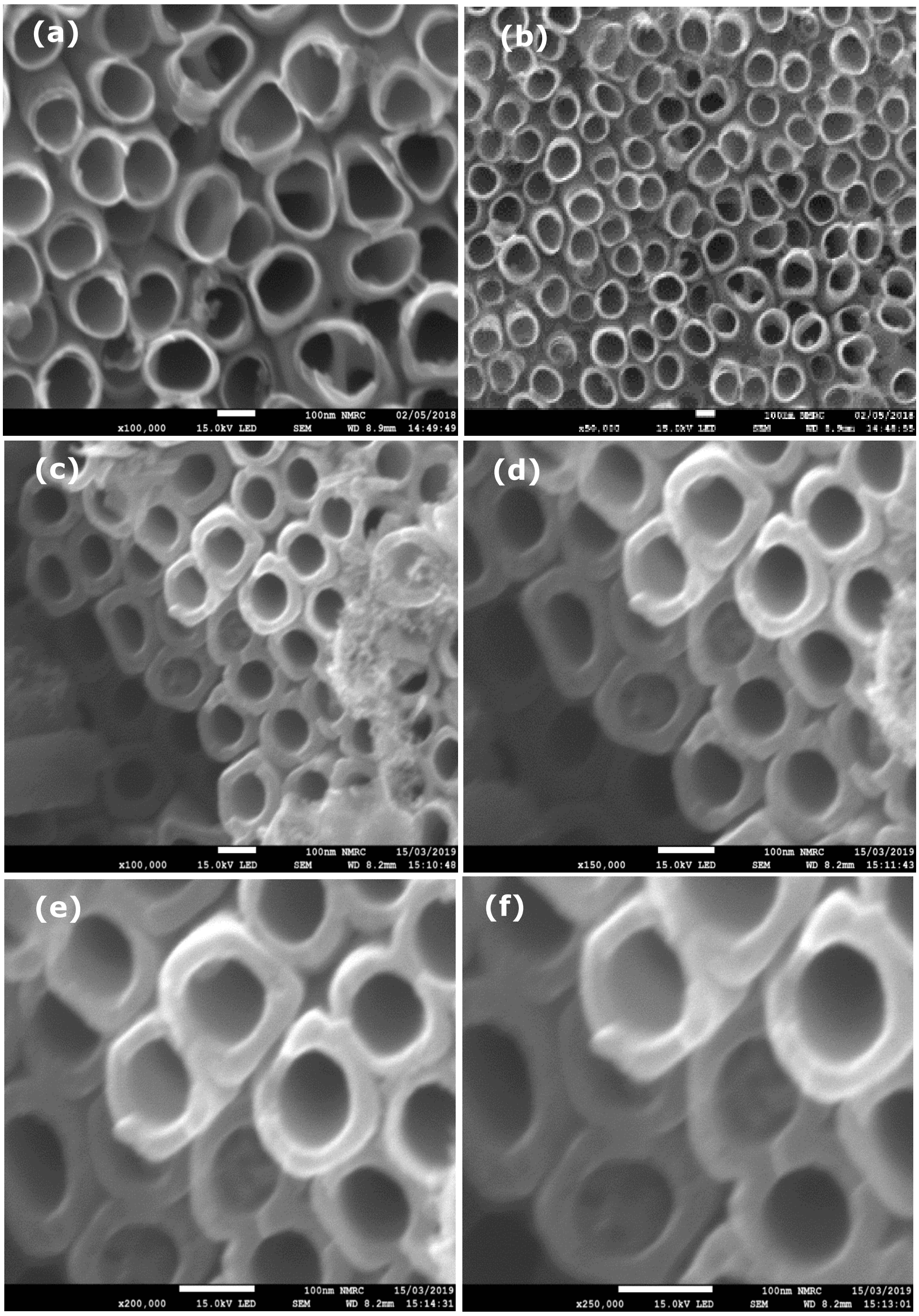

Figure 6-3: Top surface FEG-SEM micrographs of pure TiO_2 NTAs (a and b) and the as-synthesised CZTS/TiO_2 NTAs electrodeposited onto TiO_2 NTAs substrate at different magnifications (c, d, e and f). The deposition of each element was conducted at UPD = −0.650 V for 1.0 h.

Figure 6-4-a shows the measured photocurrent density of the CZTS/TiO_2 NTAs coaxial heterogeneous structure that fabricated *via* a mixture of precursor solutions at deposition potential = –0.500 V for 7.0 h (red curve) and *via* separate precursor solutions at deposition potential = –0.650 V for 1.0 h each (blue curve).

The photoelectrochemical measurements of CZTS/TiO_2 NTAs also showed the presence of plenty of H_2 bubbles on the counter electrode (Pt wire), this certainly attributed to a significant enhancement in the water-splitting process, corresponding to the wake of peak * and prohibiting the recombination of e^-/h^+ pairs aided by the presence of the hole scavengers that exists in the electrolyte (Na_2SO_3/Na_2S). Therefore, the photocurrent density of ca. 2000.0 μA for pure TiO_2 NTAs was enhanced to ca. 3000.0 μA for the novel CZTS/TiO_2 NTAs photoanode. The corresponding photoconversion efficiency (Figure 6-4-b) of the coaxial heterogeneous CZTS/TiO_2 NTAs photoanode was increased from 1.10 % to 2.00 % to 2.78 % for pure TiO_2 NTAs, CZTS/TiO_2 NTAs deposited from a mixture of precursor solutions and for CZTS/TiO_2 NTAs deposited from separate precursor solutions, respectively.

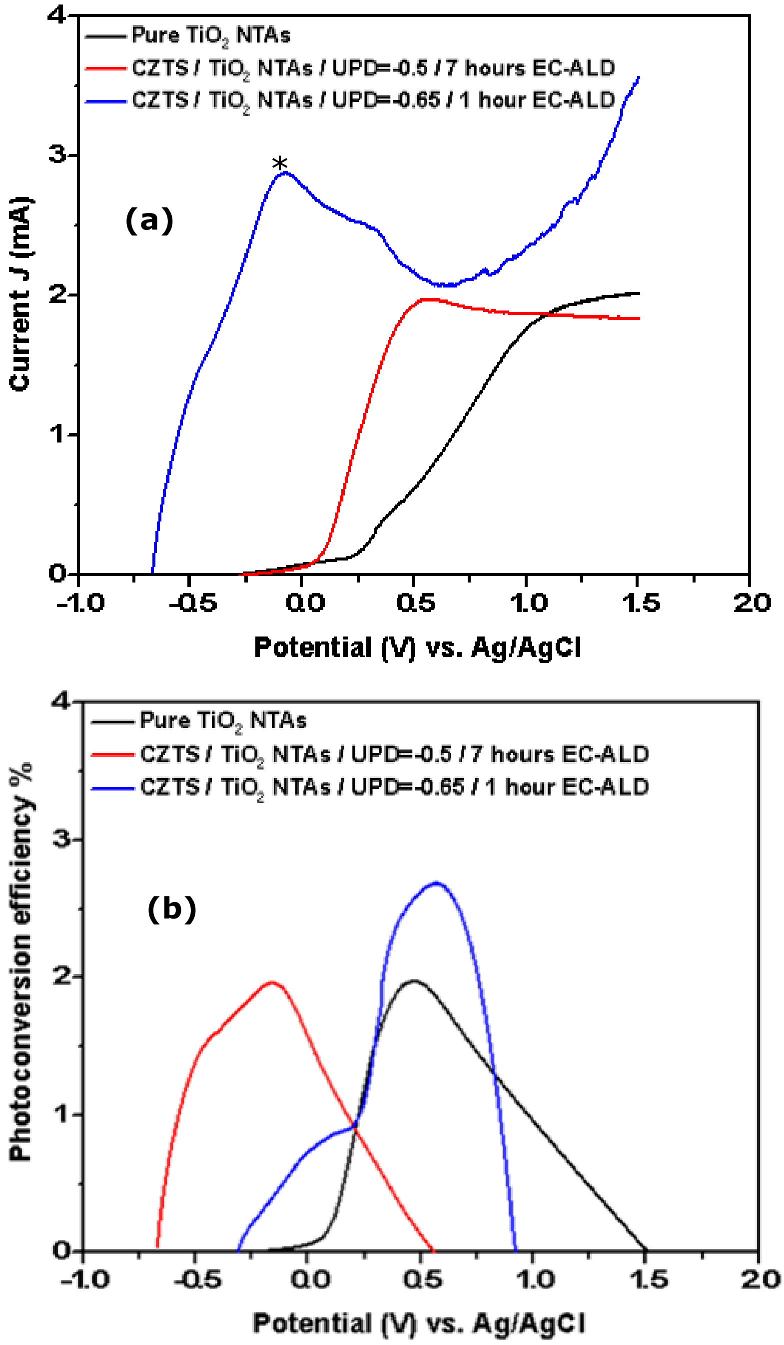

Figure 6-4: (a) Photocurrent density and (b) corresponding photoconversion efficiency of pure TiO_2 NTAs and CZTS/TiO_2 NTAs coaxial heterogeneous structure fabricated from mixture and separate precursor solutions of Cu, Zn and Sn, respectively. The astrike [*] represents the wake of the water splitting at the counter electrode (Pt) under light illumination.

6.3 Summary

In comparison with CZTS/TiO_2 NTAs are produced by EC-ALD from a mixed precursor solution of Cu, Zn and Sn, the novel CZTS/TiO_2 NTAs photoanode was fabricated *via* separate precursor solutions to avoid the influence of the complexing agent (EDTA) that exists in the Cu solution, and also to allow sufficient time for Zn and Sn to bond with TiO_2 NTAs substrate. The results revealed a significant improvement in the morphology of CZTS/TiO_2 NTAs photoanode, the average inner diameter of the tubes was reduced to ca. 95.0 nm, and the coating layer CZTS was estimated to be ca. 8.0 nm.

Furthermore, the photocurrent density achieved ca. 3000.0 μA and the photoconversion efficiency demonstrated an enhancement from 1.10 % to 2.00 % to 2.78 % for pure TiO_2 NTAs, CZTS/TiO_2 NTAs deposited from a mixture of precursor solutions and for CZTS/TiO_2 NTAs deposited from separate precursor solutions, respectively. In terms of crystalline structure, the peaks of CZTS was clearly identified as a single compound and became stronger in comparison with that synthesised from a mixture of precursor solutions.

Chapter 7: Metal Doping

7.1 Metal ion doping of the as-synthesised CZTS/TiO_2 NTAs

Although Cu_2ZnSnS_4 has a narrow bandgap that responds to all visible light range from the solar spectrum, its valence band level is higher than water oxidation (around 0.30 eV, higher than the potential of oxygen evolution). Therefore, it is unable to produce oxygen by water photolysis. Moreover, despite this is an excellent characteristic for higher conduction band level than the redox potential of H^+, which can promote electron injection into the conduction band of TiO_2, it is unable to bring about the overall water splitting due this higher valence band level (Figure 7-1).

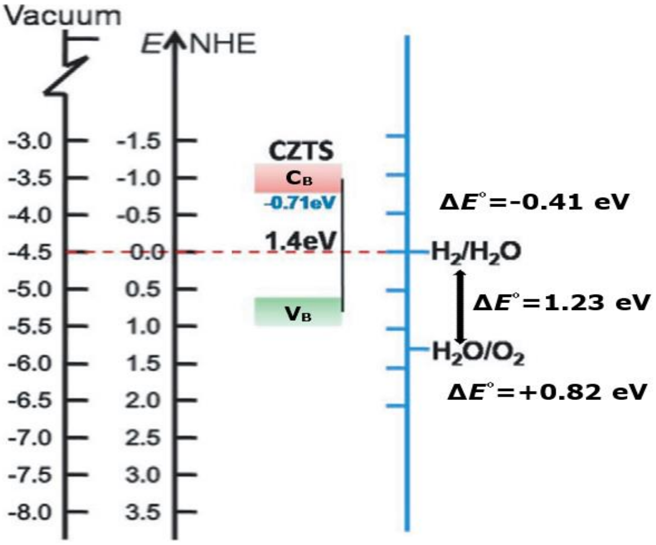

Figure 7-1: Bandgap energy level position of CZTS corresponding to the overall water splitting level. Reprinted from (Huang et al., 2013).

7.2 Doping CZTS/TiO_2 NTAs with Ag and Ge

Ag doping and Ge doping have a different impact on the energy band structure of CZTS. According to the result using First-principles calculation based on density functional theory. Ag substitution for Cu can reduce the valence band. While the position of the conduction band can remain the same. On the other hand, replacing Sn with Ge that is in the identical group of IVA of Periodic Table of Elements can further enhance its conduction band energy level, which is favourable to electron injection into the conduction band of TiO_2 NTAs.

The metal doping can then be used to tailor the bandgap of CZTS, and effectively enhance the photogenerated electron/hole pairs of the photoelectrode CZTS/TiO_2 NTAs. "On the contrary, the photocatalytic activity depends strongly on the exposed crystalline faces (Pan et al., 2012) (Xu et al., 2014). Given that different crystal surfaces have different surface energy levels for the conduction band (CB) and valence band (VB), such differences in the energy levels will drive the electrons and holes to different crystal faces. Doping can effectively modulate the lattice face structures through the substitutional of the metal ions'' (Huang et al., 2016).

7.3 Discussion of the results

7.3.1 Determination of UPD potential of Ag and Ge on pure TiO_2 NTAs and CZTS/TiO_2 NTAs

Before doping the nanofilm CZTS with Ag and Ge, it is crucial to determine a suitable deposition potential (UPD) for Ag and Ge on the CZTS underlayer by employing the CV measurements. These were utilised to determine the UPD potential in order to ensure that the UPD oxidation and reduction peaks of Ag and Ge do not lay in the UPD potential region of CZTS and to check the stability of the CZTS film during the doping process to prevent the decomposition of CZTS from the substrate.

The cyclic voltammograms (CVs) of Ag and Ge on TiO_2 NTAs substrates in solutions contain (a) 0.005 M $AgNO_3$ + 0.200 M trisodium citrate, (pH=8.27) and (b) 0.005 M GeO_2 + 0.200 M trisodium citrate, (pH=8.57) are shown in Figure 7-2-a and b, respectively.

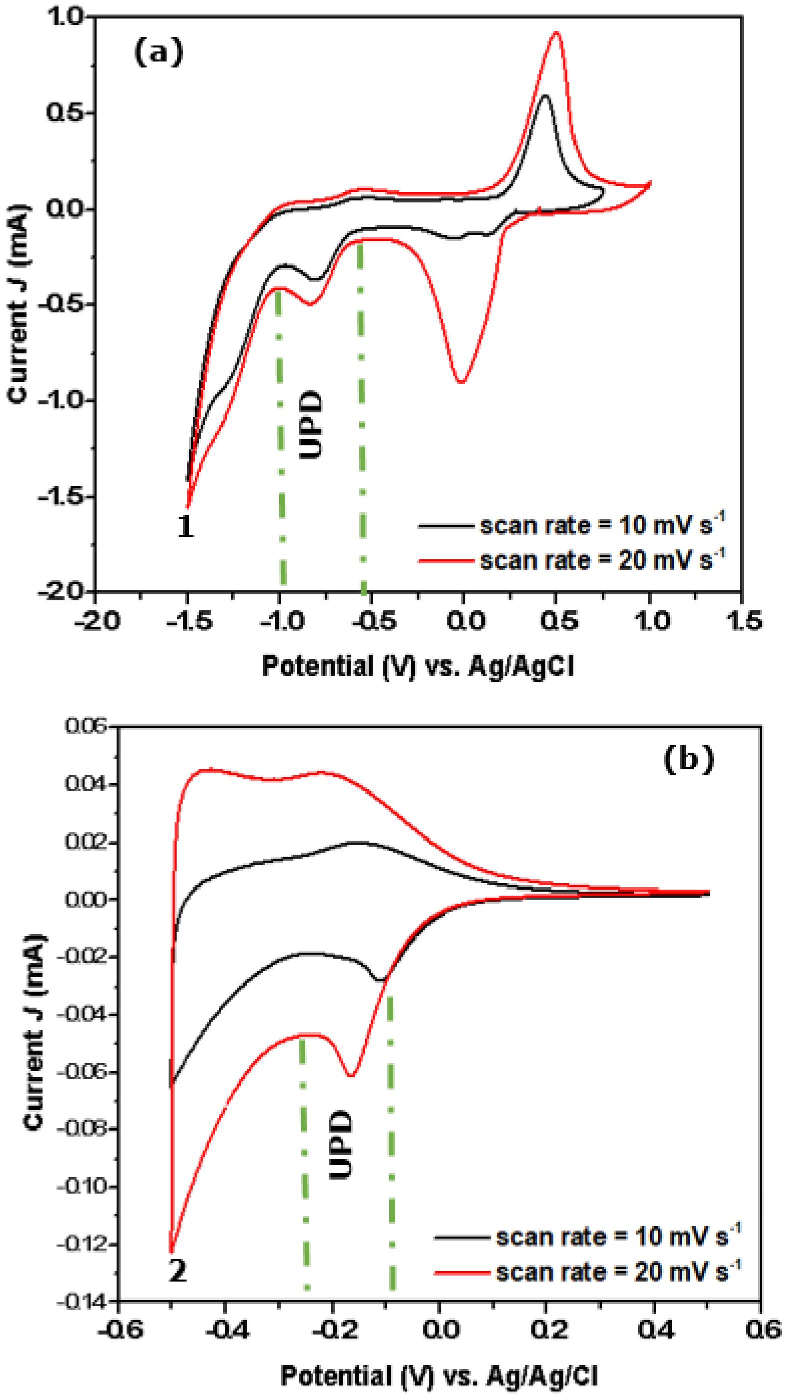

Figure 7-2: Cyclic voltammograms of TiO_2 NTAs electrode recorded at scan rate = 10.0 and 20.0 mV s^{-1} in solutions contain: (a) 0.005 M $AgNO_3$ (pH=8.27) and (b) 0.005 M GeO_2 (pH=8.57). Both solutions include 0.200 M trisodium citrate.

The CVs in Figure 7-2-a exhibit a reduction peak around −0.750 V, which is an indication of the UPD potential of Ag, while the reduction peak 1 represents the bulk potential. Although more than one peak occurred during the measurements, the one before the bulk potential is considered the UPD potential of Ag (according to the fact of the UPD potential of the metal ion is more positive than the bulk potential). Therefore, the doping with Ag onto CZTS/TiO_2 NTAs should be limited between the UPD potential range within the dashed green line to avoid any bulk deposition of Ag.

Regarding the CVs of Ge (Figure 7-2-b), the reduction peak of UPD potential was identified at around −0.160 V, and the bulk potential corresponds to the reduction peak 2. It is also essential to limit the doping of Ge between the UPD potential range (between the dashed green line) to prevent any bulk deposition of Ge at positive potentials.

7.3.2 Effects of the doping time and position on the photoactivity and charge carrier transfer of CZTS/TiO_2 NTAs

Several parameters can affect the metal doping (mentioned in Chapter 2), such as time and position of doping, and dopant concentration. In this study, the microstructure and the photoactivity of the novel CZTS/TiO_2 NTAs photoanode was accurately controlled and manipulated by changing the doping site and time for Ge and Ag individually, in order to optimise the most efficient conditions to enhance the photoelectrocatalytic activity and the charge carrier transfer of CZTS/TiO_2 NTAs photoanode. As a result, this may help with modifying its energy bandgap to achieve a best match for water-splitting. Ag and Ge were loaded in various deposition sites and time, including the inner layer, the intermediate layer, and near the outer layer of the substrate with the corresponding structural formula (Table 7-1). In this table, the deposited thin film was recorded as CZT, referring to the deposition of Cu, Zn, and Sn, before the sulfurization process in the tube furnace. The structural formula for the doping of Ag and Ge will be mentioned as Ag1, 2, 3, and 4 and Ge1, 2, 3, and 4 throughout the upcoming discussion to simplify utilising them within the text. The total deposition time of CZT was 3.0 h (1.0 h for Cu, Zn and Sn separately) during each doping process.

Table 7-1: Structural formula for the doping of silver and germanium with their corresponding deposition sites and time.

Dopant	**Deposition sites**	**Structural formula**
Ag	**outer layer (near the surface)**	**CZT(20 min)/Ag(10 min)/CZT (40 min) = Ag1**
	Intermediate layer	**CZT(30 min)/Ag(10 min)/CZT (30 min) = Ag2**
	Inner layer (near the substrate)	**CZT(40 min)/Ag(10 min)/CZT (20 min) = Ag3**
	Inner layer (near the substrate)	**CZT(50 min)/Ag(10 min)/CZT(10 min) = Ag4**
Ge	**outer layer (near the surface)**	**CZT(20 min)/Ge(10 min)/CZT(40 min) = Ge1**
	Intermediate layer	**CZT(30 min)/Ge(10 min)/CZT(30 min) = Ge2**
	Inner layer (near the substrate)	**CZT(40 min)/Ge (10 min)/CZT(20 min) = Ge3**
	Inner layer (near the substrate)	**CZT(50 min)/Ge (10 min)/CZT(10 min) = Ge4**

Figure 7-3-a and b show the measured photocurrent density of the as-synthesised CZTS/TiO_2 NTAs photoanodes and doped with Ag and Ge in different doping sites and periods. The maximum stable current of ca. 7.5 mA cm^{-2} was achieved from the samples Ag4 and Ge4 among the other examined samples. In contrast, Ag1 and Ge1 exhibited a photocurrent density of ca. 3.5 mA cm^{-2} only.

Interestingly, both Ag and Ge exhibited an approximately similar effect on the photocurrent density performance of the CZTS/TiO_2 NTAs photoanode. This suggests that when the silver injected into the crystal of CZTS is close to the substrate (Ag4 / inner layer), it can reduce the VB level of CZTS near the substrate and promote the photogenerated holes to move towards the outer layer of CZTS. As a result, it will assist in accelerating the reaction with the electrolyte to generate protons in the interface between the CZTS outer layer and electrolyte. In contrast, if the silver doping is injected into the outer layer of CZTS (Ag1), the photogenerated holes from both CZTS inner layer and the TiO_2 substrate could not move into the CZTS outer layer.

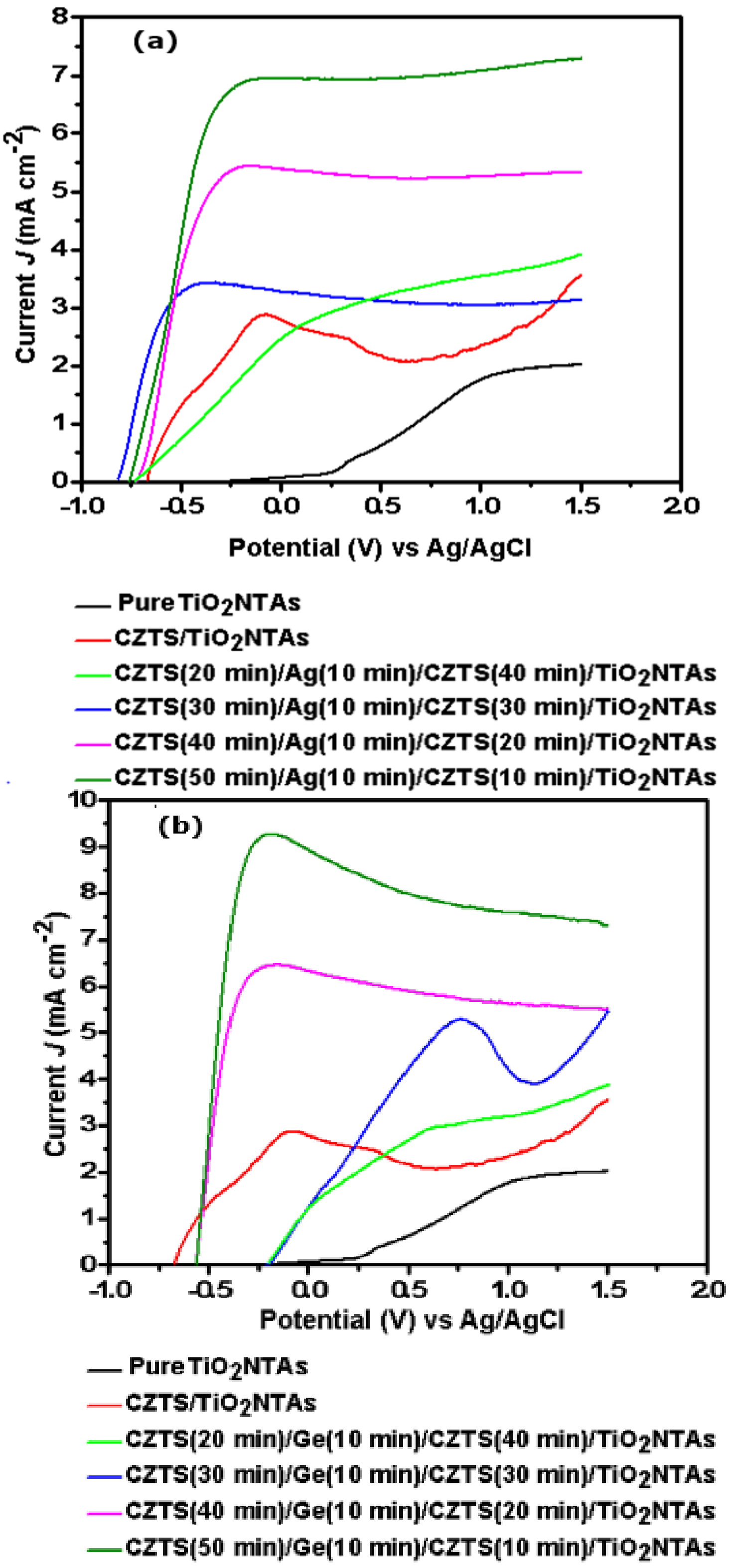

Figure 7-3: Optical response of (a) Ag-doped CZTS/TiO_2 NTAs and (b) Ge-doped CZTS/TiO_2 NTAs with various doping sites and periods, the total deposition time of CZTS was 3.0 h from separate precursor soluions of Cu, Zn and Sn.

The doping played a vital role in hindering the movement of these photogenerated holes, owing to the reduction in their valance band level, which led to prevent transferring electrons from the inner layer (with higher VB) to the outer layer (with lower VB) to facilitate the reaction with the electrolyte. When Ge was loaded at the inner layer, it further assisted in enhancing the conductivity of CZTS/TiO_2 NTAs, this can be attributed to the coherence between the growth layer of Ge and CZTS that helped to modify the CB; consequently, it assisted in transferring the electrons between the interface of TiO_2 NTAs and the doped layer.

7.3.3 Effect of doping on Fermi level position at the semiconductor-metal interface

Figure 7-4-a and b illustrate the schematic formulas for the Ag-doped CZTS/TiO_2 NTAs and Ge-doped CZTS/TiO_2 NTAs photoanodes that fabricated from separate precursor solutions of Cu, Zn and Sn and doped (a) near the substrate and (b) near the surface, respectively. It was proposed that selecting Ag and Ge doping near the inner layer caused the formation of the structure CZTS/Ag/TiO_2 NTAs and CZTS/Ge/TiO_2 NTAs. This doping step provided Ag and Ge on the inner layer where the deposition time was 50.0 m, resulting in a thick layer of CZT; therefore, Ag and Ge will be close to the substrate (Figure 7-4-a).

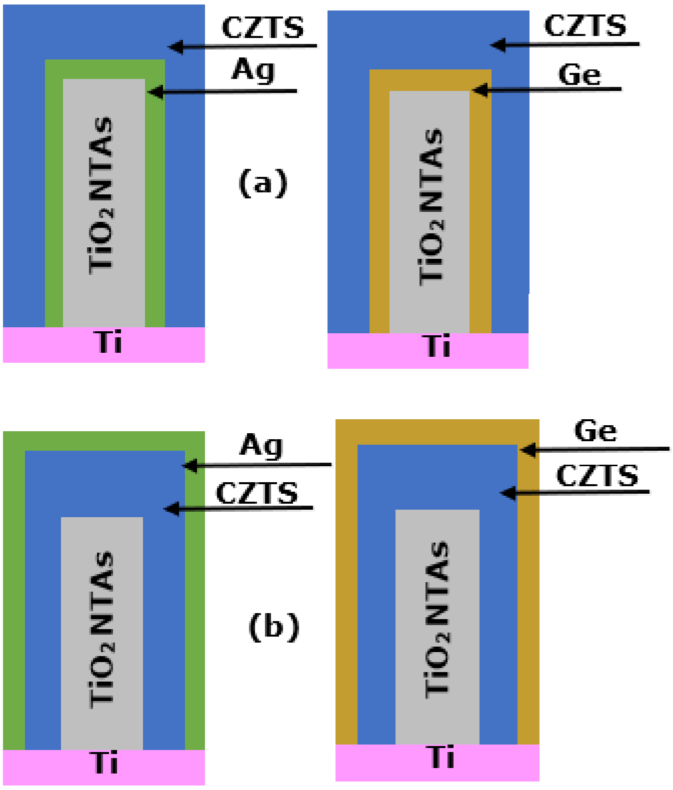

Figure 7-4: Schematic formulas for the Ag-doped CZTS/TiO_2 NTAs and Ge-doped CZTS/TiO_2 NTAs coaxial heterogeneous structure fabricated from separate precursor solutions of Cu, Zn and Sn and doped (a) near the substrate (inner layer) and (b) near the surface (outer layer), respectively.

In contrast, providing Ag and Ge near the outer layer, the formulas Ag/CZTS/TiO_2 NTAs and Ge/CZTS/TiO_2 NTAs will be obtained due to growth of thin layer of CZT as the deposition time was 20.0 m only; hence, Ag and Ge will be close to the surface (Figure 7-4-b). Both formulas were structured during the integral annealing process in the sulfur environment as CAZTS and CZTGS. It was suggested that the energy band alignment controls the charge transfer at the semiconductor-metal interface (Chong et al., 2016, Zur et al., 1983, Lee et al., 2009).

A stepwise structure was constructed for the bandgap edge level of the Ag-doped and Ge-doped CZTS/TiO_2 NTAs photoanodes to describe the Fermi-level alignment between TiO_2 NTAs and CZTS (Figure 7-5-a and b).

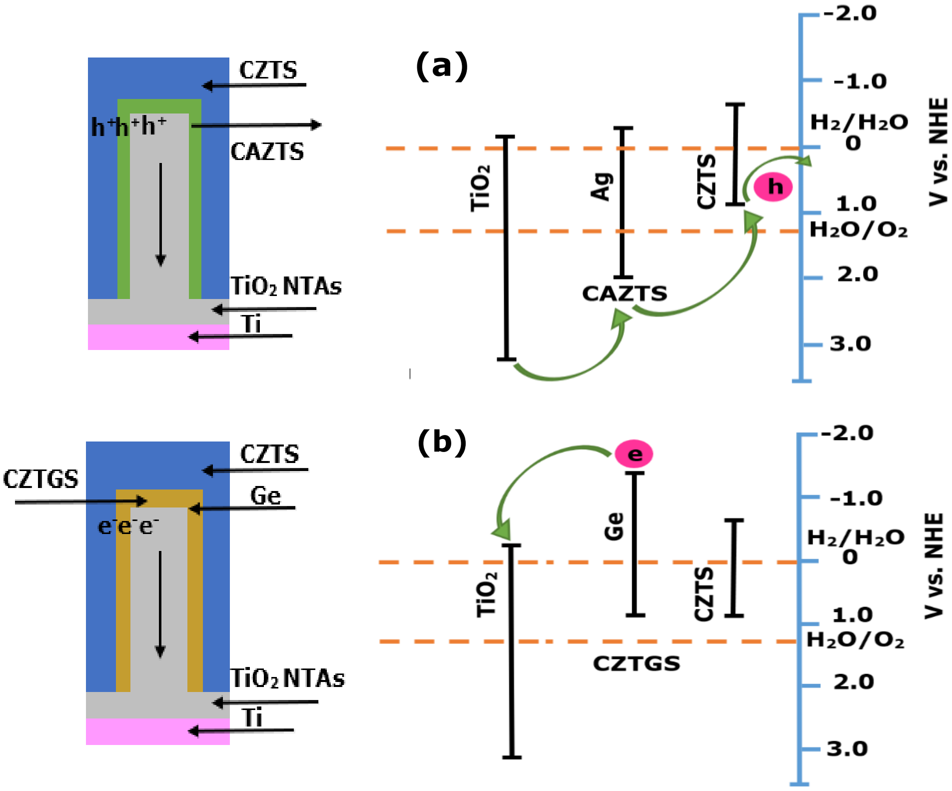

Figure 7-5: Charge transfer mechanism for (a) Ag-doped CZTS/TiO_2 NTAs and (b) Ge-doped CZTS/TiO_2 NTAs photoanodes Reprinted from (Chong et al., 2016).

This structure was proposed based on the ideal fact for a photoanode material that the CB and VB of any photoanode should straddle the electrochemical potentials E0 (H^+/H_2) and E0 (O_2/H_2O) to facilitate the water-splitting process. Therefore, the hydrogen and oxygen evolution reactions can be derived from the generated charge carriers (e^-/h^+) under light irradiation (Walter et al., 2010).

Since the valance band of the CZTS thin film is less positive than the oxygen evolution potential then employing silver (Ag) as a metal dopant had a vital role as a hole scavenger for the photoexcited holes (Figure 7-5-a). These photoexcited holes will then accumulate in the crystal lattice of CZTS.

The as-synthesised and doped CZTS/TiO_2 NTAs photoanodes were exposed to pulsed illumination for 20.0 m (Figure 7-6-a and b). The light was pulsed 1.0 m (on/off illumination) at an applied bias of 0.500 V vs. Ag/AgCl (corresponds to a stable photocurrent density in Figure 7-3-a and b).

The samples that were doped near the inner layer (Ag4 and Ge4) showed approximately a similar photocurrent density of 6.8 mA cm^{-2} in comparison with the samples that doped near the outer layer (Ag1 and Ge1), which exhibited a photocurrent density of 1.8 mA cm^{-2} only. This variation in the photocurrent proves the improvement in their electrical conjunction leads to an enhancement in the light absorption ability of CZTS/TiO_2 NTAs photoanode.

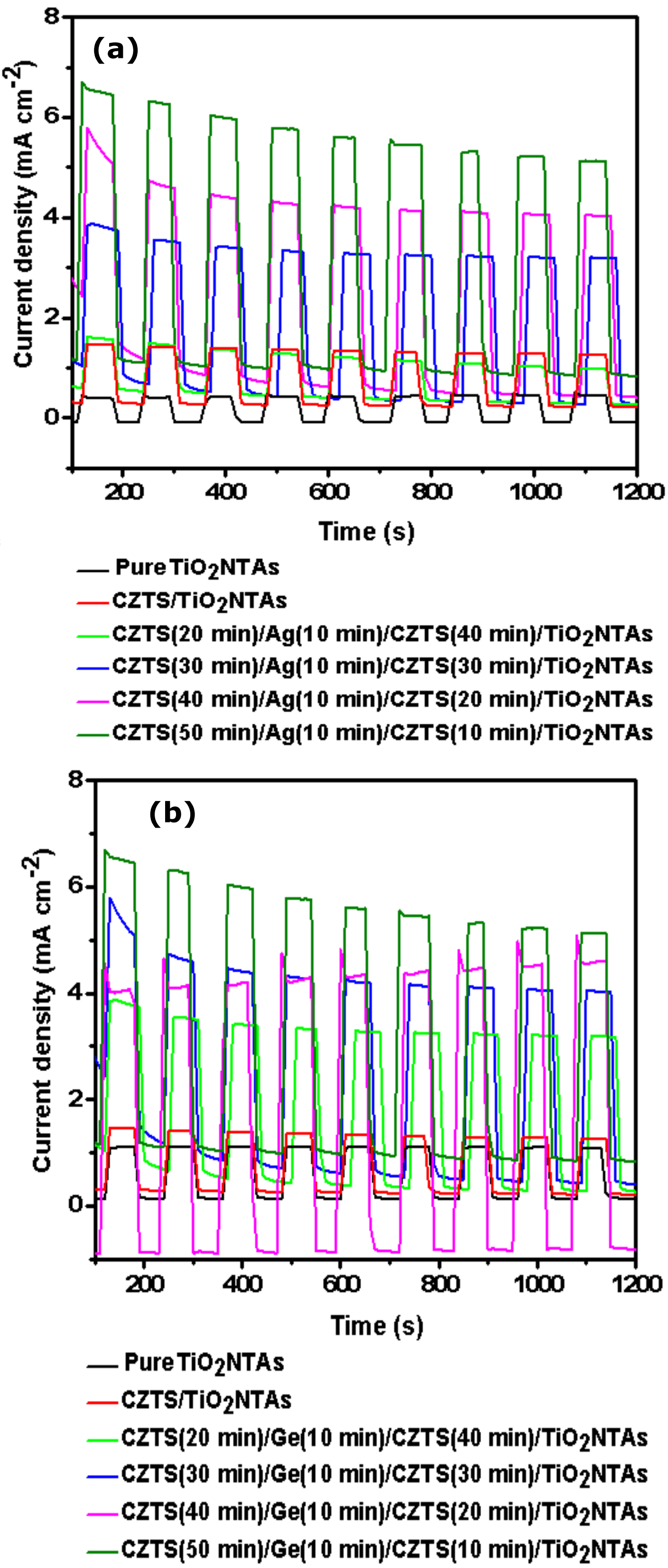

Figure 7-6: Photocurrent response of pulse illumination of Ag-doped and Ge-doped CZTS/TiO_2 NTAs photoanodes fabricated from separate precursor solutions of Cu, Zn and Sn. These measurements compare the photocurrent stability at applied bias of 0.500 V vs Ag/AgCl at various doping sites and periods, respectively.

Figure 7-7-a and b show the XRD patterns of the samples with the structural formula CZTS (50 m) /Ag (10 m) / CZTS (10 m) / TiO_2 NTAs and CZTS (50 m) / Ge (10 m) / CZTS (10 m) / TiO_2 NTAs. In comparison with the previous XRD pattern of the un-doped CZTS/TiO_2 NTAs, the Ag and Ge doped CZTS/TiO_2 NTAs exhibited approximately similar intensity peaks that correspond to CZTS and TiO_2 NTAs.

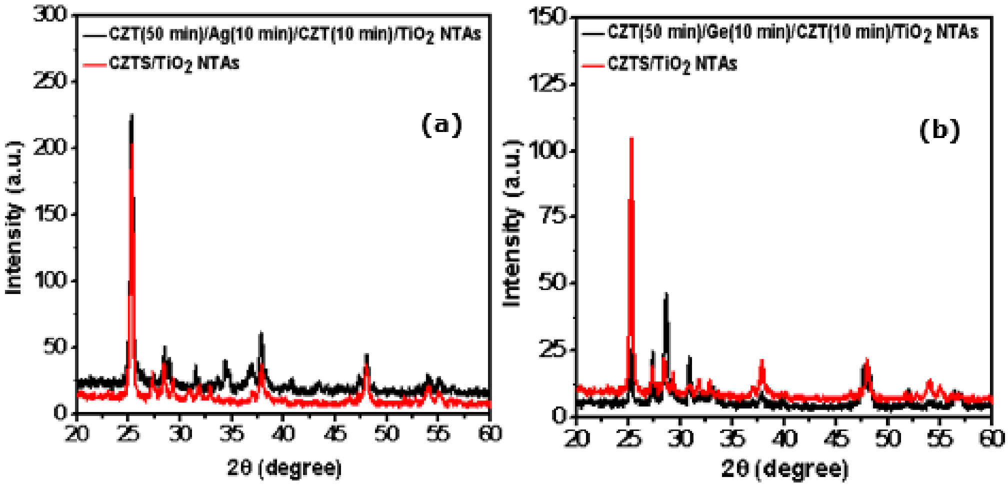

Figure 7-7: XRD diffractograms of (a) Ag-doped CZTS/TiO_2 NTAs and (b) Ge-doped CZTS/TiO_2 NTAs coaxial heterogeneous structure fabricated from separate precursor solutions of Cu, Zn and at UPD potential = –0.650 V for 1.0 h.

This may suggest that the doped metals (Ag and Ge) were uniformly diffused into the crystalline structure of CZTS/TiO_2 NTAs photoanodes resulting in the formation of CZTS / CAZTS /TiO_2 NTAs (Ag substitution with Zn) and CZTS / CZTGS /TiO_2 NTAs (Ge substitution with Sn) during the integral annealing process in sulfur environment.

7.3.4 Photoactivity of the doped CZTS/TiO₂ NTAs photoanode

Figure 7-8-a and b depict the photoconversion efficiency of the Ag-doped CZTS/TiO_2 NTAs and Ge-doped CZTS/TiO_2 NTAs coaxial heterogeneous structure fabricated from separate precursor solutions of Cu, Zn, and Sn and doped at various sites and periods, respectively.

The measurements revealed the highest enhancement in the photoconversion efficiency by 8.62 % and 8.56 % for CZTS (50 m) / Ag (10 m) / CZTS (10 m) / TiO_2 NTAs and CZTS (50 m) / Ge (10 m) / CZTS (10 m) / TiO_2 NTAs, respectively.

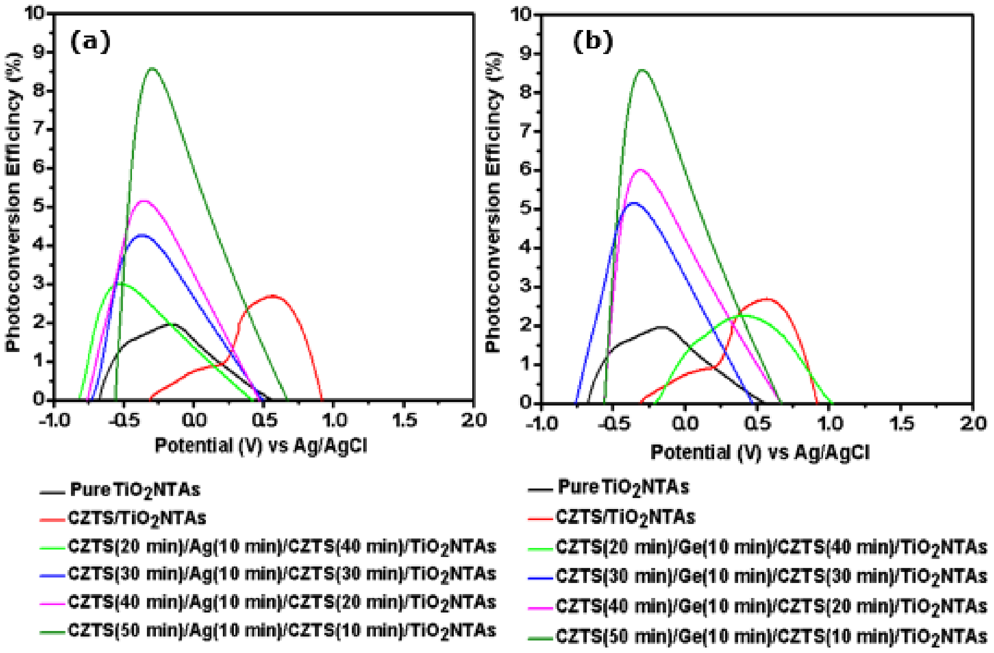

Figure 7-8: Photoconversion efficiency of Ag-doped CZTS/TiO_2 NTAs and Ge-doped CZTS/TiO_2 NTAs coaxial heterogeneous structure fabricated from separate precursor solutions of Cu, Zn, and Sn and doped at various sites and periods.

The UV-Vis measurements of the Ag-doped CZTS/TiO_2 NTAs (Figure 7-9-a-d) and Ge-doped CZTS/TiO_2 NTAs (Figure 7-9-e-h) exhibited a significant improvement in the photoactivity (Appendix B). A red shift towards the visible region between 550.0 to 700.0 nm was observed from the Ag-doped CZTS/TiO_2 NTAs photoanodes. This behaviour was also observed for the Ge-doped CZTS/TiO_2 NTAs samples that showed a red shift between 580.0 to 750.0 nm. Certainly, this indicates that the bandgap energy of these photoanodes had significantly narrowed.

The bandgap energy drastically reduced from 2.2 eV (Figure 7-9-a, Ag1) to 1.88 eV Figure 7-9-d, Ag4), and for the samples that were doped with Ge at the outer, intermediate and inner sites their bandgaps were also significantly narrowed from 2.14 eV (Figure 7-9-e, Ge1) to 1.86 eV (Figure 7-9-h, Ge4).

The modification in the optical and electrical properties of CZTS/TiO_2 NTAs photoanodes seems to be due to the generation and separation of electron-hole pairs in the photoelectrochemical reactions. These performances are key factors in transferring the charge carriers during the photocatalytic process, resulting in an improvement in the photocatalytic activity of the CZTS/TiO_2 NTAs after the doping with Ag and Ge at the inner layer (near the substrate).

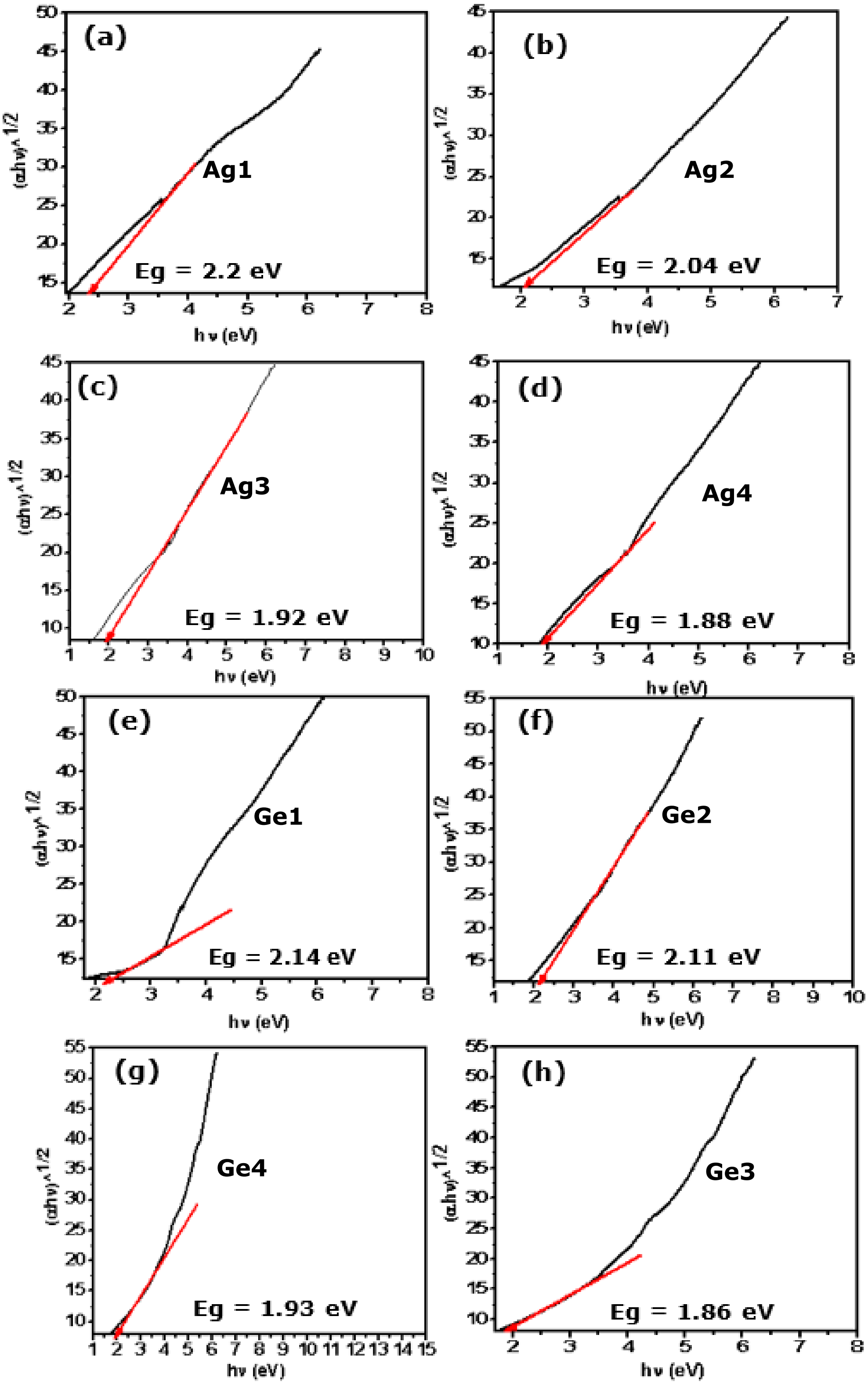

Figure 7-9: The data of UV-Vis absorbance spectra of Ag-doped CZTS/TiO_2 NTAs (a-d) and Ge-doped CZTS/TiO_2 NTAs (e-h) transformed using the Kubelka–Munk function for the extraction of the optical bandgap energy (Eg) (red arrows).

To conclude, CZTS/Ge/TiO_2 NTAs and CZTS/Ag/TiO_2 NTAs are a more suitable strategy for electron injection and hole recovery in the fabrication of the novel CZTS/TiO_2 NTAs photoelectrode. This is because the obvious improvement in the electrical and optical performance of the coaxial heterogeneous CZTS/TiO_2 NTAs photoanode. Table 7-2 summarises the photoconversion efficiencies, absorbance, and bandgap energy of the as-synthesised CZTS/TiO_2 NTAs photoanodes before and after doping with Ag and Ge.

Table 7-2: Values of photoconversion efficiencies, absorbance, and bandgap energy of the as-synthesised CZTS/TiO_2 NTAs photoanodes before and after doping with Ag and Ge.

CZTS/TiO_2 NTAs	**Photoconversion efficiency η (%)**	**Absorbance α (a.u.)**	**Bandgap energy Eg (eV)**
Undoped	3.00	1.40	2.33
Ag-inner doping near TiO_2 NTAs	3.02	1.42	2.20
Ag- inner doping near TiO_2 NTAs	4.30	1.46	2.14
Ag-intermediate doping	5.19	1.53	1.93
Ag-outer doping	8.56	1.69	1.86
CZTS/TiO_2 NTAs	**Photoconversion efficiency η (%)**	**Absorbance α (a.u.)**	**Bandgap energy Eg (eV)**
Undoped	3.00	1.40	2.33
Ge-inner doping near TiO_2 NTAs	3.10	1.65	2.14
Ge- inner doping near TiO_2 NTAs	5.14	1.68	2.11
Ge-intermediate doping	5.97	1.71	1.90
Ge-outer doping near TiO_2 NTAs	8.62	1.77	1.88

7.3.5 FEG-SEM characterisation of the doped CZTS/TiO₂ NTAs

Figure 7-10-a, b, c, and d show the fairly uniform images for the top surface FEG-SEM of pure TiO_2 NTAs, the as-synthesised $CZTS/TiO_2$ NTAs, Ag-doped $CZTS/TiO_2$ NTAs and Ge-doped $CZTS/TiO_2$ NTAs at the inner layer near the substrate, respectively. These photoanodes were synthesised from separate precursor solutions of Cu, Zn and Sn at UPD potential = −0.650 V for 1.0 h.

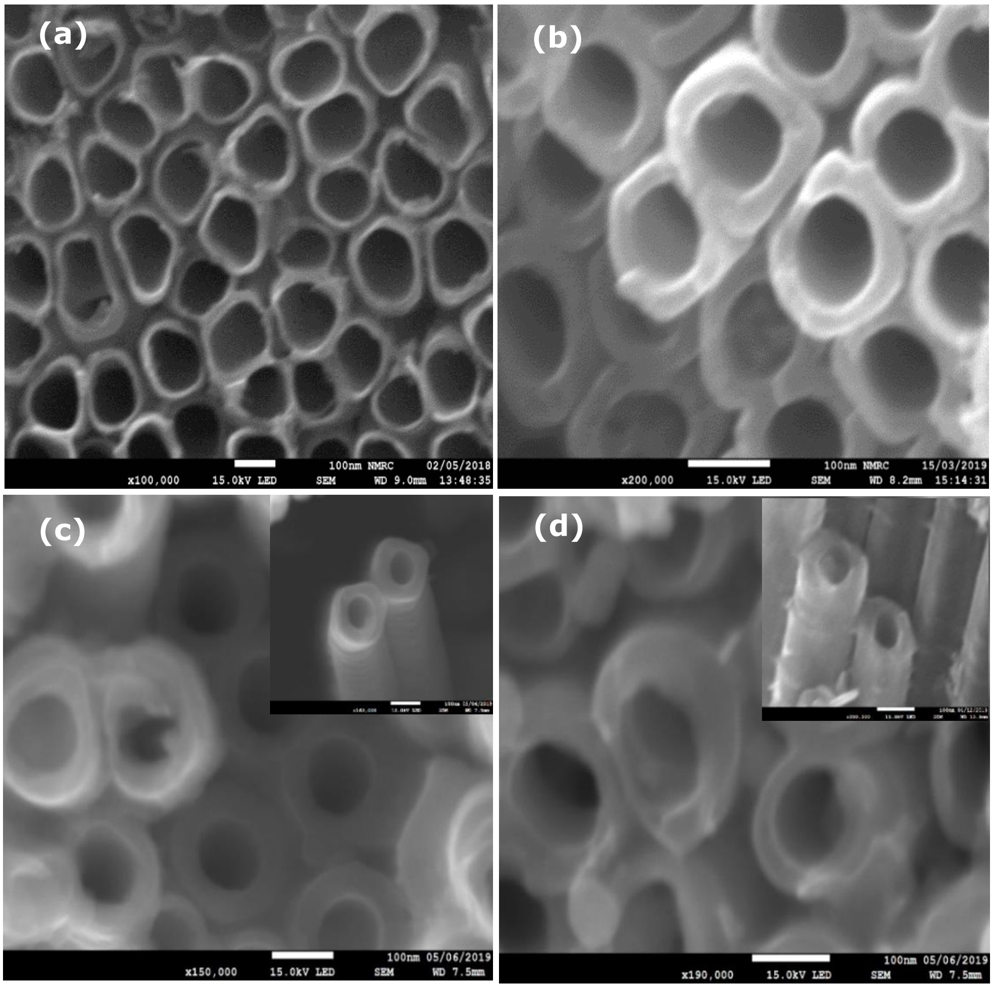

Figure 7-10: Top surface FEG-SEM micrographs of (a) pure TiO_2 NTAs, (b) $CZTS/TiO_2$ NTAs, (c) Ag-doped $CZTS/TiO_2$ NTAs and (d) Ge-doped $CZTS/TiO_2$ NTAs.

It can clearly distinguish the modification on the nanotube arrays after the coating with CZTS, which was followed by the doping with Ag and Ge. It indicated that the presence of Ag and Ge does not affect the morphology of CZTS/TiO_2 NTAs, with only a further thickening in the wall of the tubes estimated to be ca. 10.0 nm (+/-5.0 nm), and the average inner diameter was ranged from 85.0 to 90.0 nm.

Furthermore, a cross-section micrograph of TiO_2 NTAs (Figure 7-11-a, b, and c) confirms the well-ordered tubular structure of the nanotubes after the sensitisation with CZTS and the doping with Ge near the substrate (inner layer doping). Figure 7-11-b and c revealed that both the inside and outside surfaces of the nanotube walls were uniformly coated after the sensitisation and the doping with CZTS and Ge (white arrow in Figure 7-11-c), this indicates formation of a cascade of multiple heterogeneous junctions in a coaxial manner onto TiO_2 NTAs.

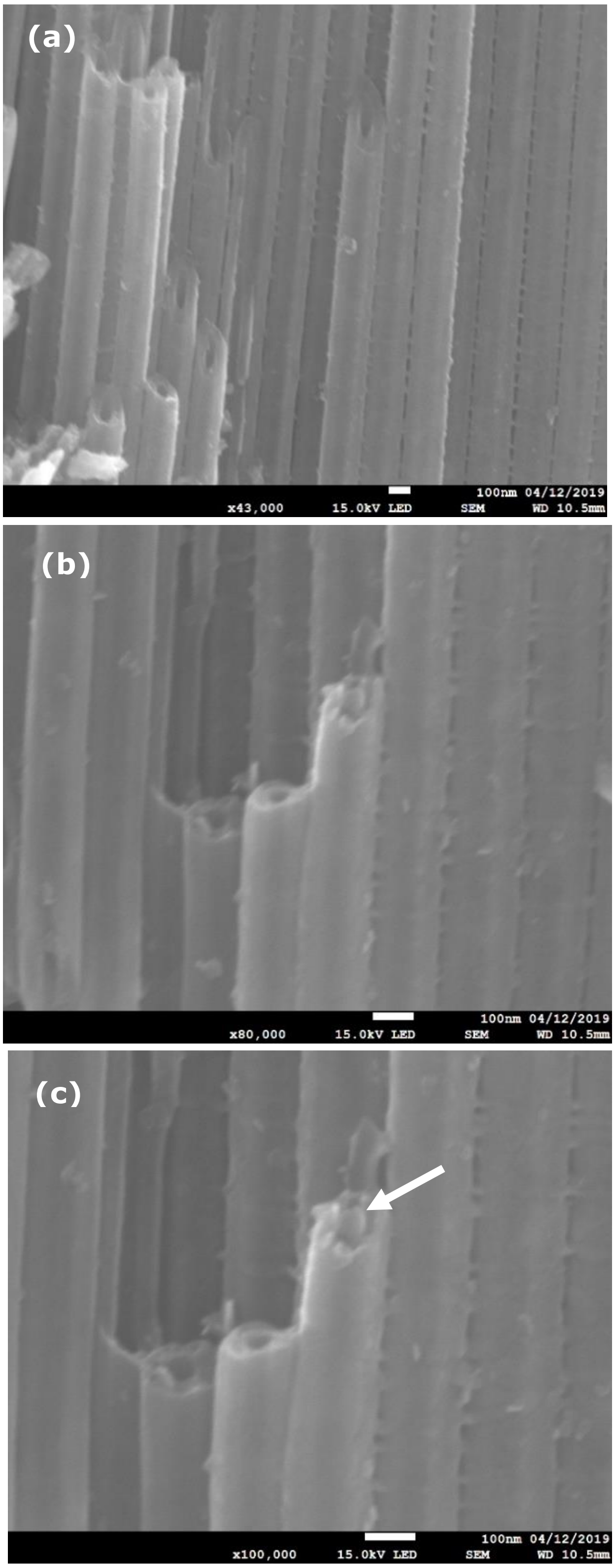

Figure 7-11: Cross-section area FEG-SEM micrographs of Ge-doped CZTS/TiO$_2$ NTAs with different magnifications (a) at X43,000.0; (b) at X80,000.0 and (c) at X100,000.0. White arrow in (c) shows the uniform coating inside the tube, which does not damaged after doping with Ge.

7.4 Conclusions

Comprehensive studied were conducted to investigate the influence of metal doping with Ag and Ge on the optical and electrical properties of the as-synthesised and doped CZTS/TiO_2 NTAs photoanode. The results revealed that:

1. The doping process of Ag and Ge should be performed at the identified deposition potentials (UPD) of –0.750 V and –0.160 V, respectively. This suggest that avoiding the bulk potentials of Ag (–1.500 V) and Ge (–0.500 V) assists in maintaining the well-organised coaxial heterogeneous structure of CZTS/TiO_2 NTAs.
2. The samples that doped near the inner layer including CZTS (50 m) / Ag (10 m) / CZTS (10 m) / TiO_2 NTAs and CZTS (50 m) / Ge (10 m) / CZTS (10 m) / TiO_2 NTAs exhibited a maximum stable photocurrent density of ca. 7.5 mA cm^{-2}. The metal doping near the inner layer was more effective than near the outer or the middle layer on the performance of CZTS/TiO_2 NTAs.
3. The bandgap of Ag-doped CZTS/TiO_2 NTAs and Ge-doped CZTS/ TiO_2 NTAs were significantly reduced to values of 1.88 and 1.86 eV. This suggested that the optical performance of CZTS/TiO_2 NTAs was successfully improved aided by the doping process.

4. The morphology of the nanotubes was maintained after the sensitisation and the doping with Ag and Ge.
5. A further thickening of the wall of the tubes estimated to be ca. 20.0 nm (+/-5.0 nm) and the inner diameter was ranging from 85.0 to 90.0 nm after the sensitisation with CZTS followed by the metal doping with Ag and Ge.
6. Both inside and outside surfaces of the nanotube walls were uniformly covered after the sensitisation and the doping with CZTS and Ge.

Chapter 8: Conclusion and future works

8.1 Conclusion

This study presents the first efforts to fabricate the coaxial heterogeneous CZTS/TiO_2 NTAs photoanode by employing the simultaneous underpotential deposition of multiple elements onto TiO_2 NTAs substrates using the EC-ALD technique to form sensitiser of kesterite (Cu_2ZnSnS_4). The ultimate target was to enhance the photoconversion efficiency and narrow the bandgap of the substrate TiO_2 NTAs arrays to make them as effective as possible for the splitting of water. Synthesising a well-organised substrate (TiO_2 NTAs arrays) was the key factor in achieving a homogeneous deposition.

For the preparation of TiO_2 NTAs, for the first time, it was confirmed that drying the as-prepared TiO_2 NTAs by acetonitrile vacuum can enhance the photocurrent density by 2.5 times compared to the TiO_2 NTAs that dried naturally in the air. This is due to the improved cohesion with the metal substrate, which reduced the defects between the TiO_2 NTAs and the metal and caused an enhancement of the conductivity of the TiO_2 NTAs. The nanotubes dehydrated from acetonitrile in vacuum showed a resistance of 10.0 Ω less than the resistance of the nanotubes dehydrated naturally. In the same concept, the pulse illumination results revealed a stable photocurrent density with an increment up to 0.0058 A in contrast with the sample dehydrated naturally in the air which exhibited 0.0038 A.

Prior to this research, no recorded studies regarding the deposition of the thin film Cu_2ZnSnS_4 on TiO_2 NTAs by electrochemical atomic layer deposition (EC-ALD) were reported. By precisely adjusting the UPD potential of the deposition bath to –0.650 V, and reducing the pH value to 4.7 and maintaining EDTA concentration of Cu precursor solution at 0.3 M, the expected stoichiometric ratio of 2:1:1:4 of Cu_2ZnSnS_4 was simultaneously obtained. This observation suggests that adjusting the deposition parameters is a crucial step for a successful electrodeposition. Although previous studies (Zhu et al., 2010, Zhang et al., 2009) investigated the effect of deposition parameters such as EDTA concentration and UPD potential, no studies are recorded with quaternary sensitiser on TiO_2 NTAs using the UPD route and the results obtained here open up this field. The bandgap of the novel CZTS/TiO_2 NTAs photoanode was significantly narrowed from 3.10 eV for the pure TiO_2 NTAs to 2.43 eV and accompanied by a red shift from 400.0 nm for pure nanotubes to 510.0 nm for CZTS/TiO_2 NTAs. Reducing the bandgap assists with enhancing the conductivity and the charge carrier transfer of the novel compound CZTS/TiO_2 NTAs photoanode. An enhancement in the photocurrent density achieved also results in enhancement in water oxidation, with wider implications for the development of improved hydrogen production systems.

After the sensitisation by CZTS, the photocatalytic properties of TiO_2 NTAs were synergistically affected, giving a maximum hydrogen generation rate of 49.0 mL h^{-1} cm^{-2} and achieving an enhancement in photoconversion efficiency from 1.1 % to 2.0. It was found that synthesising the novel CZTS/TiO_2 NTAs *via* separate precursor solutions for 1.0 h at co-deposition UPD potential = –0.650 V, significantly improved the morphology and the photoconversion efficiency of CZTS/TiO_2 NTAs by maintaining unclogged pore mouths of the tubes. Employing this route in fabricating quaternary compounds would be essential in case one of the metals may dominate the others due to its affinity towards the substrate. Therefore, the approach in this thesis is the recommended route to control and manage the variation in pH value and EDTA concentration to deposit multiple elements and avoid bulk deposition.

For further conductivity enhancement, the novel CZTS/TiO_2 NTAs photoanode required metal doping with metal dopants such as Ag and Ge due to the high level of valence band of CZTS relative to the potential of oxygen evolution, and as a result, which was unable to straddle the overall water splitting. The UPD potential of Ag and Ge should be limited at –0.750 V and –0.160 V, respectively, to avoid any bulk deposition of Ag or Ge, which may affect the tube morphology by reducing the pore mouth causing suppression in the photoefficiency, consequently dropping the water splitting ability.

It was emphasised that doping the photoanode CZTS/TiO_2 NTAs near the inner layer exhibited a maximum stable photocurrent density of ca. 7.5 mA cm^{-2} and showed a significant enhancement in the photocatalytic performance. The bandgap was also drastically narrowed to a value of 1.88 and 1.86 eV, respectively, with a red shift of ca. 700.0 nm. Doping with metal ions can facilitate the enhancement of the photoefficiency of generated e^-/h^+ pairs and effectively modulate the lattice structure of the substrate.

A further thickening in the wall of the tubes was estimated to be 10.0 nm (+/-5 nm), and the inner diameter was ranging from 85.0 to 90.0 nm after the sensitisation with CZTS followed by the metal doping with Ag and Ge. It can suggest that adjusting the time and the position of the dopant is an efficient way to maintain the well organised structure of the nanotubes and prevent peeling off the coating layer.

A cascade of multiple heterogeneous junctions in a coaxial manner was formed onto TiO_2 NTAs after the sensitisation and the doping with CZTS and Ge (the surface of the walls of the nanotubes was uniformly and homogeneously coated). Diverse advantages were gained from the metal doping involving a good cohesion between CZTS and the doped metals (Ge and Ag), the transporting of the charge carrier that arises from the alignment in the stepwise band edge level of the produced photoanode. In addition to a significant enhancement in light-harvesting ability. The main aim from doping the novel

$CZTS/TiO_2$ NTAs was applying EC-ALD route and control the deposition and the doping of multiple elements.

8.2 Future works

The simultaneous underpotential deposition of multiple elements using the modified EC-ALD route still requires further investigation using the UPD mechanism. Based on the author's experience with the UPD mechanism, there are also some recommendations for future studies by fellow researchers:

- Studying the influence of annealing temperature could be efficient parameter to improve the crystallinity of the fabricated novel photoanode $CZTS/TiO_2$ NTAs. Thus, to improve the cohesion between CZTS and TiO_2 NTAs in future, a scan of temperatures from 250-600 ℃ would be helpful in enhancing the photocatalytic performance and the charge carrier transfer of the photoanode. Consistent with Tao et al. (2014), they indicated that CZTS thin films are fully sulfurized with Cu-poor and Zn-rich composition (Kesterite) at 560 ℃, and the bandgap was close to the optimum value of 1.5 eV in CZTS-based solar cells An AZO/I, which supports that a further investigation into the temperature effect on the novel compound $CZTS/TiO_2$ NTAs is warranted.

- In order to utilise the novel photoanode CZTS/TiO_2 NTAs in energy-related applications, especially water splitting to produce the green fuel H_2 as an alternative to the fossil fuel, scaling-up of the substrate and the amounts of materials required needs to be conducted for the PEC cell. Future investigations should focus on an alternative cathode to the expensive Pt cathode to be used in a scaled-up PEC cell, as the recent global industries are moving towards employing affordable materials. Investigating a new cathode was also recommended by Kim (2014), and it is never been examined up to date. Thus, it would be necessary to investigate affordable cathode for PEC cells.
- Further experiments could employ a broader range of metal ions for the doping process as alternatives to Ag, such as Pb^{2+}, Rh^{3+}, Bi^{3+} which would allow the full dopant space to be explored. Chen et al. (2010b) suggested that this approach would be helpful for higher VB of CZTS to straddle the oxygen evolution level. In contrast, enhancing the photoactivity towards H_2 evolution requires creating an acceptor level below the CB of CZTS by employing alternative to Ge such as Ta^{5+} Sb^{5+}, Nb^{5+}, Rh^{3+}, La^{3+}, Rh^{5+}, Cr^{3+} as indicated by (Li et al., 2015). This could shed more light on improving the photoactivity of CZTS/TiO_2 NTAs photoanode. Clearly there is a balance to be reached. Comparing the influence of various

dopants (acceptors and doners) are poorly explored in the literature. The novel CZTS/TiO_2 NTAs is expected to exhibit different or further photoactivity improvement in comparison with Ag and Ge, and this necessitates a structured approach.

- To summarise, TiO_2 NTAs are *N*-type semiconductors with improvement in electrical and optical properties relative to existing materials, especially reducing the bandgap from 3.10 to 2.43 to 1.88 eV after it merged with *P*-type semiconductor (CZTS), and doped with Ag and Ge, respectively. Therefore, employing the composite CZTS/TiO_2 NTAs would be a valuable approach in areas such as solar cell manufacturing or in the production of hydrogen as a fossil fuel alternative, due to the narrow bandgap of CZTS (1.5 eV) in the visible region, which provided enhancement in the photoconversion efficiency of TiO_2 NTAs (1.1% of pure TiO_2 NTAs to 2.78% and 8.62% after the deposition and doping, respectively).

EC-ALD is highly recommended as a suitable approach in synthesising multijunction semiconductor materials for the coating of highly structured substrates; and since EC-ALD is cost effective and can be applied at room temperature (Zhang et al., 2009), and it provides tuneable route in terms of experiment time and scope for scale up (Tiznado et al., 2008).

Employing the multiple elements sensitiser CZTS was relatively challenging and productive as it enhanced the photocurrent density of TiO_2 NTAs from 1.8 mA.cm^{-2} to 7.5 mA.cm^{-2} after only 1 hour deposition and metal doping. These impacts are globally applicable as they meet the green and economic industrial requirements if environmentally friendly materials employed.

Appendices

Appendix A7

Electrochemical atomic layer deposition (EC-ALD) process of Cu_2ZnSnS_4 onto TiO_2 NTAs with the experimental parameters and corresponding EDX results.

Table A 1

EC-ALD parameters	1			2			3		
	Cu	Zn	Sn	Cu	Zn	Sn	Cu	Zn	Sn
Concentration (M)	0.02	0.2	0.01	0.02	0.2	0.01	0.02	0.2	0.01
Trisodium citrate $Na_3C_6H_5O_7$ Concentration (M)	0.2			0.2			0.2		
pH value of the individual solution	6.4	6.5	6.8	6.4	6.5	6.8	6.4	6.5	6.8
deposition potential UPD (V)	-0.2			-0.5			-0.6		
EDTA concentration (M)	free	0.3	free	free	0.3	free	free	0.3	free
pH value of the deposition bath	6.51			6.24			6.34		
Deposition time (hr)	7			7			7		
EDX results (atom%)	Cu	1.25		Cu	0.04		Cu	0.07	
	Zn	0.00		Zn	0.14		Zn	0.03	
	Sn	0.00		Sn	0.06		Sn	0.14	
	S	0.49		S	0.01		S	0.06	
	Ti	19.20		Ti	24.52		Ti	22.86	
	O	79.06		O	75.24		O	76.85	

Table A 2

EC-ALD parameters	4			5			6		
	Cu	Zn	Sn	Cu	Zn	Sn	Cu	Zn	Sn
Concentration (M)	0.02	0.2	0.01	0.02	0.4	0.02	0.01	0.4	0.02
Trisodium citrate $Na_3C_6H_5O_7$ Concentration (M)	0.2			0.2			0.2		
pH value of the individual solution	6.4	6.5	6.78	6.42	6.2	6.28	6.51	6.5	6.5
Deposition potential UPD (V)	-0.7			-0.65			-0.65		
EDTA concentration (M)	free	0.3	free	free	0.3	free	0.3	0.3	free
pH value of the deposition bath	6.34			6.88			6.03		
Deposition time (hr)	7			7			7		
EDX results (atom%)	Cu	35.35		Cu	39.14		Cu	2.11	
	Zn	0.06		Zn	1.16		Zn	0.03	
	Sn	0.03		Sn	1.14		Sn	0.08	
	S	23.76		S	12.31		S	2049	
	Ti	11.09		Ti	28.28		Ti	28.50	
	O	29.72		O	17.98		O	66.78	

Table A 3

EC-ALD parameters	7			8			9		
	Cu	Zn	Sn	Cu	Zn	Sn	Cu	Zn	Sn
Concentration (M)	0.02	0.4	0.02	0.01	0.4	0.02	0.02	0.4	0.02
Trisodium citrate $Na_3C_6H_5O_7$ Concentration (M)	0.2			0.2			0.2		
pH value of the individual solution	6.52	6.5	6.5	6.25	6.3	6.31	6.35	6.31	6.4
Deposition potential UPD (V)	-0.6			-0.65			-0.65		
EDTA concentration (M)	0.3	0.3	free	0.3	0.3	free	0.3	0.3	free
pH value of the deposition bath	6.5			6.1			6.1		
Deposition time (hr)	7			7			7		
EDX results (atom%)	Cu	8.69		Cu	0.87		Cu	9.16	
	Zn	0.02		Zn	0.01		Zn	0.28	
	Sn	0.24		Sn	0.05		Sn	0.17	
	S	5.14		S	0.83		S	6	
	Ti	20.43		Ti	28.82		Ti	24.06	
	O	66.58		O	70.29		O	60.97	

Table A 4

EC-ALD parameters	10			11			12		
	Cu	Zn	Sn	Cu	Zn	Sn	Cu	Zn	Sn
Concentration (M)	0.02	0.4	0.02	0.01	0.4	0.02	0.01	0.4	0.02
Trisodium citrate $Na_3C_6H_5O_7$ Concentration (M)	0.2			0.2			0.2		
pH value of the individual solution	6.5	6.62	6.42	6.5	6.52	6.34	6.63	3.46	6.28
Deposition potential UPD (V)	-0.65			-0.65			-0.65		
EDTA concentration (M)	0.1	0.3	free	free	0.3	free	0.3	0.1	free
pH value of the deposition bath	6.05			6.45			4.81		
Deposition time (hr)	7			7			7		
EDX results (atom%)	Cu	63.34		Cu	7.07		Cu	42.60	
	Zn	0.15		Zn	0.23		Zn	0.34	
	Sn	6.27		Sn	0.78		Sn	0.29	
	S	20.08		S	4.66		S	23.06	
	Ti	1.99		Ti	20.16		Ti	9.93	
	O	6.81		O	66.19		O	23.8	

Table A 5

EC-ALD parameters	13			14			15		
	Cu	Zn	Sn	Cu	Zn	Sn	Cu	Zn	Sn
Concentration (M)	0.02	0.4	0.02	0.005	0.4	0.02	0.005	0.4	0.02
Trisodium citrate $Na_3C_6H_5O_7$ Concentration (M)	0.2			0.2			0.2		
pH value of the individual solution	6.42	6.24	6.28	6.35	6.48	6.8	6.35	6.41	6.8
Deposition potential UPD (V)	-0.65			-0.65			-0.65		
EDTA concentration (M)	free	0.3	free	free	0.4	free	0.05	0.3	free
pH value of the deposition bath	6.88			6.55			6.58		
Deposition time (hr)	7			7			7		
EDX results (atom%)	Cu	19.14		Cu	14		Cu	4.12	
	Zn	1.86		Zn	0.11		Zn	0.13	
	Sn	3.92		Sn	4.03		Sn	0.18	
	S	11.50		S	14.58		S	2.65	
	Ti	0.08		Ti	0.74		Ti	26.79	
	O	64.25		O	66.96		O	66.14	

Table A 6

EC-ALD parameters	16			17			18		
	Cu	Zn	Sn	Cu	Zn	Sn	Cu	Zn	Sn
Concentration (M)	0.005	0.4	0.02	0.005	0.4	0.02	0.005	0.4	0.04
Trisodium citrate $Na_3C_6H_5O_7$ Concentration (M)	0.2			0.2			0.2		
pH value of the individual solution	6.35	4.01	6.42	7	4.89	6.43	6.07	4.92	6.02
Deposition potential UPD (V)	-0.65			-0.65			-0.65		
EDTA concentration (M)	0.05	0.05	free	0.3	free	free	0.2	free	free
pH value of the deposition bath	5.05			5.07			6.57		
Deposition time (hr)	7			7			7		
EDX results (atom%)	Cu	28.4		Cu	16.58		Cu	8.74	
	Zn	0.51		Zn	0.13		Zn	0.13	
	Sn	0.05		Sn	5.14		Sn	1.15	
	S	10.17		S	17.36		S	4.64	
	Ti	22.9		Ti	24.42		Ti	24.94	
	O	37.8		O	38.54		O	60.41	

Table A 7

EC-ALD parameters	19			20			21		
	Cu	Zn	Sn	Cu	Zn	Sn	Cu	Zn	Sn
Concentration (M)	0.005	0.4	0.02	0.005	0.4	0.02	0.005	0.4	0.04
Trisodium citrate $Na_3C_6H_5O_7$ Concentration (M)	0.2			0.2			0.2		
pH value of the individual solution	6.91	3.15	6.35	5.84	4.81	6.49	6.91	6.5	6.35
Deposition potential UPD (V)	-0.65			-0.65			-0.68		
EDTA concentration (M)	0.2	0.2	free	0.4	free	free	free	0.4	free
pH value of the deposition bath	6.76			6.5			6.76		
Deposition time (hr)	7			7			7		
EDX results (atom%)	Cu	12.91		Cu	2.45		Cu	41	
	Zn	0.06		Zn	0.09		Zn	0.16	
	Sn	0.99		Sn	0.46		Sn	6.46	
	S	9.29		S	2.39		S	29.7	
	Ti	27.08		Ti	25.69		Ti	12.10	
	O	49.68		O	65.03		O	10.13	

Appendix B

Figure B 1: Top surface FEG-SEM micrographs the as-synthesised CZTS/TiO_2 NTAs electrodeposited onto TiO_2 NTAs substrate from separate precursor solutions of Cu, Zn and Sn. The deposition of each element was conducted at UPD = -0.65 V for 1 h.

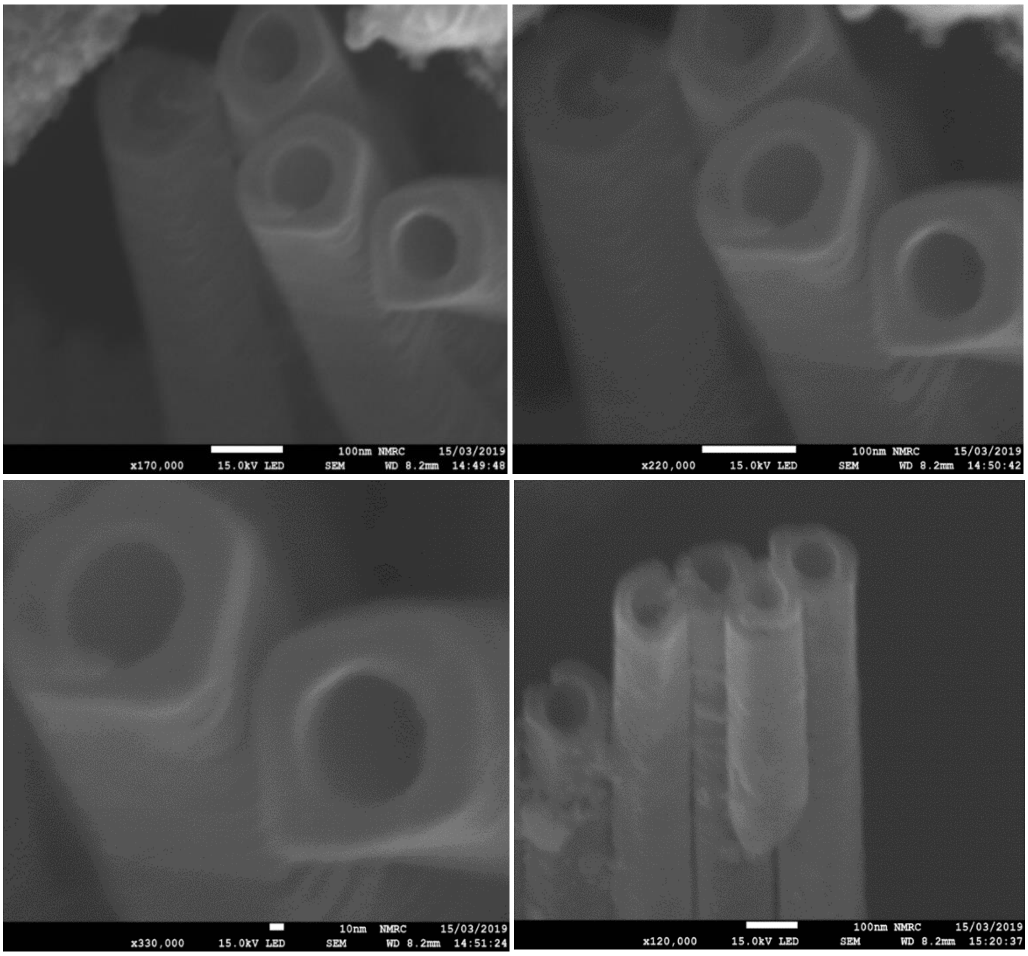

Figure B 2: UV-Vis absorbance spectra of Ag-doped CZTS/TiO_2 NTAs (a-d) and Ge-doped CZTS/TiO_2 NTAs (e-h).

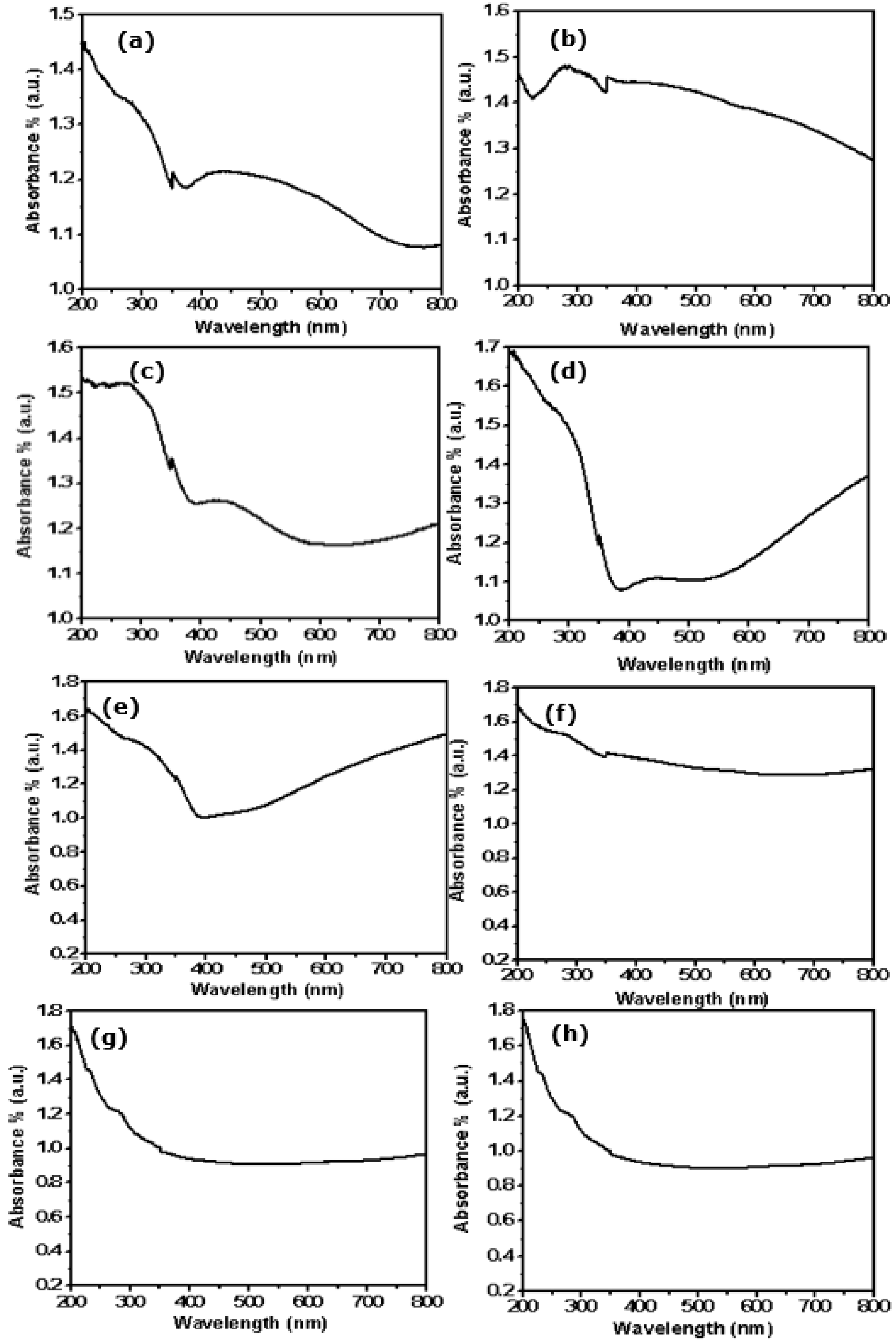

Figure B 3: Various magnifications of cross-section FEG-SEM micrographs for (a-c) Ag-doped and (d-f) Ge-doped CZTS/TiO_2 NTAs photoanodes electrodeposited onto TiO_2 NTAs substrate from separate precursor solutions of Cu, Zn and Sn. The deposition of each element was conducted at UPD = -0.65 V for 1 h.

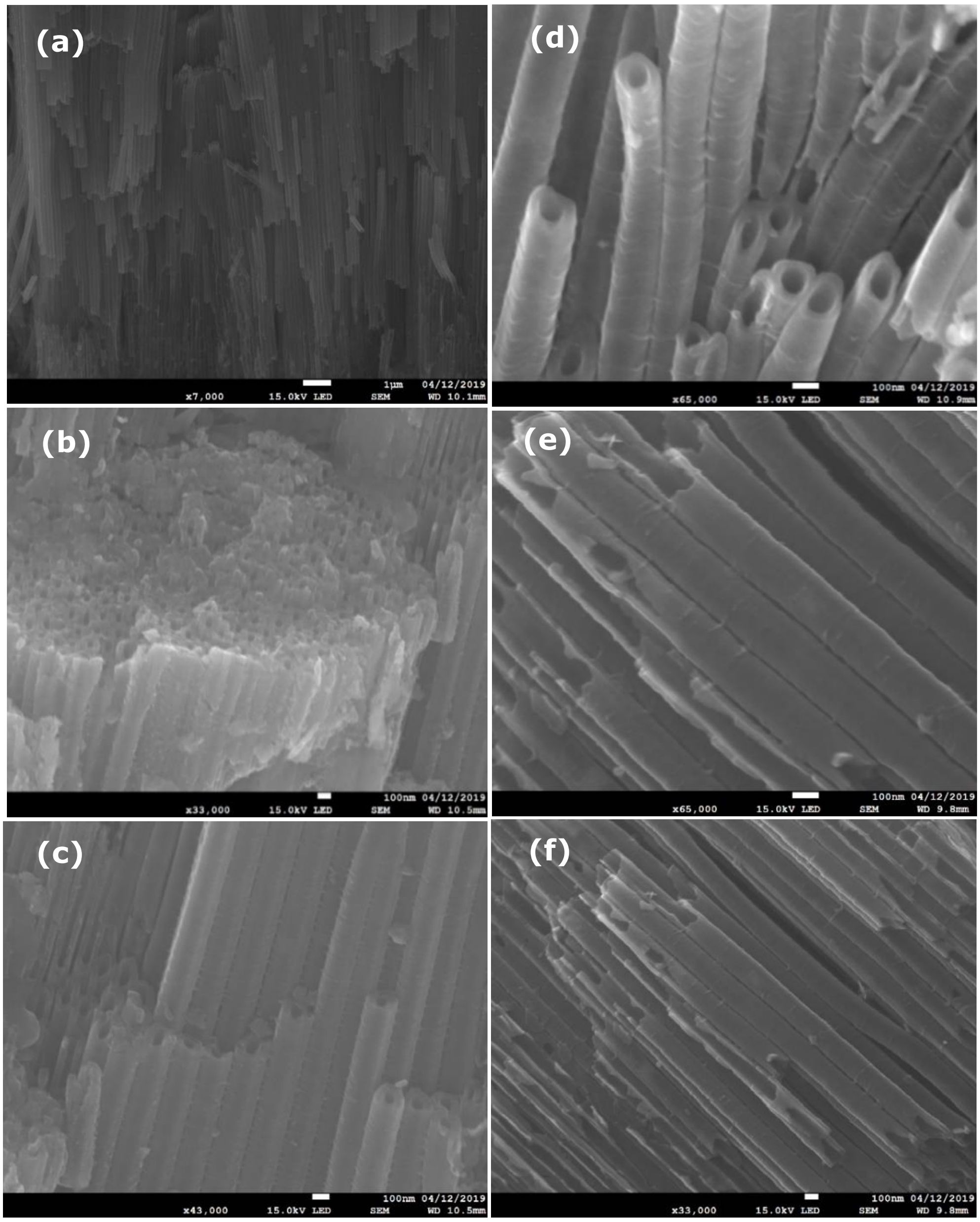

Figure B 4: Repeatability for the cyclic voltammograms of TiO_2 NTAs electrodes recorded at scan rate=20 mV s^{-1} in solution contains 0.02 M $CuSO_4$+ 0.2 trisodium citrate by applying potential ranges (1) (-1.25 to o.5)V; (2) (-1.35 to 0.85) V and (3) (-1.5 to 0.8) V.

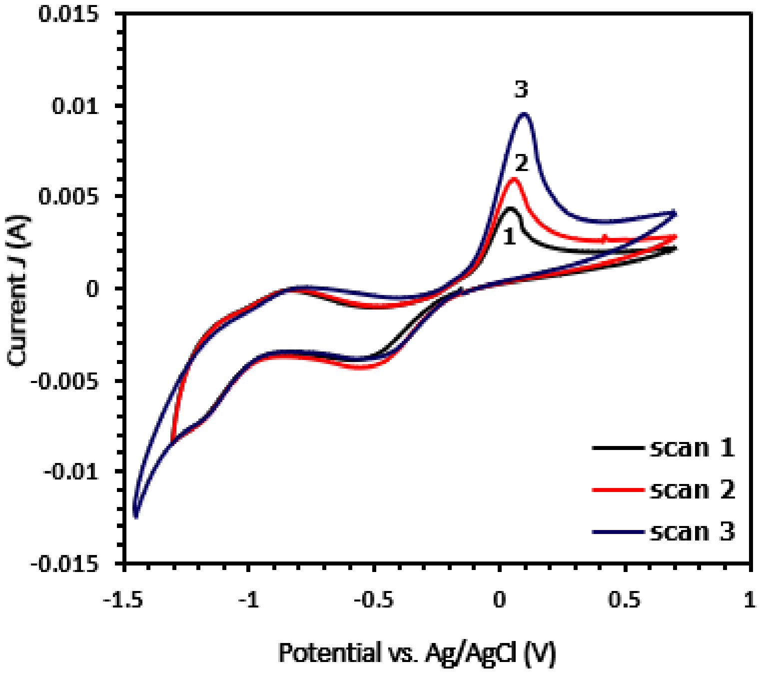

Figure B 5: Repeatability for the cyclic voltammograms of TiO_2 NTAs electrode recorded at scan rate=20 mV mV s^{-1} in solution contains 0.01 M $SnCl_2$+ 0.2 trisodium citrate by applying potential ranges (dotes) (-0.7.05 to 2); (dashed line) (-0.35 to 0.7.05) V and (blue line) (-0.35 to 0.85) V.

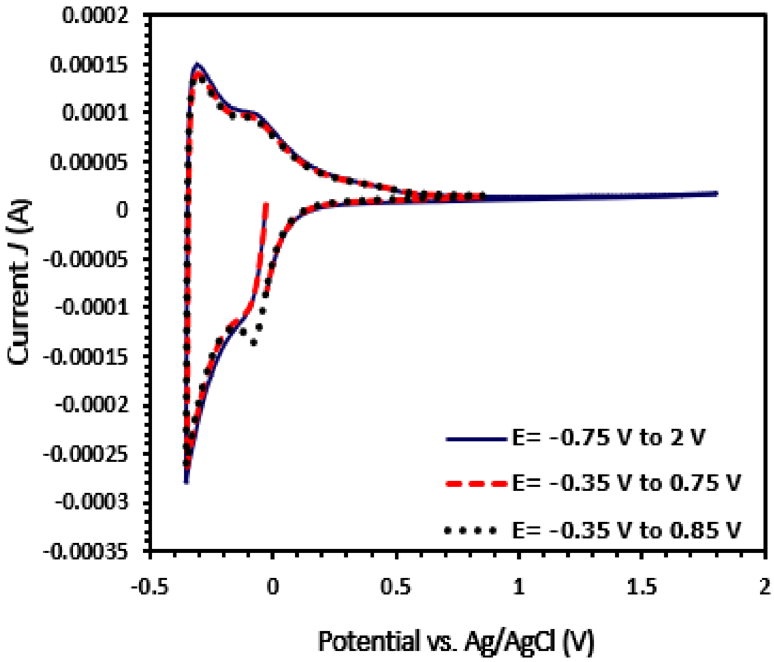

Figure B 6: Repeatability for the cyclic voltammograms of TiO_2 NTAs electrode recorded at scan rate=20 mV mV s^{-1} in solution contains

0.2 M $ZnSO_4$+ 0.2 trisodium citrate+ 40 mL DIW, at potential ranges (black) (-1 to 1.6) V; (red) (-0.48 to 1.4) V and (blue) (-0.5 to 1.5) V.

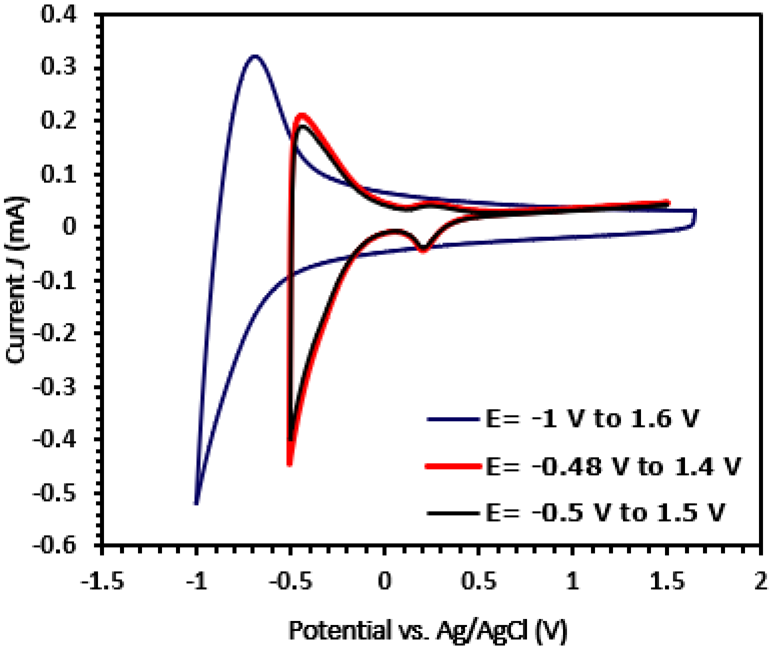

References

AALTONEN, T. 2005. Atomic layer deposition of noble metal thin films.

ABEDINISOHI, P. 2013. *Design and Fabrication of Silver Deposited TiO_2 Nanotubes: Antibacterial Applications.* Concordia University.

ABERMANN, S. 2013. Non-vacuum processed next generation thin film photovoltaics: towards marketable efficiency and production of CZTS based solar cells. *Solar Energy,* 94**,** 37-70.

ABUSNINA, M. 2016. Synthesis and characterization of kesterite Cu_2ZnSnS_4 (CZTS) thin films for solar cell application.

ALANYALıOĞLU, M., ÇAKAL, H., ÖZTÜRK, E. & DEMIR, Ü. 2001. Electrochemical studies of the effects of pH and the surface structure of gold substrates on the underpotential deposition of sulfur. *The Journal of Physical Chemistry B,* 105**,** 10588-10593.

ALUOCH, A. O., SADIK, O. A. & BEDI, G. 2005. Development of an oral biosensor for salivary amylase using a monodispersed silver for signal amplification. *Analytical biochemistry,* 340**,** 136-144.

ANANTHOJU, B., MOHAPATRA, J., JANGID, M. K., BAHADUR, D., MEDHEKAR, N. & ASLAM, M. 2016. Cation/anion substitution in Cu_2ZnSnS_4 for improved photovoltaic performance. *Scientific reports,* 6**,** 35369.

ANPO, M., KISHIGUCHI, S., ICHIHASHI, Y., TAKEUCHI, M., YAMASHITA, H., IKEUE, K., MORIN, B., DAVIDSON, A. & CHE, M. 2001. The design and development of second-generation titanium oxide photocatalysts able to operate under visible light irradiation by applying a metal ion-implantation method. *Research on Chemical Intermediates,* 27**,** 459-467.

ANSARI, S. A., KHAN, M. M., ANSARI, M. O. & CHO, M. H. 2016. Nitrogen-doped titanium dioxide (N-doped TiO_2) for visible light photocatalysis. *New Journal of Chemistry,* 40**,** 3000-3009.

ARAKI, H., KUBO, Y., MIKADUKI, A., JIMBO, K., MAW, W. S., KATAGIRI, H., YAMAZAKI, M., OISHI, K. & TAKEUCHI, A. 2009. Preparation of Cu_2ZnSnS_4 thin films by sulfurizing electroplated precursors. *Solar Energy Materials and Solar Cells,* 93**,** 996-999.

ARTERO, V., CHAVAROT-KERLIDOU, M. & FONTECAVE, M. 2011. Splitting water with cobalt. *Angewandte Chemie International Edition,* 50**,** 7238-7266.

ASAHI, R., MORIKAWA, T., OHWAKI, T., AOKI, K. & TAGA, Y. 2001. Visible-light photocatalysis in nitrogen-doped titanium oxides. *science,* 293**,** 269-271.

ASIKAINEN, T., RITALA, M., LESKELÄ, M., PROHASKA, T., FRIEDBACHER, G. & GRASSERBAUER, M. 1996. AFM and STM studies on In_2O_3 and ITO thin films deposited by atomic layer epitaxy. *Applied surface science,* 99**,** 91-98.

BABU, G. S., KUMAR, Y. K., BHASKAR, P. U. & RAJA, V. S. 2008. Effect of post-deposition annealing on the growth of $Cu_2ZnSnSe_4$ thin films for a solar cell absorber layer. *Semiconductor Science and Technology,* 23**,** 085023.

BAKOS, I., SZABO, S., NAGY, F., MALLA, T. & BODNA, Z. 1991. Study of the underpotential deposition of germanium onto polycrystalline palladium surfaces. *Journal of electroanalytical chemistry and interfacial electrochemistry,* 309**,** 293-301.

BARD, A. J. & WRIGHTON, M. S. 1977. Thermodynamic Potential for the Anodic Dissolution of n-Type Semiconductors A Crucial Factor Controlling Durability and Efficiency in Photoelectrochemical Cells and an Important Criterion in the Selection of New Electrode/Electrolyte Systems. *Journal of the Electrochemical Society,* 124**,** 1706-1710.

BAUR, W. H. 1961. Atomabstaende und bindungswinkel im brookit, TiO_2. *Acta Crystallographica,* 14**,** 214-216.

BECKER, J. S. 2003. *Atomic layer deposition of metal oxide and nitride thin films*.

BEHERA, G. 2015. *NANOSTRUCTURED COPPER SELENIDE: SYNTHESIS AND CHARACTERIZATION.*

BENSON, E. E., KUBIAK, C. P., SATHRUM, A. J. & SMIEJA, J. M. 2009. Electrocatalytic and homogeneous approaches to conversion of CO_2 to liquid fuels. *Chemical Society Reviews,* 38**,** 89-99.

BERNARDINI, G., BORRINI, D., CANESCHI, A., DI BENEDETTO, F., GATTESCHI, D., RISTORI, S. & ROMANELLI, M. 2000. EPR and SQUID magnetometry study of Cu_2FeSnS_4 (stannite) and Cu_2ZnSnS_4 (kesterite). *Physics and Chemistry of Minerals,* 27**,** 453-461.

BESSEGATO, G. G., GUARALDO, T. T., DE BRITO, J. F., BRUGNERA, M. F. & ZANONI, M. V. B. 2015. Achievements and Trends in Photoelectrocatalysis: from Environmental to Energy Applications. *Electrocatalysis,* 6**,** 415-441.

BOLTON, E. E., CHEN, J., KIM, S., HAN, L., HE, S., SHI, W., SIMONYAN, V., SUN, Y., THIESSEN, P. A. & WANG, J. 2011. PubChem3D: a new resource for scientists. *Journal of cheminformatics,* 3**,** 32.

BUDEVSKI, E., STAIKOV, G. & LORENZ, W. 1996. Electrochemical phase formation—an introduction to the initial stages of metal deposition. *VCH, Weiheim*.

BUDEVSKI, E., STAIKOV, G. & LORENZ, W. 2000. Electrocrystallization: nucleation and growth phenomena. *Electrochimica Acta,* 45**,** 2559-2574.

BUDEVSKI, E., STAIKOV, G., LORENZ, W. & KEUSLER, K. 1997. Electrochemical phase formation and growth. *Angewandte Chemie-German Edition,* 109**,** 1418-1418.

CARP, O., HUISMAN, C. L. & RELLER, A. 2004. Photoinduced reactivity of titanium dioxide. *Progress in solid state chemistry,* 32**,** 33-177.

CARUSO, R. A., SCHATTKA, J. H. & GREINER, A. 2001. Titanium dioxide tubes from sol–gel coating of electrospun polymer fibers. *Advanced Materials,* 13**,** 1577-1579.

CHANG, H.-T. 2013. High-efficiency photochemical water splitting of CdZnS/CdZnSe nanostructures. *Journal of Materials,* 2013.

CHANG, H., KAO, M.-J., KUO, C.-G. & CHOU, C.-Y. 2014. Effects of NH_4F concentrations of electrolytes and reaction time in the anodic oxidation process on the photovoltaic properties of back-illuminated DSSC. *International journal of precision engineering and manufacturing,* 15**,** 1187-1192.

CHANNEI, D., INCEESUNGVORN, B., WETCHAKUN, N., UKRITNUKUN, S., NATTESTAD, A., CHEN, J. & PHANICHPHANT, S. 2014. Photocatalytic degradation of methyl orange by CeO_2 and Fe–doped CeO_2 films under visible light irradiation. *Scientific reports,* 4**,** 5757.

CHEN, C. H., VESECKY, S. M. & GEWIRTH, A. A. 1992. In situ atomic force microscopy of underpotential deposition of silver on gold (111). *Journal of the American Chemical Society,* 114**,** 451-458.

CHEN, D., TAO, Q., LIAO, L. W., LIU, S. X., CHEN, Y. X. & YE, S. 2011a. Determining the active surface area for various platinum electrodes. *Electrocatalysis,* 2**,** 207.

CHEN, R., KIM, H., MCINTYRE, P. C. & BENT, S. F. 2005. Investigation of self-assembled monolayer resists for hafnium dioxide atomic layer deposition. *Chemistry of materials,* 17**,** 536-544.

CHEN, S.-Z., ZHANG, P.-Y., ZHUANG, D.-M. & ZHU, W.-P. 2004. Investigation of nitrogen doped TiO_2 photocatalytic films prepared by reactive magnetron sputtering. *Catalysis Communications,* 5**,** 677-680.

CHEN, S., GONG, X.-G., WALSH, A. & WEI, S.-H. 2011b. Structural, Electronic and Defect Properties of $Cu_2ZnSn(S, Se)_4$ Alloys. *MRS Online Proceedings Library Archive,* 1370.

CHEN, S., GONG, X., WALSH, A. & WEI, S.-H. 2009. Crystal and electronic band structure of Cu_2ZnSnX_4(X=S and Se) photovoltaic absorbers: First-principles insights. *Applied Physics Letters,* 94**,** 041903.

CHEN, S., GONG, X., WALSH, A. & WEI, S.-H. 2010a. Defect physics of the kesterite thin-film solar cell absorber Cu_2ZnSnS_4. *Applied Physics Letters,* 96**,** 021902.

CHEN, S., WALSH, A., GONG, X. G. & WEI, S. H. 2013a. Classification of lattice defects in the kesterite Cu_2ZnSnS_4 and $Cu_2ZnSnSe_4$ earth-abundant solar cell absorbers. *Advanced Materials,* 25**,** 1522-1539.

CHEN, S. & WANG, L.-W. 2012. Thermodynamic oxidation and reduction potentials of photocatalytic semiconductors in aqueous solution. *Chemistry of Materials,* 24**,** 3659-3666.

CHEN, X., LI, C., GRÄTZEL, M., KOSTECKI, R. & MAO, S. S. 2012. Nanomaterials for renewable energy production and storage. *Chemical Society Reviews,* 41**,** 7909-7937.

CHEN, X. & MAO, S. S. 2007. Titanium dioxide nanomaterials: synthesis, properties, modifications, and applications. *Chemical reviews,* 107**,** 2891-2959.

CHEN, X., SHEN, S., GUO, L. & MAO, S. S. 2010b. Semiconductor-based photocatalytic hydrogen generation. *Chemical reviews,* 110**,** 6503-6570.

CHEN, Z., DINH, H. N. & MILLER, E. 2013b. *Photoelectrochemical water splitting*, Springer.

CHONG, B., ZHU, W., LIU, Y., GUAN, L. & CHEN, G. Z. 2016. Highly efficient photoanodes based on cascade structural semiconductors of $Cu_2Se/CdSe/TiO_2$: a multifaceted approach to achieving microstructural and compositional control. *Journal of Materials Chemistry A,* 4**,** 1336-1344.

COLLETTI, L. P., FLOWERS, B. H. & STICKNEY, J. L. 1998. Formation of thin films of CdTe, CdSe, and CdS by electrochemical atomic layer epitaxy. *Journal of the Electrochemical Society,* 145**,** 1442-1449.

CRAP, O., HUISMAN, C. L., & RELLER, A. 2004. Photoinduced reactivity of titanium dioxide. *Progress in Solid State Chemistry,* 32(1-2)**,** 33-177.

CROMER, D. T. & HERRINGTON, K. 1955. The structures of anatase and rutile. *Journal of the American Chemical Society,* 77**,** 4708-4709.

CULLITY, B. 1978. Elements of X-ray Diffraction, 2nd edn.(Addision-Wesley, Reading, 1978). *Google Scholar***,** 1866.

D.M. KOLB, M. P., H. GERISCHER 1975. Further aspects concerning the correlation between underpotential deposition and work function differences. *Surface Science,* 51**,** 323.

DAGHRIR, R., DROGUI, P. & ROBERT, D. 2012. Photoelectrocatalytic technologies for environmental applications. *Journal of Photochemistry and Photobiology A: Chemistry,* 238**,** 41-52.

DEMIR, U. & SHANNON, C. 1994. A scanning tunneling microscopy study of electrochemically grown cadmium sulfide monolayers on Au (111). *Langmuir,* 10**,** 2794-2799.

DEMIR, U. & SHANNON, C. 1996. Reconstruction of cadmium sulfide monolayers on Au (100). *Langmuir,* 12**,** 594-596.

DHANALAKSHMI, K., LATHA, S., ANANDAN, S. & MARUTHAMUTHU, P. 2001. Dye sensitized hydrogen evolution from water. *International Journal of Hydrogen Energy,* 26**,** 669-674.

DHARMA, J., PISAL, A. & SHELTON, C. 2009. Simple method of measuring the band gap energy value of TiO_2 in the powder form using a UV/Vis/NIR spectrometer. *Application Note*.

DIEBOLD, U. 2003. The surface science of titanium dioxide. *Surface science reports,* 48**,** 53-229.

DIEBOLD, U. 2011. Photocatalysts: Closing the gap. *Nature chemistry,* 3**,** 271.

DILLI, Z. 2009. Intrinsic and extrinsic semiconductors, Fermi-Dirac distribution function, the Fermi level and carrier concentrations.

DÖNMEZ, İ. 2013. *Atomic layer deposition of metal oxide thin films and nanostructures.* Bilkent University.

DOYLE, M., RAJENDRAN, G., VIELSTICH, W., GASTEIGER, H. & LAMM, A. 2003. Handbook of Fuel Cells Fundamentals, Technology and Applications. *Fuel cell technology and applications,* 3.

EBRAHEEM, S. & EL-SAIED, A. 2013. Band gap determination from diffuse reflectance measurements of irradiated lead borate glass system doped with TiO_2 by using diffuse reflectance technique.

EHRLICH, G. & HUDDA, F. 1966. Atomic view of surface self-diffusion: tungsten on tungsten. *The Journal of Chemical Physics,* 44**,** 1039-1049.

FARINELLA, M., INGUANTA, R., SPANÒ, T., LIVRERI, P., PIAZZA, S. & SUNSERI, C. 2014. Electrochemical deposition of CZTS thin films on flexible substrate. *Energy Procedia,* 44**,** 105-110.

FERNANDES, P., SALOMÉ, P. & DA CUNHA, A. 2010. A study of ternary Cu_2SnS_3 and Cu_3SnS_4 thin films prepared by sulfurizing stacked metal precursors. *Journal of Physics D: Applied Physics,* 43**,** 215403.

FERNANDES, V., SALVIETTI, E., LOGLIO, F., LASTRAIOLI, E., INNOCENTI, M., MASCARO, L. & FORESTI, M. 2009. Electrodeposition of PbS multilayers on Ag (111) by ECALE. *Journal of applied electrochemistry,* 39**,** 2191.

FINKLEA, H. O., ED. 1988. Semiconductor Electrodes. *Amsterdam,*.

FLAMMERSBERGER, H. 2010. *Experimental study of* Cu_2ZnSnS_4 *thin films for solar cells*.

FLEGLER, S. L., HECKMAN JR, J. W. & KLOMPARENS, K. L. 1993. Scanning and transmission electron microscopy: an introduction. *Oxford University Press(UK), 1993*, 225.

FLOWERS, B. H., WADE, T. L., GARVEY, J. W., LAY, M., HAPPEK, U. & STICKNEY, J. L. 2002. Atomic layer epitaxy of CdTe using an automated electrochemical thin-layer flow deposition reactor. *Journal of Electroanalytical Chemistry,* 524-525**,** 273-285.

FORESTI, M., PEZZATINI, G., CAVALLINI, M., ALOISI, G., INNOCENTI, M. & GUIDELLI, R. 1998. Electrochemical atomic layer epitaxy deposition of CdS on Ag (111): An electrochemical and STM investigation. *The Journal of Physical Chemistry B,* 102**,** 7413-7420.

FRIEDLMEIER, T. M., WIESER, N., WALTER, T., DITTRICH, H. & SCHOCK, H. Heterojunctions based on Cu_2ZnSnS_4 and $Cu_2ZnSnSe_4$ thin films. Proceedings of the 14th European Conference of Photovoltaic Science and Engineering and Exhibition, 1997.

FRÖSCHL, T., HÖRMANN, U., KUBIAK, P., KUČEROVÁ, G., PFANZELT, M., WEISS, C. K., BEHM, R., HÜSING, N., KAISER, U. & LANDFESTER, K. 2012. High surface area crystalline titanium dioxide: potential and limits in electrochemical energy storage and catalysis. *Chemical Society Reviews,* 41**,** 5313-5360.

FUJISHIMA, A. & HONDA, K. 1972. Electrochemical Photolysis of Water at a Semiconductor Electrode. *Nature,* 238**,** 37.

GAO, D., LU, Z., WANG, C., LI, W. & DONG, P. 2018. Enhanced Photocatalytic Properties of Ag-Loaded N-Doped TiO_2 Nanotube Arrays. *Autex Research Journal,* 18**,** 67-72.

GARCIA, S., SALINAS, D., MAYER, C., SCHMIDT, E., STAIKOV, G. & LORENZ, W. 1998. Ag UPD on Au (100) and Au (111). *Electrochimica acta,* 43**,** 3007-3019.

GE, R., FU, W., YANG, H., ZHANG, Y., ZHAO, W., LIU, Z., WANG, C., ZHU, H., YU, Q. & ZOU, G. 2008. Fabrication and characterization of highly-ordered titania nanotubes via electrochemical anodization. *Materials Letters,* 62**,** 2688-2691.

GEORGE, S., OTT, A. & KLAUS, J. 1996. Surface chemistry for atomic layer growth. *The Journal of Physical Chemistry,* 100**,** 13121-13131.

GEORGE, S. M. 2009. Atomic layer deposition: an overview. *Chemical reviews,* 110**,** 111-131.

GERISCHER, H. 1977. On the stability of semiconductor electrodes against photodecomposition. *Journal of Electroanalytical Chemistry and Interfacial Electrochemistry,* 82**,** 133-143.

GERISCHER, H., KOLB, D. & PRZASNYSKI, M. 1974. Chemisorption of metal atoms on metal surfaces in correlation to work function differences. *Surface Science,* 43**,** 662-666.

GHOSH, P. Deposition of Thin Films on Solid Surfaces.

GHOSH, S., AVASTHI, D., SHAH, P., GANESAN, V., GUPTA, A., SARANGI, D., BHATTACHARYA, R. & ASSMANN, W. 2000. Deposition of thin films of different oxides of copper by RF reactive sputtering and their characterization. *Vacuum,* 57**,** 377-385.

GHRAIRI, N. & BOUAICHA, M. 2012. Structural, morphological, and optical properties of TiO_2 thin films synthesized by the electro phoretic deposition technique. *Nanoscale research letters,* 7**,** 357.

GICHUHI, A., BOONE, B. E., DEMIR, U. & SHANNON, C. 1998. Electrochemistry of S Adlayers at underpotentially deposited Cd on

Au (111): Implications for the electrosynthesis of high-quality CdS thin films. *The Journal of Physical Chemistry B,* 102**,** 6499-6506.

GICHUHI, A., SHANNON, C. & PERRY, S. S. 1999. A scanning tunneling microscopy and X-ray photoelectron spectroscopy study of electrochemically grown ZnS monolayers on Au (111). *Langmuir,* 15**,** 5654-5661.

GONG, D., GRIMES, C. A., VARGHESE, O. K., HU, W., SINGH, R., CHEN, Z. & DICKEY, E. C. 2001. Titanium oxide nanotube arrays prepared by anodic oxidation. *Journal of Materials Research,* 16**,** 3331-3334.

GRÄTZEL, M. 2001. Photoelectrochemical cells. *nature,* 414**,** 338.

GREGORY, B. W. & STICKNEY, J. L. 1991. Electrochemical atomic layer epitaxy (ECALE). *Journal of electroanalytical chemistry and interfacial electrochemistry,* 300**,** 543-561.

GRIMES, C. A. & MOR, G. K. 2009. *TiO_2 nanotube arrays: synthesis, properties, and applications*, Springer Science & Business Media.

GUPTA, S. M. & TRIPATHI, M. 2011. A review of TiO_2 nanoparticles. *Chinese Science Bulletin,* 56**,** 1639.

GURAV, K., PAWAR, S., SHIN, S. W., AGAWANE, G., PATIL, P., MOON, J.-H., YUN, J. & KIM, J. H. 2013. Electrosynthesis of CZTS films by sulfurization of CZT precursor: Effect of soft annealing treatment. *Applied Surface Science,* 283**,** 74-80.

H. KISCH , A. 2012. *Chem. Int. Ed.,* 51.

HABISREUTINGER, S. N., SCHMIDT-MENDE, L. & STOLARCZYK, J. K. 2013. Photocatalytic reduction of CO_2 on TiO_2 and other semiconductors. *Angewandte Chemie International Edition,* 52**,** 7372-7408.

HALL, S., SZYMANSKI, J. & STEWART, J. 1978. Kesterite, Cu<2)(Zn, Fe) SnS<4), and stannite, Cu<2)(Fe, Zn) SnS<4), structurally similar but distinct minerals. *The Canadian Mineralogist,* 16**,** 131-137.

HASHIMOTO, K., IRIE, H. & FUJISHIMA, A. 2005. TiO_2 photocatalysis: a historical overview and future prospects. *Japanese journal of applied physics,* 44**,** 8269.

HASSANIEN, A. & AKL, A. A. 2016. Effect of Se addition on optical and electrical properties of chalcogenide CdSSe thin films. *Superlattices and Microstructures,* 89**,** 153-169.

HENSEL, J., WANG, G., LI, Y. & ZHANG, J. Z. 2010. Synergistic effect of CdSe quantum dot sensitization and nitrogen doping of TiO_2 nanostructures for photoelectrochemical solar hydrogen generation. *Nano letters,* 10**,** 478-483.

HISATOMI, T., KUBOTA, J. & DOMEN, K. 2014. Recent advances in semiconductors for photocatalytic and photoelectrochemical water splitting. *Chemical Society Reviews,* 43**,** 7520-7535.

HOFFMANN, M. R., MARTIN, S. T., CHOI, W. & BAHNEMANN, D. W. 1995. Environmental applications of semiconductor photocatalysis. *Chemical reviews,* 95**,** 69-96.

HÖNES, K., ZSCHERPEL, E., SCRAGG, J. & SIEBENTRITT, S. 2009. Shallow defects in Cu_2ZnSnS_4. *Physica B: Condensed Matter,* 404**,** 4949-4952.

HOU, X., LI, Y., YAN, J.-J. & WANG, C.-W. 2014. Highly efficient photocatalysis of p-type Cu_2ZnSnS_4 under visible-light illumination. *Materials Research Bulletin,* 60**,** 628-633.

HUANG, B., COLLETTI, L., GREGORY, B., ANDERSON, J. & STICKNEY, J. 1995. Preliminary Studies of the Use of an Automated Flow-Cell

Electrodeposition System for the Formation of CdTe Thin Films by Electrochemical Atomic Layer Epitaxy. *Journal of the Electrochemical Society,* 142, 3007-3016.

HUANG, F., YAN, A. & ZHAO, H. 2016. Influences of doping on photocatalytic properties of TiO_2 photocatalyst. *Semiconductor Photocatalysis-Materials, Mechanisms and Applications.* InTech.

HUANG, L., SUN, C. & LIU, Y. 2007. Pt/N-codoped TiO_2 nanotubes and its photocatalytic activity under visible light. *Applied Surface Science,* 253, 7029-7035.

HUANG, M. H., WU, Y., FEICK, H., TRAN, N., WEBER, E. & YANG, P. 2001. Catalytic growth of zinc oxide nanowires by vapor transport. *Advanced Materials,* 13, 113-116.

HUANG, S., LUO, W. & ZOU, Z. 2013. Band positions and photoelectrochemical properties of Cu_2ZnSnS_4 thin films by the ultrasonic spray pyrolysis method. *Journal of Physics D: Applied Physics,* 46, 235108.

IBANEZ, J. G. & RAJESHWAR, K. 1997. *Environmental Electrochemistry*, Academic Press.

IBHADON, A. O. & FITZPATRICK, P. 2013. Heterogeneous photocatalysis: recent advances and applications. *Catalysts,* 3, 189-218.

IHANUS, J., RITALA, M., LESKELÄ, M., PROHASKA, T., RESCH, R., FRIEDBACHER, G. & GRASSERBAUER, M. 1997. AFM studies on ZnS thin films grown by atomic layer epitaxy. *Applied Surface Science,* 120, 43-50.

IHLENFELDT, W. D., BOLTON, E. E. & BRYANT, S. H. 2009. The PubChem chemical structure sketcher. *Journal of cheminformatics,* 1, 20.

IIJIMA, S. 1991. Helical microtubules of graphitic carbon. *nature,* 354, 56.

INNOCENTI, M., FORNI, F., PEZZATINI, G., RAITERI, R., LOGLIO, F. & FORESTI, M. 2001. Electrochemical behavior of As on silver single crystals and experimental conditions for InAs growth by ECALE. *Journal of Electroanalytical Chemistry,* 514, 75-82.

ISMAIL, A. A., AL-SAYARI, S. A. & BAHNEMANN, D. 2013. Photodeposition of precious metals onto mesoporous TiO_2 nanocrystals with enhanced their photocatalytic activity for methanol oxidation. *Catalysis today,* 209, 2-7.

ITO, K. & NAKAZAWA, T. 1988. Electrical and optical properties of stannite-type quaternary semiconductor thin films. *Japanese Journal of Applied Physics,* 27, 2094.

IWASHINA, K. & KUDO, A. 2011. Rh-doped $SrTiO_3$ photocatalyst electrode showing cathodic photocurrent for water splitting under visible-light irradiation. *Journal of the American Chemical Society,* 133, 13272-13275.

JAFARI, T., MOHARRERI, E., AMIN, A. S., MIAO, R., SONG, W. & SUIB, S. L. 2016. Photocatalytic water splitting—the untamed dream: a review of recent advances. *Molecules,* 21, 900.

JAROSZ, M., KAPUSTA-KOŁODZIEJ, J., JASKUŁA, M. & SULKA, G. D. 2015. Effect of different polishing methods on anodic titanium dioxide formation. *Journal of Nanomaterials,* 2015, 86.

JARVI, T. D. & STUVE, E. M. 1998. *Fundamental aspects of vacuum and electrocatalytic reactions of methanol and formic acid on platinum surfaces*, Wiley-VCH: New York.

JENNINGS, J. R., GHICOV, A., PETER, L. M., SCHMUKI, P. & WALKER, A. B. 2008. Dye-sensitized solar cells based on oriented TiO_2 nanotube arrays: transport, trapping, and transfer of electrons. *Journal of the American Chemical Society,* 130, 13364-13372.

JUNG, J. H., KOBAYASHI, H., VAN BOMMEL, K. J., SHINKAI, S. & SHIMIZU, T. 2002. Creation of novel helical ribbon and double-layered nanotube TiO_2 structures using an organogel template. *Chemistry of materials,* 14, 1445-1447.

KÄÄRIÄINEN, T., CAMERON, D., KÄÄRIÄINEN, M.-L. & SHERMAN, A. 2013. *Atomic layer deposition: principles, characteristics, and nanotechnology applications*, John Wiley & Sons.

KAR, A., RAJA, K. & MISRA, M. 2006. Electrodeposition of hydroxyapatite onto nanotubular TiO_2 for implant applications. *Surface and Coatings Technology,* 201, 3723-3731.

KASUGA, T., HIRAMATSU, M., HOSON, A., SEKINO, T. & NIIHARA, K. 1998. Formation of titanium oxide nanotube. *Langmuir,* 14, 3160-3163.

KATAGIRI, H. 2005. Cu_2ZnSnS_4 thin film solar cells. *Thin Solid Films,* 480, 426-432.

KATAGIRI, H., JIMBO, K., MAW, W. S., OISHI, K., YAMAZAKI, M., ARAKI, H. & TAKEUCHI, A. 2009. Development of CZTS-based thin film solar cells. *Thin Solid Films,* 517, 2455-2460.

KATAGIRI, H., SASAGUCHI, N., HANDO, S., HOSHINO, S., OHASHI, J. & YOKOTA, T. 1997. Preparation and evaluation of Cu_2ZnSnS_4 thin films by sulfurization of E□ B evaporated precursors. *Solar Energy Materials and Solar Cells,* 49, 407-414.

KATOH, M. 1979. Acetonitrile vacuum drying method. *Journal of Electron Microscopy,* 28, 145-145.

KHARE, A., HIMMETOGLU, B., JOHNSON, M., NORRIS, D. J., COCOCCIONI, M. & AYDIL, E. S. 2012. Calculation of the lattice dynamics and Raman spectra of copper zinc tin chalcogenides and comparison to experiments. *Journal of Applied Physics,* 111, 083707.

KIM, G. 2014. *A visible-light assisted dual purpose photoelectrochemical cell for simultaneous removal of heavy metals and organic pollutants in wastewater.* University of Nottingham.

KIM, H., SEOL, M., LEE, J. & YONG, K. 2011. Highly efficient photoelectrochemical hydrogen generation using hierarchical ZnO/WO_x nanowires cosensitized with CdSe/CdS. *The Journal of Physical Chemistry C,* 115, 25429-25436.

KIM, K., KIM, M.-J., KIM, S.-I. & JANG, J.-H. 2013. Towards visible light hydrogen generation: quantum dot-sensitization via efficient light harvesting of hybrid-TiO_2. *Scientific reports,* 3.

KISCH, H. 2014. Semiconductor Photocatalysis : Principles and Applications. 1 ed. Somerset: Wiley.

KLAUS, J., OTT, A., JOHNSON, J. & GEORGE, S. 1997. Atomic layer controlled growth of SiO_2 films using binary reaction sequence chemistry. *Applied Physics Letters,* 70, 1092-1094.

KNEZ, M., NIELSCH, K. & NIINISTÖ, L. 2007. Synthesis and surface engineering of complex nanostructures by atomic layer deposition. *Advanced Materials,* 19, 3425-3438.

KOKKINIDIS, G. 1986. Underpotential deposition and electrocatalysis. Elsevier.

KOLB, D., PRZASNYSKI, M. & GERISCHER, H. 1974. Underpotential deposition of metals and work function differences. *Journal of Electroanalytical Chemistry and Interfacial Electrochemistry,* 54**,** 25-38.

KONDARIDES, D. I. 2010a. PHOTOCATALYSIS. *[Ed. Gabriele Centi], in Encyclopedia of Life Support Systems (EOLSS)*.

KONDARIDES, D. I. 2010b. PHOTOCATALYSIS, in Catalysis. *Encyclopedia of Life Support Systems (EOLSS).* Paris, France: Eolss.

KUDO, A. & MISEKI, Y. 2009. Heterogeneous photocatalyst materials for water splitting. *Chemical Society Reviews,* 38**,** 253-278.

KUMAR, M. & PERSSON, C. 2013. Cu_2ZnSnS_4 and $Cu_2ZnSnSe_4$ as Potential Earth-Abundant Thin-Film Absorber Materials: A Density Functional Theory Study. *Int. J. Theor. Appl. Sci,* 5**,** 1-8.

KUMAR, Y. K., BABU, G. S., BHASKAR, P. U. & RAJA, V. S. 2009a. Effect of starting-solution pH on the growth of Cu_2ZnSnS_4 thin films deposited by spray pyrolysis. *physica status solidi (a),* 206**,** 1525-1530.

KUMAR, Y. K., BABU, G. S., BHASKAR, P. U. & RAJA, V. S. 2009b. Preparation and characterization of spray-deposited Cu_2ZnSnS_4 thin films. *Solar Energy Materials and Solar Cells,* 93**,** 1230-1237.

LABCONCO, I. 2008. A Guide to Freeze Drying for the Laboratory.

LATROCHE, M., BROHAN, L., MARCHAND, R. & TOURNOUX, M. 1989. New hollandite oxides: $TiO_2(H)$ and $K_{0.06}TiO_2$. *Journal of Solid State Chemistry,* 81**,** 78-82.

LEARY, R. & WESTWOOD, A. 2011. Carbonaceous nanomaterials for the enhancement of TiO_2 photocatalysis. *Carbon,* 49**,** 741-772.

LEE, J. P. & SUNG, M. M. 2004. A new patterning method using photocatalytic lithography and selective atomic layer deposition. *Journal of the American Chemical Society,* 126**,** 28-29.

LEE, S., JEON, C. & PARK, Y. 2004. Fabrication of TiO_2 tubules by template synthesis and hydrolysis with water vapor. *Chemistry of materials,* 16**,** 4292-4295.

LEE, Y.-L., CHI, C.-F. & LIAU, S.-Y. 2009. CdS/CdSe co-sensitized TiO_2 photoelectrode for efficient hydrogen generation in a photoelectrochemical cell. *Chemistry of materials,* 22**,** 922-927.

LESKELÄ, M. & RITALA, M. 1995. Atomic layer epitaxy in deposition of various oxide and nitride thin films. *Le Journal de Physique IV,* 5**,** C5-937-C5-951.

LESKELÄ, M. & RITALA, M. 2003. Atomic layer deposition chemistry: recent developments and future challenges. *Angewandte Chemie International Edition,* 42**,** 5548-5554.

LEWIS, N. S. 2007. Toward cost-effective solar energy use. *science,* 315**,** 798-801.

LEWIS, N. S. & NOCERA, D. G. 2006. Powering the planet: Chemical challenges in solar energy utilization. *Proceedings of the National Academy of Sciences,* 103**,** 15729-15735.

LI, D., LIN, S., LI, S., HUANG, X., CAO, X. & LI, J. 2012. Effects of geometric and crystal structures on the photoelectrical properties of highly ordered TiO_2 nanotube arrays. *Journal of Materials Research,* 27**,** 1029-1036.

LI, J. & WU, N. 2015. Semiconductor-based photocatalysts and photoelectrochemical cells for solar fuel generation: a review. *Catalysis Science & Technology,* 5**,** 1360-1384.

LI, X., YU, J., LOW, J., FANG, Y., XIAO, J. & CHEN, X. 2015. Engineering heterogeneous semiconductors for solar water splitting. *Journal of Materials Chemistry A,* 3**,** 2485-2534.

LI, Y., LU, Q., WU, S., WANG, L. & SHI, X. 2013a. Hydrogen peroxide sensing using ultrathin platinum-coated gold nanoparticles with core@ shell structure. *Biosensors and Bioelectronics,* 41**,** 576-581.

LI, Y., YU, H., ZHANG, C., SONG, W., LI, G., SHAO, Z. & YI, B. 2013b. Effect of water and annealing temperature of anodized TiO_2 nanotubes on hydrogen production in photoelectrochemical cell. *Electrochimica Acta,* 107**,** 313-319.

LIANG, X., JAYARAJU, N. & STICKNEY, J. L. 2007. Aqueous Ge Atomic Layer Deposition on Au. *ECS Transactions,* 11**,** 249-258.

LIANG, X., KIM, Y.-G., GEBERGZIABIHER, D. K. & STICKNEY, J. L. 2009. Aqueous electrodeposition of Ge monolayers. *Langmuir,* 26**,** 2877-2884.

LIANG, Y.-C., WANG, C.-C., KEI, C.-C., HSUEH, Y.-C., CHO, W.-H. & PERNG, T.-P. 2011. Photocatalysis of Ag-loaded TiO_2 nanotube arrays formed by atomic layer deposition. *The Journal of Physical Chemistry C,* 115**,** 9498-9502.

LIN, S., LI, D., WU, J., LI, X. & AKBAR, S. 2011. A selective room temperature formaldehyde gas sensor using TiO_2 nanotube arrays. *Sensors and Actuators B: Chemical,* 156**,** 505-509.

LIN, X., KAVALAKKATT, J., KORNHUBER, K., LEVCENKO, S., LUX-STEINER, M. C. & ENNAOUI, A. 2013. Structural and optical properties of Cu_2ZnSnS_4 thin film absorbers from ZnS and Cu_3SnS_4 nanoparticle precursors. *Thin Solid Films,* 535**,** 10-13.

LIN, Y.-P., CHI, Y.-F., HSIEH, T.-E., CHEN, Y.-C. & HUANG, K.-P. 2016a. Preparation of Cu_2ZnSnS_4 (CZTS) sputtering target and its application to the fabrication of CZTS thin-film solar cells. *Journal of Alloys and Compounds,* 654**,** 498-508.

LIN, Y.-P., CHI, Y.-F., HSIEH, T.-E., CHEN, Y.-C. & HUANG, K.-P. 2016b. Preparation of Cu_2ZnSnS_4 (CZTS) sputtering target and its application to the fabrication of CZTS thin-film solar cells. *Journal of Alloys and Compounds,* 654**,** 498-508.

LINSEBIGLER, A. L., LU, G. & YATES JR, J. T. 1995. Photocatalysis on TiO_2 surfaces: principles, mechanisms, and selected results. *Chemical reviews,* 95**,** 735-758.

LIU, S., GAN, L., LIU, L., ZHANG, W. & ZENG, H. 2002. Synthesis of single-crystalline TiO_2 nanotubes. *Chemistry of materials,* 14**,** 1391-1397.

LIU, X., LIU, Z., HAO, S. & CHU, W. 2012. Facile fabrication of well-dispersed silver nanoparticles loading on TiO_2 nanotube arrays by electrodeposition. *Materials Letters,* 80**,** 66-68.

LOGLIO, F., INNOCENTI, M., JAREK, A., CAPORALI, S., PASQUINI, I. & FORESTI, M. 2010. Nickel sulfur thin films deposited by ECALE: Electrochemical, XPS and AFM characterization. *Journal of Electroanalytical Chemistry,* 638**,** 15-20.

LU, J., ELAM, J. W. & STAIR, P. C. 2013. Synthesis and stabilization of supported metal catalysts by atomic layer deposition. *Accounts of chemical research,* 46**,** 1806-1815.

LU, J., ELAM, J. W. & STAIR, P. C. 2016. Atomic layer deposition—Sequential self-limiting surface reactions for advanced catalyst "bottom-up" synthesis. *Surface Science Reports,* 71**,** 410-472.

LY, N. T., DAO, T. H., PHAM, D. L., DO, H. M. & VU, D. L. 2013. Optical properties of TiO_2 nanotube arrays fabricated by the electrochemical anodization method. *Advances in Natural Sciences: Nanoscience and Nanotechnology,* 5**,** 015004.

MACDONALD, J. R. & BARSOUKOV, E. 2005. Impedance spectroscopy: theory, experiment, and applications. *History,* 1**,** 1-13.

MAGNFÄLT, D. 2014. *Fundamental processes in thin film growth: The origin of compressive stress and the dynamics of the early growth stages.* Linköping University Electronic Press.

MARSCHALL, R. 2014. Semiconductor composites: strategies for enhancing charge carrier separation to improve photocatalytic activity. *Advanced Functional Materials,* 24**,** 2421-2440.

MAYER, T., ELAM, J., GEORGE, S., KOTULA, P. & GOEKE, R. 2003. Atomic-layer deposition of wear-resistant coatings for microelectromechanical devices. *Applied Physics Letters,* 82**,** 2883-2885.

MEISSNER, D., MEMMING, R. & KASTENING, B. 1988. Photoelectrochemistry of cadmium sulfide. 1. Reanalysis of photocorrosion and flat-band potential. *The Journal of Physical Chemistry,* 92**,** 3476-3483.

MERKA, O., BAHNEMANN, D. W. & WARK, M. 2012. Improved photocatalytic hydrogen production by structure optimized nonstoichiometric $Y_2Ti_2O_7$. *ChemCatChem,* 4**,** 1819-1827.

MO, S.-D. & CHING, W. 1995. Electronic and optical properties of three phases of titanium dioxide: Rutile, anatase, and brookite. *Physical Review B,* 51**,** 13023.

MOCATTA, D., COHEN, G., SCHATTNER, J., MILLO, O., RABANI, E. & BANIN, U. 2011. Heavily doped semiconductor nanocrystal quantum dots. *Science,* 332**,** 77-81.

MONFORT, O. & PLESCH, G. 2018. Bismuth vanadate-based semiconductor photocatalysts: a short critical review on the efficiency and the mechanism of photodegradation of organic pollutants. *Environmental Science and Pollution Research***,** 1-18.

MOR, G. K., SHANKAR, K., PAULOSE, M., VARGHESE, O. K. & GRIMES, C. A. 2006. Use of highly-ordered TiO_2 nanotube arrays in dye-sensitized solar cells. *Nano letters,* 6**,** 215-218.

MORIYA, K., WATABE, J., TANAKA, K. & UCHIKI, H. 2006. Characterization of Cu_2ZnSnS_4 thin films prepared by photo-chemical deposition. *physica status solidi c,* 3**,** 2848-2852.

MOSHE, H. & MASTAI, Y. 2013. Atomic layer deposition on self-assembled-monolayers. *Materials Science-Advanced Topics.* InTech.

MROZEK, P., SUNG, Y.-E., HAN, M., GAMBOA-ALDECO, M., WIECKOWSKI, A., CHEN, C.-H. & GEWIRTH, A. A. 1995. Coadsorption of sulfate anions and silver adatoms on the Au (111) single crystal electrode. Ex situ and in situ comparison. *Electrochimica acta,* 40**,** 17-28.

MUNNIK, P., DE JONGH, P. E. & DE JONG, K. P. 2015. Recent developments in the synthesis of supported catalysts. *Chemical reviews,* 115**,** 6687-6718.

MURPHY, A. 2007. Band-gap determination from diffuse reflectance measurements of semiconductor films, and application to photoelectrochemical water-splitting. *Solar Energy Materials and Solar Cells,* 91**,** 1326-1337.

MUSCAT, J., SWAMY, V. & HARRISON, N. M. 2002. First-principles calculations of the phase stability of TiO_2. *Physical Review B,* 65**,** 224112.

NAGAVENI, K., HEGDE, M. & MADRAS, G. 2004. Structure and photocatalytic activity of $Ti_{1-x}M_xO_{2\pm\delta}$(M=W, V, Ce, Zr, Fe, and Cu) synthesized by solution combustion method. *The Journal of Physical Chemistry B,* 108**,** 20204-20212.

NAKAYAMA, N. & ITO, K. 1996. Sprayed films of stannite Cu_2ZnSnS_4. *Applied Surface Science,* 92**,** 171-175.

NAVROTSKY, A., JAMIESON, J. C. & KLEPPA, O. J. 1967. Enthalpy of transformation of a high-pressure polymorph of titanium dioxide to the rutile modification. *Science,* 158**,** 388-389.

NELSON, J. 2003. *The physics of solar cells*, World Scientific Publishing Company.

NGUYEN, D.-C., ITO, S. & DUNG, D. V. A. 2015. Effects of annealing conditions on crystallization of the CZTS absorber and photovoltaic properties of Cu(Zn, Sn)(S, Se)$_2$ solar cells. *Journal of Alloys and Compounds,* 632**,** 676-680.

NI, M., LEUNG, M. K., LEUNG, D. Y. & SUMATHY, K. 2007. A review and recent developments in photocatalytic water-splitting using TiO_2 for hydrogen production. *Renewable and Sustainable Energy Reviews,* 11**,** 401-425.

NIINISTÖ, L., RITALA, M. & LESKELÄ, M. 1996. Synthesis of oxide thin films and overlayers by atomic layer epitaxy for advanced applications. *Materials Science and Engineering: B,* 41**,** 23-29.

NOAH, N. M., MARCELLS, O., ALMALLETI, A., LIM, J. & SADIK, O. A. 2011. Metal Enhanced Electrochemical Cyclooxygenase-2(COX-2) Sensor for Biological Applications. *Electroanalysis,* 23**,** 2392-2399.

NORTON, B. 2013. *Harnessing solar heat*, Springer.

O'REGAN, B. & GRÄTZEL, M. 1991. A low-cost, high-efficiency solar cell based on dye-sensitized colloidal TiO_2 films. *nature,* 353**,** 737.

OGAKI, K. & ITAYA, K. 1995. In situ scanning tunneling microscopy of underpotential and bulk deposition of silver on gold (111). *Electrochimica acta,* 40**,** 1249-1257.

OHTANI, B. 2010. Photocatalysis A to Z—What we know and what we do not know in a scientific sense. *Journal of Photochemistry and Photobiology C: Photochemistry Reviews,* 11**,** 157-178.

ONG, K. G., VARGHESE, O. K., MOR, G. K. & GRIMES, C. A. 2005. Numerical simulation of light propagation through highly-ordered titania nanotube arrays: Dimension optimization for improved photoabsorption. *Journal of nanoscience and nanotechnology,* 5**,** 1801-1808.

OSTERLOH, F. E. & PARKINSON, B. A. 2011. Recent developments in solar water-splitting photocatalysis. *MRS bulletin,* 36**,** 17-22.

OTHMER, K. 1983. Encyclopedia of Chemical Technology, vol. 23. John Wiley & Sons, New York.

OTT, A., MCCARLEY, K., KLAUS, J., WAY, J. & GEORGE, S. 1996. Atomic layer controlled deposition of Al_2O_3 films using binary reaction sequence chemistry. *Applied Surface Science,* 107**,** 128-136.

OVIEDO, O. A., REINAUDI, L., GARCÍA, S. G. & LEIVA, E. P. M. 2015. *Underpotential deposition: from fundamentals and theory to applications at the nanoscale*, Springer.

OVIEDO, O. A., REINAUDI, L., GARCÍA, S. G. & LEIVA, E. P. M. 2016. Experimental Techniques and Structure of the Underpotential Deposition Phase. *Underpotential Deposition.* Springer.

ÖZNÜLÜER, T., ERDOĞAN, İ., ŞIŞMAN, İ. & DEMIR, Ü. 2005. Electrochemical atom-by-atom growth of PbS by modified ECALE method. *Chemistry of materials,* 17**,** 935-937.

PAIER, J., ASAHI, R., NAGOYA, A. & KRESSE, G. 2009. Cu_2ZnSnS_4 as a potential photovoltaic material: a hybrid Hartree-Fock density functional theory study. *Physical Review B,* 79**,** 115126.

PALMAS, S., DA POZZO, A., MASCIA, M., VACCA, A., ARDU, A., MATARRESE, R. & NOVA, I. 2011. Effect of the preparation conditions on the performance of TiO_2 nanotube arrays obtained by electrochemical oxidation. *international journal of hydrogen energy,* 36**,** 8894-8901.

PAN, L., ZOU, J.-J., WANG, S., LIU, X.-Y., ZHANG, X. & WANG, L. 2012. Morphology evolution of TiO_2 facets and vital influences on photocatalytic activity. *ACS applied materials & interfaces,* 4**,** 1650-1655.

PARK, H., PARK, Y., KIM, W. & CHOI, W. 2013. Surface modification of TiO_2 photocatalyst for environmental applications. *Journal of Photochemistry and Photobiology C: Photochemistry Reviews,* 15**,** 1-20.

PARK, M. H., JANG, Y. J., SUNG-SUH, H. M. & SUNG, M. M. 2004. Selective atomic layer deposition of titanium oxide on patterned self-assembled monolayers formed by microcontact printing. *Langmuir,* 20**,** 2257-2260.

PARSONS, R. & VANDERNOOT, T. 1988. The oxidation of small organic molecules: A survey of recent fuel cell related research. *Journal of electroanalytical chemistry and interfacial electrochemistry,* 257**,** 9-45.

PAULOSE, M., SHANKAR, K., VARGHESE, O. K., MOR, G. K., HARDIN, B. & GRIMES, C. A. 2006a. Backside illuminated dye-sensitized solar cells based on titania nanotube array electrodes. *Nanotechnology,* 17**,** 1446.

PAULOSE, M., SHANKAR, K., YORIYA, S., PRAKASAM, H. E., VARGHESE, O. K., MOR, G. K., LATEMPA, T. A., FITZGERALD, A. & GRIMES, C. A. 2006b. Anodic growth of highly ordered TiO_2 nanotube arrays to 134 µm in length. *The Journal of Physical Chemistry B,* 110**,** 16179-16184.

PELÁEZ-ABELLÁN, E., FERNÁNDEZ-CONDE, D. & VALDÉS-PEDROSO, M. 2012. First Approach to the Synthesis and Applications of TitaniaNanotube Primera Aproximación a la Síntesis y Aplicaciones de Nanotubos de Oxido de Titanio. *Revista CENIC Ciencias Químicas,* 43.

PERERA, S. D., MARIANO, R. G., VU, K., NOUR, N., SEITZ, O., CHABAL, Y. & BALKUS JR, K. J. 2012. Hydrothermal synthesis of graphene-TiO_2 nanotube composites with enhanced photocatalytic activity. *Acs Catalysis,* 2**,** 949-956.

PERILLO, P. M. & RODRIGUEZ, D. F. 2012. Growth control of TiO_2 nanotubes in different physical environments. *Nanoscience Methods,* 1**,** 194-200.

PERSSON, C. 2010. Electronic and optical properties of Cu_2ZnSnS_4 and $Cu_2ZnSnSe_4$. *Journal of Applied Physics,* 107**,** 053710.

PHOTOMETRIC, I. 2015, Oct 23. *Field emission scanning electron microscopy (FESEM)* [Online]. Available: https://photometrics.net/field-emission-scanning-electron-microscopy-fesem/ [Accessed].

PICHAT, P. 2014. Are TiO_2 nanotubes worth using in photocatalytic purification of air and water? *Molecules,* 19**,** 15075-15087.

PIRKANNIEMI, K. 2007. A Study of Short-term Toxicity, Catalytic Oxidative Degradation and Concentrations in Industrial Waste Waters. *Department of Environmental Sciences, University of Kuopio*.

PLESKOV, Y. V. & GUREVICH, Y. Y. 1986. Semiconductor photoelectrochemistry.

PORE, V. 2010. Atomic layer deposition and photocatalytic properties of titanium dioxide thin films.

PUURUNEN, R. L. 2005. Surface chemistry of atomic layer deposition: A case study for the trimethylaluminum/water process. *Journal of applied physics,* 97**,** 9.

QIAO, Z., SHANG, W. & WANG, C. 2005. Fabrication of Sn–Se compounds on a gold electrode by electrochemical atomic layer epitaxy. *Journal of Electroanalytical Chemistry,* 576**,** 171-175.

QUEISSER, H. J. & HALLER, E. E. 1998. Defects in semiconductors: some fatal, some vital. *Science,* 281**,** 945-950.

RAJA, K., MAHAJAN, V. & MISRA, M. 2006a. Determination of photo conversion efficiency of nanotubular titanium oxide photo-electrochemical cell for solar hydrogen generation. *Journal of power sources,* 159**,** 1258-1265.

RAJA, K. S., MAHAJAN, V. K. & MISRA, M. 2006b. Determination of photo conversion efficiency of nanotubular titanium oxide photo-electrochemical cell for solar hydrogen generation. *Journal of Power Sources,* 159**,** 1258-1265.

RAJESHWAR, K., DE TACCONI, N. R. & CHENTHAMARAKSHAN, C. 2001. Semiconductor-based composite materials: preparation, properties, and performance. *Chemistry of Materials,* 13**,** 2765-2782.

RAJESHWAR, K. & IBANEZ, J. G. 1995. Electrochemical aspects of photocatalysis: application to detoxification and disinfection scenarios. *Journal of chemical education,* 72**,** 1044.

RAJH, T., DIMITRIJEVIC, N. M., BISSONNETTE, M., KORITAROV, T. & KONDA, V. 2014. Titanium dioxide in the service of the biomedical revolution. *Chemical reviews,* 114**,** 10177-10216.

RAVELLI, D., DONDI, D., FAGNONI, M. & ALBINI, A. 2009. Photocatalysis. A multi-faceted concept for green chemistry. *Chemical Society Reviews,* 38**,** 1999-2011.

REITH, P. & HOPMAN, G. 2012. *Investigating electrodeposition to grow CZTS thin films for solar cell applications.* University of Twente.

RITALA, M. & LESKELA, M. 2001. Handbook of thin film materials. *Deposition and processing of thin films,* 1**,** 103.

RITALA, M. & LESKELÄ, M. 1999. Atomic layer epitaxy-a valuable tool for nanotechnology? *Nanotechnology,* 10**,** 19.

RITALA, M. & LESKELÄ, M. 2002. Atomic layer deposition. *Handbook of Thin Films.* Elsevier.

RITALA, M., LESKELÄ, M., JOHANSSON, L.-S. & NIINISTÖ, L. 1993. Atomic force microscopy study of titanium dioxide thin films grown by atomic layer epitaxy. *Thin Solid Films,* 228**,** 32-35.

RITALA, M., LESKELÄ, M., NIINISTÖ, L., PROHASKA, T., FRIEDBACHER, G. & GRASSERBAUER, M. 1994. Development of crystallinity and morphology in hafnium dioxide thin films grown by atomic layer epitaxy. *Thin solid films,* 250**,** 72-80.

RITALA, M., SALONIEMI, H., LESKELÄ, M., PROHASKA, T., FRIEDBACHER, G. & GRASSERBAUER, M. 1996. Studies on the morphology of Al_2O_3 thin films grown by atomic layer epitaxy. *Thin Solid Films,* 286**,** 54-58.

ROORYCK, V., RENIERS, F., BUESS-HERMAN, C., ATTARD, G. & YANG, X. 2000. The silver upd on gold (111) revisited. *Journal of electroanalytical chemistry,* 482**,** 93-101.

ROY, P., BERGER, S. & SCHMUKI, P. 2011. TiO_2 nanotubes: synthesis and applications. *Angewandte Chemie International Edition,* 50**,** 2904-2939.

SADANANDAM, G., LALITHA, K., KUMARI, V. D., SHANKAR, M. V. & SUBRAHMANYAM, M. 2013. Cobalt doped TiO_2: A stable and efficient photocatalyst for continuous hydrogen production from glycerol: Water mixtures under solar light irradiation. *international journal of hydrogen energy,* 38**,** 9655-9664.

SAJI, V. S. & LEE, C.-W. 2013. Selenium electrochemistry. *RSC Advances,* 3**,** 10058-10077.

SAKTHIVEL, S., SHANKAR, M. V., PALANICHAMY, M., ARABINDOO, B., BAHNEMANN, D. W. & MURUGESAN, V. 2004. Enhancement of photocatalytic activity by metal deposition: characterisation and photonic efficiency of Pt, Au and Pd deposited on TiO_2 catalyst. *Water Research,* 38**,** 3001-3008.

SALEEM, M. R., ALI, R., KHAN, M. B., HONKANEN, S. & TURUNEN, J. 2014. Impact of atomic layer deposition to nanophotonic structures and devices. *Frontiers in Materials,* 1**,** 18.

SARSWAT, P. K., BHATTACHARYYA, D., FREE, M. L. & MISRA, M. 2016. Augmented Z scheme blueprint for efficient solar water splitting system using quaternary chalcogenide absorber material. *Physical Chemistry Chemical Physics,* 18**,** 3788-3803.

SARSWAT, P. K. & FREE, M. L. 2012. A comparative study of co-electrodeposited Cu_2ZnSnS_4 absorber material on fluorinated tin oxide and molybdenum substrates. *Journal of electronic materials,* 41**,** 2210-2215.

SARSWAT, P. K., SNURE, M., FREE, M. L. & TIWARI, A. 2012. CZTS thin films on transparent conducting electrodes by electrochemical technique. *Thin Solid Films,* 520**,** 1694-1697.

SATO, N. 1998. *Electrochemistry at metal and semiconductor electrodes*, Elsevier.

SCARAMUZZO, F. A., PASQUALIA, M., MURAA, F., POZIOB, A., DELL'ERAA, A. & CURULLIC, A. 2014a. TiO_2 nanotubes photo-anode: An innovative cell design. *Chem. Eng,* 41.

SCARAMUZZO, F. A., PASQUALIA, M., MURAA, F., POZIOB, A., DELL'ERAA, A. & CURULLIC, A. 2014b. TiO_2 nanotubes photo-anode: An innovative cell design. *CHEMICAL ENGINEERING,* 41.

SCHORR, S. 2007. Structural aspects of adamantine like multinary chalcogenides. *Thin Solid Films,* 515**,** 5985-5991.

SCHORR, S. 2011. The crystal structure of kesterite type compounds: A neutron and X-ray diffraction study. *Solar Energy Materials and Solar Cells,* 95**,** 1482-1488.

SCHWARZ, J. A., CONTESCU, C. & CONTESCU, A. 1995. Methods for preparation of catalytic materials. *Chemical Reviews,* 95**,** 477-510.

SCHWOEBEL, R. L. & SHIPSEY, E. J. 1966. Step motion on crystal surfaces. *Journal of Applied Physics,* 37**,** 3682-3686.

SCLAFANI, A., PALMISANO, L. & SCHIAVELLO, M. 1990. Influence of the preparation methods of titanium dioxide on the photocatalytic degradation of phenol in aqueous dispersion. *Journal of physical chemistry,* 94**,** 829-832.

SCRAGG, J. J. 2010. *Studies of Cu_2ZnSnS_4 films prepared by sulfurisation of electrodeposited precursors.* University of Bath.

SEABOLD, J. A., SHANKAR, K., WILKE, R. H., PAULOSE, M., VARGHESE, O. K., GRIMES, C. A. & CHOI, K.-S. 2008. Photoelectrochemical properties of heterojunction CdTe/TiO_2 electrodes constructed using highly ordered TiO_2 nanotube arrays. *Chemistry of Materials,* 20**,** 5266-5273.

SEKINO, T. 2010. Synthesis and applications of titanium oxide nanotubes. *Inorganic and Metallic Nanotubular Materials.* Springer.

ŞENNIK, E., COLAK, Z., KıLıNÇ, N. & ÖZTÜRK, Z. Z. 2010. Synthesis of highly-ordered TiO_2 nanotubes for a hydrogen sensor. *International Journal of Hydrogen Energy,* 35**,** 4420-4427.

SEOL, J.-S., LEE, S.-Y., LEE, J.-C., NAM, H.-D. & KIM, K.-H. 2003. Electrical and optical properties of Cu_2ZnSnS_4 thin films prepared by rf magnetron sputtering process. *Solar Energy Materials and Solar Cells,* 75**,** 155-162.

SERPONE, N. & EMELINE, A. 2012. Semiconductor Photocatalysis☐ Past, Present, and Future Outlook. ACS Publications.

SERPONE, N. & PELIZZETTI, E. 1989. *Photocatalysis: fundamentals and applications*.

SETIADI, S. A. 2011. Photocatalytic hydrogen generation from glycerol and water using Pt loaded N-doped TiO_2 nanotube.

SHANGGUAN, W., YOSHIDA, A. & CHEN, M. 2003. Physicochemical properties and photocatalytic hydrogen evolution of TiO_2 films prepared by sol–gel processes. *Solar Energy Materials and Solar Cells,* 80**,** 433-441.

SHAO, M., ODELL, J. H., CHOI, S.-I. & XIA, Y. 2013. Electrochemical surface area measurements of platinum-and palladium-based nanoparticles. *Electrochemistry Communications,* 31**,** 46-48.

SHERIDAN, L. B., GEBREGZIABIHER, D. K., STICKNEY, J. L. & ROBINSON, D. B. 2013. Formation of palladium nanofilms using electrochemical atomic layer deposition (E-ALD) with chloride complexation. *Langmuir,* 29**,** 1592-1600.

SIEBENTRITT, S. & SCHORR, S. 2012. Kesterites—a challenging material for solar cells. *Progress in Photovoltaics: Research and Applications,* 20**,** 512-519.

SIMONS, P. & DACHILLE, F. 1967. The structure of TiO_2II, a high-pressure phase of TiO_2. *Acta Crystallographica,* 23**,** 334-336.

ŞIŞMAN, İ., ALANYALıOĞLU, M. & DEMIR, Ü. 2007. Atom-by-atom growth of CdS thin films by an electrochemical co-deposition method: Effects of pH on the growth mechanism and structure. *The Journal of Physical Chemistry C,* 111**,** 2670-2674.

SMITH, R. A. 1964. Semiconductors.

SRIMUANGMAK, K. & NIYOMWAS, S. 2011. Effects of voltage and addition of water on photocatalytic activity of TiO_2 nanotubes prepared by anodization method. *Energy Procedia,* 9**,** 435-439.

ŠTENGL, V. & KRÁLOVÁ, D. 2011. TiO_2/ZnS/CdS nanocomposite for hydrogen evolution and orange II dye degradation. *International Journal of Photoenergy,* 2011.

STICKNEY, J. L. 1999. Electrochemical atomic layer epitaxy. *Electroanalytical chemistry,* 21**,** 75-209.

STICKNEY, J. L. W., T. L.; FLOWERS, B. H., JR.; VAIDYANATHAN, R.; HAPPEK, U. 2002. Encyclopedia of Electrochemistry.

SU, Z., YAN, C., SUN, K., HAN, Z., LIU, F., LIU, J., LAI, Y., LI, J. & LIU, Y. 2012. Preparation of Cu_2ZnSnS_4 thin films by sulfurizing stacked precursor thin films via successive ionic layer adsorption and reaction method. *Applied Surface Science,* 258**,** 7678-7682.

SUDHA, V. & SANGARANARAYANAN, M. 2002. Underpotential deposition of metals: structural and thermodynamic considerations. *The Journal of Physical Chemistry B,* 106**,** 2699-2707.

SUN, H., ZHAO, P., ZHANG, F., LIU, Y. & HAO, J. 2015. Ag_2S/CdS/TiO_2 nanotube array films with high photocurrent density by spotting sample method. *Nanoscale research letters,* 10**,** 1.

SUN, S., ZHANG, J., GAO, P., WANG, Y., LI, X., WU, T., WANG, Y., CHEN, Y. & YANG, P. 2017. Full visible-light absorption of TiO_2 nanotubes induced by anionic S22−doping and their greatly enhanced photocatalytic hydrogen production abilities. *Applied Catalysis B: Environmental,* 206**,** 168-174.

SUNTOLA, T. 1989. Atomic layer epitaxy. *Materials Science Reports,* 4**,** 261-312.

SWIERK, J. R. & MALLOUK, T. E. 2013. Design and development of photoanodes for water-splitting dye-sensitized photoelectrochemical cells. *Chemical Society Reviews,* 42**,** 2357-2387.

TAFALLA, D., SALVADOR, P. & BENITO, R. 1990. Kinetic Approach to the Photocurrent Transients in Water Photoelectrolysis at n-TiO_2 Electrodes II. Analysis of the Photocurrent-Time Dependence. *Journal of The Electrochemical Society,* 137**,** 1810-1815.

TANAKA, K., CAPULE, M. F. & HISANAGA, T. 1991. Effect of crystallinity of TiO_2 on its photocatalytic action. *Chemical Physics Letters,* 187**,** 73-76.

TANAKA, K., OONUKI, M., MORITAKE, N. & UCHIKI, H. 2009. Cu_2ZnSnS_4 thin film solar cells prepared by non-vacuum processing. *Solar Energy Materials and Solar Cells,* 93**,** 583-587.

TANAKA, T., KAWASAKI, D., NISHIO, M., GUO, Q. & OGAWA, H. 2006. Fabrication of Cu_2ZnSnS_4 thin films by co-evaporation. *physica status solidi C,* 3**,** 2844-2847.

TANAKA, T., NAGATOMO, T., KAWASAKI, D., NISHIO, M., GUO, Q., WAKAHARA, A., YOSHIDA, A. & OGAWA, H. 2005. Preparation of Cu_2ZnSnS_4 thin films by hybrid sputtering. *Journal of Physics and Chemistry of Solids,* 66**,** 1978-1981.

TANSKANEN, J. T., BAKKE, J. R., BENT, S. F. & PAKKANEN, T. A. 2010. ALD growth characteristics of ZnS films deposited from organozinc and hydrogen sulfide precursors. *Langmuir,* 26**,** 11899-11906.

TAO, J., LIU, J., HE, J., ZHANG, K., JIANG, J., SUN, L., YANG, P. & CHU, J. 2014. Synthesis and characterization of Cu_2ZnSnS_4 thin films by the sulfurization of co-electrodeposited Cu–Zn–Sn–S precursor layers for solar cell applications. *RSC Advances,* 4**,** 23977-23984.

THAMBIDURAI, C., KIM, Y.-G. & STICKNEY, J. L. 2008. Electrodeposition of Ru by atomic layer deposition (ALD). *Electrochimica Acta,* 53**,** 6157-6164.

THOMPSON, T. L. & YATES, J. T. 2006. Surface science studies of the photoactivation of TiO_2 new photochemical processes. *Chemical Reviews,* 106**,** 4428-4453.

TIZNADO, H., BOUMAN, M., KANG, B.-C., LEE, I. & ZAERA, F. 2008. Mechanistic details of atomic layer deposition (ALD) processes for metal nitride film growth. *Journal of Molecular Catalysis A: Chemical,* 281**,** 35-43.

TLEMÇANI, T. S., BENAMAR, E. B., EL MOURSLI, F. C., HAJJI, F., EDFOUF, Z., TAIBI, M., LABRIM, H., BELHORMA, B., AAZOU, S. & SCHMERBER, G. 2015. Deposition Time Effect on the Physical Properties of Cu_2ZnSnS_4 (CZTS) Thin Films Obtained by Electrodeposition Route onto Mo-coated Glass Substrates. *Energy Procedia,* 84**,** 127-133.

TORIMOTO, T., OBAYASHI, A., KUWABATA, S., YASUDA, H., MORI, H. & YONEYAMA, H. 2000. Preparation of size-quantized ZnS thin films using electrochemical atomic layer epitaxy and their photoelectrochemical properties. *Langmuir,* 16**,** 5820-5824.

TORRES, I. Z., BUENO, J. P. & VONG, Y. M. 2014. Process of growth TiO_2 nanotubes by anodization in an organic media.

TRAN, P. D., XI, L., BATABYAL, S. K., WONG, L. H., BARBER, J. & LOO, J. S. C. 2012. Enhancing the photocatalytic efficiency of TiO_2 nanopowders for H_2 production by using non-noble transition metal co-catalysts. *Physical Chemistry Chemical Physics,* 14**,** 11596-11599.

TRAVIS, C. D. & ADOMAITIS, R. A. 2013. Dynamic modeling for the design and cyclic operation of an atomic layer deposition (ALD) reactor. *Processes,* 1**,** 128-152.

UCHIDA, H., MIURA, M. & WATANABE, M. 1995. Electrochemical quartz crystal microbalance study of silver ad-atoms on highly ordered Au (111) electrodes in sulfuric acid. *Journal of Electroanalytical Chemistry,* 386**,** 261-265.

VAIDYANATHAN, R., COX, S. M., HAPPEK, U., BANGA, D., MATHE, M. K. & STICKNEY, J. L. 2006. Preliminary studies in the electrodeposition of PbSe/PbTe superlattice thin films via electrochemical atomic layer deposition (ALD). *Langmuir,* 22**,** 10590-10595.

VAIDYANATHAN, R., STICKNEY, J. L., COX, S. M., COMPTON, S. P. & HAPPEK, U. 2003. Formation of In_2Se_3 thin films and nanostructures using electrochemical atomic layer epitaxy. *Journal of Electroanalytical Chemistry,* 559**,** 55-61.

VALOTA, A., LECLERE, D., SKELDON, P., CURIONI, M., HASHIMOTO, T., BERGER, S., KUNZE, J., SCHMUKI, P. & THOMPSON, G. 2009. Influence of water content on nanotubular anodic titania formed in fluoride/glycerol electrolytes. *Electrochimica Acta,* 54**,** 4321-4327.

VARGHESE, O. K. & GRIMES, C. A. 2008. Appropriate strategies for determining the photoconversion efficiency of water photoelectrolysis cells: a review with examples using titania nanotube array photoanodes. *Solar Energy Materials and Solar Cells,* 92**,** 374-384.

VASEKAR, P. S. & DHAKAL, T. P. 2013. Thin film solar cells using earth-abundant materials. *Solar Cells-Research and Application Perspectives.* InTech.

WADE, T. L., VAIDYANATHAN, R., HAPPEK, U. & STICKNEY, J. L. 2001. Electrochemical formation of a III–V compound semiconductor superlattice: InAs/InSb. *Journal of Electroanalytical Chemistry,* 500**,** 322-332.

WALSH, F. C. & HERRON, M. E. 1991. Electrocrystallization and electrochemical control of crystal growth: fundamental considerations and electrodeposition of metals. *Journal of Physics D: Applied Physics,* 24**,** 217.

WALTER, M. G., WARREN, E. L., MCKONE, J. R., BOETTCHER, S. W., MI, Q., SANTORI, E. A. & LEWIS, N. S. 2010. Solar water splitting cells. *Chemical reviews,* 110**,** 6446-6473.

WALUKIEWICZ, W. 1989. Amphoteric native defects in semiconductors. *Applied physics letters,* 54**,** 2094-2096.

WANG, C., HU, Q., HUANG, J., ZHU, C., DENG, Z., SHI, H., WU, L., LIU, Z. & CAO, Y. 2014a. Enhanced hydrogen production by water splitting using Cu-doped TiO_2 film with preferred (0 0 1) orientation. *Applied Surface Science,* 292**,** 161-164.

WANG, D., ZHOU, F., LIU, Y. & LIU, W. 2008. Synthesis and characterization of anatase TiO_2 nanotubes with uniform diameter from titanium powder. *Materials Letters,* 62**,** 1819-1822.

WANG, H., ZHU, W., CHONG, B. & QIN, K. 2014b. Improvement of photocatalytic hydrogen generation from CdSe/CdS/TiO_2 nanotube-array coaxial heterogeneous structure. *International Journal of Hydrogen Energy,* 39**,** 90-99.

WANG, L.-N. & LUO, J.-L. 2011. Formation of hydroxyapatite coating on anodic titanium dioxide nanotubes via an efficient dipping treatment. *Metallurgical and Materials Transactions A,* 42**,** 3255-3264.

WANG, M., CHEN, L. & SUN, L. 2012. Recent progress in electrochemical hydrogen production with earth-abundant metal complexes as catalysts. *Energy & Environmental Science,* 5**,** 6763-6778.

WANG, W.-Y. & CHEN, B.-R. 2013. Characterization and photocatalytic activity of TiO_2 nanotube films prepared by anodization. *International Journal of Photoenergy,* 2013.

WANG, W., WINKLER, M. T., GUNAWAN, O., GOKMEN, T., TODOROV, T. K., ZHU, Y. & MITZI, D. B. 2014c. Device characteristics of CZTSSe thin-film solar cells with 12.6% efficiency. *Advanced Energy Materials,* 4**,** 1301465.

WANG, X.-J., WANG, Q., LI, F.-T., YANG, W.-Y., ZHAO, Y., HAO, Y.-J. & LIU, S.-J. 2013. Novel BiOCl–C_3N_4 heterojunction photocatalysts: in situ preparation via an ionic-liquid-assisted solvent-thermal route and their visible-light photocatalytic activities. *Chemical engineering journal,* 234**,** 361-371.

WANG, Z. & DEMOPOULOS, G. P. 2015. Growth of Cu_2ZnSnS_4 nanocrystallites on TiO_2 nanorod arrays as novel extremely thin absorber solar cell structure via the successive-ion-layer-adsorption-reaction method. *ACS applied materials & interfaces,* 7**,** 22888-22897.

WATTS, J. F. & WOLSTENHOLME, J. 2003. An introduction to surface analysis by XPS and AES. *An Introduction to Surface Analysis by XPS and AES, by John F. Watts, John Wolstenholme, pp. 224. ISBN 0-470-84713-1. Wiley-VCH, May 2003.***,** 224.

WEI, L., CHEN, Y., ZHAO, J. & LI, Z. 2013. Preparation of NiS/$ZnIn_2S_4$ as a superior photocatalyst for hydrogen evolution under visible light irradiation. *Beilstein journal of nanotechnology,* 4**,** 949-955.

XU, H., OUYANG, S., LIU, L., REUNCHAN, P., UMEZAWA, N. & YE, J. 2014. Recent advances in TiO_2-based photocatalysis. *Journal of Materials Chemistry A,* 2**,** 12642-12661.

YAN, M., KOIDE, Y., BABCOCK, J., MARKWORTH, P., BELOT, J., MARKS, T. & CHANG, R. 2001. Selective-area atomic layer epitaxy growth of ZnO features on soft lithography-patterned substrates. *Applied Physics Letters,* 79**,** 1709-1711.

YANG, J., WANG, D., HAN, H. & LI, C. 2013. Roles of cocatalysts in photocatalysis and photoelectrocatalysis. *Accounts of chemical research,* 46**,** 1900-1909.

YANG, J., ZHU, W., GAO, X., BAO, S., FAN, X., DUAN, X. & HOU, J. 2006. Formation and characterization of Sb_2Te_3 nanofilms on Pt by electrochemical atomic layer epitaxy. *The Journal of Physical Chemistry B,* 110**,** 4599-4604.

YANG, W. S. & KANG, S. W. 2006. Comparative study on chemical stability of dielectric oxide films under HF wet and vapor etching for radiofrequency microelectromechanical system application. *Thin solid films,* 500**,** 231-236.

YE, M., GONG, J., LAI, Y., LIN, C. & LIN, Z. 2012. High-efficiency photoelectrocatalytic hydrogen generation enabled by palladium quantum dots-sensitized TiO_2 nanotube arrays. *Journal of the American Chemical Society,* 134**,** 15720-15723.

YEH, M. Y., LEE, C. C. & WUU, D. S. 2009. Influences of synthesizing temperatures on the properties of Cu_2ZnSnS_4 prepared by sol–gel spin-coated deposition. *Journal of sol-gel science and technology,* 52**,** 65-68.

YIN, Y., JIN, Z. & HOU, F. 2007. Enhanced solar water-splitting efficiency using core/sheath heterostructure CdS/TiO_2 nanotube arrays. *Nanotechnology,* 18**,** 495608.

YOKOYAMA, H., TANIMOTO, M., SHINOHARA, M. & INOUE, N. 1994. Self-limiting and step-propagating nature of GaAs atomic layer epitaxy revealed by atomic force microscopy. *Applied surface science,* 82**,** 158-163.

YONG, K. & JEONG, J. 2002. Applications of atomic layer chemical vapor deposition for the processing of nanolaminate structures. *Korean Journal of Chemical Engineering,* 19**,** 451-462.

YOUNGBLOOD, W. J., LEE, S.-H. A., MAEDA, K. & MALLOUK, T. E. 2009. Visible light water splitting using dye-sensitized oxide semiconductors. *Accounts of chemical research,* 42**,** 1966-1973.

ZHANG, J., ZHOU, P., LIU, J. & YU, J. 2014. New understanding of the difference of photocatalytic activity among anatase, rutile and brookite TiO_2. *Physical Chemistry Chemical Physics,* 16**,** 20382-20386.

ZHANG, Q., GAO, L. & GUO, J. 2000. Effects of calcination on the photocatalytic properties of nanosized TiO_2 powders prepared by $TiCl_4$ hydrolysis. *Applied Catalysis B: Environmental,* 26**,** 207-215.

ZHANG, X., SHI, X., YE, W., MA, C. & WANG, C. 2009. Electrochemical deposition of quaternary Cu_2ZnSnS_4 thin films as potential solar cell material. *Applied Physics A,* 94**,** 381-386.

ZHAO, J., CHEN, C. & MA, W. 2005. Photocatalytic degradation of organic pollutants under visible light irradiation. *Topics in catalysis,* 35**,** 269-278.

ZHOU, W., YANG, J., WANG, J., LI, Y., KUANG, X., TANG, J. & LIANG, H. 2012. Study on the effects of 5d energy locations of Ce^{3+} ions on NIR quantum cutting process in Y_2SiO_5: Ce^+, Yb^{3+}. *Optics express,* 20**,** A510-A518.

ZHU, J. & ZÄCH, M. 2009. Nanostructured materials for photocatalytic hydrogen production. *Current Opinion in Colloid & Interface Science,* 4**,** 260-269.

ZHU, W., LIU, X., LIU, H., TONG, D., YANG, J. & PENG, J. 2010. Coaxial heterogeneous structure of TiO_2 nanotube arrays with CdS as a superthin coating synthesized *via* modified electrochemical atomic layer deposition. *Journal of the American Chemical Society,* 132**,** 12619-12626.

ZHU, W., LIU, X., LIU, H., TONG, D., YANG, J. & PENG, J. 2011a. An efficient approach to control the morphology and the adhesion properties of anodized TiO_2 nanotube arrays for improved photoconversion efficiency. *Electrochimica Acta,* 56**,** 2618-2626.

ZHU, W., LIU, X., LIU, H., TONG, D., YANG, J. & PENG, J. 2011b. An efficient approach to control the morphology and the adhesion properties of anodized TiO_2 nanotube arrays for improved photoconversion efficiency. *Electrochimica Acta,* 56**,** 2618-2626.

ZHU, W., YANG, J., HOU, J., GAO, X., BAO, S. & FAN, X. 2005. Optimization of the formation of bismuth telluride thin film by using ECALE. *Journal of Electroanalytical Chemistry,* 585**,** 83-88.

ZHU, W., YANG, J., ZHOU, D., BAO, S., FAN, X. & DUAN, X. 2007. Electrochemical characterization of the underpotential deposition of tellurium on Au electrode. *Electrochimica acta,* 52**,** 3660-3666.

ZIMMERMANN, H. 2000. Basics of optical emission and absorption. *Integrated Silicon Optoelectronics.* Springer.

ZUR, A., MCGILL, T. & SMITH, D. 1983. *The effect of doping on Fermi level position at a semiconductor–metal interface.* AVS.